

The Vertical City Weather Generator

by
Mohsen Moradi

A Thesis
presented to
The University of Guelph

In partial fulfillment of requirements
for the degree of
Doctor of Philosophy
in
Engineering

Guelph, Ontario, Canada
© Mohsen Moradi, July, 2021

ABSTRACT

THE VERTICAL CITY WEATHER GENERATOR

Mohsen Moradi

University of Guelph, 2021

Advisors:

Dr. Amir A. Aliabadi

Dr. E. Scott Krayenhoff

The increased rates of urban expansion and replacement of natural areas by artificial surfaces have drastically changed the land use and land cover, and consequently have brought numerous environmental issues at various scales. Urban climate models can predict the environmental impacts of cities through incorporating energy, mass, and momentum analyses.

A comprehensive simulation of urban climate requires adequate representation of the essential physical processes that involve exchanges of momentum (via drag), heat (via radiation, convection, and conduction), and water (via precipitation, evaporation, or evapotranspiration) between the atmosphere and the impervious, vegetated, or soil surfaces.

In this thesis, a new urban microclimate model, called Vertical City Weather Generator (VCWG), is presented, which attempts to overcome some limitations in the previous studies. It consists of a rural model, an urban vertical diffusion model, a building energy model, a radiation model with trees, an urban surface energy balance model, and an urban hydrology model. VCWG models the dynamic interaction between the mentioned sub-models to resolve vertical profiles of climate variables, including temperature, wind, and specific hu-

midity; to compute temperatures and water content in urban surfaces and sub-surfaces; to compute building environmental variables such as indoor temperature and specific humidity; and to compute energy metrics such as building water/energy/electricity demands and the associated heat or humidity fluxes imposed on the outdoor environment.

VCWG is evaluated against the Basel UrBan Boundary Layer Experiment (BUBBLE) field measurements conducted in Basel, Switzerland, in 2001-2002 and the Sunset neighborhood field measurements conducted in Vancouver, Canada, in 2008. The simulation results exhibit reasonable agreement with the measured datasets. The performance of VCWG is further assessed by conducting various explorations on the model's components, which are in reasonable agreement with the previous studies. VCWG can be used as a design, prediction, or investigation tool to understand how urban climate variables are influenced as a function of forcing environmental conditions and urban configurations. It can be used for simulations to provide details at micro-scale, while it is very computationally-efficient and suitable for large spatio-temporal scale analyses.

Contribution Statement

Dr. Bruno Bueno developed the original Urban Weather Generator (UWG) program in MATLAB, parts of which are used in VCWG v1.3.2 (Building Energy Model (BEM) and the Urban Canopy Model (UCM)) and VCWG v2.0.0 (BEM). Chris Mackey and Saeran Vasanthakumar translated UWG from MATLAB to Python. Dr. Alberto Martilli developed the original one-dimensional vertical diffusion model in Fortran. Prof. E. Scott Krayenhoff and Dr. Negin Nazarian refined the one-dimensional vertical diffusion model in Fortran, which was integrated into both versions of VCWG. Prof. E. Scott Krayenhoff modified the one-dimensional vertical diffusion model to account for trees. This model was used in both versions of VCWG. Dr. Naika Meili developed the radiation (integrated into both versions of VCWG) and hydrology (integrated into VCWG v2.0.0) models in MATLAB. Prof. James Voogt and Prof. Andreas Christen supplied field observation data for the purpose of model evaluation. Mohsen Moradi integrated and refined the above models into one or both versions of VCWG, translated codes from MATLAB and Fortran to Python, evaluated VCWG against field observations, and explored both versions of VCWG for different urban morphometric parameters, radiation configurations, urban vegetation, building energy configuration, climate zones, and seasons.

Acknowledgements

In the course of my doctoral work, I had the privilege to meet and collaborate with great scientists in urban climates. I would first like to express my sincere gratitude to my supervisors Prof. Amir A. Aliabadi and Prof. E. Scott Krayenhoff for their invaluable advice and providing me with this opportunity to do this research project. This dissertation would not have been possible without their never ending guidance and support. I am also grateful to committee member Prof. Andrew Binns for his insightful comments on my thesis.

I would like to acknowledge the invaluable contribution of Prof. Leslie K. Norford from Department of Architecture, MIT, MA, USA and Dr. Bruno Bueno at Fraunhofer Institute for Solar Energy Systems ISE, Freiburg, Germany, who developed and shared the Urban Weather Generator (UWG) program. Their partnership in our work together solved many of the questions arisen in the exploration of building energy and urban climatology studies.

I express my sincere appreciation to Dr. Alberto Martilli at the Center for Energy, Environment and Technology (CIEMAT) in Madrid, Spain, who developed and shared an earlier version of the one-dimensional vertical diffusion model for the urban climate.

I would like to thank Prof. Andreas Christen at Environmental Meteorology, University of Freiburg, Freiburg, Germany, who provided the observation data from an extended period of the BUBBLE campaign, and Prof. James Voogt from Department of Geography and Environment, University of Western Ontario, Canada, for giving access to the observation data from the Vancouver Sunset campaign.

Many thanks go to Dr. Negin Nazarian at ARC Centre of Excellence for Climate Extremes, University of New South Wales, Sydney, Australia, who contributed to the development of VCWG v1.3.2 and providing me with valuable comments on the simulation results.

I would also like to thank Chris Mackey and Saeran Vasanthakumar who translated UWG from MATLAB to Python and Dr. Naika Meili at Institute of Environmental Engineering, ETH Zürich, Zürich, Switzerland, who developed and shared an earlier version of the urban radiation and hydrology model.

I am grateful for all the support I have received from the entire University of Guelph; other academics: Prof. Jon Warland, Prof. William David Lubitz, Prof. Prasad Daggupati, Prof. Rafael Santos, and Prof. Shohel Mahmud; School of Engineering staff: Jeff Madge, Joel Best, and Matthew Kent; and my colleagues at the AIR lab.

Finally, my deep and sincere gratitude to my family, who provided me with love and support to follow my dreams.

This work was supported by the University of Guelph through the International Graduate Tuition Scholarship (IGTS) for the author; Accelerate program (460847) from Mathematics of Information Technology and Complex Systems (MITACS); Discovery Grant program (401231) from the Natural Sciences and Engineering Research Council (NSERC) of Canada; Government of Ontario through the Ontario Centres of Excellence (OCE) under the Alberta-Ontario Innovation Program (AOIP) (053450); and Emission Reduction Alberta (ERA) (053498). OCE is a member of the Ontario Network of Entrepreneurs (ONE).

Contents

Abstract	ii
Acknowledgements	v
List of Tables	x
List of Figures	xv
List of Abbreviations	xvi
List of Mathematical Symbols	xviii
1 Introduction and Motivations	1
1.1 Background	1
1.1.1 Scales of Climate	2
1.1.2 Urban Heat Island	4
1.1.3 Urban Hydrology	8
1.1.4 Modeling of Urban Climate	11
1.2 Research Gaps	18
1.3 Objectives	19
2 Methodology	23
2.1 Rural Model	25
2.1.1 Surface Energy Balance Model	27
2.1.2 Monin-Obukhov Similarity Theory	30
2.2 Urban Model	32
2.2.1 Radiation Model	32
2.2.2 Surface Energy Balance Model	41
2.2.3 Urban Vertical Diffusion Model	52
2.2.4 Building Energy Model	57
2.2.5 Hydrology Model	59

3	Results and Discussion: VCWG v1.3.2	66
3.1	Model Configuration	66
3.2	Evaluation	67
3.2.1	Observation and Forcing Datasets	67
3.2.2	Potential Temperature	69
3.2.3	Wind Speed	72
3.2.4	Specific Humidity	74
3.2.5	Urban Heat Island (UHI)	77
3.3	Exploration	78
3.3.1	Forcing Datasets	78
3.3.2	Urban Plan and Frontal Area Densities	80
3.3.3	Leaf Area Density	83
3.3.4	Building Energy Configuration	83
3.3.5	Radiation Configuration	88
3.3.6	Seasonal Variations	92
3.3.7	Other Climates	93
4	Results and Discussion: VCWG v2.0.0	95
4.1	Model Configuration	95
4.2	Evaluation	97
4.2.1	Observation and Forcing Datasets	97
4.2.2	Potential Temperature, Wind Speed, and Specific Humidity	99
4.2.3	Sensible and Latent Heat Fluxes	99
4.3	Exploration	102
4.3.1	Forcing Datasets	102
4.3.2	Seasonal Variations	104
4.3.3	Effect of Urban Trees on Model Output Variables	113
4.3.4	Effect of Low Vegetation on Model Output Variables	115
4.3.5	Effects of Green and Cool Roofs on Model Output Variables	117
4.3.6	Variation of Local Climate Zone and Model Output Variables	118
4.3.7	Spatial Distribution of Model Output Variables for a Neighborhood	123
5	Summary and Conclusions	128
5.1	Vertical City Weather Generator (VCWG) v1.3.2	129
5.2	Vertical City Weather Generator (VCWG) v2.0.0	130
5.3	Limitations and Future Work	132
	Bibliography	133
A	Published Work	153
A.1	Peer-Reviewed Journal Papers	153
A.2	Refereed Conferences	154

List of Tables

1.1	Summary of urban canopy models (VF: View Factor)	20
3.1	List of input parameters used in VCWG for model evaluation; input variables are extracted from assumptions, datasets, and simulation codes available in the literature [26, 37, 55, 63, 75, 84, 129, 145, 165, 174, 210].	70
3.2	BIAS [K], RMSE [K], and R^2 [-] for VCWG predictions of potential temperature against the BUBBLE observations for different altitudes and months.	71
3.3	BIAS [m s^{-1}], RMSE [m s^{-1}], and R^2 [-] for VCWG predictions of wind speed against the BUBBLE observations for different altitudes and months.	75
3.4	BIAS [kg kg^{-1}], RMSE [kg kg^{-1}], and R^2 [-] for VCWG predictions of specific humidity against the BUBBLE observations for different altitudes and months.	76
3.5	BIAS [K], RMSE [K], and R^2 [-] for VCWG predictions of UHI [K] against the BUBBLE observations for different months.	78
3.6	Specifications of the building energy configuration for two building types; values extracted from the Urban Weather Generator (UWG) model [26]; the infiltration is expressed as Air Changes per Hour (ACH [-]).	85
4.1	List of input parameters used in VCWG v2.0.0 for model evaluation in Vancouver; input variables are extracted from assumptions, datasets, and simulation codes available in the literature [47, 100].	98
4.2	BIAS, RMSE, and R^2 for VCWG v1.3.2 and v2.0.0 predictions of potential temperature $\bar{\Theta}$ [K], wind speed \bar{S} [m s^{-1}], and specific humidity \bar{Q} [kg kg^{-1}] against the BUBBLE observations for different altitudes and months (green shaded cells show improvement and red shaded cells show deterioration in the predictions).	100
4.3	BIAS, RMSE, and R^2 for VCWG predictions of sensible and latent heat fluxes [W m^{-2}] against the observations and previous studies.	103
4.4	List of input parameters used in VCWG v2.0.0 for seasonal exploration in Vancouver.	104

List of Figures

1.1	Boundary layer structure over an urban area.	3
1.2	Illustration of heat dome flow.	6
1.3	Illustration of water balance of an urban area (a) and a rural area (b).	9
1.4	Generalized partitioning of precipitation into evaporation, runoff, and infiltration for different climate zones [156].	12
1.5	Generalized partitioning of incoming shortwave and longwave radiation into sensible, latent, and ground heat fluxes. In the urban area (a) and the rural area (b). Urban energy fluxes at the facades are shown (c).	14
1.6	Urban canopy models with different levels of complexity. From left to right the complexity of the model increase from a single point (slab model) to multi points at a single layer (single-layer model) and multi layers (multi-layer model).	16
2.1	Illustration of VCWG.	26
2.2	Illustration of surface energy balance in a rural area.	28
2.3	Illustration of interaction between solar radiation beam, the urban surface, and the shadow provided by trees. θ_1 to θ_4 are the reference angles.	35
2.4	Illustration of surface energy balance in an urban area.	41
2.5	Detailed description of sensible heat flux from urban surfaces.	43
2.6	Detailed description of latent heat flux from urban surfaces.	45
2.7	Building Energy Model (BEM).	59
2.8	Water balance in the urban area; blue arrows are the source terms, red arrows are the sink terms, and black arrow is indicator.	60
2.9	Partitioning of Soil Column.	63
3.1	Overview of the Vertical City Weather Generator (VCWG) v1.3.2.	68
3.2	Scatter plots of observed (BUBBLE) versus simulated (VCWG) values of potential temperature for different altitudes and months; each data point corresponds to a 1-hour comparison between the model and observation.	72
3.3	Comparison between the observed (BUBBLE) versus simulated (VCWG) values of potential temperature; the hourly means are shown; nighttime indicated with shaded regions; solid line: model and dashed line: observation; times in Local Standard Time (LST).	73

3.4	Scatter plots of observed (BUBBLE) versus simulated (VCWG) values of wind speed for different altitudes and months; each data point corresponds to a 1-hour comparison between the model and observation.	74
3.5	Scatter plots of observed (BUBBLE) versus simulated (VCWG) values of specific humidity for different altitudes and months; each data point corresponds to a 1-hour comparison between the model and observation.	76
3.6	Comparison between the observed (BUBBLE) versus simulated (VCWG) values of specific humidity; the hourly means are shown; nighttime indicated with shaded regions; solid line: model and dashed line: observation; times in Local Standard Time (LST).	77
3.7	Hourly mean and standard deviation (band) of UHI [K] in each month for the observed (BUBBLE) and predicted (VCWG) values; nighttime indicated with shaded regions; times in Local Standard Time (LST).	79
3.8	Effect of plan area density λ_p [-] on the profiles of potential temperature, horizontal wind speed, specific humidity, and turbulence kinetic energy during nighttime (averaged from 0000 to 0400 LST) and daytime (averaged from 1200 to 1600 LST); red: $\lambda_p = 0.54$ [-], blue: $\lambda_p = 0.46$ [-]; tree crown with non-zero LAD [$m^2 m^{-3}$] shown in shaded green; building height shown with grey line; times in Local Standard Time (LST).	81
3.9	Effect of frontal area density λ_f [-] on the profiles of potential temperature, horizontal wind speed, specific humidity, and turbulence kinetic energy during nighttime (averaged from 0000 to 0400 LST) and daytime (averaged from 1200 to 1600 LST); red: $\lambda_f = 0.51$ [-], blue: $\lambda_f = 0.37$ [-]; tree crown with non-zero LAD [$m^2 m^{-3}$] shown in shaded green; building heights shown with red and blue lines; times in Local Standard Time (LST).	82
3.10	Effect of leaf area density profiles LAD [$m^2 m^{-3}$] on the profiles of potential temperature, horizontal wind speed, specific humidity, and turbulence kinetic energy during nighttime (averaged from 0000 to 0400 LST) and daytime (averaged from 1200 to 1600 LST); red: $LAD = 0.2$ [$m^2 m^{-3}$], blue: $LAD = 0.1$ [$m^2 m^{-3}$]; tree crown with non-zero LAD [$m^2 m^{-3}$] shown in shaded green; building height shown with a grey line; times in Local Standard Time (LST).	84
3.11	Effect of building type on cooling/heating waste heat, dehumidification waste heat, gas combustion waste heat, water heating waste heat, and UHI [K]; diurnal variation of mean and standard variation (band) are shown using data obtained over a two-week period; nighttime is shown with shaded regions; times in Local Standard Time (LST).	86
3.12	Effect of building cooling system Coefficient Of Performance (COP [-]) and heating system thermal efficiency (η_{heat} [-]) on cooling/heating waste heat, dehumidification waste heat, gas combustion waste heat, water heating waste heat, and UHI [K]; diurnal variation of mean and standard variation (band) are shown using data obtained over a two-week period; nighttime is shown with shaded regions; times in Local Standard Time (LST).	87

3.13	Effect of the location of waste heat release on UHI [K]; diurnal variation of mean and standard deviation (band) are shown using data obtained over a two-week period; nighttime is shown with shaded regions; times in Local Standard Time (LST); blue: all waste heat released at street level ($F_{st} = 1$); red: half of the waste heat released at street level ($F_{st} = 0.5$); green: all waste heat released at roof level ($F_{st} = 0$).	88
3.14	Effect of canyon aspect ratio H_{avg}/w [-] on hourly mean absolute values of shortwave S [$W\ m^{-2}$] and longwave L [$W\ m^{-2}$] radiation fluxes after reflections; incoming fluxes (S^\downarrow and L^\downarrow [$W\ m^{-2}$]) shown using dashed lines; outgoing fluxes (S^\uparrow and L^\uparrow [$W\ m^{-2}$]) shown using dotted lines; diurnal variation of mean is shown using data obtained over a two-week period; nighttime is shown with shaded regions; times in Local Standard Time (LST).	90
3.15	Effect of street canyon axis angle θ_{can} [$^\circ$] on hourly mean absolute values of shortwave S [$W\ m^{-2}$] and longwave L [$W\ m^{-2}$] radiation fluxes; incoming fluxes (S^\downarrow and L^\downarrow [$W\ m^{-2}$]) shown using dashed lines; outgoing fluxes (S^\uparrow and L^\uparrow [$W\ m^{-2}$]) shown using dotted lines; diurnal variation of mean is shown using data obtained over a two-week period; nighttime is shown with shaded regions; times in Local Standard Time (LST).	91
3.16	Hourly mean values of UHI [K] in each month in Vancouver, Canada, as predicted by VCWG; sunrise and sunset times are denoted by dashed lines; times in Local Standard Time (LST).	92
3.17	Profiles of potential temperature, horizontal wind speed, specific humidity, and turbulence kinetic energy during nighttime (averaged at 0200 LST) and daytime (averaged at 1400 LST) in different seasons; black: winter, green: spring, red: summer, and blue: fall; building height shown with grey line; times in Local Standard Time (LST).	93
3.18	Diurnal variation of the UHI [K], as predicted by VCWG, in Buenos Aires, Vancouver, Osaka, and Copenhagen; diurnal variation of mean and standard deviation (band) are shown using data obtained over a two-week period; nighttime is shown with shaded regions; times in Local Standard Time (LST).	94
4.1	Overview of the Vertical City Weather Generator (VCWG) v2.0.0. The new additions in VCWG v2.0.0 are highlighted in blue.	97
4.2	Comparison between the BUBBLE dataset (blue) versus simulated values of sensible and latent heat fluxes above the urban area using VCWG v1.3.2 (green) and VCWG v2.0.0 (red); the hourly means are shown; times in Local Standard Time (LST); simulation for a two-week period in June 2002.	102
4.3	Comparison between the Vancouver Sunset dataset versus simulated values of sensible and latent heat fluxes above the urban area using VCWG v2.0.0; the hourly means are shown; times in Local Standard Time (LST); simulation for a 5-month period in 2008.	103

4.4	Hourly sensible and latent heat fluxes [W m^{-2}] in Vancouver: (top) sensible heat flux above the canyon over the course of a year; (middle) latent heat flux above the canyon over the course of a year; (bottom) mean diurnal variation of latent (blue) and sensible (red) heat fluxes for Jan-Mar, Apr-Jun, Jul-Sep, and Oct-Dec. The black line shows daily precipitation [mm day^{-1}].	106
4.5	Variability of urban surface temperatures in January, May, August, and November in Vancouver; roof is impervious and ground is partially covered by vegetation; the box plot represents 5 th , 25 th , 50 th , 75 th , and 95 th percentiles for temperature; red line is canyon air temperature; top row is daytime and bottom row is nighttime; daytime temperatures are sampled from 1000 to 1400 LST and nighttime temperatures are sampled from 2200 to 0200 LST.	108
4.6	Seasonal variation of hourly mean and maximum building energy fluxes including cooling demand (Q_{cool}), dehumidification demand (Q_{dehum}), heating demand (Q_{heat}), and building waste heat (Q_{waste}); the solid line is daily mean and dashed line is daily maximum of the variable. The bar plot is the integrated energy flux within JFM (January, February, and March), AMJ (April, May, and June), JAS (July, August, and September), and OND (October, November, and December) months. The simulation is conducted for Vancouver.	109
4.7	Monthly variation of water balance components for Vancouver in 2007; hourly terms in the water balance equation are integrated over time to calculate the monthly magnitude for all sink and source terms.	111
4.8	Soil moisture content in soil columns of impervious ground (top) and vegetated ground (bottom) at 0.75, 8.75, 53.75, and 103.75 [cm] depth measured from the surface, positive, downward into the soil over the course of a year in Vancouver; the black line is daily precipitation [mm day^{-1}].	112
4.9	Effect of urban trees on the sensible and latent heat fluxes above the canyon in July. The heat fluxes are diurnally averaged at the height of 30 [m] from ground in July 2007 in Vancouver.	114
4.10	Effect of urban trees on the dehumidification demand, cooling energy demand, and waste heat of building. The building energy fluxes are mean of daily maximum in July 2007 in Vancouver.	114
4.11	Effect of low vegetation coverage (f_{veg}) on urban sensible and latent heat fluxes [W m^{-2}] above the canyon for Vancouver in July 2007; f_{veg} varies from 0 (road is all impervious surface) to 1 (road is all vegetation).	115
4.12	Effect of low vegetation coverage (f_{veg}) on mean daily water budget terms [mm day^{-1}] for Vancouver in July 2007; storage term is not significant, so it is added to the evaporation term; f_{veg} varies from 0 (road is all covered by impervious surface) to 1 (road is all covered by vegetation); blue line is mean daily rainfall [mm day^{-1}].	116
4.13	Comparison between the response of traditional, green, and cool roofs to solar radiation fluxes.	117

4.14	Effects of green and cool roofs on urban sensible heat flux [W m^{-2}] in different seasons; the sensible heat fluxes are diurnally-averaged over January-February-March (JFM), April-May-June (AMJ), July-August-September (JAS), and October-November-December (OND) for Vancouver in 2007.	119
4.15	Effects of green and cool roofs on roof surface temperature [K] in different seasons; the surface temperatures are diurnally-averaged over January-February-March (JFM), April-May-June (AMJ), July-August-September (JAS), and October-November-December (OND) in Vancouver 2007.	120
4.16	Effects of green and cool roofs on building energy performance in different seasons; the building energy fluxes are mean of daily maximum over January-February-March (JFM), April-May-June (AMJ), July-August-September (JAS), and October-November-December (OND) in Vancouver 2007.	121
4.17	Spatial variation of urban morphometric parameters including plan area density (λ_p [-]), leaf area index of urban trees (LAI_{tree} [$\text{m}^2 \text{m}^{-2}$]), canyon aspect ratio (H/W [-]), and fraction of ground covered by vegetation (f_{veg} [-]) for a typical city.	122
4.18	Color plots of air potential temperature distribution from Local Climate Zone (LCZ) 1 to LCZ 9 at 1300 LST (left) and 2100 LST (right) in the summer; simulations are for Vancouver in 2007 for July.	123
4.19	Color plots of wind speed distribution from Local Climate Zone (LCZ) 1 to LCZ 9 at 1300 LST (left) and 2100 LST (right) in the summer; simulations are for Vancouver in 2007 for July.	124
4.20	Diurnal variation of sensible heat flux (left) and latent heat flux (right) of urban and sub-urban areas for LCZ 1 to LCZ 9.	125
4.21	The VCWG domain for spatial analysis in Vancouver.	125
4.22	Plan area density (λ_p [-]) calculated at 1 [m] resolution (left) and 100 [m] resolution (right) in Vancouver.	126
4.23	Spatial distribution of mean daytime (left) and nighttime (right) canyon air potential temperature Θ_{can} [K] from July 1 to July 7 in Vancouver in 2007; a neighborhood is chosen in the Lower Main Land.	126
4.24	Spatial distribution of mean daytime (left) and nighttime (right) latent heat flux LE_{urban} [W m^{-2}] from July 1 to July 7 in Vancouver in 2007; a neighborhood is chosen in the Lower Main Land.	127
4.25	Spatial distribution of mean daytime (left) and nighttime (right) sensible heat flux H_{urban} [W m^{-2}] from July 1 to July 7 in Vancouver in 2007; a neighborhood is chosen in the Lower Main Land.	127
4.26	Spatial distribution of daily maximum building waste heat (left) and cooling demand (right) [W m^{-2}] from July 1 to July 7 in Vancouver in 2007; a neighborhood is chosen in the Lower Main Land.	127

LIST OF ABBREVIATIONS

ABL	Atmospheric Boundary Layer
BEM	Building Energy Model
BEP	Building Effect Parameterization
BUBBLE	Basel UrBan Boundary Layer Experiment
CAT	Canyon Air Temperature
CFD	Computational Fluid Dynamics
ECCC	Environment and Climate Change Canada
EPW	EnergyPlus Weather
FFD	Fast Fluid Dynamics
GEM	Global Environmental Multiscale
GIS	Geographic Information System
HYSPLIT	Hybrid Single-Particle Lagrangian Integrated Trajectory
IOBES	Indoor-Outdoor Building Energy Simulator
OpenFOAM	Open-source Field Operation And Manipulation
PALM	Parallelized Large-Eddy Simulation Model
RSL	Roughness Sub-Layer
SLUCM	Single-Layer Urban Canopy Model
SUEWS	Surface Urban Energy and Water Balance Scheme
SVS	Soil, Vegetation, and Snow scheme
TEB	Town Energy Balance
TMY	Typical Meteorological Year
TUF	Temperatures of Urban Facets

UCI	Urban Cool Island
UCL	Urban Canopy Layer
UCM	Urban Canopy Model
UHI	Urban Heat Island
UHIC	Urban Heat Island-Induced Circulation
UT&C	Urban Tethys-Chloris
UWG	Urban Weather Generator
VCWG	Vertical City Weather Generator
WRF	Weather Research and Forecasting

LIST OF MATHEMATICAL SYMBOLS

Latin Symbols

A_g	Road area [m^2]
B_D	Sectional building area density [m^{-1}]
C_{DBv}	Sectional drag coefficient in the presence of trees [-]
C_{Dv}	Drag coefficient for tree foliage [-]
C_{GV}	Boolean operator to consider presence or absence of vegetated ground [-]
C_{GB}	Boolean operator to consider presence or absence of bare ground [-]
C_{GI}	Boolean operator to consider presence or absence of impervious ground [-]
C_p	Air specific heat capacity [$\text{J kg}^{-1} \text{K}^{-1}$]
c_{PM}	Molar heat capacity for air [$\text{J mol}^{-1} \text{K}^{-1}$]
$C_{v,\text{bld}}$	Building envelop volumetric heat capacity [$\text{J m}^{-3} \text{K}^{-1}$]
cv_{soil}	Soil volumetric heat capacity [$\text{J m}^{-3} \text{K}^{-1}$]
C_{soil}	Soil thermal conductance [$\text{W m}^{-2} \text{K}^{-1}$]
COP	Coefficient of performance [-]
d_{leaf}	Leaf dimension [m]
d_{rur}	Displacement height in the rural area [m]
d_{soil}	Soil layer thickness [m]
d_t	Tree distance from canyon walls [m]
$d_{w,\text{veg}}$	Fraction of low vegetation covered by intercepted water [-]
D	Water system outflow in forms of infiltration [mm s^{-1}]

D_{drip}	Dripping water [mm s^{-1}]
D_{lk}	Leakage [mm s^{-1}]
D_{runoff}	Surface runoff [mm s^{-1}]
D_{sat}	Saturation excess from the interception storage of foliage [mm s^{-1}]
D_x	Vegetation drag in cross canyon direction [-]
D_y	Vegetation drag in along canyon direction [-]
EB_{lwr}	Conservation of longwave radiation energy [W m^{-2}]
EB_{swr}	Conservation of shortwave radiation energy [W m^{-2}]
e_s	Saturated vapor pressure [Pa] or [kPa]
e_{soil}	Sink term due to soil evaporation [s^{-1}]
e_a	Vapor pressure [Pa] or [kPa]
E_{imp}	Evaporation from impervious surface [$\text{kg m}^{-2} \text{s}^{-1}$]
E_{int}	Evaporation from intercepted water [mm s^{-1}]
E_{bare}	Evaporation from bare ground [$\text{kg m}^{-2} \text{s}^{-1}$]
E_{veg}	Evaporation from vegetated surface [$\text{kg m}^{-2} \text{s}^{-1}$]
$E_{\text{veg,int}}$	Evaporation from intercepted water on low vegetation [$\text{kg m}^{-2} \text{s}^{-1}$]
F_h	Stability function [-]
$f_{\text{veg,rur}}$	Fraction of rural area covered by vegetation [-]
f_{gv}	Fraction of ground covered by vegetation [-]
f_{gb}	Fraction of ground covered by bare soil [-]
f_{gi}	Fraction of ground covered by impervious surface [-]
$F_{\text{sun,veg}}$	Fraction of sunlit low vegetation [-]
$F_{\text{shd,veg}}$	Fraction of shaded low vegetation [-]
g	Gravitational acceleration [m s^{-2}]
G	Ground heat flux [W m^{-2}]
G_{rur}	Ground heat flux in the rural area [W m^{-2}]
$g_{\text{b,free}}$	Leaf boundary conductance at free convection [m s^{-1}]
$g_{\text{b,force}}$	Leaf boundary conductance at forced convection [m s^{-1}]
g_{Ha}	Heat conductance [$\text{mol m}^{-2} \text{s}^{-1}$]

Gr	Grashof number [-]
$G_{\text{shd,bld}}$	Shadow length on the ground due to the building [-]
$G_{\text{shd,tree}}$	Shadow length on the ground due to the tree [-]
g_v	Average surface and boundary-layer conductance for humidity [$\text{mol m}^{-2} \text{s}^{-1}$]
H	Sensible heat flux [W m^{-2}]
h_c	Convective heat transfer coefficient [m s^{-1}]
H_{rur}	Sensible heat flux in the rural area [W m^{-2}]
h_{rur}	Obstacle height in the rural area [m]
h_t	Tree Height [m]
H_{top}	Domain Height [m]
H_{HVAC}	Total sensible waste heat released into the atmosphere [W m^{-2}]
HW	Ratio of building height to canyon width [-]
Inf	Infiltration rate [mm s^{-1}]
Int	Intercepted water [mm]
Int_{max}	Maximum interception capacity [mm]
H_tW	Ratio of tree height to canyon width [-]
k	Turbulence kinetic energy [$\text{m}^2 \text{s}^{-2}$]
k_{bld}	Thermal diffusivity of building envelop [$\text{m}^2 \text{s}^{-1}$]
K_m	Turbulent diffusion coefficient [$\text{m}^2 \text{s}^{-1}$]
K_{opt}	Optical transmittance [-]
L	Latent heat of vaporization [J kg^{-1}]
L^\downarrow	Incoming longwave radiation flux [W m^{-2}]
L_{rur}^\uparrow	Outgoing longwave radiation flux from rural surface [W m^{-2}]
L^\uparrow	Outgoing longwave radiation flux [W m^{-2}]
LE	Latent heat flux [W m^{-2}]
LE_{rur}	Latent heat flux in the rural area [W m^{-2}]
L_n	Net longwave radiation flux [W m^{-2}]
$L_{n,\text{rur}}$	Net longwave radiation flux in the rural area [W m^{-2}]
L_{obk}	Obukhov length [m]

LAD	Leaf area density [$\text{m}^2 \text{m}^{-3}$]
LAI_{tree}	Leaf area index of individual tree [$\text{m}^2 \text{m}^{-2}$]
$LAI_{\text{tree,can}}$	Leaf area index of tree per total ground area [$\text{m}^2 \text{m}^{-2}$]
LAI_{veg}	Leaf area index of individual low vegetation [$\text{m}^2 \text{m}^{-2}$]
\dot{m}_{inf}	Mass flow rate of infiltration per unit building footprint area [$\text{kg s}^{-1} \text{m}^{-2}$]
\dot{m}_{ven}	Mass flow rate of ventilated air per unit building footprint area [$\text{kg s}^{-1} \text{m}^{-2}$]
P_{a}	Atmospheric pressure [Pa]
P_{precip}	Fraction of total precipitation that reaches the surface [mm s^{-1}]
P_{runon}	Runon [mm s^{-1}]
Pr_t	Turbulent Prandtl number [-]
\bar{Q}	Specific humidity of air [kg kg^{-1}]
Q_{cool}	Cooling demand [W m^{-2}]
Q_{dehum}	Dehumidification demand [W m^{-2}]
Q_{gas}	Energy consumption by gas combustion [W m^{-2}]
Q_{inf}	Sensible heat flux from air infiltration [W m^{-2}]
Q_{int}	Internal sensible heat flux [W m^{-2}]
Q_{lat}	Lateral water fluxes between soil columns [mm s^{-1}]
\bar{Q}_{sat}	Saturated specific humidity [kg kg^{-1}]
Q_{surf}	Sensible heat flux from interior wall [W m^{-2}]
Q_{ven}	Sensible heat flux from air ventilation [W m^{-2}]
Q_{ver}	Vertical water fluxes in a soil column [mm s^{-1}]
Q_{water}	Energy consumption for water heating [W m^{-2}]
r_{a}	Aerodynamic resistance in the rural area [s m^{-1}]
R_{drag}	Ratio of drag coefficient for momentum to heat [-]
Ri_B	Bulk Richardson number [-]
r_1	Stomatal resistance in the rural area [s m^{-1}]
R_{n}	Net allwave radiation flux [W m^{-2}]
r_{aero}	Horizontal surface aerodynamic resistance [s m^{-1}]
$r_{\text{lb,veg}}$	Low vegetation leaf boundary resistance [s m^{-1}]

$\hat{r}_{\text{lb,veg}}$	Re-scaled low vegetation leaf boundary resistance [s m^{-1}]
$\hat{r}_{\text{lb,veg,sun}}$	Re-scaled leaf boundary resistance of sunlit low vegetation [s m^{-1}]
$\hat{r}_{\text{lb,veg,shd}}$	Re-scaled leaf boundary resistance of shaded low vegetation [s m^{-1}]
$\hat{r}_{\text{lb,tree}}$	Re-scaled tree leaf boundary resistance [s m^{-1}]
$\hat{r}_{\text{lb,tree,sun}}$	Re-scaled leaf boundary resistance of sunlit tree [s m^{-1}]
$\hat{r}_{\text{lb,tree,shd}}$	Re-scaled leaf boundary resistance of shaded tree [s m^{-1}]
r_{imp}	Impervious surface thermal resistance [s m^{-1}]
r_{bare}	Bare ground thermal resistance [s m^{-1}]
r_{veg}	Vegetated surface thermal resistance [s m^{-1}]
r_{s}	Surface resistance in the rural area [s m^{-1}]
r_{sbl}	Soil resistance to transport water from soil surface [s m^{-1}]
$\hat{r}_{\text{s,tree,sun}}$	Re-scaled stomatal resistance of sunlit tree [s m^{-1}]
$r_{\text{s,tree,sun}}$	Stomatal resistance of sunlit tree [s m^{-1}]
$\hat{r}_{\text{s,tree,shd}}$	Re-scaled stomatal resistance of shaded tree [s m^{-1}]
$r_{\text{s,tree,shd}}$	Stomatal resistance of shaded tree [s m^{-1}]
$\hat{r}_{\text{s,veg,sun}}$	Re-scaled stomatal resistance of sunlit low vegetation [s m^{-1}]
$r_{\text{s,veg,sun}}$	Stomatal resistance of sunlit low vegetation [s m^{-1}]
$\hat{r}_{\text{s,veg,shd}}$	Re-scaled stomatal resistance of shaded low vegetation [s m^{-1}]
$r_{\text{s,veg,shd}}$	Stomatal resistance of shaded low vegetation [s m^{-1}]
r_{soil}	Soil resistance [s m^{-1}]
r_{sv}	Soil resistance to transport water within soil column [s m^{-1}]
$r_{\text{s,water}}$	Stomatal resistance to water exchange [$\text{m}^2 \text{ s } \mu\text{mol}^{-1} \text{ CO}_2$]
$\hat{r}_{\text{lb,veg,sun}}$	Re-scaled leaf boundary resistance of sunlit low vegetation [s m^{-1}]
$\hat{r}_{\text{lb,veg,shd}}$	Re-scaled leaf boundary resistance of shaded low vegetation [s m^{-1}]
r_{t}	Tree crown radius [m]
r_{tree}	Tree thermal resistance [s m^{-1}]
r_{wall}	Wall thermal resistance [s m^{-1}]
S_{EA}	Sink/source term corresponding to radiative divergence [K s^{-1}]
S_{EG}	Sink/source term corresponding to sensible heat exchange with ground [K s^{-1}]

$S_{\Theta R}$	Sink/source term corresponding to sensible heat exchange with roof [$K s^{-1}$]
$S_{\Theta V}$	Sink/source term corresponding to sensible heat exchange with vegetation [$K s^{-1}$]
$S_{\Theta waste}$	Source term corresponding to building waste heat [$K s^{-1}$]
SAI	Stem area index [$m^2 m^{-2}$]
S^{\downarrow}	Incoming shortwave radiation flux [$W m^{-2}$]
S^{\uparrow}	Outgoing shortwave radiation flux [$W m^{-2}$]
$S^{\downarrow direct}$	Incoming direct shortwave radiation flux [$W m^{-2}$]
$S_T^{\downarrow direct}$	Incoming direct shortwave radiation flux at the tree level [$W m^{-2}$]
$S_{Wshd}^{\downarrow direct}$	Incoming direct shortwave radiation flux at the shaded wall [$W m^{-2}$]
$S_{Wsun}^{\downarrow direct}$	Incoming direct shortwave radiation flux at the sunlit wall [$W m^{-2}$]
$S_G^{\downarrow direct}$	Incoming direct shortwave radiation flux at the ground [$W m^{-2}$]
$S^{\downarrow diffuse}$	Incoming diffuse shortwave radiation flux [$W m^{-2}$]
S_n	Net shortwave radiation flux [$W m^{-2}$]
$S_{n,rur}$	Net shortwave radiation flux in the rural area [$W m^{-2}$]
\bar{S}	Wind speed [$m s^{-1}$]
$\bar{S}_{rur,10m}$	Wind speed in the rural area at 10 m height [$m s^{-1}$]
Sc_t	Turbulent Schmidt number [-]
S_{wake}	Wake production by urban obstacles and trees [$m^2 s^{-3}$]
T_{deep}	Deep soil temperature [K]
$T_{s,rur}$	Rural surface temperature [K]
t_{tree}	Sink term due to water uptake for transpiration of trees [s^{-1}]
t_{veg}	Sink term due to water uptake for transpiration of low vegetation [s^{-1}]
$TE_{veg,shd}$	Transpiration from shaded low vegetation [$kg m^{-2} s^{-1}$]
$TE_{veg,sun}$	Transpiration from sunlit low vegetation [$kg m^{-2} s^{-1}$]
u_*	Friction velocity [$m s^{-1}$]
\bar{U}	Cross canyon wind [$m s^{-1}$]
\bar{V}	Along canyon wind [$m s^{-1}$]
VF	View factor [-]

VPD	Vapor pressure deficit [Pa] or [kPa]
W_{cool}	Energy consumption of the cooling system [$W\ m^{-2}$]
$W_{shd,bld}$	Shadow length on the wall due to the building [-]
$W_{shd,tree}$	Shadow length on the wall due to the tree [-]
x_{shd}	Shade position on the ground [-]
y_{shd}	Shade position on the wall [-]
z	Distance from surface [m]
$z_{0,rur}$	Aerodynamic roughness length in the rural area [m]
z_m	Measured wind speed height [m]
z_h	Measured temperature height [m]
$z_{\bar{\theta},rur}$	Rural roughness length for temperature [m]
$z_{\bar{Q},rur}$	Rural roughness length for specific humidity [m]

Greek Symbols

α	Attenuation coefficient [-]
α_{GB}	Bare ground albedo [-]
α_{GI}	Impervious ground albedo [-]
α_{GV}	Vegetated ground albedo [-]
α_{rur}	Rural albedo [-]
α_S	Sky albedo [-]
α_T	Tree albedo [-]
α_V	Vegetation albedo [-]
α_W	Wall albedo [-]
β_{rur}	Bowen ratio [-]
γ^*	Conductive-radiative conductance
γ_1	Psychrometric constant [$kPa\ K^{-1}$]
δ_m	Boundary layer thickness of soil [m]
Δ	Slope of saturated vapor pressure [$kPa\ K^{-1}$]
ε_{GB}	Bare ground emissivity [-]

ε_{GI}	Impervious ground emissivity [-]
ε_{GV}	Vegetated ground emissivity [-]
ε_{rur}	Rural emissivity [-]
ε_T	Tree emissivity [-]
ε_V	Vegetation emissivity [-]
η_{heat}	Thermal efficiency of heating system [-]
θ	Soil moisture content [$\text{m}^3 \text{m}^{-3}$]
θ_a	Difference between solar azimuth angle and canyon orientation [rad]
θ_z	Solar zenith angle [rad]
$\bar{\Theta}$	Potential air temperature [K]
$\bar{\Theta}_s$	Surface temperature [K]
κ	von Kármán constant [-]
λ_f	Frontal area density [-]
λ_m	Thermal conductivity of building envelope [$\text{W m}^{-1} \text{K}^{-1}$]
λ_p	Plan area density [-]
Λ_m	Molar latent heat of vaporization [J mol^{-1}]
ξ	Solar position [-]
ρ	Air density [kg m^{-3}]
τ	Tree canopy transmittance [-]
σ	Stephen Boltzman constant [$\text{W m}^{-2} \text{K}^{-4}$]
Φ_H	Universal dimensionless temperature gradient [-]
Φ_M	Universal dimensionless wind shear [-]
Φ_Q	Universal dimensionless specific humidity gradient [-]
ω	Clumping factor [-]

Chapter 1

Introduction and Motivations

1.1 Background

Urban expansion and conversion of the Earth's surface to urban uses have brought numerous environmental issues at various scales. Cities and industrial areas disturb the natural water cycle and thermal energy exchange between the earth's surface and the atmosphere. In addition, these areas release anthropogenic pollutants into the atmosphere with negative impacts from local to global scales.

Urbanization is accompanied by dramatic changes in land use and surface energy balance that drive local climate change. These climate modifications lead to an increase in air temperature in the built-up areas in comparison to the surrounding undeveloped areas. This phenomenon is called the Urban Heat Island (UHI). This warming trend has been observed in most cities around the world for almost 200 years, indicating that the UHI is the most well-documented example of anthropogenic climate modification [191]. Increasing heat storage in urban areas, trapping of solar radiation, reduced ventilation, heat release from vehicles, power plants, and building energy systems, are just some examples of mechanisms that are responsible for anthropogenic heat release in the urban environment. The local climate modification induced by urbanization is also attributed to the urban configuration, surface albedo, thermal conductivity, and changes in convective heat removal [130].

Building a city also disturbs the pre-existing hydrological processes in natural areas. This perturbation is mainly caused by replacing low vegetation and trees with artificial surfaces, which results in a reduction in surface water exchanges and infiltration and increases in surface runoff and sensible heat flux [156]. Therefore, in addition to temperature and humidity control, proper mitigation strategies are required to prevent urban flooding and

damage to the infrastructure.

Urban areas interact with the atmosphere through various exchange processes of heat, momentum, and mass, which substantially impact human comfort, air quality, and urban energy consumption. These complex interactions are observable from the Urban Canopy Layer (UCL) to a few hundred meters within the Atmospheric Boundary Layer (ABL) [22]. Much of the urban climate research has focused on UCL, which is characterized by a heterogeneous urban structure, a variety of human activities, and pollution sources. There is evidence that urban development can modify the urban climate by changing the atmosphere-earth surface interactions [153]. It can noticeably affect atmospheric stability, dispersion of pollutants, and the UHI. The latter can often have significant negative influences on building energy performance and human health [5].

To capture the physical processes occurring in the urban environment, various urban atmospheric models have been developed. Modeling the interaction between urban elements (e.g. trees, buildings, vehicles) and their impacts on energy and water exchanges can help urban planners develop cities more sustainably for climate control, reduced flooding, and improved air quality.

1.1.1 Scales of Climate

Aerodynamic and thermodynamic properties of the urban areas differ from those of permeable natural areas that cause distinct features of turbulent structures and turbulent transports of momentum, heat, and scalars within and outside the urban areas [58]. The urban boundary layer can be divided into different regimes, including the urban canopy layer, the roughness sublayer, the surface layer, and the mixed layer (see Figure 1.1) [193]. The lowest atmospheric layer, from the ground to the rooftop level, is defined as the urban canopy layer, where the texture of the urban surfaces, including all urban elements with a variety of properties, is a key factor in the turbulent and radiative exchanges between urban canyons and the above atmosphere. The Roughness Sub-Layer (RSL) is the next atmospheric layer extending up to approximately 2-5 times of average building height. Within this layer, the flow and turbulence are still influenced by the individual roughness elements and show strong variation in both horizontal and vertical directions. The RSL can also be affected by the distance downstream of a roughness element change. Above the RSL, the Surface Layer (SL), which is also known as the constant flux layer, is characterized by the shears that are induced by turbulence and vertical gradients of meteorological quantities [166]. The strength

of turbulence is a function of surface roughness and stability conditions. The next layer during daytime is the mixed layer, where the turbulence is vigorous and tends to uniformly mix the atmosphere in the vertical and horizontal directions. This vigorous turbulence can be generated by either forced or free convection. The latter is generally unstable and is caused by bottom heating (upward heat flux from the surface) or radiative cooling at the tops of cloud or fog layers [13, 40].

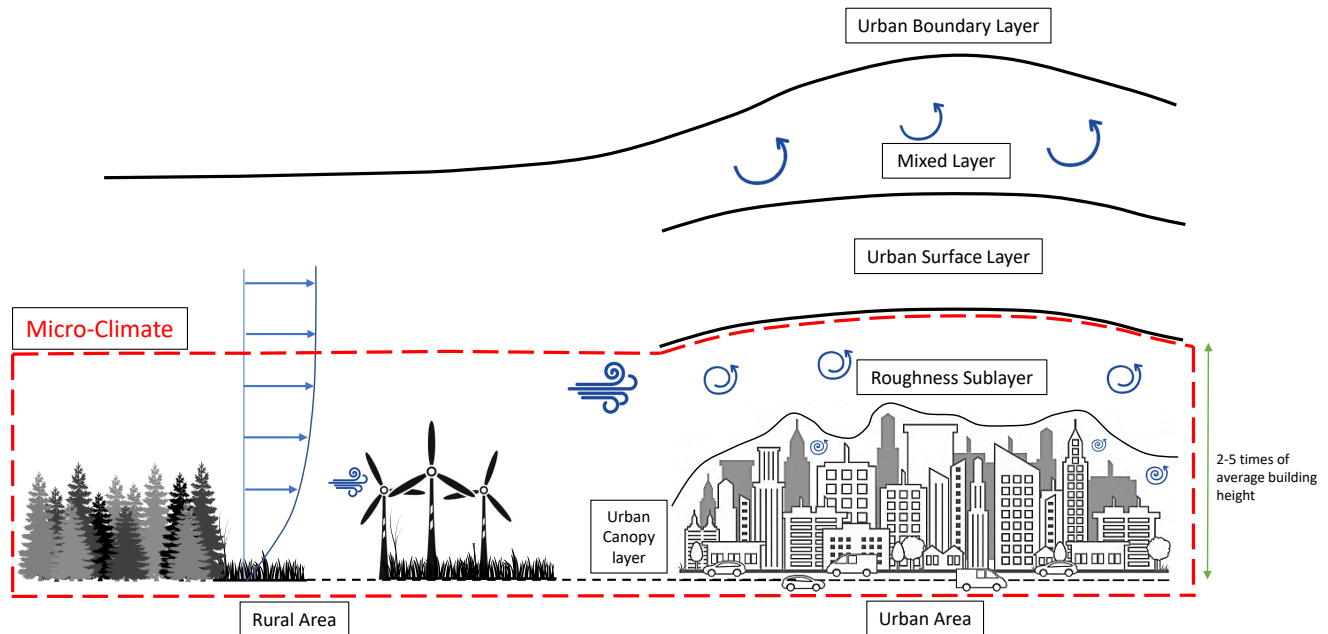


Figure 1.1: Boundary layer structure over an urban area.

In urban climatology, the scale of analysis specifies the key parameters that contribute to climate modifications. At the microscale, for example, the lowest atmospheric layer, individual building, and surrounding area properties influence the microclimate. An individual building consists of walls and roof facets, each with a different heat storage capacity and different time-varying exposure to solar radiation. Also, the horizontal ground surfaces consist of several elements such as irrigated or non-irrigated green space and paved areas, each with different radiative, thermal, aerodynamic, and moisture properties [22]. At neighborhood-scale, the inclusion of urban trees and buildings with different geometry adds more complexity. The building walls and the elements lying between buildings define the urban canyon. The city blocks are recognized by the urban canyons and the roofs of adjacent buildings [21]. At the city-scale, the amalgamation of city blocks determines the climate

modifications. At this scale overall aerodynamic and thermodynamic properties of multiple blocks are important. While spatial variation of climate variables decreases as the resolution of analysis decreases, it is important to understand and parameterize, when modeling, the heterogeneity, and complexity associated with urban climate at all scales [64].

Urbanization alters the natural terrain by the construction of new surfaces and structures with different properties. This process also introduces new sources and sinks for heat and water vapor. These changes modify the climate and render it different from the rural surrounding areas [13, 58]. Urban elements change patterns of air and surface temperature, humidity, precipitation, wind speed, runoff, and the energy balance in general. By replacing green spaces with human-made structures, the amount of evapotranspiration to the atmosphere decreases compared to the vegetated rural area. Also, the relative humidity can be reduced due to the increase in runoff of precipitation [128]. At the microscale, rougher urban terrains reduce wind speed by 20-30 % in comparison to the open spaces [13, 58].

The land-use changes induced by urbanization are the main drivers of micro to mesoscale climate change. At the mesoscale, the increased surface roughness and heat flux released from the urban areas modify flow patterns and wind speed with altitude. The aerosol emissions, surface and boundary-layer feedbacks, mesoscale convergence, and thermodynamic considerations over the whole range of scales contribute to the process of cloud formation. Such two-way interactions modify precipitation and urban climate, particularly over a long-term period [111, 131, 196].

1.1.2 Urban Heat Island

The Urban Heat Island (UHI) is recognized as one of the clearest examples of climate modification caused by replacing natural areas with artificial surfaces. This phenomenon causes a greater temperature in cities compared with their surroundings. Built-up areas make changes to the energy balance at the lower atmospheric layer (roughness sublayer), which are identified as the main causes of UHI [156].

The UHI is mainly attributed to the reduction in loss of longwave radiation at street level, increased heat storage, anthropogenic heat released from human activities, urban greenhouse effect, inter-reflections of radiation between the urban elements, and loss of evaporation from surfaces compared to vegetated surfaces [155], all of which affect the energy performance of buildings [67]. Surface temperatures of urban facets are mainly controlled by geometric, radiative, thermal, moisture, and aerodynamic properties. View factors control the amount

of radiation that can reach the surfaces and the visibility of the solar path over the course of the day. Albedo and emissivity of the urban surfaces provide control to the shortwave and longwave radiation components reflected and emitted, respectively. Thermal properties including heat capacity and thermal conductivity control the ability of the surfaces to store and conduct heat, respectively. Latent heat flux is another term in the surface energy balance, which is not well investigated, particularly for humid regions and rainy days. The amount of moisture available at the surface and near the surface control the heat removal by the latent heat flux. Aerodynamic roughness length, which influences the exchange processes between the surface and the adjacent atmosphere, provides control on surface temperature by changing the flow regime and wind speed. When convective thermal energy loss for a surface is desired, smooth surfaces experience higher temperatures, as less turbulent flows lower the convective heat transfer coefficient for a surface [156].

UHI can be viewed as a primarily nighttime phenomenon, but it can also be occasionally observed during daytime. It has been suggested that the UHI pattern is strongly influenced by wind speed, wind direction, and the daily maximum air temperature at a rural site nearby a city [59]. During extreme high temperatures, which may be accompanied by high humidity and higher absorption and storage of heat in urban areas, as opposed to rural areas, the sensible heat released from urban surfaces amplifies due to higher surface temperatures [59, 110]. Daytime atmospheric UHI has been reported in Hong Kong [185], where UHI was detected in the early afternoon and at its peak just before sunset. Most commonly during nighttime, urban areas cool down at a lower rate than the surrounding rural areas due to radiation trapping and reduced convection so that the UHI is at its maximum at nights. In addition, the excessively absorbed heat by the urban area during a heat wave will be released at nights with noticeable atmospheric UHI [59, 153]. Nevertheless, the UHI phenomenon cannot be easily generalized because it depends on multiple factors such as built density, ventilation rate, shading, radiation heat transfer, evaporation, background climate, and more, to the extent that occasionally, an Urban Cool Island (UCI) can also be observed in the same climate zone [210].

The UHI can be investigated at different levels or layers, including surface heat island, canopy-layer heat island, and boundary-layer heat island [152]. At the surface level, all urban elements with different optical and thermal properties interact directly with the incoming radiation. Large differences between the properties of rural and urban surfaces in terms of thermal and moisture capacity cause significant temperature differences between rural and urban surfaces during the day.

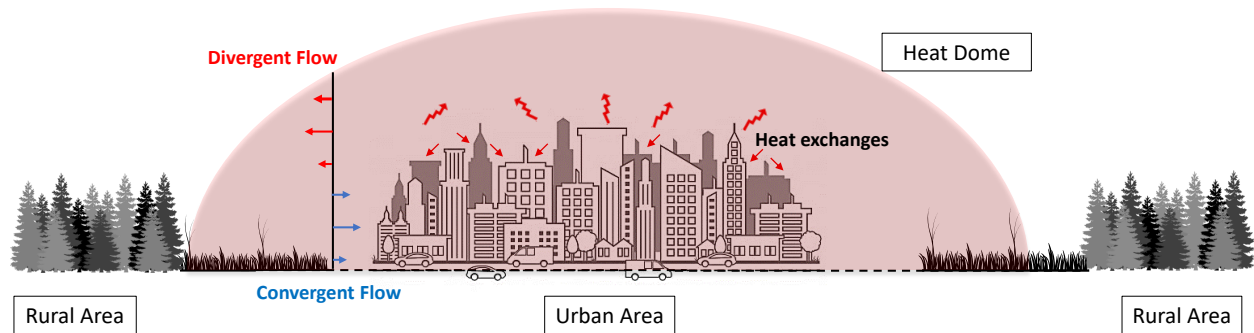


Figure 1.2: Illustration of heat dome flow.

The heat island at the canopy layer is defined by flow within and above the built-up area, and can be extended to two or three times of average building height. At this layer, the aerodynamic and thermal effects of the elements and surfaces cause spatial temperature gradients in both vertical and horizontal directions. Negative heat island can be observed in parts of the urban area where more shade is provided by buildings and trees. The atmospheric UHI usually reaches the maximum peak a few hours after sunset and remains warmer for a few hours after sunrise. Spatially, canopy-layer temperature increases where the rural area meets a city and reaches a peak at the center of the urban area. The thermal profile of atmospheric UHI shows an island-shaped profile, which indicates the size of the area it influences [52].

The boundary-layer heat island follows the same trend as the canopy-layer heat island, but the magnitude of temperature difference tends to remain constant and has less spatial variation. A dome-shape profile, which is also called Urban Heat Island-induced Circulation (UHIC), can form at this layer (see Fig. 1.2). UHIC is driven by UHI and is spatially extended in both horizontal and vertical directions. This phenomenon reveals how the climate of adjacent cities can affect one another via urban ventilation and pollutant transport. From the regional scale point of view, the heat dome of the adjacent cities can merge together and cause regional UHICs. Additionally, the horizontal extent of the UHIC represents the footprint of this heat flow. UHIC generally occurs when the temperature difference between rural and urban areas is large enough to cause a buoyancy-driven flow, and the synoptic wind is weak. Under such conditions, the excess heat in the urban areas lifts up the air,

and causes an upward turbulent plume and a divergent outflow pattern over the city. At the lower level, the lower pressure in the city results in convergent inflow through the urban edges [52–54, 78]. It has been found that this heat transport can have interference effects on atmospheric convection and boundary-layer structure. Recently, the simulation results from a Lagrangian atmospheric transport model, which is called Hybrid Single-Particle Lagrangian Integrated Trajectory-Weather Research and Forecasting-Urban Canopy Model (HYSPLIT-WRF-UCM), showed the three-dimensional map of an urban heat plume for an urban area in the vicinity of a lake [43]. It was suggested that the lake acts as a sink (source) of urban heat during the summer (winter). Furthermore, the scale of UHI can be determined by the ability of the urban surfaces to move heat upward into the atmosphere and away from the city. The shape and size of an urban area can affect the UHI in different forms, including the direction and the amount of convergent flow and, consequently heat exchanges within the urban environment. A water tank experiment revealed that a square urban area experiences non-uniform convergent and divergent flows, while for a circular city both inflow and outflow patterns are axisymmetric [54]. Depending on the mixing heights within the boundary layer of the adjacent cities, pollutant dispersion patterns induced by UHICs can vary. Findings from water tank modelling experiments suggested that pollutants are transported from the smaller to the larger UHI, and the outflows of a city with larger mixing heights limit the vertical pollutant dispersion of the smaller one [54]. However, this process is much more complicated in reality, and more field measurements and numerical simulations at different scales are needed.

Much of the studies on UHI define it as the temperature difference between urban and surrounding undeveloped areas. The poor knowledge of the spatial variation of UHI can challenge this definition and cause a large bias in the estimation of UHI. For example, observational investigations in Oklahoma City showed that atmospheric UHI intensity can vary from 2.1 [K] in the urban area to 0.4 [K] when approaching sub-urban and rural areas [80]. Thus, not only temporal variation but also spatial variation of UHI should be better understood. Also depending on the climate zone, the footprint of UHI effect can extend to several times of the city size, and it can vary during day and night [214, 216]. Zhou et al. (2015) [216] showed that the surface UHI decayed exponentially along urban-rural gradients in China. The surface UHI intensity is also a function of city size, which can, for example, increase with the logarithm of the city size in Europe [215].

1.1.3 Urban Hydrology

Replacing green spaces with impervious surfaces (e.g., roads and buildings) disrupts the watershed's drainage and hydrology. The rivers and streams crossing urban areas have been channelized, dammed, and diverted for water supply. Urbanization generally includes vegetation removal and soil aridation, which reduce the available area for infiltration and increase surface runoff. Therefore, understanding the effect of urbanization on hydrological processes is important for urban water management [156].

The hydrologic cycle (or water cycle) is a phenomenon that involves the continuous circulation of water through the three phases of water vapor, liquid water, and ice. The water cycle is mainly driven by the surface energy balance through evaporation of water from water bodies (e.g., lakes and rivers) and moist surfaces (e.g., vegetation and soils), vertical mixing, condensation into small particles of ice and water, and finally by various forms of precipitation [156, 199].

In general, the assessment of meteorological processes involved in the hydrologic cycle requires a water balance analysis at the surface and its interaction with the groundwater. Depending on the type of the surface, the fraction of precipitation reaching the ground can be stored in the soil and reaches the deeper soil layers. Vegetation intercepts water, increases its return to the atmosphere via evaporation, retains a small fraction, and causes the remainder of water to reach the ground in forms of dripping and throughfall. The unsaturated soil allows the precipitation reaching the surface to infiltrate and recharge the groundwater. The hydraulic conductivity of substrate and the slope of water table control the water fluxes between soil columns. Runoff occurs when the infiltration capacity of the soil and the storage capacity of the surface are exceeded, and water moves overland. Strong and long-lasting precipitation drives more surface runoff, while it can be blocked and delayed by vegetation [156, 199].

As mentioned earlier, urban growth is associated with vegetation removal, soil compaction, and presence of more impervious surfaces [156]. These modifications can threaten to reduce the amount of groundwater, and ultimately increases demand to import water from distant sources by developing significant network of channels and pipes. So, built-up environments require the careful design of drainage systems to cope with the increase in volume and speed of surface runoff [119].

1.1.3.1 Water Balance

Water balance can be outlined for natural or artificial surfaces at different scales (see Figure 1.3). In the rural area, the incoming precipitation (P) is balanced with the evaporation from the surface and soil (E), change in soil water storage (ΔS), leakage at the bedrock (Lk), and the surface runoff which moves overland (R). The surface water balance equation for a rural area is

$$P = E + \Delta S + Lk + R. \quad (1.1)$$

If we apply the water balance equation for an urban neighborhood, an additional source term needs to account for anthropogenic water (I)

$$P + I = E + \Delta S + Lk + R. \quad (1.2)$$

The anthropogenic water can be caused by human activities with different temporal and spatial scales, such as irrigation or industrial processes. The urban areas involve surfaces with different hygrothermal properties and vegetation coverage that can influence the above mentioned terms.

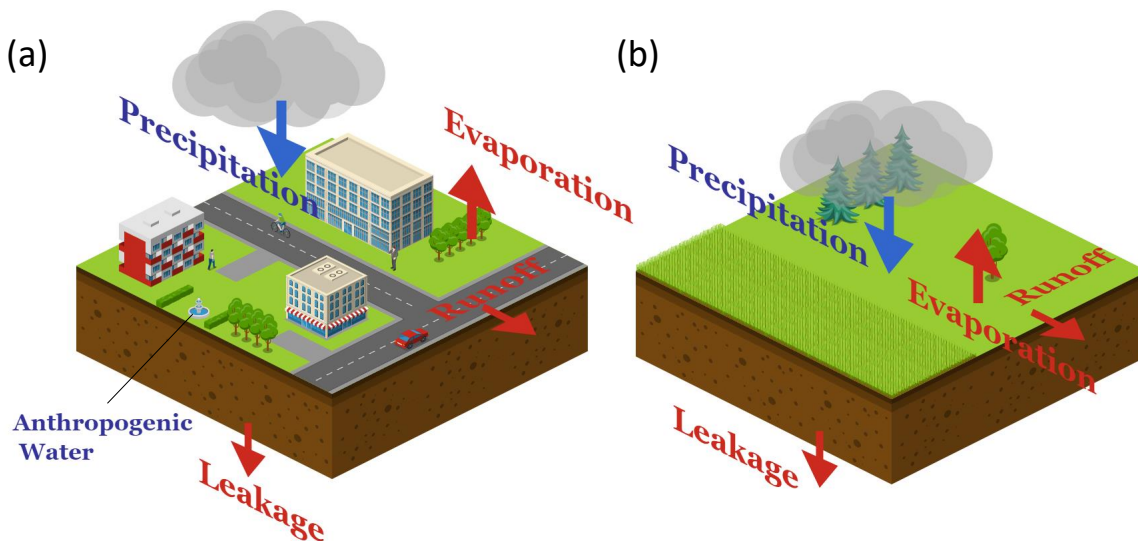


Figure 1.3: Illustration of water balance of an urban area (a) and a rural area (b).

Many studies have indicated that urban areas affect the processes of cloud formation and precipitation patterns [74, 87, 132, 196]. Urban areas modify the moisture and thermody-

dynamic properties of surfaces that consequently affect thermal stratification of the atmosphere and cause heat dome structures. As a result, the atmospheric convection and wind convergence over and downwind of urban areas are affected. Another mechanism that can alter the precipitation patterns in the urban areas is related to greater roughness which can affect the spatial distribution of precipitation by increasing airflow convergence over and downwind of cities [74, 156]. Additionally, anthropogenic aerosols released into the urban atmosphere can modify microphysical processes, including formation, timing, phase, and duration of precipitation [87]. Interception of rainfall by urban surfaces, tree crown, and stems plays an important role in spatial and temporal distribution of moisture in cities. It has been suggested that around 6% of intercepted water is stored in the system before any evaporation or leaving the system as runoff. This fraction is less for the intercepted water at the roof, which is often removed through gutters and possibly down to the sewer system. Recently, green roof technologies, which utilize roofs that are partially or completely covered by vegetation, have been established to retain more water and reduce the peak rates of runoff [156].

Another source term in Equation 1.2 is piped water that is used for green space irrigation with a strong seasonal pattern. Irrigation has a small time scale, but can significantly alter water and energy balances by changing soil water storage, ground evaporation, and vegetation transpiration [114, 156]. Depending on the climate zone, irrigation can be the largest source term in the surface water balance in the summer. Another source of anthropogenic water in urban areas is due to water vapor released to the outdoor environment from various human activities such as emissions from building energy systems and industrial processes. Building energy systems contribute indirectly to the urban water balance by changing the outdoor humidity. The amounts of latent and sensible heat fluxes released into the atmosphere are functions of building energy system operation [138, 156].

Natural areas act as a source of evapotranspiration and replacing them by artificial surfaces causes depletion of evapotranspiration in cities. During wet periods, a small amount of cumulative evapotranspiration is associated with high soil water content and the subsequent rainfall contributes more to runoff. However, high rate of evapotranspiration makes soil dry and leaves the soil with high water capacity. So, low soil water storage provides the precipitation with high probability of infiltration. Impervious surfaces are believed to contribute to evaporation for a shorter period of time after rainfall events than the natural surfaces [164]. However, urban vegetation and pervious surfaces are often the main source of evapotranspiration [119, 156].

Effects of urban growth on streamflow are characterized by larger amounts of surface

runoff, shorter time to find its way to drainage systems and rivers, and lower depth of base flow that decrease water infiltration. Generally, large fractions of smooth and impervious surfaces in cities make the overland flow move faster than those in rural areas. Urban runoff is also recognized as the main form of pollutant transport into the urban drainage systems and freshwater ecosystems [35, 156].

Water storage can occur in the air, surface, and soil columns. Change in the amount of water in the air, which is measured as humidity, has a short time scale due to the turbulence and it is orders of magnitude smaller than water storage in the surface and soil [119, 156]. The storage change in vegetation is also negligible, but it can have an immediate effect on vegetation water use. Due to the high variability of soil moisture content across an urban area and drainage properties of the urban element surfaces, the change in water storage is highly variable.

Figure 1.4 shows a rough visualization of the effect of land use change on the partitioning of precipitation [156]. Over the long term, intercepted water in natural areas is effectively stored and provides a great source of evapotranspiration. As expected, only a small fraction of total precipitation is partitioned into surface runoff. On the other hand, transition from a rural area to a built-up area is associated with more impervious surfaces, hence great volume of surface runoff is generated.

1.1.4 Modeling of Urban Climate

Recently, numerical models have been extensively employed to simulate exchanges of momentum, mass, and energy within the urban boundary layer. They can either be forced by the atmospheric variables to determine energy and water balances at the surface or vice versa. If these two types of models are coupled together, it results in an urban climate model where exchange processes provide the link between the urban atmosphere and the urban surfaces.

The numerical models used to simulate urban climate typically contain equations that conserve momentum, mass, and energy. These equations determine the relationships between meteorological quantities and surface conditions under different large scale meteorological forcing conditions. The aerodynamic, thermal, and radiative properties of the urban surfaces provide boundary conditions to solve the governing equations within the urban boundary layer. The surface roughness slows down air parcels and removes a fraction of momentum from the atmospheric flow [156]. The incoming shortwave and longwave radiation fluxes are

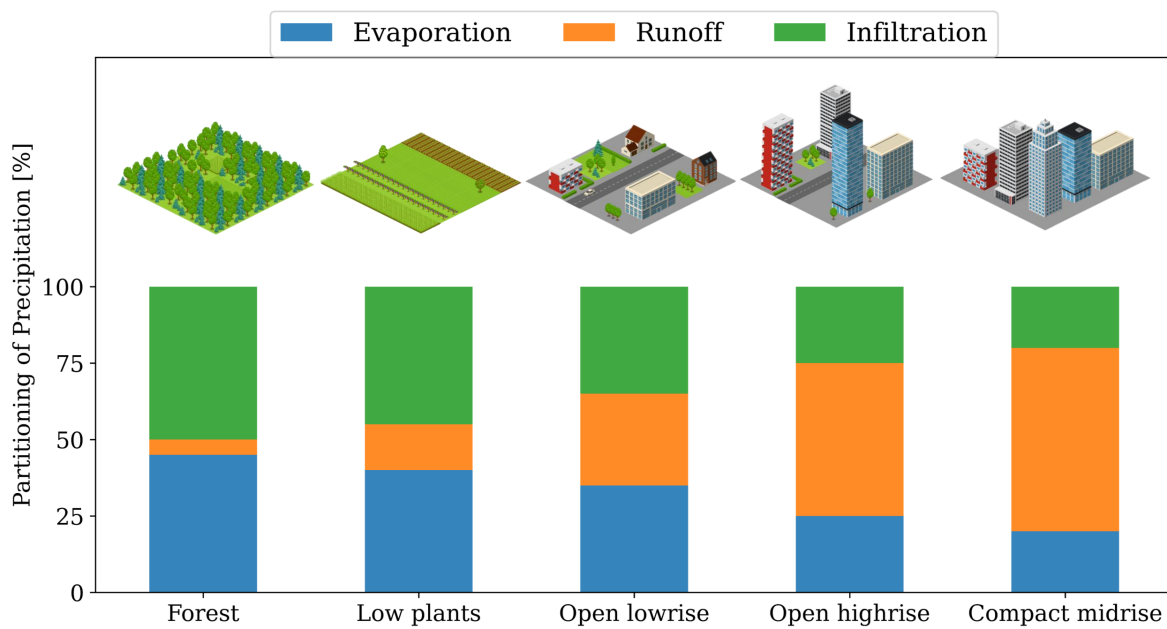


Figure 1.4: Generalized partitioning of precipitation into evaporation, runoff, and infiltration for different climate zones [156].

the driving forces to the surface and are balanced by sensible heat flux (Q_{sens}), latent heat flux (Q_{lat}), and ground heat flux (Q_{grd})

$$Q_S + Q_L = Q_{\text{sens}} + Q_{\text{lat}} + Q_{\text{grd}}. \quad (1.3)$$

This equation can be used for any surface in an open green rural area (Figure 1.5b) or individual urban facets such as road, roof, and walls. However, the energy balance of a volume in an urban area is more complex as there are new sink and source terms within the volume, energy exchanges across the volume surfaces, and the interaction with the urban facets should be taken into account (Figure 1.5a). As mentioned earlier, the boundary conditions for the mass conservation can be obtained from surface water balance equations (Equations 1.1 and 1.2).

Urban climate models are generally designed for certain spatial and temporal scales that cover the atmospheric processes of interest. For example, if the model aims to determine the exchange processes between an entire city and the atmosphere, the computational domain should be extended far beyond the horizontal and vertical size of the city. The numerical models are limited to the processes relevant to the given phenomena. For example, air pollution models generally cover atmospheric flow and air chemistry processes. Urban climate models are usually designed to simulate the interaction between the surface and the atmosphere. Depending on the scale of analysis, the surface representation can vary from a simple one-dimensional slab in a mesoscale model to more realistic forms that include vertical and horizontal dimensions. In the latter case, simplifying the urban canopy layer into a street canyon with representative dimensions and orientation is a common practice. These Urban Canopy Models (UCMs) are either used stand-alone to obtain the exchanges in an urban area or coupled with the mesoscale models that provide more realistic boundary conditions for them.

Mesoscale models incorporating the urban climate were initially aimed to resolve weather features with grid resolutions of at best few hundred meters horizontally and a few meters vertically, without the functionality to resolve microscale three-dimensional flows or to account for atmospheric interactions with specific urban elements such as roads, roofs, and walls [19]. These models usually consider the effect of built-up areas by introducing an urban aerodynamic roughness length [69] or adding source or sink terms in the momentum (drag) and energy (anthropogenic heat) equations [48]. Therefore, if higher grid resolutions less than ten meters (horizontal and vertical) are desired [135, 194, 201], microscale climate

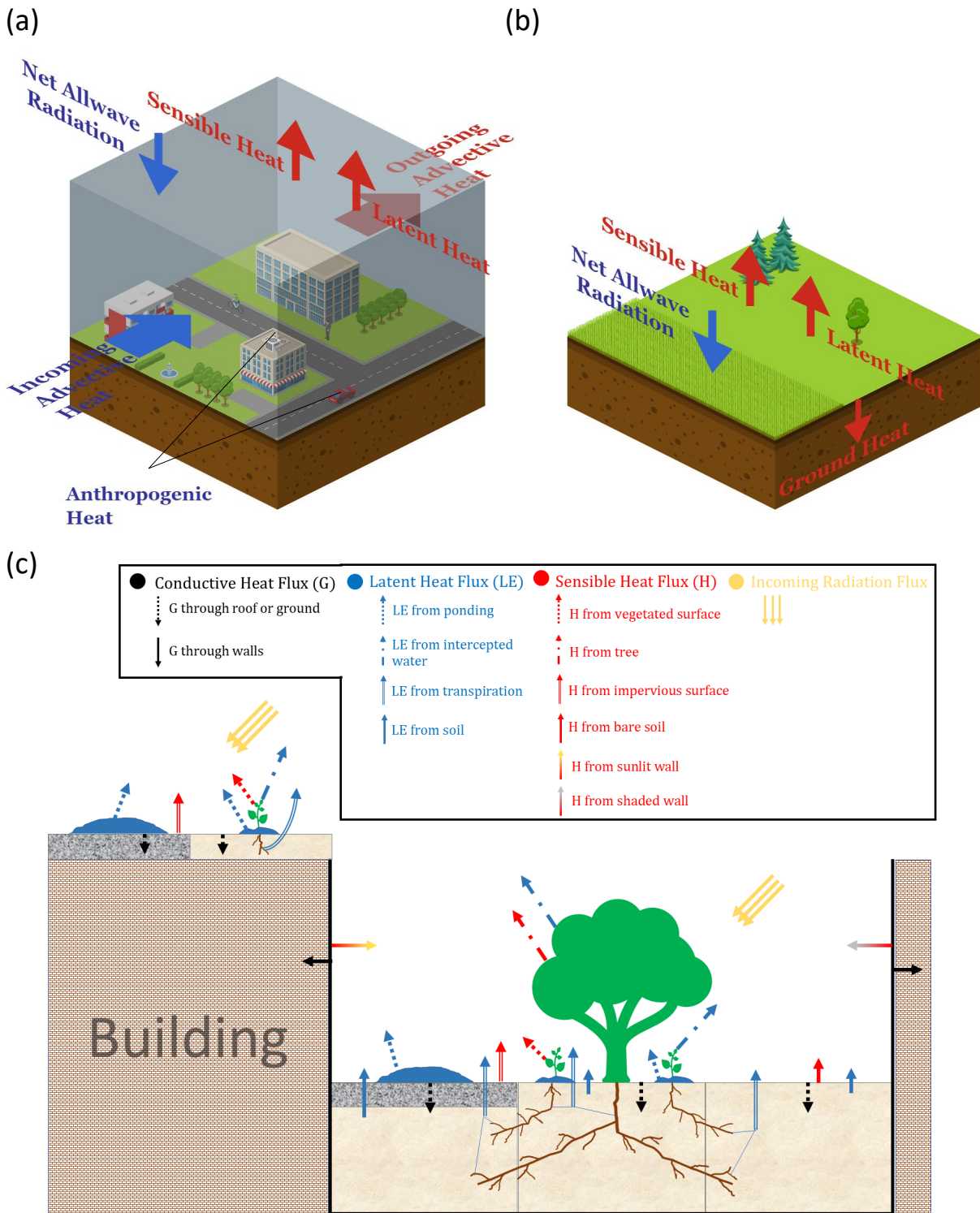


Figure 1.5: Generalized partitioning of incoming shortwave and longwave radiation into sensible, latent, and ground heat fluxes. In the urban area (a) and the rural area (b). Urban energy fluxes at the facades are shown (c).

models should be deployed.

Computational Fluid Dynamics (CFD) can be used to investigate the urban microclimate taking into account interactions between the atmosphere and the urban elements with full three-dimensional flow analysis [6, 16, 141–143, 146, 148, 180]. However, these models are usually used for airflow simulation around generic building arrays or individual buildings. Despite accurate predictions, CFD models are not computationally efficient, particularly for simulations at larger scales and for a long period of time, and they usually do not represent many processes in the real atmosphere, such as clouds and precipitation. For example, Mortezaadeh and Wang (2020) [144] developed a Fast Fluid Dynamics (FFD) model based on semi-Lagrangian approach that only solves transient flow around blocks of buildings.

As an alternative, Urban Canopy Models (UCMs) require an understanding of the interactions between the atmosphere and urban elements to parameterize various exchange processes of radiation, momentum, heat, and moisture within and just above the canopy. UCMs have been developed based on experimental data [7, 8, 34, 104, 124], three-dimensional simulations, or simplified urban configurations [39, 99, 101, 122, 146]. These urban canopy models are more computationally efficient than CFD models. They are designed to provide more details on heat storage and radiation exchange, while they employ less detailed flow calculations. Models are frequently simplified into one direction, particularly the vertical direction, assuming horizontal uniformity. This means that exchanges between air parcels are considered only in the vertical direction and horizontal exchanges are set to zero. These type of models are called column models. Higher dimensional models are usually used when exchanges are considerable in other directions such as flow around individual buildings.

Development of energy balance models has been underway with different levels of complexity (see Figure 1.6). The first generation models simplified the urban canopy into a slab associated with the thermal and aerodynamic properties that describe the urban canyon. In the next generations of the models, two and three-dimensional structures have been introduced to consider more features of the urban streets. In other words, the models can be designed to solve the energy and mass balance equations either at a single layer or at multiple layers. The single-layer models solve the equilibrium equations for each urban facet as they interact with air state variables at a single hypothetical point. The multi-layer models can provide higher resolution to the urban canopy model, most commonly considering the change of state variables in the vertical direction. Multi-layer models solve the energy, mass, and momentum equations at multiple layers extending from ground up to an elevation above canyon height. Multi-layer models usually link the layers by solving prognostic equations,

which distribute energy, mass, and momentum fluxes vertically.

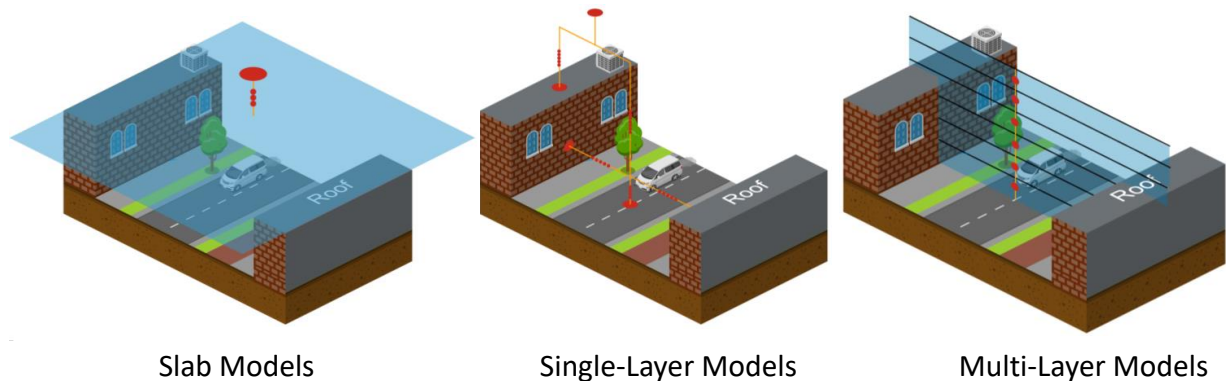


Figure 1.6: Urban canopy models with different levels of complexity. From left to right the complexity of the model increase from a single point (slab model) to multi points at a single layer (single-layer model) and multi layers (multi-layer model).

Urban microclimate models must account for a few unique features of the urban environment. Urban obstacles such as trees and buildings contribute substantially to the changing of flow and turbulence patterns in cities [88]. Difficulties arise when spatially-inhomogeneous urban areas create highly three-dimensional wind patterns that are difficult to model [168, 171]. For example, the surfaces of urban obstacles exert form and skin drag and consequently alter flow direction and speed and produce eddies at different spatiotemporal scales. This can lead to the formation of shear layers at roof level with variable oscillation frequencies [125, 197, 212]. All such phenomena should be properly approximated in parameterizations.

Heat exchanges between the indoor and outdoor environments significantly influence the urban microclimate. Various studies have attempted to parametrize heat sources and sinks caused by buildings such as heat fluxes due to infiltration, exfiltration, ventilation, walls, roofs, roads, windows, and building energy systems [90, 179, 206]. Therefore, a Building Energy Model (BEM) is required to be properly integrated in an urban microclimate model to take account of the impact of building energy performance on the urban microclimate and vice versa [27, 28, 71]. This feedback interaction between the urban microclimate and indoor environment can significantly affect UHI and energy consumption of buildings [1, 178].

Urban vegetation can substantially reduce the adverse effects of UHI, particularly during heat waves, resulting in improved thermal comfort [5, 12, 70]. Urban trees can potentially increase the overall albedo of a city, provide shade and shelter, and, therefore, change the

energy balance of the individual buildings as well as the entire city [5]. A study of the local-scale surface energy balance revealed that the amount of energy dissipated due to the cooling effect of trees is not negligible and should be parameterized properly [70]. In addition, the interaction between urban elements, most importantly trees and buildings, is evident in radiation trapping within the canyon and, most importantly, shading impact of trees [23, 99, 167]. Buildings and trees obstruct the sky with implications in long and shortwave radiation fluxes downward, and upward that may create unpredictable diurnal and seasonal changes for the UHI [61, 91, 209]. Also, it has been shown that not only trees but also the fractional vegetation coverage on urban surfaces can alter urban temperatures with implications in UHI [12]. Trees also exert drag and alter flow patterns within the canopy. However, this effect is not as significant as that drag induced by buildings [101]. Such complex interactions must be accounted for in successful urban microclimate models.

Some efforts also have begun to develop multi-scale climate models by coupling the mesoscale and the microscale models [33, 42, 94, 127, 140]. The mesoscale models are generally designed to use either single-layer or multi-layer canopy models using feedback interaction with the atmospheric models. The coupling approach between the Weather Research and Forecasting (WRF) and the urban canopy models have been extensively used for weather predictions, regional climates, air quality, and water resources. Different parameterizations have attempted to provide this coupling such as the Noah land-surface model, the Single-Layer Urban Canopy Model (SLUCM) [104, 124], and the multi-layer urban canopy model [122, 178, 179].

Fewer existing models provide an accurate representation of hydrological processes in the urban environment. Attempts have been made to include the impact of surface energy and water budgets for the different surface elements, such as soil, vegetation, and urban canopy. The Environment and Climate Change Canada (ECCC) has developed the Soil, Vegetation, and Snow (SVS) scheme. SVS uses the tiling approach, and instead of a single energy budget for the entire surface, separate energy budgets for bare ground, vegetation, and snow cover are considered [81]. Wang et al. (2013) [204] developed an urban hydrological model, which was coupled to an urban canopy model, accounting for water transport from natural and engineered surfaces. Recently, the SLUCM in WRF was modified by integration of anthropogenic latent heat, urban irrigation, evaporation from paved surfaces, and the urban oasis effect [207, 208]. Yang et al. (2016) [208] evaluated the new WRF-SLUCM model and found that the model prediction underestimates precipitation in the summer and overestimates it in the fall. The results from this coupled model indicated that hydrological

processes decrease air temperature and increase dew point temperature in the urban areas, and there is a complex relationship between surface temperature and 2-m air temperature. Järvi et al. (2011) [84] developed the Surface Urban Energy and Water balance Scheme (SUEWS), which calculates energy and water balances in the urban area with multiple surface types using hourly meteorological forcing data. The capability of WRF to capture land-atmosphere interactions and rainfall patterns has been investigated. It was shown that WRF is sensitive to surface characteristics and can significantly affect energy and water balances. While it can capture radiative fluxes and mean profile of meteorological quantities, wind and flow pattern at the lower level cannot be simulated accurately [110]. The Global Environmental Multiscale (GEM) atmospheric model can also be used at the mesoscale. In GEM, the tile approach is used to parameterize the land-atmosphere interactions and the tiles represent the urban and rural surfaces, water, continental ice, and sea ice [82].

1.2 Research Gaps

Numerous studies have focused on high-fidelity urban microclimate models with high spatio-temporal flow resolution, capturing important features of the urban microclimate with acceptable accuracy [16, 66, 148, 187]. Some example CFD models of this kind include Open-source Field Operation And Manipulation (OpenFOAM) [3, 6, 10], Parallelized Large-Eddy Simulation Model (PALM) [120, 168], and ENVI-met [46]. Despite the advances, however, high-fidelity models capable of resolving three-dimensional flows at microscale are not computationally efficient and they are complex to implement for operational applications. As a remedy, lower-dimensional flow urban microclimate models have been developed with many practical applications in city planning, architecture, and engineering consulting (see Table 1.1). For example, bulk flow (single-layer) models such as Urban Weather Generator (UWG) calculate the flow dynamics at one point, usually the centre of a hypothetical urban canyon, which is representative of a neighborhood [26, 29, 104, 133, 173, 179]. Another bulk flow (single-layer) model is the Canyon Air Temperature (CAT) model, which utilizes standard data from a meteorological station to estimate air temperature in a street canyon [51]. The Town Energy Balance (TEB) calculates energy balances for urban surfaces, which is forced by meteorological data and incoming solar radiation in the urban site on top of the modeling domain [126]. The Temperatures of Urban Facets - 3D (TUF-3D) model calculates urban surface temperatures with a focus on three-dimensional radiation exchange, but it adopts bulk flow (single-layer) modeling, and it is forced by meteorological data on top of its domain

[102]. More recently, TUF-3D was coupled to an Indoor-Outdoor Building Energy Simulator (TUF-3D-IOBES), but this model adopted a bulk flow (single-layer) parameterization [206]. The multi-layer Building Effect Parametrization-Tree (BEP-Tree) model includes variable building heights, the vertical variation of climate variables, and the effects of trees, but it is not linked to a building energy model [98, 100, 122]. More recently, the BEP model has been coupled to a Building Energy Model (BEP+BEM) but it is forced with meteorological variables from higher altitudes above a city using mesoscale models, instead of near-surface meteorological variables measured outside the city (rural areas).

Precipitation is known as the primary driver of land surface hydrological processes and a major component in water and energy circulations [84]. In recent years, this recognition has motivated efforts to include urban hydrology in urban canopy models. The Urban Tethys-Chloris (UT&C) model [129] has shown that the biophysical and ecophysiological behavior of urban vegetation can be a major contributor to urban energy and water balances. Recent model development studies have improved the energy and water exchanges by including the effect of ground vegetation [109, 204], trees [101, 108, 167, 174] and solving surface water balance equations [23, 84, 149, 189]. Despite growing demand to consider these effects, the present models are still oversimplified, not considering precipitation effects and hydrological processes.

An overview of the literature reveals no independent urban microclimate model that accounts for spatio-temporal variation of meteorological parameters in the urban environment and considers the effects of trees, precipitation, urban hydrology, building energy, radiation, and the connection to the near-surface rural meteorological conditions measured outside a city. Additionally, there is a lack of an urban climate model which is independent of mesoscale modeling, computationally efficient, and operationally simple for practical applications.

1.3 Objectives

As discussed earlier, adequate representation of urban vegetation, precipitation, hydrological processes, and building energy are critical for comprehensive simulation of urban climate. Trees can provide shade and shelter, cool down air and surface temperature, and ultimately change the energy and water balances. The inclusion of urban hydrology provides better prediction for evaporation and transpiration, particularly during precipitation events. Depending on the local climate zone, energy fluxes from buildings can significantly alter the urban climate and vice versa. Hence, the goal of this thesis is to develop a new urban

Table 1.1: Summary of urban canopy models (VF: View Factor)

Model Name	Model Components						Reference
	Building Energy	Urban Canopy	Radiation Model	Urban Hydrology	Urban Vegetation	Forcing	
UWG	single thermal zone model	single layer	single layer, VF:analytical	No	bulk parameterization of low/high veg.	EPW weather data	Bueno et al. (2012) [26]
CAT	No	single layer	single layer, VF:analytical	No	No	canyon top forcing	Erell et al. (2006) [51]
TEB	No	single layer	single layer, VF:analytical	No	No	canyon top forcing	Masson et al. (2002) [126]
TUF-3D	No	3D raster	radiosity model	No	No	canyon top forcing	Krayenhoff and Voogt (2007) [102]
TUF-3D-IOBES	single thermal zone model	3D raster	radiosity model	No	No	canyon top forcing	Yaghoobian and Kleissl (2012) [206]
BEP	No	multi-layer	multi layer, VF:analytical	No	No	mesoscale modeling	Martilli et al. (2002)[122]
BEP-Tree	No	multi-layer	multi layer, VF:Ray Tracing	No	multi-layer parameterization of high veg.	canyon top forcing	Krayenhoff et al. (2020) [100]
BEP-BEM	single thermal zone model	multi-layer	multi layer, VF:analytical	No	No	canyon top forcing	Salamanca et al. 2010 [179]
UT&C	No	two layers	single layer, VF:Ray Tracing	Yes	single-layer parameterization of low/high veg. at road and roof levels	canyon top forcing	Meili et al. (2020) [129]
-	No	single layer	single layer, VF:analytical	No	bulk parameterization of high veg.	canyon top forcing	Kusaka et al. (2001) [104]
VUCM	No	single layer	single layer, VF:analytical	Yes	single-layer parameterization of high veg.	canyon top forcing	Lee and Park (2008) [108]
-	No	single layer	single layer, VF:ray tracing	Yes	single-layer parameterization of high veg.	canyon top forcing	Ryu et al. (2016) [174]

microclimate model, called the Vertical City Weather Generator (VCWG), which attempts to overcome some of the limitations mentioned in the previous sections. VCWG resolves vertical profiles of climate variables, such as potential temperature, wind, specific humidity, and turbulence kinetic energy in relation to surface energy and water balance models and urban design parameters. VCWG also includes a building energy model. It allows parametric investigation of design options on urban climate control at multiple heights, particularly if multi-storey building design options are considered. This is a significant advantage over the bulk flow (single-layer) models such as UWG, which only consider one point for flow dynamics inside a hypothetical canyon [26, 29, 48, 102, 104, 108, 124]. The advantages of VCWG are as follows

- It can either be used as a standalone model (forced by rural climate data) or coupled with mesoscale models.
- Unlike many UCMs that are forced with climate variables above the urban roughness sublayer (e.g. TUF-3D), VCWG can also be forced with rural climate variables measured at 2 m (temperature and humidity) and 10 m (wind) above ground level (a.g.l.) that are widely accessible and available around the world, making VCWG highly practical for urban design investigations in different climates.
- Vertical profiles of the variables are calculated in the rural area considering effects of thermal stability, aerodynamic, temperature, and humidity roughness lengths. This will provide more accurate boundary condition for the urban model compared to the predecessor models (e.g. UWG).
- VCWG provides urban climate information in one dimension, i.e., resolved vertically, which is advantageous over bulk flow (single-layer) models (e.g., UWG).
- The model accounts for hydrological processes, including transpiration from ground vegetation and trees as a function of photosynthetic activities, evaporation from surface and subsurface, water interception, runoff, and runoff at most urban surfaces.
- VCWG is coupled with a building energy model using two-way interaction.
- Unlike UWG, VCWG considers the effect of trees in the urban climate by modelling evapotranspiration (latent heat transfer), sensible heat transfer, radiation transfer, drag, and other processes introduced by trees.

Chapter 2 introduces the methodologies for rural and urban climate modeling. In the first stage of this thesis, VCWG v1.3.2 is developed with the main components of a radiation model to calculate net allwave radiation fluxes at the urban and rural surfaces, a rural model to calculate the required boundary conditions at the top of an urban area, a surface energy balance model to calculate the heat exchanges and surface temperatures, a column model to determine the vertical profile of climate variables in the urban area, and a building energy model to predict the performance of a building. In this version of the model, the only source term for the evaporative fluxes is the transpiration from trees. In the next step, VCWG v2.0.0 is developed that overcomes the limitations of the previous version by including an urban hydrology model. The new version simulates the hydrologic processes, including evapotranspiration from low and high vegetation at the roof and ground levels, soil evaporation, runoff, surface runoff, and infiltration. In addition, this version of the model can be forced by more realistic weather data, which is obtained from reanalysis datasets. Both versions of VCWG are evaluated against field observations from the Basel UrBan Boundary Layer Experiment (BUBBLE) (Chapters 3 and 4). Additionally, VCWG v2.0.0 is evaluated against observations in Vancouver in 2008 (Chapter 4). The performance of VCWG is explored in numerous case studies in Basel and Vancouver (Chapters 3 and 4).

Chapter 2

Methodology

Figure 2.1 shows the VCWG model schematic. VCWG consists of six integrated sub-models

1. A rural model (Section 2.1) provides meteorological boundary conditions to the urban components of VCWG based on a surface energy balance model (Section 2.1.1). The surface energy balance model is used to calculate the surface heat fluxes and the soil temperature profile in the rural site [26, 29]. The Monin-Obukhov similarity theory (Section 2.1.2) is used to compute friction velocity and vertical profiles of temperature and specific humidity in the atmospheric surface layer [30, 49, 161];
2. A radiation model with vegetation (Section 2.2.1) is used to compute the longwave and shortwave heat exchanges between the urban canyon, trees, and the atmosphere/sky. This model was originally developed by Meili et al. (2020) [129];
3. An urban surface energy balance model (Section 2.2.2) is used to calculate surface heat fluxes including sensible, latent, and conductive heat fluxes. This model is coupled with a hydrology model to account for latent heat fluxes from intercepted water, transpiration, and soil columns. The model also computes the soil temperature profile;
4. An urban one-dimensional vertical diffusion model (Section 2.2.3) is used to calculate the vertical profiles of urban microclimate variables including potential temperature, wind speed, specific humidity, and turbulence kinetic energy, considering the effects of urban hydrology, trees, buildings, and building energy systems (e.g. condensers and exhaust stacks). This model was initially developed by Santiago and Martilli (2010) [182] and Simón-Moral et al. (2017) [183], while it was later ingested into another

model called the Building Effect Parametrization with Trees (BEP-Tree), considering the effects of trees [98, 100, 101];

5. A Building Energy Model (BEM) (Section 2.2.4) is used to determine the waste heat of buildings imposed on the urban environment. This model is a component of the Urban Weather Generator (UWG) model developed by Bueno et al. (2012) [26] and Bueno et al. (2014) [29]; and
6. A hydrology model (Section 2.2.5) is used to obtain ecophysiological behavior of urban trees and low vegetation at the ground and roof levels and calculate urban hydrological exchanges and soil water content profile in the presence of precipitation. This model is a component of the UT&C model originally developed by Meili et al. (2020) [129].

These sub-models are integrated to predict vertical variation of urban micro-climate variables including potential temperature, wind speed, specific humidity, and turbulence kinetic energy, as influenced by aerodynamic and thermal effects of urban elements, including long-wave and shortwave radiation exchanges, sensible heat fluxes released from urban elements, latent heat fluxes from intercepted water, vegetation, and soil columns, and the induced drag by urban obstacles. The rural model takes latitude, longitude, dry bulb temperature, relative humidity, dew point temperature, and pressure at 2 m a.g.l., wind speed and direction at 10 m a.g.l., down-welling direct shortwave radiation flux, down-welling diffuse shortwave radiation flux, down-welling longwave radiation flux, deep soil temperature, and potentially precipitation from a file in an EnergyPlus Weather (EPW) file format [137]. Note that EPW files generally contain historical records for the Typical Meteorological Year (TMY), but VCWG simply takes data in this format, which can be specific to any time period. If EPW datasets are not available for the region of interest, alternatively VCWG retrieves forcing data from the ERA5-Land dataset. ERA5-Land is a real-time reanalysis dataset that provides hourly atmospheric variables with a spatial resolution of 9 km from 1981 to present [175]. For every time step, and forced with the set of weather data, the rural model then computes a potential temperature profile, a specific humidity profile, friction velocity, and a horizontal pressure gradient as a function of friction velocity, all of which are forced as boundary conditions or source terms on the one-dimensional vertical diffusion model in the urban area. The potential temperature and specific humidity are forced as fixed values on top of the domain for the urban vertical diffusion model in the temperature and specific humidity equations, respectively. The horizontal pressure gradient is included as a source

term for the urban vertical diffusion model in the momentum equation. It must be acknowledged that the model does not consider the horizontal advection from the rural area. The model assumes that the internal urban boundary layer has developed sufficiently to be in equilibrium with the underlying urban surface, and the top of the domain is above the urban boundary layer. As an alternative to the rural model, VCWG can read an external forcing file containing wind speed, wind direction, temperature, humidity, and precipitation on an hourly basis at the top of the urban domain. This option is particularly useful when the user wants to couple VCWG with a mesoscale model. While forced by the rural model or an external forcing file, the urban one-dimensional vertical diffusion model is also coupled with the building energy, radiation, surface energy balance, and hydrology models. The five models are fully interactive with each other. The urban one-dimensional vertical diffusion model calculates the flow quantities at the centre of control volumes, which are generated by splitting the urban computational domain into multiple layers within and above the urban canyon. The urban domain extends to three times building height that conservatively falls closer to the top of the atmospheric roughness sublayer in the urban area [6, 182], but within the inertial layer in the rural area, where Monin-Obukhov similarity theory can be applied [14]. In VCWG, buildings with uniformly-distributed height, equal width, and equal spacing from one another, represent the urban area. The two-way interaction among the building energy model, radiation model, surface energy balance model, hydrology model, and the urban one-dimensional vertical diffusion model is designed to update the boundary conditions, surface temperatures, and the source/sink terms in the transport equations in successive time step iterations. More details about the sub-models are provided in the subsequent sections.

2.1 Rural Model

The rural model reads the forcing meteorological variables including wind speed, temperature, and relative humidity near the ground, incoming shortwave and longwave radiation from sky and possibly precipitation, and then calculates the vertical profile of potential temperature and specific humidity using Monin-Obukhov Similarity Theory (MOST). The model is based on the surface energy balance using either the model developed by Louis (1979) [113] or Penman-Monteith method [11]. Deep soil temperature and surface heat fluxes are used to solve the transient heat diffusion equation and ultimately determine the surface temperature.

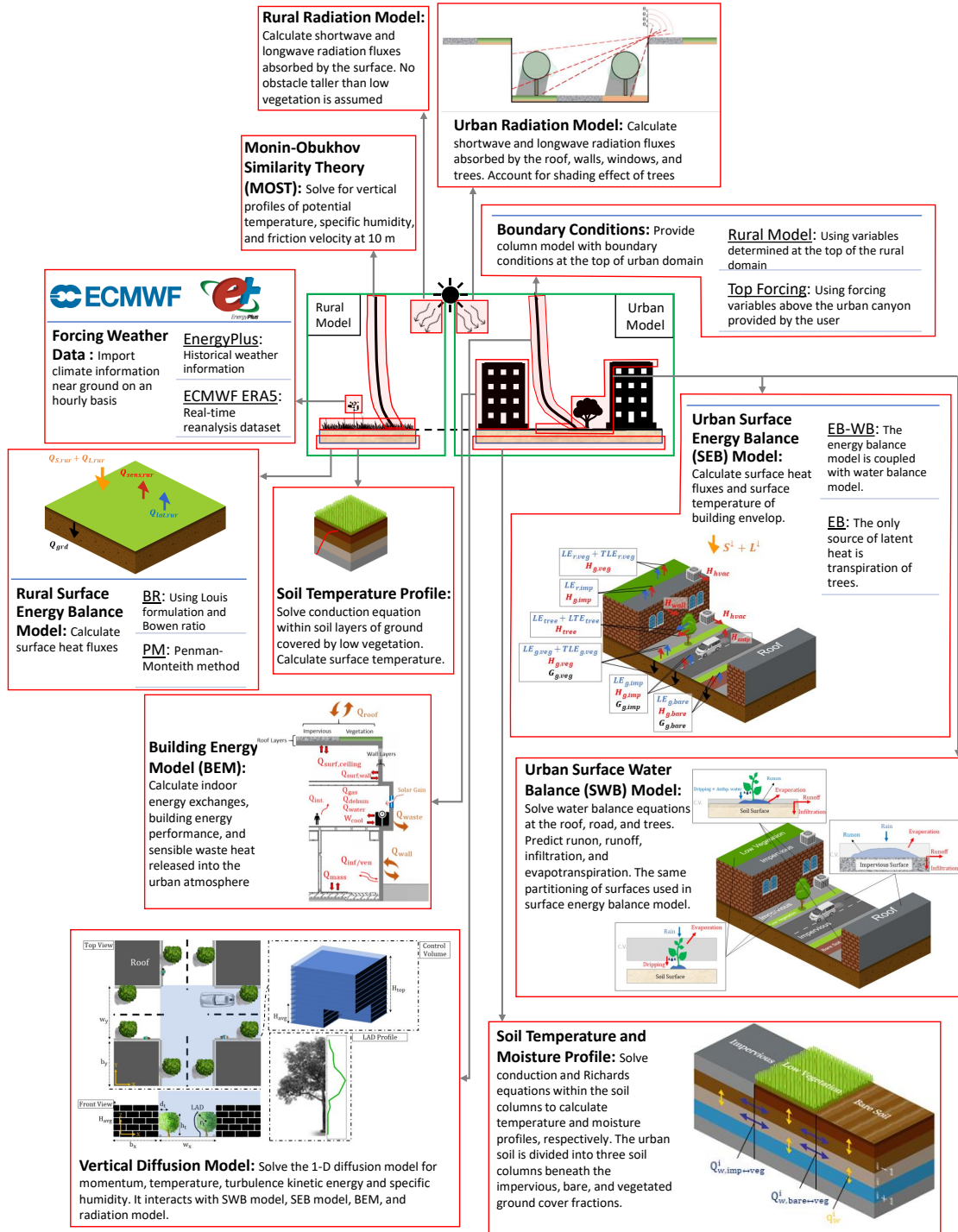


Figure 2.1: Illustration of VCWG.

2.1.1 Surface Energy Balance Model

As shown in Figure 2.2, the surface energy balance for a flat surface or rural area involves the net allwave radiation fluxes $S_{n,rur} + L_{n,rur}$ [W m^{-2}] into sensible H_{rur} [W m^{-2}], latent LE_{rur} [W m^{-2}], and ground conductive G_{rur} [W m^{-2}] heat fluxes

$$S_{n,rur} + L_{n,rur} = H_{rur} + LE_{rur} + G_{rur}, \quad (2.1)$$

where the net shortwave solar radiation flux absorbed at the surface can be calculated from

$$S_{n,rur} = ((1 - f_{veg,rur})(1 - \alpha_{rur}) + f_{veg,rur}(1 - \alpha_V))(S^{\downarrow direct} + S^{\downarrow diffuse}), \quad (2.2)$$

where $f_{veg,rur}$ [-] is the fraction of the rural area covered by vegetation, α_{rur} [-] is albedo of the surface of rural area, α_V [-] is the albedo of vegetation (here considered to be the same for rural and urban vegetation), and $S^{\downarrow direct}$ and $S^{\downarrow diffuse}$ [W m^{-2}] are the forcing direct and diffuse shortwave radiation fluxes from the EPW file or the ERA5-Land dataset, respectively. The net longwave radiation flux absorbed at the surface can be calculated as

$$L_{n,rur} = L^{\downarrow} - L_{rur}^{\uparrow} = \varepsilon_{rur} (L^{\downarrow} - \sigma T_{s,rur}^4), \quad (2.3)$$

where L^{\downarrow} [W m^{-2}] is the forcing longwave radiation flux from the EPW file, L_{rur}^{\uparrow} [W m^{-2}] is the longwave radiation flux leaving the rural surface at temperature $T_{s,rur}$ [K], and ε_{rur} [-] is rural surface emissivity.

In VCWG, the sensible and latent heat fluxes in the rural area can be calculated using either the model developed by Louis (1979) [113] or the widely used formulation of Penman-Monteith originally developed by Penman (1948) [162]. The former is recommended when the Bowen ratio in the rural are is available to calculate the latent heat flux, otherwise the Penman-Monteith equations can be used to determine the latent heat flux.

In the first approach, the net sensible heat flux can be computed using the formulation of Louis (1979) [113]

$$H_{rur} = -\rho C_p \frac{\kappa^2}{\left(\ln \frac{z}{z_{0,rur}}\right)^2} \frac{1}{R_{drag}} \bar{S}_{rur,10m} (\bar{\Theta}_{rur,2m} - \bar{\Theta}_{s,rur}) F_h \left(\frac{z}{z_{0,rur}}, Ri_B \right), \quad (2.4)$$

where $R_{drag} = 0.74$ [-] is the ratio of the drag coefficients for momentum to heat [30], $Ri_B = gz\Delta\bar{\Theta}/(\bar{\Theta}_{ref}\bar{S}_{rur}^2)$ [-] is the bulk Richardson number, $\Delta\bar{\Theta}$ [K] is temperature difference

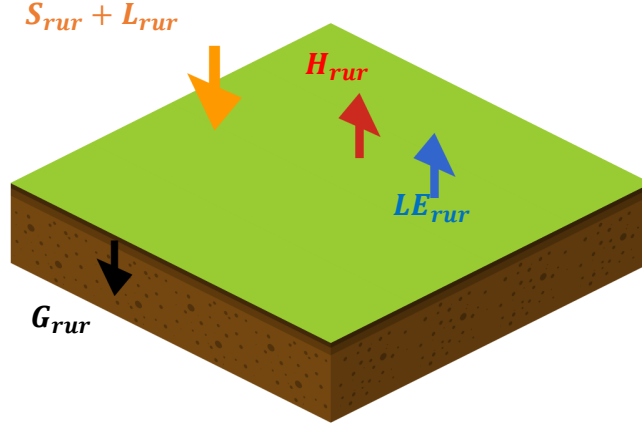


Figure 2.2: Illustration of surface energy balance in a rural area.

between the surface and the atmosphere, $\bar{\Theta}_{\text{ref}}$ [K] is reference temperature, g [m s^{-2}] is gravitational acceleration, $\kappa = 0.4$ [-] is von Kármán constant, $z_{0,\text{rur}}$ [m] is aerodynamic roughness length in the rural area, and \bar{S}_{rur} [m s^{-1}] is wind speed. F_h [-] is the stability function for sensible heat flux and can be computed as [113]

$$F_h = \begin{cases} 1/(1 + 0.5bRi_B)^2 & Ri_B > 0, \\ 1 - bRi_B/(1 + c\sqrt{-Ri_B}) & Ri_B \leq 0, \end{cases} \quad (2.5)$$

where b and c are model constants and can be determined by fitting the equation to the results from numerical simulations and experimental results [113]. After calculating the sensible heat flux, the net latent heat flux is calculated using the Bowen ratio β_{rur} [-] such that $LE_{\text{rur}} = H_{\text{rur}}/\beta_{\text{rur}}$ [W m^{-2}].

VCWG is alternatively designed to calculate latent heat flux in the rural area using the Penman-Monteith method, if there is no reliable information about Bowen ratio. Evapotranspiration in an open area covered by low vegetation depends on meteorological quantities (including solar radiation, air temperature, vapor pressure deficit, wind speed near the ground), and types of vegetation, which have different transpiration rates. For an area with low leaf area index, the water is mainly lost by the soil evaporation as the soil surface is exposed to the atmosphere at a larger area. However, rural areas with high vegetation index provide more coverage of the ground underneath, so the transpiration becomes dominant.

So, based on the Penman-Monteith method the latent heat flux can be calculated as follows [11]

$$LE_{\text{rur}} = \frac{\Delta(S_{\text{n,rur}} + L_{\text{n,rur}} - G_{\text{rur}}) + \frac{\rho \cdot C_p \cdot VPD}{r_a}}{\Delta + \gamma_1 \left(\frac{r_a + r_s}{r_a}\right)}, \quad (2.6)$$

where G_{rur} can be calculated as a fraction of net allwave radiation flux [11], $\gamma_1 = 0.00163P_b/L$ [kPa K⁻¹] is the psychrometric constant and can be calculated as a function of barometric pressure P_b and latent heat of vaporization L [J kg⁻¹], Δ is the slope of saturated vapor pressure [kPa K⁻¹]

$$\Delta = \frac{\partial e_s}{\partial T_a} = \frac{4098(0.6108e^{17.27T/(T+237.3)})}{(T + 237.3)^2}, \quad (2.7)$$

e_s is saturated vapor pressure [kPa] and T_a [°C] is air temperature, $VPD = e_s - e_a$ [kPa] is vapor pressure deficit, e_a is vapor pressure [kPa], r_a [s m⁻¹] is the aerodynamic resistance

$$r_a = \frac{\ln\left(\frac{z_m - d_{\text{rur}}}{z_{0,\text{rur}}}\right) \ln\left(\frac{z_h - d_{\text{rur}}}{z_{\Theta,\text{rur}}}\right)}{\kappa S_{\text{rur},z_m}}, \quad (2.8)$$

z_m [m] and z_h [m] are the heights at which wind speed and temperature are measured, respectively, $z_{0,\text{rur}}$ [m] and $z_{\Theta,\text{rur}}$ [m] are the rural roughness lengths for momentum and temperature respectively, d_{rur} [m] is displacement height, and S_{rur,z_m} [m s⁻¹] is wind speed measured at z_m [m]. The surface resistance r_s [s m⁻¹] can be calculated as a function of stomatal resistance r_1 [s m⁻¹] and leaf area index LAI [m² m⁻²]

$$r_s = r_1 / (0.5LAI). \quad (2.9)$$

The ground heat flux drives the conduction equation at the upper-most soil layer via [26]

$$d_{\text{soil}} cv_{\text{soil}} \frac{dT_1}{dt} = C_{\text{soil}}(T_2 - T_1) + G_{\text{rur}}, \quad (2.10)$$

where d_{soil} [m] is the soil layer thickness, cv_{soil} [J m⁻³ K⁻¹] is volumetric heat capacity of soil, T_1 [K] is soil upper layer temperature (the same as soil surface temperature), C_{soil} [W m⁻² K⁻¹] is the soil thermal conductance, and T_2 [K] is soil temperature in the second layer under ground. In the lowest layer (n) of soil the conduction equation is forced by a deep soil temperature T_{deep} [K] as

$$d_{\text{soil}} cv_{\text{soil}} \frac{dT_{n-1}}{dt} = C_{\text{soil}}(T_{\text{deep}} - T_{n-1}). \quad (2.11)$$

2.1.2 Monin-Obukhov Similarity Theory

In the rural model, the Monin-Obukhov Similarity Theory (MOST) is used to solve for the vertical profiles of potential temperature, specific humidity, and friction velocity at 10 m a.g.l. using meteorological measurements near the surface. MOST is usually applied to the atmospheric surface layer over flat and homogeneous lands to describe the vertical profiles of wind speed, potential temperature, and specific humidity as functions of momentum flux, sensible heat flux, and latent heat flux measured near the surface, respectively. Using MOST the gradient of potential temperature is given by

$$\frac{d\bar{\Theta}_{\text{rur}}}{dz} = -\frac{H_{\text{rur}}}{\rho C_p \kappa u_* z} \Phi_H \left(\frac{z}{L_{\text{obk}}} \right), \quad (2.12)$$

where $\bar{\Theta}_{\text{rur}}$ [K] is mean potential temperature in the rural area, H_{rur} [W m^{-2}] is net rural sensible heat flux, ρ [kg m^{-3}] is air density near the rural surface, C_p [$\text{J kg}^{-1} \text{K}^{-1}$] is air specific heat capacity, u_* [m s^{-1}] is friction velocity, and $\kappa = 0.4$ [-] is the von Kármán constant. Φ_H [-] is known as the universal dimensionless temperature gradient. This term is estimated for different thermal stability conditions based on experimental data as [30, 49]

$$\Phi_H \left(\frac{z}{L_{\text{obk}}} \right) = \begin{cases} 1 + 5 \frac{z}{L_{\text{obk}}}, & \frac{z}{L_{\text{obk}}} > 0 (\text{Stable}) \\ 1, & \frac{z}{L_{\text{obk}}} = 0 (\text{Neutral}) \\ \left(1 - \frac{16z}{L_{\text{obk}}}\right)^{-1/2}, & \frac{z}{L_{\text{obk}}} < 0 (\text{Unstable}), \end{cases} \quad (2.13)$$

where z/L_{obk} [-] is dimensionless stability parameter, z [m] is height above ground, and L_{obk} [m] is Obukhov-Length given by

$$L_{\text{obk}} = -\frac{\bar{\Theta}_{\text{rur},2\text{m}} u_*^3}{g \kappa \frac{H_{\text{rur}}}{\rho C_p}}. \quad (2.14)$$

It has been observed that there is a monotonic reduction in friction velocity with increasing stratification [85]. So, friction velocity in Equation 2.12 is estimated from momentum flux generalization [136]

$$\frac{d\bar{S}_{\text{rur}}}{dz} = \frac{u_*}{\kappa z} \Phi_M \left(\frac{z}{L_{\text{obk}}} \right), \quad (2.15)$$

where \bar{S}_{rur} [m s^{-1}] is the mean horizontal wind speed in the rural area and Φ_M [-] is the universal dimensionless wind shear and is estimated for different thermal stability conditions

based on experimental data [30, 49]

$$\Phi_M \left(\frac{z}{L_{\text{obk}}} \right) = \begin{cases} 1 + 5 \frac{z}{L_{\text{obk}}}, & \frac{z}{L_{\text{obk}}} > 0 (\text{Stable}) \\ 1, & \frac{z}{L_{\text{obk}}} = 0 (\text{Neutral}) \\ \left(1 - \frac{16z}{L_{\text{obk}}} \right)^{-1/4}, & \frac{z}{L_{\text{obk}}} < 0 (\text{Unstable}). \end{cases} \quad (2.16)$$

Friction velocity can be determined by integrating Equation 2.15, iteratively, from the elevation of the rural aerodynamic roughness length $z_{0,\text{rur}}$ [m] to $z - d_{\text{rur}}$ [m], where $z = 10$ [m] is the reference height for wind measurement and d_{rur} [m] is the zero displacement height. The aerodynamic roughness length and zero displacement height have been rigorously studied and parameterized in the literature as functions of obstacle height h_{rur} [m] and the type of rural area [75, 165]. VCWG permits this specification, but the approximate values used in this study are $z_{0,\text{rur}} = 0.1h_{\text{rur}}$ and $d_{\text{rur}} = 0.5h_{\text{rur}}$. This method provides a friction velocity that is corrected for thermal stability effects.

The potential temperature profiles are also obtained by integration of Equation 2.12 [161] from rural roughness length for temperature $z_{\bar{\Theta},\text{rur}}$ [m] to $z - d_{\text{rur}}$ [m], where z [m] is the desired elevation above ground (here the top of the domain). A typical value of $z_{\bar{\Theta},\text{rur}} = 0.1z_{0,\text{rur}}$ [m] is often used [25, 63, 84, 129].

Given the similarity of heat and mass transfer (sensible and latent heat fluxes), the same universal dimensionless temperature gradient can be used for the universal dimensionless specific humidity gradient, i.e., $\Phi_Q = \Phi_H$ [-] [213]. So the gradient of the specific humidity can be given by the following expression, employing latent heat of vaporization L [J kg⁻¹], as

$$\frac{d\bar{Q}_{\text{rur}}}{dz} = - \frac{LE_{\text{rur}}}{\rho L \kappa u_* z} \Phi_Q \left(\frac{z}{L_{\text{obk}}} \right), \quad (2.17)$$

which can also be integrated to give the vertical profile of specific humidity. This expression should be integrated from rural roughness length for specific humidity $z_{\bar{Q},\text{rur}}$ [m] to $z - d_{\text{rur}}$ [m], where z [m] is the desired elevation above ground (here the top of the domain). It is often assumed that $z_{\bar{Q},\text{rur}} = z_{\bar{\Theta},\text{rur}}$ [m] [25, 84, 129].

The rural model also outputs a horizontal pressure gradient based on the friction velocity calculation that is later used as a source term for the urban one-dimensional vertical diffusion momentum equation. The pressure gradient is parameterized as $\rho u_*^2 / H_{\text{top}}$ [kg m⁻² s⁻²], where H_{top} [m] is the height of the top of the domain [101, 147], here three times the average building height.

After calculating potential temperature and specific humidity at the top of the domain by the rural model, these values can be applied as fixed-value boundary conditions at the top of the domain in the urban one-dimensional vertical diffusion model in the temperature and specific humidity transport equations.

2.2 Urban Model

2.2.1 Radiation Model

In our notation for the radiation model, indices g (G), v (V), i (I), b (B), t (T), w (W), s (S), r (R) refer to ground, vegetation, impervious, bare, tree, wall, sky, and roof. In VCWG, there are two types of vegetation: ground vegetation cover and trees. Tree vegetation is specified by four parameters: tree height h_t [m], tree crown radius r_t [m], tree distance from canyon walls d_t [m], and Leaf Area Index ($LAI_{\text{tree,can}}$) [$\text{m}^2 \text{m}^{-2}$], which is the vertical integral of the Leaf Area Density (LAD) [$\text{m}^2 \text{m}^{-3}$] profile. In this thesis, LAI_i , where i can be tree (for high vegetation) or veg (for low vegetation), refers to the leaf area index of the individual tree or ground vegetation, and $LAI_{i,\text{can}}$ refers to the leaf area of tree or ground vegetation per total ground area. VCWG considers two trees spaced from the walls of the canyon with distance d_t [m]. Trees cannot be higher than the building height. Both types of vegetation are specified with the same albedo α_v [-] and emissivity ε_v [-]. The VCWG user can change these input parameters for different vegetation structures. The radiation model in VCWG is adapted from the model developed by Ryu et al. (2016) [174] and Meili et al. (2020) [129]. The net all-wave radiation flux is the sum of the net shortwave and longwave radiation fluxes

$$R_n = S^\downarrow - S^\uparrow + L^\downarrow - L^\uparrow, \quad (2.18)$$

where S^\downarrow , S^\uparrow , L^\downarrow , and L^\uparrow [all in W m^{-2}] represent the incoming shortwave, outgoing shortwave, incoming longwave, and outgoing longwave radiation fluxes. The incoming shortwave radiation fluxes (direct and diffuse) and the longwave radiation flux from the sky are forced by the EPW file or ERA5-Land dataset.

2.2.1.1 Shortwave Radiation

The direct and diffuse shortwave radiation fluxes absorbed by each urban element are computed as a function of canyon height, street width, tree shape, and albedo. The urban

geometry creates shading effects by blocking a fraction of the incoming direct solar radiation flux. This flux is further decreased by the sky view factor, which reduces the incoming diffuse solar radiation flux from sky and traps reflected solar rays within the canyon. Two steps are involved to calculate the net shortwave radiation flux: 1a) the direct shortwave radiation flux received by each urban element is calculated as a function of the sun position and shading effects created by buildings and trees; 1b) the diffuse shortwave radiation received by each urban element is computed as a function of the corresponding sky view factor; and 2) infinite radiation reflections within the urban canyon are calculated using view factors and the net shortwave radiation flux for each urban element is then calculated. All urban elements are assumed to be Lambertian with isotropic scattering and reflections.

The absorbed (net) shortwave radiation flux on surface i is given by

$$S_{n,i} = (1 - \alpha_i) \left(S_i^\downarrow \right) = (1 - \alpha_i) \left(S_i^{\downarrow \text{direct}} + S_i^{\downarrow \text{diffuse}} \right), \quad (2.19)$$

where α_i is the albedo of the surface and $S_i^{\downarrow \text{direct}}$ and $S_i^{\downarrow \text{diffuse}}$ [W m^{-2}] are the direct and diffuse incoming shortwave radiation fluxes to surface i . The amount of direct shortwave radiation flux received by each urban surface is calculated considering shade effects according to well-established methodologies for the case with no trees [104, 124, 200] and with trees [174].

There is no obstacle at the roof level which can shade the roof surface. So $S_i^{\downarrow \text{direct}}$ and $S_i^{\downarrow \text{diffuse}}$ in Equation 2.19 are the incoming direct and the incoming diffuse shortwave radiation fluxes from sky. If there are no trees, the shortwave radiation reaches the walls and the ground should account for the shading effect provided by buildings. The shade position on the ground x_{shd} [-] and on the wall y_{shd} [-] can be calculated as follows [129]

$$x_{\text{shd}} = \max[1 - \text{HW}\xi, 0] \quad (2.20)$$

$$y_{\text{shd}} = \max[\text{HW} - 1/\xi, 0], \quad (2.21)$$

where HW [-] is the building height divided by width of the canyon, and ξ represents the solar position with respect to canyon orientation

$$\xi = \tan \theta_z |\sin \theta_a|, \quad (2.22)$$

where θ_z [rad] is solar zenith angle and θ_a [rad] is the difference between solar azimuth angle and canyon orientation. Then, the shadow length on the ground and the wall can

be obtained from $G_{\text{shd,bld}} = 1 - x_{\text{shd}}$ [-] and $W_{\text{shd,bld}} = y_{\text{shd}}/\text{HW}$ [-], respectively. Finally, the direct shortwave radiation flux reaches the sunlit wall $S_{\text{Wsun}}^{\downarrow\text{direct}}$ [W m^{-2}], the shaded wall $S_{\text{Wshd}}^{\downarrow\text{direct}}$ [W m^{-2}] and the ground $S_{\text{G}}^{\downarrow\text{direct}}$ [W m^{-2}] can be computed as follows

$$S_{\text{G}}^{\downarrow\text{direct}} = S^{\downarrow\text{direct}}[1 - G_{\text{shd}}] \quad (2.23)$$

$$S_{\text{Wsun}}^{\downarrow\text{direct}} = S^{\downarrow\text{direct}}\xi[1 - W_{\text{shd}}] \quad (2.24)$$

$$S_{\text{Wshd}}^{\downarrow\text{direct}} = 0. \quad (2.25)$$

Presence of trees increases the fraction of shaded surfaces. Hence, Equations 2.23-2.25 can be modified as

$$S_{\text{G}}^{\downarrow\text{direct}} = S^{\downarrow\text{direct}}[1 - G_{\text{shd,bld}} + \tau G_{\text{shd,tree}}] \quad (2.26)$$

$$S_{\text{Wsun}}^{\downarrow\text{direct}} = S^{\downarrow\text{direct}}\xi[HW - W_{\text{shd,bld}} + \tau W_{\text{shd,tree}}] \quad (2.27)$$

$$S_{\text{Wshd}}^{\downarrow\text{direct}} = 0, \quad (2.28)$$

where $G_{\text{shd,tree}}$ [-] and $W_{\text{shd,tree}}$ [-] are the shadow length on the ground and wall, respectively, due to the presence of trees. The tree canopy transmittance τ can be calculated as a function of LAI_{can} and optical transmittance K_{opt} [-] using $\tau = e^{-K_{\text{opt}}LAI_{\text{can}}}$ [-]. It is assumed that K_{opt} is constant and is equal to 0.5 [129]. The total shadow length due to the presence of trees can be calculated as a function of tree height and the location of shadow on the ground and walls over the course of a day [174].

The direct shortwave radiation flux reaches the urban trees and is determined as

$$S_{\text{T}}^{\downarrow\text{direct}} = (1 - \tau)(S_{\text{T1}}^{\downarrow\text{direct}} + S_{\text{T2}}^{\downarrow\text{direct}})/2, \quad (2.29)$$

where $S_{\text{T1}}^{\downarrow\text{direct}}$ [W m^{-2}] and $S_{\text{T2}}^{\downarrow\text{direct}}$ [W m^{-2}] are the direct shortwave radiation fluxes received

by two trees in the canyon and can be calculated using the following equations

$$S_{T1}^{\downarrow \text{direct}} = \begin{cases} 0 & \xi \geq \tan \theta_1 \\ S^{\downarrow \text{direct}} [r_t \sqrt{1 + \xi^2} + (1 - d_t) - (HW - H_t W) \xi] / (2\pi r_t) & \tan \theta_2 \leq \xi < \tan \theta_1 \\ S^{\downarrow \text{direct}} [2r_t \sqrt{1 + \xi^2}] / (2\pi r_t) & \xi < \tan \theta_2 \end{cases} \quad (2.30)$$

$$S_{T2}^{\downarrow \text{direct}} = \begin{cases} 0 & \xi \geq \tan \theta_3 \\ S^{\downarrow \text{direct}} [r_t \sqrt{1 + \xi^2} + d_t - (HW - H_t W) \xi] / (2\pi r_t) & \tan \theta_4 \leq \xi < \tan \theta_3 \\ S^{\downarrow \text{direct}} [2r_t \sqrt{1 + \xi^2}] / (2\pi r_t) & \xi < \tan \theta_4 \end{cases} \quad (2.31)$$

where $H_t W$ [-] is normalized height of tree, and θ_1 to θ_4 are angles that represent interaction between tree and radiation beams (see Figure 2.3) [174].

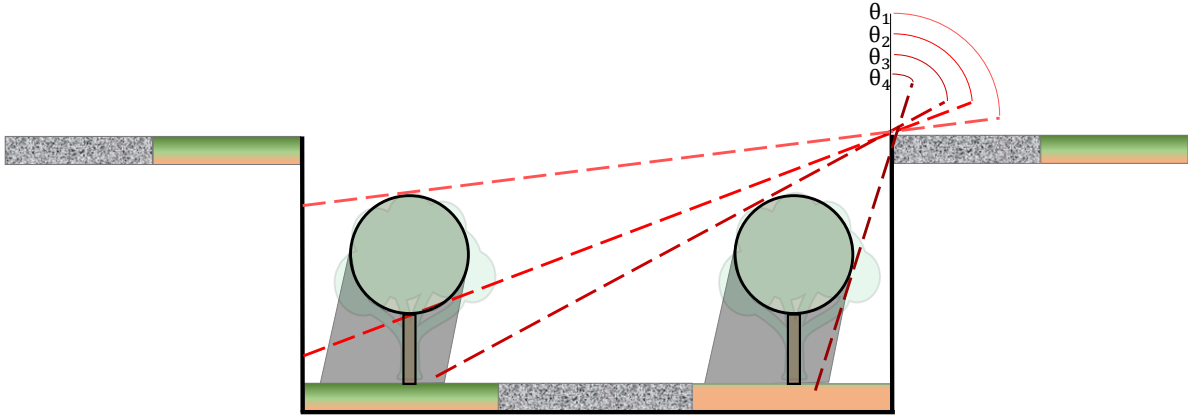


Figure 2.3: Illustration of interaction between solar radiation beam, the urban surface, and the shadow provided by trees. θ_1 to θ_4 are the reference angles.

Sky view factors are used to determine the amount of diffuse shortwave radiation flux that reaches a surface from the sky. Infinite reflections of diffuse shortwave radiation flux are calculated within the urban canyon using view factors for each pair of urban surfaces [202, 203]

$$S_i^{\downarrow \text{diffuse}} = S^{\downarrow \text{diffuse}} V F_{s,i}, \quad (2.32)$$

where $V F_i$ is the view factor between the surface i and the sky. For the case of no trees,

analytical view factors are calculated using standard equations [108, 124, 173, 204], while for trees the method developed by Ryu et al. (2016) [174] is used. No obstructions are considered for roofs, i.e. trees cannot be taller than buildings. View factors meet a set of three requirements: 1) the self view factor of a flat surface is zero, 2) energy at the surface is conserved, and 3) view factors are reciprocal. The view factors for the case with trees are calculated using the Monte Carlo ray tracing algorithm [60, 203]. This algorithm performs a probabilistic sampling of all rays emitted by an urban element. The relative frequency of rays emitted by one element that hit another element is an estimation of the view factor between the two elements. On each element, a large number of randomly distributed emitting points are considered. These view factors are also corrected for the three requirements mentioned above.

In the radiation model, the total shortwave radiation absorbed by the surfaces account for infinite shortwave reflections within the canyon [76, 203]. Applying this method leads to a system of equations that can output outgoing shortwave radiation S_i^\uparrow from the urban surfaces for the case with no trees

$$\left\{ \begin{array}{l}
C_{GV}\alpha_{GV}(S_G^{\downarrow\text{direct}} + VF_{S,G}S^{\downarrow\text{diffuse}}) = S_{GV}^\uparrow - S_{W\text{sun}}^\uparrow C_{GV}\alpha_{GV}VF_{G,W} - S_{W\text{shd}}^\uparrow C_{GV}\alpha_{GV}VF_{G,W} \\
C_{GB}\alpha_{GB}(S_G^{\downarrow\text{direct}} + VF_{S,G}S^{\downarrow\text{diffuse}}) = S_{GB}^\uparrow - S_{W\text{sun}}^\uparrow C_{GB}\alpha_{GB}VF_{G,W} - S_{W\text{shd}}^\uparrow C_{GB}\alpha_{GB}VF_{G,W} \\
C_{GI}\alpha_{GI}(S_G^{\downarrow\text{direct}} + VF_{S,G}S^{\downarrow\text{diffuse}}) = S_{GI}^\uparrow - S_{W\text{sun}}^\uparrow C_{GI}\alpha_{GI}VF_{G,W} - S_{W\text{shd}}^\uparrow C_{GI}\alpha_{GI}VF_{G,W} \\
\alpha_W(S_{W\text{sun}}^{\downarrow\text{direct}} + VF_{W,S}S^{\downarrow\text{diffuse}}) = -S_{GV}^\uparrow C_{GV}f_{GV}\alpha_WVF_{W,G} - S_{GV}^\uparrow C_{GV}f_{GV}\alpha_WVF_{W,G} - \\
\quad S_{GI}^\uparrow C_{GI}f_{GI}\alpha_WVF_{W,G} + S_{W\text{sun}}^\uparrow - S_{W\text{shd}}^\uparrow \alpha_WVF_{W,W} \\
\alpha_W(VF_{W,S}S^{\downarrow\text{diffuse}}) = -S_{GV}^\uparrow C_{GV}f_{GV}\alpha_WVF_{W,G} - S_{GB}^\uparrow C_{GB}f_{GB}\alpha_WVF_{W,G} - \\
\quad S_{GI}^\uparrow C_{GI}f_{GI}\alpha_WVF_{W,G} - S_{W\text{sun}}^\uparrow \alpha_WVF_{W,W} + S_{W\text{shd}}^\uparrow
\end{array} \right. , \tag{2.33}$$

and if trees are considered, the equations are modified as follows

$$\left\{ \begin{array}{l}
C_{GV}\alpha_{GV}(S_G^{\downarrow\text{direct}} + VF_{S,G}^T S^{\downarrow\text{diffuse}}) = S_{GV}^{\uparrow} - S_{W\text{sun}}^{\uparrow} C_{GV}\alpha_{GV}VF_{G,W}^T - S_{W\text{shd}}^{\uparrow} C_{GV}\alpha_{GV}VF_{G,W}^T - \\
\quad S_T^{\uparrow} C_{GV}\alpha_{GV}VF_{G,T}^T \\
C_{GB}\alpha_{GB}(S_G^{\downarrow\text{direct}} + VF_{S,G}^T S^{\downarrow\text{diffuse}}) = S_{GB}^{\uparrow} - S_{W\text{sun}}^{\uparrow} C_{GB}\alpha_{GB}VF_{G,W}^T - S_{W\text{shd}}^{\uparrow} C_{GB}\alpha_{GB}VF_{G,W}^T - \\
\quad S_T^{\uparrow} C_{GV}\alpha_{GV}VF_{G,T}^T \\
C_{GI}\alpha_{GI}(S_G^{\downarrow\text{direct}} + VF_{S,G}^T S^{\downarrow\text{diffuse}}) = S_{GI}^{\uparrow} - S_{W\text{sun}}^{\uparrow} C_{GI}\alpha_{GI}VF_{G,W}^T - S_{W\text{shd}}^{\uparrow} C_{GI}\alpha_{GI}VF_{G,W}^T - \\
\quad S_T^{\uparrow} C_{GV}\alpha_{GV}VF_{G,T}^T \\
\alpha_W(S_{W\text{sun}}^{\downarrow\text{direct}} + VF_{W,S}^T S^{\downarrow\text{diffuse}}) = -S_{GV}^{\uparrow} C_{GV}f_{GV}\alpha_W VF_{W,G}^T - S_{GB}^{\uparrow} C_{GB}f_{GB}\alpha_W VF_{W,G}^T - \\
\quad S_{GI}^{\uparrow} C_{GI}f_{GI}\alpha_W VF_{W,G}^T + S_{W\text{sun}}^{\uparrow} - S_{W\text{shd}}^{\uparrow} \alpha_W VF_{W,W}^T - \\
\quad S_T^{\uparrow} \alpha_W VF_{W,T}^T \\
\alpha_W(VF_{W,S}^T S^{\downarrow\text{diffuse}}) = -S_{GV}^{\uparrow} C_{GV}f_{GV}\alpha_W VF_{W,G}^T - S_{GB}^{\uparrow} C_{GB}f_{GB}\alpha_W VF_{W,G}^T - \\
\quad S_{GI}^{\uparrow} C_{GI}f_{GI}\alpha_W VF_{W,G}^T - S_{W\text{sun}}^{\uparrow} \alpha_W VF_{W,W}^T + S_{W\text{shd}}^{\uparrow} - \\
\quad S_T^{\uparrow} \alpha_W VF_{W,T}^T \\
\alpha_T(S_T^{\downarrow\text{direct}} + VF_{S,T}^T S^{\downarrow\text{diffuse}}) = -S_{GV}^{\uparrow} C_{GV}f_{GV}\alpha_T VF_{T,G}^T - S_{GB}^{\uparrow} C_{GB}f_{GB}\alpha_T VF_{T,G}^T - \\
\quad S_{GI}^{\uparrow} C_{GI}f_{GI}\alpha_T VF_{T,G}^T - S_{W\text{sun}}^{\uparrow} \alpha_T VF_{T,W}^T - \\
\quad S_{W\text{shd}}^{\uparrow} \alpha_T VF_{T,W}^T + S_T^{\uparrow} (1 - \alpha_T VF_{T,T}^T)
\end{array} \right. , \quad (2.34)$$

where VF^T are view factors in the presence of trees, C_{GV} , C_{GB} , and C_{GI} are boolean operators to consider presence or absence of vegetated, bare, and impervious ground respectively, α_i is albedo of the surface i , f_{GV} , f_{GB} , and f_{GI} are the fractions of ground covered by vegetation, bare soil, and impervious surface, respectively.

The radiation model also checks that the reciprocity criterion is met. The conservation of radiation energy at the surfaces can be determined as

$$EB_{\text{swr}} = \sum_i \frac{f_i A_i}{A_G} S_i^{\downarrow} - \sum_i \frac{f_i A_i}{A_G} S_{n,i} - \sum_i \frac{f_i A_i}{A_G} S_i^{\uparrow}, \quad (2.35)$$

where A_i is the surface area and A_G is the road area which is equal to the width of canyon for a 2D case.

2.2.1.2 Longwave Radiation

The net longwave radiation flux on the urban surfaces can be calculated as the difference between the incoming L_i^\downarrow [W m^{-2}] and outgoing longwave radiation L_i^\uparrow [W m^{-2}] fluxes. The emitted radiation fluxes depend on surface temperatures T_i . Infinite reflections of longwave radiation within the urban canyon are considered. Again, no obstructions are considered for roofs, i.e. trees cannot be taller than buildings. These fluxes can be calculated as

$$L_i^\downarrow = \sum_j V F_{i,j} L_j^\uparrow, \quad (2.36)$$

where outgoing longwave radiation can be obtained from

$$L_i^\uparrow = L_i^{\text{emit}} + (1 - \varepsilon_i) L_i^\downarrow, \quad (2.37)$$

where ε_i [-] is the emissivity of the surface, $(1 - \varepsilon_i)$ [-] is the reflectivity of the surface, and the emitted longwave radiation is $L_i^{\text{emit}} = \varepsilon_i \sigma T_i^4$ for the urban surfaces. Hence, the net longwave radiation at surface i can be calculated as

$$L_{n,i} = L_i^\downarrow - L_i^\uparrow. \quad (2.38)$$

Following the method proposed by Harman (2004) [76] and Wang (2014) [203], the outgoing longwave radiation flux from surfaces can be determined by solving the following system

of equations for the case with no trees

$$\left\{ \begin{array}{l}
C_{GV}(\varepsilon_{GV}\sigma T_{GV}^4 + (1 - \varepsilon_{GV})VF_{S,G}L^\downarrow) = L_{GV}^\uparrow - L_{Wsun}^\uparrow C_{GV}(1 - \varepsilon_{GV})VF_{G,W} - \\
\quad L_{Wshd}^\uparrow C_{GV}(1 - \varepsilon_{GV})VF_{G,W} \\
C_{GB}(\varepsilon_{GB}\sigma T_{GB}^4 + (1 - \varepsilon_{GB})VF_{S,G}L^\downarrow) = L_{GB}^\uparrow - L_{Wsun}^\uparrow C_{GB}(1 - \varepsilon_{GB})VF_{G,W} - \\
\quad L_{Wshd}^\uparrow C_{GB}(1 - \varepsilon_{GB})VF_{G,W} \\
C_{GI}(\varepsilon_{GI}\sigma T_{GI}^4 + (1 - \varepsilon_{GI})VF_{S,G}L^\downarrow) = L_{GI}^\uparrow - L_{Wsun}^\uparrow C_{GI}(1 - \varepsilon_{GI})VF_{G,W} - \\
\quad L_{Wshd}^\uparrow C_{GI}(1 - \varepsilon_{GI})VF_{G,W} \\
\varepsilon_W\sigma T_{Wsun}^4 + (1 - \varepsilon_W)VF_{S,W}L^\downarrow = -L_{GV}^\uparrow C_{GV}f_{GV}(1 - \varepsilon_W)VF_{W,G} - \\
\quad L_{GB}^\uparrow C_{GB}f_{GB}(1 - \varepsilon_W)VF_{W,G} - \\
\quad L_{GI}^\uparrow C_{GI}f_{GI}(1 - \varepsilon_W)VF_{W,G} + \\
\quad L_{Wsun}^\uparrow - L_{Wshd}^\uparrow(1 - \varepsilon_W)VF_{WW} \\
\varepsilon_W\sigma T_{Wshd}^4 + (1 - \varepsilon_W)VF_{S,W}L^\downarrow = -L_{GV}^\uparrow C_{GV}f_{GV}(1 - \varepsilon_W)VF_{W,G} - \\
\quad L_{GB}^\uparrow C_{GB}f_{GB}(1 - \varepsilon_W)VF_{W,G} - \\
\quad L_{GI}^\uparrow C_{GI}f_{GI}(1 - \varepsilon_W)VF_{W,G} - \\
\quad L_{Wsun}^\uparrow(1 - \varepsilon_W)VF_{WW} + L_{Wshd}^\uparrow.
\end{array} \right. \quad (2.39)$$

If trees are present, the view factors are calculated with a simplified two-dimensional

Monte Carlo ray-tracing algorithm [60, 203] and the equations are modified as follows

$$\left\{ \begin{array}{l}
C_{GV}(\varepsilon_{GV}\sigma T_{GV}^4 + (1 - \varepsilon_{GV})VF_{S,G}^T L^\downarrow) = L_{GV}^\uparrow - L_{Wsun}^\uparrow C_{GV}(1 - \varepsilon_{GV})VF_{G,W}^T - \\
\quad L_{Wshd}^\uparrow C_{GV}(1 - \varepsilon_{GV})VF_{G,W}^T - \\
\quad L_T^\uparrow C_{GV}(1 - \varepsilon_{GV})VF_{G,T}^T \\
C_{GB}(\varepsilon_{GB}\sigma T_{GB}^4 + (1 - \varepsilon_{GB})VF_{S,G}^T L^\downarrow) = L_{GB}^\uparrow - L_{Wsun}^\uparrow C_{GB}(1 - \varepsilon_{GB})VF_{G,W}^T - \\
\quad L_{Wshd}^\uparrow C_{GB}(1 - \varepsilon_{GB})VF_{G,W}^T - \\
\quad L_T^\uparrow C_{GV}(1 - \varepsilon_{GV})VF_{G,T}^T \\
C_{GI}(\varepsilon_{GI}\sigma T_{GI}^4 + (1 - \varepsilon_{GI})VF_{S,G}^T L^\downarrow) = L_{GI}^\uparrow - L_{Wsun}^\uparrow C_{GI}(1 - \varepsilon_{GI})VF_{G,W}^T - \\
\quad L_{Wshd}^\uparrow C_{GI}(1 - \varepsilon_{GI})VF_{G,W}^T - \\
\quad L_T^\uparrow C_{GV}(1 - \varepsilon_{GV})VF_{G,T}^T \\
\varepsilon_W\sigma T_{Wsun}^4 + (1 - \varepsilon_W)VF_{S,W}^T L^\downarrow = -L_{GV}^\uparrow C_{GV}f_{GV}(1 - \varepsilon_W)VF_{W,G}^T - \\
\quad L_{GB}^\uparrow C_{GB}f_{GB}(1 - \varepsilon_W)VF_{W,G}^T - \\
\quad L_{GI}^\uparrow C_{GI}f_{GI}(1 - \varepsilon_W)VF_{W,G}^T + L_{Wsun}^\uparrow - \\
\quad L_{Wshd}^\uparrow(1 - \varepsilon_W)VF_{WW}^T - \\
\quad L_T^\uparrow(1 - \varepsilon_W)VF_{W,T}^T \\
\varepsilon_W\sigma T_{Wshd}^4 + (1 - \varepsilon_W)VF_{S,W}^T L^\downarrow = -L_{GV}^\uparrow C_{GV}f_{GV}(1 - \varepsilon_W)VF_{W,G}^T - \\
\quad L_{GB}^\uparrow C_{GB}f_{GB}(1 - \varepsilon_W)VF_{W,G}^T - \\
\quad L_{GI}^\uparrow C_{GI}f_{GI}(1 - \varepsilon_W)VF_{W,G}^T - \\
\quad L_{Wsun}^\uparrow(1 - \varepsilon_W)VF_{WW}^T + L_{Wshd}^\uparrow - \\
\quad L_T^\uparrow(1 - \varepsilon_W)VF_{W,T}^T \\
\varepsilon_T\sigma T_T^4 + (1 - \varepsilon_T)VF_{S,T} L^\downarrow = -L_{GV}^\uparrow C_{GV}f_{GV}(1 - \varepsilon_T)VF_{T,G}^T - \\
\quad L_{GB}^\uparrow C_{GB}f_{GB}(1 - \varepsilon_T)VF_{T,G}^T - \\
\quad L_{GI}^\uparrow C_{GI}f_{GI}(1 - \varepsilon_T)VF_{T,G}^T - \\
\quad L_{Wsun}^\uparrow(1 - \varepsilon_T)VF_{TW}^t - \\
\quad L_{Wshd}^\uparrow(1 - \varepsilon_T)VF_{TW}^T + \\
\quad L_T^\uparrow(1 - (1 - \varepsilon_T)VF_{T,T}^T)
\end{array} \right. \quad (2.40)$$

The energy associated with the longwave radiation exchanges on the urban surfaces is

conserved and can be calculated as

$$EB_{\text{lwr}} = \sum_i \frac{f_i A_i}{A_G} L_i^\downarrow - \sum_i \frac{f_i A_i}{A_G} L_{n,i} - \sum_i \frac{f_i A_i}{A_G} L_i^\uparrow. \quad (2.41)$$

2.2.2 Surface Energy Balance Model

The surface energy balance is the key to understand and model the microclimate at the surface and exchange processes in the atmospheric boundary layer. When the buoyant forcing, which arises from the sensible heat fluxes of urban facades, is coupled with the synoptic wind, it provides the required energy for vertical heat, mass, and momentum fluxes [154, 157]. Due to the diversity of shape, size, and composition of urban elements, the surface energy balances in the urban areas are more difficult to model. Figure 2.4 shows the energy fluxes from urban elements.

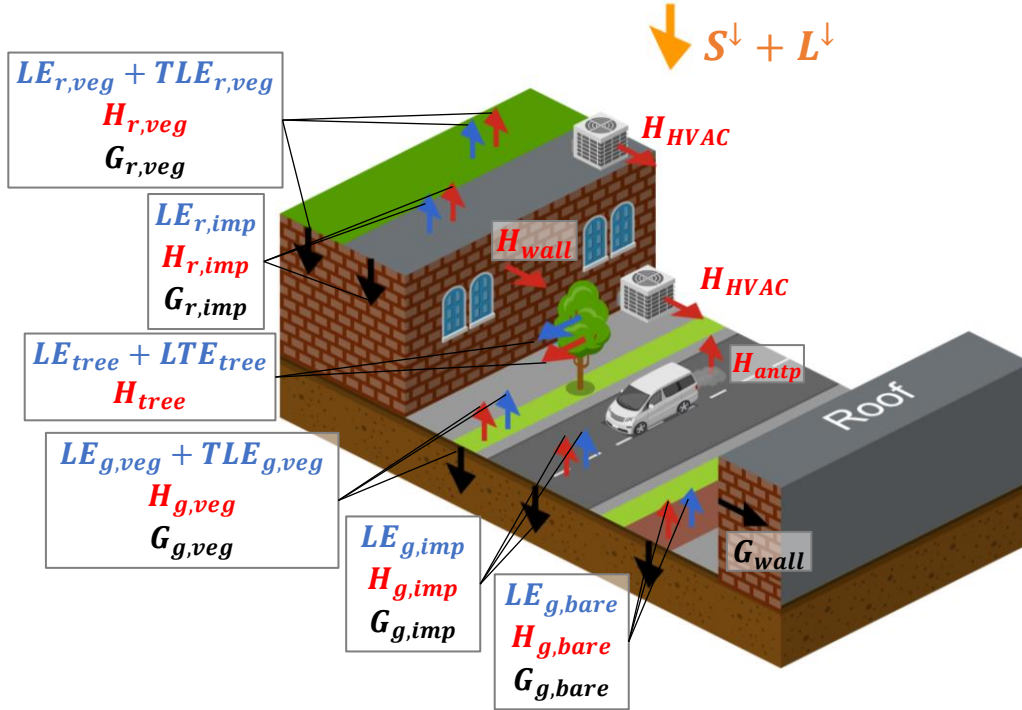


Figure 2.4: Illustration of surface energy balance in an urban area.

In VCWG, one can express the energy balance equation for the individual urban surface i as follows

$$L_{n,i} + S_{n,i} = H_i + LE_i + G_i, \quad (2.42)$$

where the left hand side of the equation represents net allwave radiation fluxes at the surface i (vegetated roof: (r,veg), impervious roof: (r,imp), vegetated ground: (g,veg), bare ground: (g,bare), impervious ground: (g,imp), wall, and tree), H_i [W m^{-2}] is sensible heat flux, LE_i [W m^{-2}] is latent heat flux, and G_i [W m^{-2}] is conductive heat flux. The latent heat flux at the walls are assumed to be zero. In the subsequent sections, detailed calculation of heat fluxes are provided.

2.2.2.1 Sensible Heat Flux

The sensible heat flux from ground, roof, and sunlit and shaded walls H_i [W m^{-2}] can be calculated as [129]

$$H_i = -\rho C_p \frac{\bar{\Theta}_{\text{atm}} - \bar{\Theta}_i}{\sum_j r_{i,j}}, \quad (2.43)$$

where i represent the urban surfaces ($i=(g,imp)$ is impervious ground, $i=(g,veg)$ is vegetated ground, $i=(g,bare)$ is bare ground, $i=(r,imp)$ is impervious roof, $i=(r,veg)$ is vegetated roof, $i=(sun,wall)$ is sunlit wall, $i=(shd,wall)$ is shaded wall), ρ [kg m^{-3}] is density of air at the air temperature of $\bar{\Theta}_{\text{atm}}$ [K] adjacent to the surface, and $\sum_j r_{i,j}$ [s m^{-1}] is the sum of thermal resistances between the surface and the atmosphere. Detail description of the sensible heat fluxes from surfaces are shown in Figure 2.5 and discussed in the subsequent sections.

Horizontal Surfaces

The resistances for the horizontal surfaces covered by vegetation r_{veg} , bare soil r_{bare} , and vegetation r_{imp} can be formulated as [56, 129]

$$r_{\text{imp}} = r_{\text{aero}} \quad (2.44)$$

$$r_{\text{bare}} = r_{\text{aero}} \quad (2.45)$$

$$r_{\text{veg}} = r_{\text{aero}} + \hat{r}_{\text{lb,veg}}, \quad (2.46)$$

where r_{aero} [s m^{-1}] is aerodynamic resistance and $\hat{r}_{\text{lb,veg}}$ [s m^{-1}] is the re-scaled leaf boundary resistance. The aerodynamic resistance is based on study by Louis (1979) [113] and can be calculated as [113]

$$r_{\text{aero}} = R_{\text{drag}} \frac{\left(\ln \frac{z}{z_0}\right)^2}{\bar{S}_z \kappa^2} \frac{1}{F_h \left(\frac{z}{z_0}, Ri_B\right)}, \quad (2.47)$$

where $R_{\text{drag}} = 0.74$ [-] is ratio of the drag coefficients for momentum to heat [30], Ri_B [-] is the bulk Richardson number, $\kappa = 0.4$ is von Kármán constant, z_0 [m] is aerodynamic

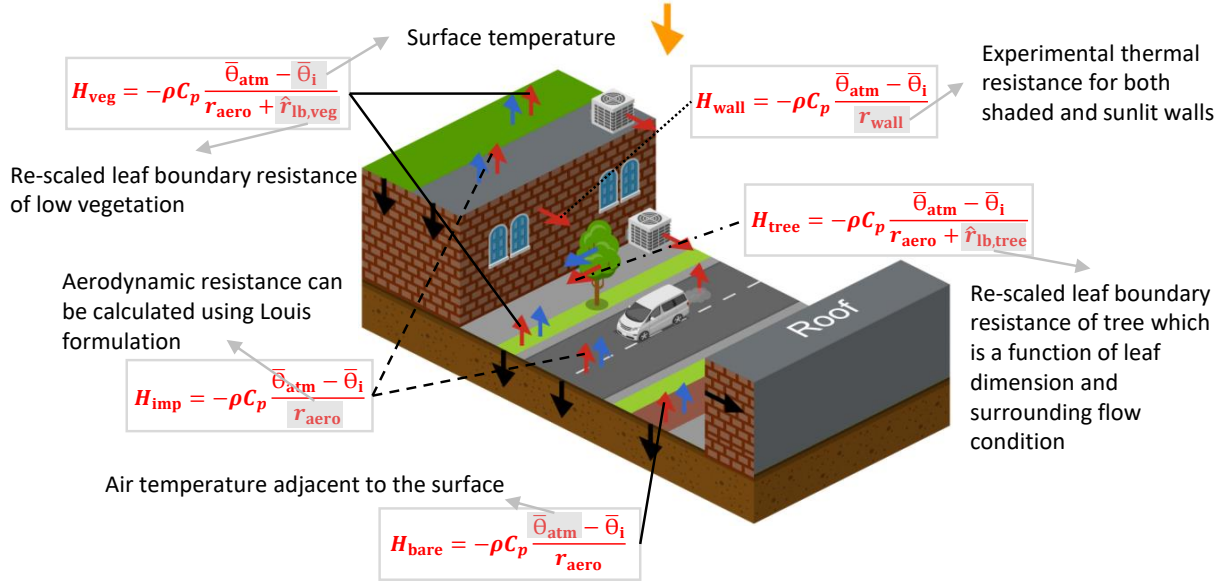


Figure 2.5: Detailed description of sensible heat flux from urban surfaces.

roughness length of the surface, and \bar{S}_z [m s^{-1}] is wind speed near the surface, and F_h [-] is the stability function for sensible heat flux and can be calculated using Equation 2.5.

The leaf boundary layer is a thin laminar layer of air surrounding leaf. Due to the high gradient of temperature, wind speed, and moisture within this layer, it controls the exchange of mass and energy between the plant and the surrounding environment. The leaf boundary resistance $r_{\text{lb,veg}}$ [s m^{-1}] can be calculated as a function of leaf morphology and wind speed. Re-scaling $r_{\text{lb,veg}}$ by a factor of 2, leaf area index LAI_{veg} , and stem area index SAI_{veg} accounts for two-sided resistance of the leaf and the whole vegetation canopy [56, 129]

$$\hat{r}_{\text{lb,veg}} = \frac{r_{\text{lb,veg}}}{2(LAI_{\text{veg}} + SAI_{\text{veg}})}. \quad (2.48)$$

Detailed calculation of leaf boundary resistance is provided in Section 2.2.2.4.

Vertical Surfaces

In VCWG, it is assumed that the sunlit and shaded walls are impervious and the thermal resistance between the surface and adjacent atmosphere (r_{wall}) can be formulated as [98]

$$r_{\text{wall}} = \frac{1}{h_c}, \quad (2.49)$$

where $h_c = 5.678(1.09 + 0.23(\overline{S}_z/0.3048))$ [m s^{-1}] is an empirical convective heat transfer coefficient calculated as a function of vertical profile of wind speed in the canyon. Note that the surface temperature in Equation 2.43 for sunlit and shaded walls is different and can be obtained from the surface energy balance equation.

Trees

The thermal resistance for tree r_{tree} [s m^{-1}] can be calculated using Equation 2.46. The leaf boundary resistance of trees ($r_{\text{lb,tree}}$) can be calculated using the formulation provided in Section 2.2.2.4, with adopted parameters for tree

$$H_{\text{tree}} = -\rho C_p \frac{\overline{\Theta}_{\text{atm}} - \Theta_{\text{tree}}}{r_{\text{tree}} + \frac{r_{\text{lb,tree}}}{2(LAI_{\text{tree}} + SAI_{\text{tree}})}}. \quad (2.50)$$

The undercanopy resistance approach is used to calculate aerodynamic resistance (r_{aero}) from the tree to the canyon [116]. In this approach, the difference between aerodynamic resistance below and above the sink of momentum in the vegetation is computed as aerodynamic resistance. The original formulation of the under canopy resistance is based on exponential and logarithmic wind speed profile within a canyon. In order to be consistent with the other physical process in VCWG, the vertical wind speed profile calculated in the column model is used, which provides more realistic representation of momentum exchange in the urban canyon.

In VCWG, an alternative formulation for sensible heat flux from trees is provided as [32, 98].

$$H_{\text{tree}} = -2c_{\text{PM}}g_{\text{Ha}}(T_a - T_t), \quad (2.51)$$

where c_{PM} is the molar heat capacity for air [J mol K^{-1}], g_{Ha} is the conductance for heat [$\text{mol m}^{-2} \text{s}^{-1}$], T_t [K] is tree temperature, T_a [K] is air temperature.

2.2.2.2 Latent Heat and Evaporative Fluxes

The latent heat flux from ground, roof, and trees LE_i [W m^{-2}] can be calculated by multiplying latent heat of vaporization by evaporative flux

$$LE_i = L \times E_i = \rho L \frac{\overline{Q}_{\text{sat}}(T_i) - \overline{Q}}{\sum_j r_{i,j}}, \quad (2.52)$$

where L [J kg^{-1}] is the latent heat of vaporization, $E_i = LE_i/L$ [$\text{kg m}^{-2} \text{s}^{-1}$] is evaporative flux from surface i , $\overline{Q}_{\text{sat}}$ [kg kg^{-1}] is saturated specific humidity at the temperature of surface

T_i , \bar{Q} [kg kg^{-1}] is specific humidity of the adjacent air, and $\sum_j r_{i,j}$ [s m^{-1}] is the sum of thermal resistances between the surface and the atmosphere. The air density profile ρ in the urban domain can be obtained from the column model. The latent heat of vaporization is a function of air temperature $L = 1000(2501 - 2.351T_a)$ [J kg^{-1}], where T_a [$^{\circ}\text{C}$] is air temperature. The saturated specific humidity can be computed as a function of saturation vapor pressure e_{sat} [Pa] at T_i [$^{\circ}\text{C}$]

$$\bar{Q}_{\text{sat}}(T_i) = \frac{0.622e_{\text{sat}}(T_i)}{P_a - 0.378e_{\text{sat}}(T_i)} \quad (2.53)$$

$$e_{\text{sat}}(T_i) = 611e^{(17.27T_i)/(237.3+T_i)}. \quad (2.54)$$

Detail description of the latent heat fluxes from surfaces are shown in Figure 2.6 and discussed in the subsequent sections.

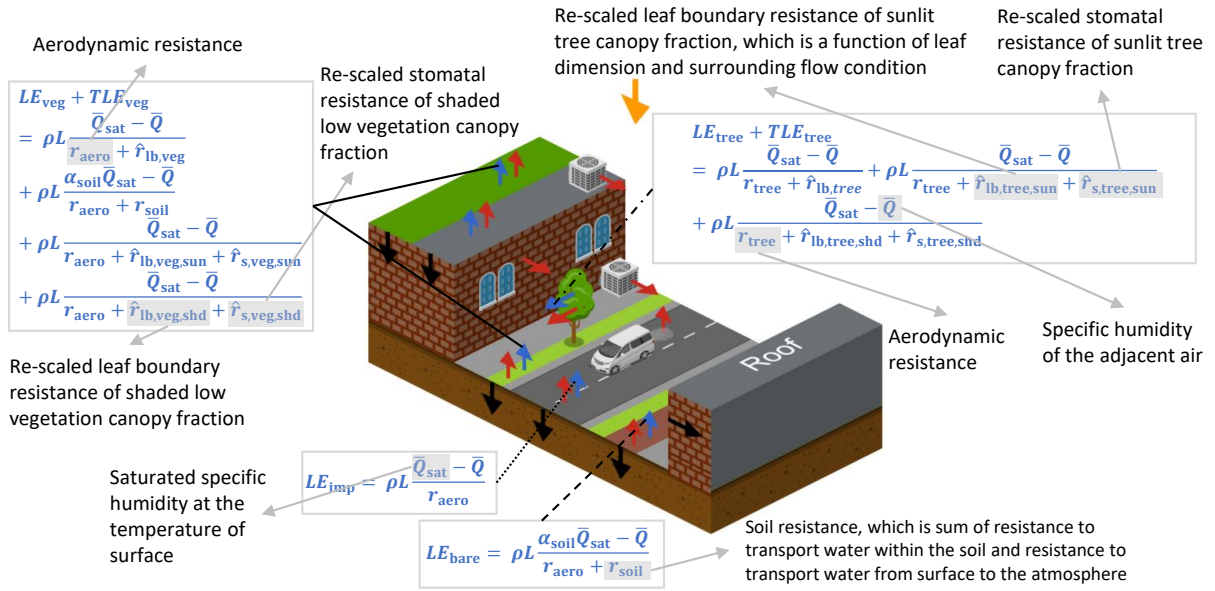


Figure 2.6: Detailed description of latent heat flux from urban surfaces.

Horizontal surfaces

The evaporative fluxes at the ground and roof levels are caused by evaporation from runoff at the impervious ground E_{imp} , evaporation from runoff at the bare ground E_{bare} , evaporation from runoff at the soil surface underneath the low vegetation E_{veg} , and evaporation from intercepted water on low vegetation $E_{\text{veg,int}}$, transpiration from sunlit low vegetation

$TE_{\text{veg,sun}}$, and transpiration from shaded low vegetation $TE_{\text{veg,shd}}$ and are all in $[\text{kg m}^{-2} \text{s}^{-1}]$. The resistance for the horizontal surfaces used in the calculation of latent heat fluxes are [129]

$$r_{\text{imp}} = r_{\text{aero}} \quad (2.55)$$

$$r_{\text{bare}} = r_{\text{aero}} + r_{\text{soil}} \quad (2.56)$$

$$r_{\text{veg}} = r_{\text{aero}} + r_{\text{soil}} \quad (2.57)$$

$$r_{\text{veg,int}} = r_{\text{aero}} + \hat{r}_{\text{lb,veg}} \quad (2.58)$$

$$r_{\text{veg,sun}} = r_{\text{aero}} + \hat{r}_{\text{lb,veg,sun}} + \hat{r}_{\text{s,veg,sun}} \quad (2.59)$$

$$r_{\text{veg,shd}} = r_{\text{aero}} + \hat{r}_{\text{lb,veg,shd}} + \hat{r}_{\text{s,veg,shd}} \quad (2.60)$$

where r_{aero} $[\text{s m}^{-1}]$ is aerodynamic resistance which can be calculated from Equation 2.47, r_{soil} is the soil resistance (see Section 2.2.2.4), $\hat{r}_{\text{lb,veg}}$ is the re-scaled leaf boundary resistance of low vegetation respectively, and $\hat{r}_{\text{s,veg}}$ is the re-scaled stomatal resistance. The subscript sun and shd denote the sunlit and shaded part of the vegetation, respectively. The re-scaled stomatal resistance can be calculated as [56, 129]

$$\hat{r}_{\text{lb,veg}} = \frac{r_{\text{lb,veg}}}{(LAI_{\text{veg}} + SAI_{\text{veg}})d_{\text{w,veg}}} \quad (2.61)$$

$$\hat{r}_{\text{lb,veg,sun}} = \frac{r_{\text{lb,veg}}}{LAI_{\text{veg}}F_{\text{sun,veg}}(1 - d_{\text{w,veg}})} \quad (2.62)$$

$$\hat{r}_{\text{lb,veg,shd}} = \frac{r_{\text{lb,veg}}}{LAI_{\text{veg}}F_{\text{shd,veg}}(1 - d_{\text{w,veg}})} \quad (2.63)$$

$$\hat{r}_{\text{s,veg,sun}} = \frac{r_{\text{s,veg,sun}}}{LAI_{\text{veg}}F_{\text{sun,veg}}(1 - d_{\text{w,veg}})} \quad (2.64)$$

$$\hat{r}_{\text{s,veg,shd}} = \frac{r_{\text{s,veg,shd}}}{LAI_{\text{veg}}F_{\text{shd,veg}}(1 - d_{\text{w,veg}})}, \quad (2.65)$$

where $r_{\text{lb,veg}}$ $[\text{s m}^{-1}]$ is leaf boundary resistance, $r_{\text{s,veg,sun}}$ and $r_{\text{s,veg,shd}}$ are stomatal resistance of the sunlit and shaded part of the vegetation all in $[\text{s m}^{-1}]$, $d_{\text{w,veg}}$ [-] is the fraction of vegetation covered by intercepted water, and $F_{\text{sun,veg}}$ and $F_{\text{shd,veg}}$ are fraction of sunlit and shaded vegetation, respectively. The detailed calculation of soil, leaf boundary, and stomatal resistances are provided in Section 2.2.2.4. The shaded and sunlit fractions of low vegetation are calculated based on the assumption of exponential decay of direct radiation within the

vegetation canopy as [129]

$$F_{\text{sun,veg}} = \frac{1}{LAI_{\text{veg}}} \frac{1 - e^{(-K_{\text{opt}} LAI_{\text{veg}})}}{K_{\text{opt}}} \quad (2.66)$$

$$F_{\text{shd,veg}} = 1 - F_{\text{sun,veg}}, \quad (2.67)$$

where $K_{\text{opt}} = 0.5$ [-] is light transmission coefficient. Equations 2.55-2.57 are the resistances used to calculate evaporation from surfaces and Equations 2.59 and 2.60 are the resistances used to calculate transpiration from vegetation. As detailed in Equations 2.61-2.65, the fraction of canopy covered by intercepted water $d_{\text{w,veg}}$ contributes to evaporation from intercepted water, while the rest of it contributes to transpiration $(1 - d_{\text{w,veg}})$, and $d_{\text{w,veg}}$ can be calculated as [129]

$$d_{\text{w,veg}} = \min [1, (Int/Int_{\text{max}})^{2/3}], \quad (2.68)$$

where Int [mm] is the intercepted water and Int_{max} [mm] is maximum interception capacity of the surface, which are discussed in Section 2.2.5.

Trees

The latent heat flux from tree accounts for evaporation from intercepted water and transpiration from sunlit and shaded fractions of the tree. The thermal resistances can be formulated as follows [129]

$$r_{\text{tree,int}} = r_{\text{tree}} + \hat{r}_{\text{lb,tree}} \quad (2.69)$$

$$r_{\text{tree,sun}} = r_{\text{tree}} + \hat{r}_{\text{lb,tree,sun}} + r_{\text{s,tree,sun}} \quad (2.70)$$

$$r_{\text{tree,shd}} = r_{\text{tree}} + \hat{r}_{\text{lb,tree,shd}} + r_{\text{s,tree,shd}}, \quad (2.71)$$

where $r_{\text{tree,int}}$, $r_{\text{tree,sun}}$, and $r_{\text{tree,shd}}$ all in [s m^{-1}] are used to determine latent heat flux of intercepted water on trees LE_{tree} [W m^{-2}], latent heat of transpiration from sunlit fraction $LTE_{\text{tree,sun}}$ [W m^{-2}], and latent heat of transpiration from shaded fraction $LTE_{\text{tree,shd}}$ [W m^{-2}], respectively. $\hat{r}_{\text{lb,tree}}$ is the re-scaled leaf boundary resistance of tree, $\hat{r}_{\text{lb,tree,sun}}$ and $\hat{r}_{\text{lb,tree,shd}}$ are re-scaled leaf boundary resistance of sunlit and shaded fractions of the tree respectively, and $\hat{r}_{\text{s,tree,sun}}$ and $\hat{r}_{\text{s,tree,shd}}$ are the re-scaled soil resistances (see Section 2.2.2.4) for the sunlit and shaded fractions of the canopy, respectively. The resistances can be

calculated as [129]

$$\hat{r}_{\text{lb,tree}} = \frac{r_{\text{lb,tree}}}{(LAI_{\text{tree}} + SAI_{\text{t}})d_{\text{w,tree}}} \quad (2.72)$$

$$\hat{r}_{\text{lb,tree,sun}} = \frac{r_{\text{lb,tree}}}{LAI_{\text{tree}}F_{\text{sun,tree}}(1 - d_{\text{w,tree}})} \quad (2.73)$$

$$\hat{r}_{\text{lb,tree,shd}} = \frac{r_{\text{lb,tree}}}{LAI_{\text{tree}}F_{\text{shd,tree}}(1 - d_{\text{w,tree}})} \quad (2.74)$$

$$\hat{r}_{\text{s,tree,sun}} = \frac{r_{\text{s,tree,sun}}}{LAI_{\text{tree}}F_{\text{sun,tree}}(1 - d_{\text{w,tree}})} \quad (2.75)$$

$$\hat{r}_{\text{s,tree,shd}} = \frac{r_{\text{s,tree,shd}}}{LAI_{\text{tree}}F_{\text{shd,tree}}(1 - d_{\text{w,tree}})}, \quad (2.76)$$

where $r_{\text{lb,tree}}$ is leaf boundary resistance, $r_{\text{s,sun}}$ and $r_{\text{s,shd}}$ are stomatal resistances of the sunlit and shaded part of the tree all in [s m^{-1}], respectively, $d_{\text{w,tree}}$ [-] is the fraction of tree covered by intercepted water, and $F_{\text{sun,tree}}$ and $F_{\text{shd,tree}}$ are fractions of sunlit and shaded tree, respectively. The detailed calculation of soil, leaf boundary, and stomatal resistances are provided in Section 2.2.2.4.

In VCWG, an alternative formulation for latent heat flux from trees is provided [32, 98]

$$LE_{\text{tree}} = \Lambda_{\text{m}}g_{\text{v}} \frac{e_{\text{s}}(T_{\text{t}}) - e_{\text{a}}}{P_{\text{a}}}, \quad (2.77)$$

where T_{t} [K] is tree temperature, T_{a} [K] is air temperature, g_{v} [$\text{mol m}^{-2} \text{s}^{-1}$] is the average surface and boundary layer conductance for humidity for the leaf, Λ_{m} [J mol^{-1}] is molar latent heat of vaporization, $e_{\text{s}}(T_{\text{t}})$ [Pa] is saturated vapor pressure of the air at tree temperature, e_{a} [Pa] is actual vapor pressure, and P_{a} [Pa] is the atmospheric pressure.

2.2.2.3 Conductive Heat Flux

Building Envelop

The interaction between indoor and outdoor environments is taken into account by calculating the conductive heat flux through the building envelop (walls and roof)

$$\frac{\partial T_{\text{i,bld}}}{\partial t} = k_{\text{i,bld}} \frac{\partial^2 T_{\text{i,bld}}}{\partial z^2}, \quad (2.78)$$

where $T_{\text{i,bld}}$ is temperature of roof (i=roof) or wall (i=wall) layers, $k_{\text{i,bld}} = \lambda_{\text{i}}/C_{\text{v,i,bld}}$ [$\text{m}^2 \text{s}^{-1}$] is the thermal diffusivity of the envelop layers and is a function of thermal conductivity λ_{i} [$\text{W m}^{-1} \text{K}^{-1}$] and volumetric heat capacity $C_{\text{v,i,bld}}$ [$\text{J m}^{-3} \text{K}^{-1}$]. The boundary conditions

required to solve the conduction equation are provided by the building energy model, which calculates the temperature and heat flux at the interior surface (see Section 2.7) and the surface energy balance model, which calculates heat flux at the exterior surface (G_i in Equation 2.43).

Ground

The ground heat flux drives the conduction equation at the upper-most soil layer via [26]

$$d \times cv_{\text{soil}} \frac{dT_1}{dt} = C_{\text{soil}}(T_2 - T_1) + G_i, \quad (2.79)$$

where d [m] is the soil layer thickness, cv_{soil} [$\text{J m}^{-3} \text{K}^{-1}$] is volumetric heat capacity of soil, $T_1 = \bar{\Theta}_{\text{rur,s}}$ [K] is soil upper layer temperature (the same as soil surface temperature), C_{soil} [$\text{W m}^{-2} \text{K}^{-1}$] is the soil thermal conductance, and T_2 [K] is soil temperature in the second layer under ground. In the lowest layer (n) of soil the conduction equation is forced by a deep soil temperature T_{deep} [K]

$$d \times cv_{\text{soil}} \frac{dT_{n-1}}{dt} = C_{\text{soil}}(T_{\text{deep}} - T_{n-1}). \quad (2.80)$$

In VCWG, the volumetric heat capacity and thermal conductivity of soil columns are determined as a function of soil properties (percentage of clay and sand in the soil) and soil water content, which is detailed in Oleson et al. (2004) [159].

Tree

VCWG computes the tree surface temperature by solving the energy balance equation. The latent and sensible heat fluxes are calculated using aerodynamic (imposed by turbulence in the atmosphere), leaf boundary (imposed by a thin layer of air around leaves), and stomatal resistances formulated in Equations 2.46, 2.69-2.71 and Section 2.2.2.4. The absorbed short-wave and longwave radiation fluxes by the tree are also determined in Section 2.2.1. Then, the following energy balance equation is solved for the tree surface temperature using the least square method

$$L_{n,\text{tree}} + S_{n,\text{tree}} = H_{\text{tree}} + LE_{\text{tree}} + LTE_{\text{tree}}. \quad (2.81)$$

This approach is used when water fluxes have significant effect on the canyon energy balance, particularly during rainfall events.

As an alternative, VCWG can simplify the problem further by linearizing the following

tree energy balance

$$(1 - \alpha_t)2\Omega S_{tree}^\downarrow + 2\varepsilon_t(\Omega L_{tree}^\downarrow - \sigma T_t^4) - H_{tree} - LE_{tree} = 0, \quad (2.82)$$

where Ω is clumping factor and H_{tree} and LE_{tree} can be calculated using Equations 2.51 and 2.77, respectively. Then the surface tree temperature can be determined explicitly by linearizing the energy balance equation [100].

2.2.2.4 Thermal Resistances

As discussed earlier, the sensible and latent heat fluxes of soil and urban vegetation are calculated using the resistance approach. This section provides detailed parameterization of soil, leaf boundary, and stomatal resistances.

Leaf Boundary Resistance

In calm air, diffusion coefficient controls the exchange of heat and water vapor from leaf to the atmosphere. As wind speed increases, the thickness of leaf boundary layer grows and turbulent flow contributes significantly to the transport of quantities [56]. VCWG calculates leaf boundary resistance r_{lb} [s m^{-1}] as a function of leaf dimension and surrounding flow condition [57, 129]

$$r_{lb} = \frac{1}{g_{b,\text{free}} + g_{b,\text{force}}}, \quad (2.83)$$

where $g_{b,\text{free}}$ and $g_{b,\text{force}}$ all in [m s^{-1}] are leaf boundary conductance at free and forced convection and can be computed as [57, 129]

$$g_{b,\text{free}} = \frac{0.5D_h Gr^{0.25}}{d_{\text{leaf}}} \quad (2.84)$$

$$g_{b,\text{force}} = \left(\frac{2a}{\alpha}\right) \left(\frac{S_{z_{\text{veg}/\text{tree}}}}{d_{\text{leaf}}}\right)^{0.5} [1 - e^{-\alpha/2}], \quad (2.85)$$

where $D_h = 1.9 \times 10^{-5}$ [$\text{m}^2 \text{s}^{-1}$] is molecular diffusivity of heat, $Gr = 1.6 \times 10^8(T_{\text{veg}/\text{tree}} - T_a)d_{\text{leaf}}^3$ [-] is Grashof number, d_{leaf} [m] is leaf dimension, $a = 0.01$ [$\text{m s}^{-1/2}$] is a model constant, α [-] is attenuation coefficient for wind speed profile, and $S_{z_{\text{veg}/\text{tree}}}$ [m s^{-1}] is wind speed at the height of vegetation which is determined from the column model.

Stomatal Resistance

Stomata of a leaf control the uptake of CO_2 from the atmosphere to its chloroplasts for photosynthesis activity. Stomata are normally open during the daytime and only a small

fraction of absorbed radiation is used for photosynthesis activity. The large portion of radiation causes inevitable water evaporation from the leaf tissue. The stomatal resistance to the water exchange $r_{s,\text{water}}$ [$\text{m}^2 \text{s} \mu\text{mol}^{-1} \text{CO}_2$] for sunlit and shaded fraction of vegetation can be calculated as a function of the process of photosynthesis [129]

$$r_{s,\text{water}} = \frac{1}{1.64g_{s,\text{CO}_2}}, \quad (2.86)$$

where g_{s,CO_2} is stomatal conductance of CO_2 , and the factor of 1.64 represents ratio of stomatal resistance to CO_2 exchange to stomatal resistance to water exchange. $r_{s,\text{water}}$ can be converted to hydrological units of [s m^{-1}] as [129]

$$r_s = \frac{1}{0.0224} \frac{273.15P_a}{T_{\text{veg/tree}}P_{\text{ref}}} 10^6 r_{s,\text{water}}, \quad (2.87)$$

where P_a and $P_{\text{ref}} = 101325$ are the atmospheric pressure and reference pressure in [Pa] and $T_{\text{veg/tree}}$ is in [K]. The stomatal conductance of CO_2 can be calculated as a function of carbon dioxide assimilation rate A_{nC} [$\mu\text{mol CO}_2 \text{m}^{-2} \text{s}^{-1}$], vapor pressure deficit of the atmosphere VPD [Pa], and intercellular CO_2 concentration c_i [Pa] [129]

$$g_{s,\text{CO}_2} = g_{0,\text{CO}_2} + a \frac{A_{\text{nC}}}{(c_c - \Gamma^*)} f \cdot P_{\text{atm}}, \quad (2.88)$$

where g_{0,CO_2} [$\mu\text{mol CO}_2 \text{m}^{-2} \text{s}^{-1}$] is the minimum stomatal conductance, c_c [Pa] is internal CO_2 concentration of the leaf, $f = 1/(1 + VPD/\Delta_0)$ [-], and Δ_0 [Pa] is a model constant. Detailed calculation of these parameters are provided in Fatichi (2010) [56] and Meili et al. (2020) [129].

Soil Resistance

Atmospheric conditions and soil water content control evaporation from soil pores to the adjacent atmosphere above. VCWG calculates soil resistance r_{soil} [s m^{-1}] using the model developed by Haghghi et al. (2013) [72] and Fatichi (2010) [56], where soil resistance is parameterized as a function of type of soil, soil water content, and atmospheric condition just above the surface. Hence, r_{soil} is the sum of resistance to transport water vapor within the soil column r_{sv} [s m^{-1}] and resistance to transport water from soil surface to the atmosphere

above r_{sbl} [s m^{-1}], where r_{sv} and r_{sbl} can be calculated as [56, 129]

$$r_{\text{sv}} = \frac{\gamma}{4K(\theta_{\text{S}})} \quad (2.89)$$

$$r_{\text{sbl}} = \frac{\delta_{\text{m}} + P_{\text{sz}}f(\theta_{\text{S}})}{Da}, \quad (2.90)$$

where K [m s^{-1}] is the soil hydraulic conductivity at soil water content θ_{S} , $\gamma = (RH_{\text{soil}}e_{\text{sat}} - e_{\text{a}})/(\rho_{\text{w}}R_{\text{d}}T_{\text{g}})$ [-], RH_{soil} [-] is relative humidity of the soil, T_{g} [K] is surface soil temperature, ρ_{w} [kg m^{-3}] is density of water, R_{d} [$\text{J kg}^{-1} \text{K}^{-1}$] is gas constant for water vapor, δ_{m} [m] is boundary layer thickness of soil, P_{sz} [m] is soil pore size, Da [$\text{m}^2 \text{s}^{-1}$] is the molecular diffusivity of water vapor, $f(\theta_{\text{S}})$ [-] is a function that relates soil moisture content θ_{S} to diffusivity. Detailed formulation of δ_{m} , P_{sz} , and $f(\theta_{\text{S}})$ are provided in Meili et al. (2020) [129].

2.2.3 Urban Vertical Diffusion Model

Numerous studies have attempted to parameterize the interaction between urban elements and the atmosphere in terms of dynamical and thermal effects, from very simple models based on MOST [193], to the bulk flow (single-layer) parameterizations [29, 102, 104, 124], and to multi-layer models [73, 100, 101, 182] with different levels of complexity. The multi-layer models usually treat aerodynamic and thermal effects of urban elements as sink or source terms in temperature, momentum, specific humidity, and turbulence kinetic energy equations. Parameterization of the exchange processes between the urban elements and the atmosphere can be accomplished using either experimental data or CFD simulations [8, 48, 95, 96, 101, 115, 122, 182]. CFD-based parameterizations use results from Reynolds-Averaged Navier-Stokes (RANS) or Large-Eddy Simulations (LES) including effects of trees and buildings [101, 123, 147, 182]. These parameterizations are based on temporally and horizontally averaged CFD results at different canopy heights.

Variables such as cross- and along-canyon wind velocities (\bar{U} and \bar{V} [m s^{-1}], respectively), potential temperature ($\bar{\Theta}$ [K]), and specific humidity (\bar{Q} [kg kg^{-1}]) are Reynolds averaged. The one-dimensional time-averaged momentum equations in the cross- and along-canyon components are [98, 100, 101, 147, 182, 183]

$$\frac{\partial \bar{U}}{\partial t} = - \underbrace{\frac{\partial \overline{uw}}{\partial z}}_{\text{I}} - \underbrace{\frac{1}{\rho} \frac{\partial \bar{P}}{\partial x}}_{\text{II}} - \underbrace{D_x}_{\text{III}}, \quad (2.91)$$

$$\frac{\partial \bar{V}}{\partial t} = - \underbrace{\frac{\partial \overline{vw}}{\partial z}}_{\text{I}} - \underbrace{\frac{1}{\rho} \frac{\partial \bar{P}}{\partial y}}_{\text{II}} - \underbrace{D_y}_{\text{III}}, \quad (2.92)$$

where \bar{P} [Pa] is time-averaged pressure. The terms on the right hand side of Equations 2.91 and 2.92 are the vertical gradient of turbulent flux of momentum (I), acceleration due to the large-scale pressure gradient (II), and the sum of pressure, building form, building skin, and vegetation drag terms (III). The pressure and skin drag force terms exerted on the flow are formulated as follows [98, 100, 101, 147, 182, 183]

$$D_x = \underbrace{\frac{1}{\rho} \frac{\partial \tilde{P}}{\partial x}}_{\text{I}} + \underbrace{\nu(\nabla^2 \tilde{U})}_{\text{II}}, \quad (2.93)$$

$$D_y = \underbrace{\frac{1}{\rho} \frac{\partial \tilde{P}}{\partial y}}_{\text{I}} + \underbrace{\nu(\nabla^2 \tilde{V})}_{\text{II}}, \quad (2.94)$$

where term I represents dispersive pressure variation (form drag) induced by vegetation and building and term II represents the dispersive viscous dissipation (skin drag) induced by horizontal surfaces. The former can be parameterized as

$$\frac{1}{\rho} \frac{\partial \tilde{P}}{\partial x} = (B_D C_{DBv} + LAD \Omega C_{DV}) \bar{U}_{\text{expl}} \bar{U}, \quad (2.95)$$

$$\frac{1}{\rho} \frac{\partial \tilde{P}}{\partial y} = (B_D C_{DBv} + LAD \Omega C_{DV}) \bar{V}_{\text{expl}} \bar{V}, \quad (2.96)$$

where B_D [m^{-1}] is sectional building area density, C_{DBv} [-] is sectional drag coefficient in the presence of trees, LAD [$\text{m}^2 \text{m}^{-3}$] is leaf area density in the canyon, Ω [-] is clumping factor, C_{DV} [-] is the drag coefficient for tree foliage, and \bar{U}_{expl} and \bar{V}_{expl} [m s^{-1}] are wind velocity components in x and y directions from a previous numerical solution, respectively, which are assumed explicitly as constants to linearize the system of equations to be solved. The skin drag can be parameterized as follows

$$\nu(\nabla^2 \tilde{U}) = \frac{1}{\Delta z} c_d f_m \bar{U}_{\text{expl}} \bar{U}, \quad (2.97)$$

$$\nu(\nabla^2 \tilde{V}) = \frac{1}{\Delta z} c_d f_m \bar{V}_{\text{expl}} \bar{V}, \quad (2.98)$$

where c_d [-] is skin drag coefficient and f_m [-] is a function of stability from Louis (1979) [113].

K -theory is used to parameterize the vertical momentum fluxes, i.e. $\overline{uw} = -K_m \partial \overline{U} / \partial z$ and $\overline{vw} = -K_m \partial \overline{V} / \partial z$ (the same approach will be used in potential temperature and specific humidity equations), where the diffusion coefficient is calculated using a $k - \ell$ turbulence model

$$K_m = C_k \ell_k k^{1/2}, \quad (2.99)$$

where C_k [-] is a constant and ℓ_k [m] is a length scale optimized using sensitivity analysis based on CFD analysis of Nazarian et al. (2020) [147]. Note that the plan area density λ_p [-] for some experimental runs of VCWG is greater than the limit considered by Nazarian et al. (2020) [147], so we assume that the parameterizations extrapolate to this value of λ_p [-]. More details on C_k [-] and ℓ_k [m] are provided in the literature [98, 147]. The turbulence kinetic energy k [$\text{m}^2 \text{s}^{-2}$] can be calculated using a prognostic equation [101]

$$\frac{\partial k}{\partial t} = \underbrace{K_m \left[\left(\frac{\partial \overline{U}}{\partial z} \right)^2 + \left(\frac{\partial \overline{V}}{\partial z} \right)^2 \right]}_{\text{I}} + \underbrace{\frac{\partial}{\partial z} \left(\frac{K_m}{\sigma_k} \frac{\partial k}{\partial z} \right)}_{\text{II}} - \underbrace{\frac{g}{\Theta_0} \frac{K_m}{Pr_t} \frac{\partial \overline{\Theta}}{\partial z}}_{\text{III}} + \underbrace{S_{\text{wake}}}_{\text{IV}} - \underbrace{\varepsilon}_{\text{V}}, \quad (2.100)$$

where g [m s^{-2}] is acceleration due to gravity and Θ_0 [K] is a reference potential temperature. The terms on the right hand side of Equation 2.100 are shear production (I), turbulent transport of kinetic energy parameterized based on K -theory (II), buoyant production/dissipation (III), wake production by urban obstacles and trees (IV), and dissipation (V). The last two terms can be parameterized as

$$S_{\text{wake}} = (B_D C_{DBV} + LAD \Omega C_{DV}) \overline{U}_{\text{expl}}^3, \quad (2.101)$$

$$\varepsilon = C_\varepsilon \frac{k^{3/2}}{\ell_{\varepsilon, \text{dissip}}}, \quad (2.102)$$

where Ω [-] is clumping factor, C_ε [-] is a model constant and $\ell_{\varepsilon, \text{dissip}}$ [m] is a dissipation length scale obtained by sensitivity study using CFD analysis of Nazarian et al. 2020 [147]. Note that plan area density λ_p [-] could be greater than the limit considered by Nazarian et al. 2020 [147], so we assume that the parameterizations extrapolate to this value of λ_p [-]. σ_k [-] is the turbulent Prandtl number for kinetic energy, which is generally suggested to be

$\sigma_k = 1$ [-] [163].

To calculate the vertical profile of potential temperature in the urban area, the energy transport equation can be derived as

$$\frac{\partial \bar{\Theta}}{\partial t} = \underbrace{\frac{\partial}{\partial z} \left(\frac{K_m}{Pr_t} \frac{\partial \bar{\Theta}}{\partial z} \right)}_I + \underbrace{S_{\Theta R} + S_{\Theta G} + S_{\Theta W} + S_{\Theta V} + S_{\Theta A} + S_{\Theta \text{waste}}}_{II}, \quad (2.103)$$

where Pr_t [-] is turbulent Prandtl number, the first term on the right hand side is turbulent transport of heat (I), and the heat sink/source terms (II) correspond to sensible heat exchanges with roof ($S_{\Theta R}$), ground ($S_{\Theta G}$), wall ($S_{\Theta W}$), urban vegetation $S_{\Theta V}$, and radiative divergence $S_{\Theta A}$ [all in K s^{-1}]. The heat source/sink terms caused by roof ($S_{\Theta R}$) and ground ($S_{\Theta G}$) are calculated based on the study by Louis (1979) [113] and the heat flux from the wall ($S_{\Theta W}$ [K s^{-1}]) is formulated in Martilli et al. (2002) [122]. The two other source/sink terms can be parameterized as follows [98]

$$S_{\Theta A} = \frac{4\rho_{\text{abs}}k_{\text{air}}}{\rho C_p v_L} \left[(1 - \lambda_p) L_A \right], \quad (2.104)$$

$$S_{\Theta V} = \frac{2g_{\text{Ha}}c_{\text{PM}}}{\rho C_p v_L} \left[LAD(1 - \lambda_p)(\bar{\Theta}_V - \bar{\Theta}) \right], \quad (2.105)$$

where L_A [W m^{-2}] is the absorbed flux density of longwave radiation in the canyon, ρ_{abs} [kg m^{-3}] is the density of absorbing molecules, k_{air} [$\text{m}^2 \text{kg}^{-1}$] is their mass extinction cross section, $v_L = (1 - \lambda_p)$ [-] is the fraction of total volume that is outdoor air, g_{Ha} [$\text{mol m}^{-2} \text{s}^{-1}$] is conductance for heat, c_{PM} [$\text{J mol}^{-1} \text{K}^{-1}$] is the molar heat capacity for the air, and $\bar{\Theta}_V$ [K] is the temperature of tree foliage. Equation 2.105 is only used when the tree temperature is calculated using the linearized tree energy balance equation. Otherwise, the least square method is used to solve tree energy balance equation for tree temperature (see Section 2.2.2.3) and then $S_{\Theta V}$ is calculated as a function of sensible heat flux. Contribution of the waste heat emissions from building Heating Ventilation and Air Conditioning (HVAC) system $S_{\Theta \text{waste}}$ [K s^{-1}] is parameterized by

$$S_{\Theta \text{waste}} = F_{\text{st}} \frac{1}{\rho C_p \Delta z} H_{\text{HVAC}}, \quad (2.106)$$

where H_{HVAC} [W m^{-2}] is total sensible waste heat released into the urban atmosphere per

building footprint area, F_{st} [-] is the fraction of waste heat released at street level, while the remainder fraction $(1 - F_{st})$ [-] is released at roof level, and Δz [m] is grid discretization in the vertical direction. Depending on the type of building, waste heat emissions can be released partially at street level and the rest at roof level, which can be adjusted by changing F_{st} [-] from 0 to 1. Term H_{HVAC} [W m^{-2}] is calculated by the building energy model as

$$H_{HVAC} = \underbrace{Q_{\text{surf}} + Q_{\text{ven}} + Q_{\text{inf}} + Q_{\text{int}}}_{Q_{\text{cool}}} + W_{\text{cool}} + Q_{\text{dehum}} + Q_{\text{gas}} + Q_{\text{water}}, \quad (2.107)$$

$$H_{HVAC} = \underbrace{(Q_{\text{surf}} + Q_{\text{ven}} + Q_{\text{inf}} + Q_{\text{int}})}_{Q_{\text{heat}}}/\eta_{\text{heat}} - Q_{\text{heat}} + Q_{\text{dehum}} + Q_{\text{gas}} + Q_{\text{water}}, \quad (2.108)$$

under cooling and heating modes, respectively. In this notation all symbols represent positive quantities unless a negative quantity is emphasized by the negative sign in front of the symbol in the equation. Under cooling mode H_{HVAC} [W m^{-2}] is calculated by adding the cooling demand (Q_{cool} [W m^{-2}], consisting of surface cooling demand, ventilation demand, infiltration (or exfiltration) demand, internal energy demand (lighting, equipment, and occupants), energy consumption of the cooling system ($W_{\text{cool}} = Q_{\text{cool}}/COP$ [W m^{-2}]; accounting for the coefficient of performance, COP [-]), dehumidification demand (Q_{dehum} [W m^{-2}], energy consumption by gas combustion (e.g., cooking) (Q_{gas} [W m^{-2}], and energy consumption for water heating (Q_{water} [W m^{-2}]). Under heating mode, H_{HVAC} [W m^{-2}] is calculated by adding the heating demand (Q_{heat} [W m^{-2}], consisting of surface heating demand, ventilation demand, infiltration (or exfiltration) demand, and internal energy demand (lighting, equipment, and occupants) (divided by thermal efficiency of the heating system, η_{heat} [-], then subtracting the heating demand and adding the dehumidification demand (Q_{dehum} [W m^{-2}], energy consumption by gas combustion (e.g., cooking) (Q_{gas} [W m^{-2}]) and energy consumption for water heating (Q_{water} [W m^{-2}]).

To complete the urban one-dimensional vertical diffusion model, the transport equation for specific humidity is

$$\frac{\partial \bar{Q}}{\partial t} = \underbrace{\frac{\partial}{\partial z} \left(\frac{K_m}{Sc_t} \frac{\partial \bar{Q}}{\partial z} \right)}_{\text{I}} + \underbrace{S_{QV}}_{\text{II}}, \quad (2.109)$$

where \bar{Q} [kg kg^{-1}] is time-averaged specific humidity. The turbulent transport of specific humidity (I) is parameterized based on K -theory, Sc_t [-] is the turbulent Schmidt number,

and source term S_{Q_V} [$\text{kg kg}^{-1} \text{s}^{-1}$] (II) is caused by latent heat from vegetation and can be calculated using the following equation [98]

$$S_{Q_V} = \frac{\Lambda_M g_v \Omega}{\rho \Lambda v_L} \left[LAD(1 - \lambda_p) \left(s[\bar{\Theta}_V - \bar{\Theta}] + \frac{VPD}{P} \right) \right], \quad (2.110)$$

where Λ_M [J mol^{-1}] is molar latent heat of vaporization, Λ [J kg^{-1}] is latent heat of vaporization, g_v [$\text{mol m}^{-2} \text{s}^{-1}$] is the average surface and boundary-layer conductance for humidity for the whole leaf, s [K^{-1}] is derivative of saturation vapour pressure with respect to temperature divided by pressure, VPD [Pa] is the vapour deficit of the atmosphere, and P [Pa] is atmospheric pressure. This equation is only used when the tree temperature is calculated using the linearized tree energy balance equation. Otherwise, the least square method is used to solve the tree energy balance equation (see Section 2.2.2.3) and then S_{Q_V} is calculated as a function of latent heat flux.

2.2.4 Building Energy Model

The Building Energy Model (BEM) solves the sensible and latent heat balance at the indoor environment to determine the indoor temperature and humidity. The BEM is a single-zone model with respect to both the indoor and outdoor (urban canopy) environments. That is, only a single temperature is assumed for indoor air, and only a single potential temperature is assumed for outdoor air by integrating the potential temperature profile from the street to roof levels. Further, all wall temperatures are assumed to be uniform with height. The building geometry is defined as average-oriented facade and a flat roof.

In this work, the balance equation for convection, conduction, and radiation heat fluxes is applied to all building elements (wall, roof, floor, windows, ceiling, and internal mass) to calculate the indoor air temperature (Figure 2.7). Then, a sensible heat balance equation, between convective heat fluxes released from indoor surfaces and internal heat gains and sensible heat fluxes from the HVAC system and infiltration (or exfiltration), is solved to obtain the time evolution of indoor temperature as

$$\forall \rho C_p \frac{dT_{in}}{dt} = \pm \underbrace{Q_{surf} \pm Q_{ven,sens} \pm Q_{inf,sens} \pm Q_{int,sens}}_{Q_{cool/heat}}, \quad (2.111)$$

where \forall [$\text{m}^3 \text{m}^{-2}$] is indoor volume per building footprint area, T_{in} [K] is indoor air tempera-

ture, and $Q_{\text{cool/heat}}$ [W m^{-2}] is cooling or heating demand as specified in Equations 2.107 and 2.108. In this notation all symbols represent positive quantities; however, in the equation either positive or negative signs should be used to emphasize if a term contributes to indoor temperature increase or decrease, depending on the operation mode (cooling versus heating) and environmental conditions (indoor, outdoor, and surface temperatures). The heat fluxes in 2.111 can be parameterized as [28].

$$Q_{\text{surf}} = \pm \Sigma h_i A_i (|T_{\text{si}} - T_{\text{in}}|) \quad (2.112)$$

$$Q_{\text{inf,sens}} = \pm \dot{m}_{\text{inf}} C_p (|T_{\text{out}} - T_{\text{in}}|) \quad (2.113)$$

$$Q_{\text{vent,sens}} = \pm \dot{m}_{\text{vent}} C_p (|T_{\text{supp}} - T_{\text{in}}|) \quad (2.114)$$

$$Q_{\text{int,sens}} = \pm Q_{\text{int}} (1 - f_{\text{rd}}) (1 - f_{\text{lat}}), \quad (2.115)$$

where h_i [$\text{W m}^{-2} \text{K}^{-1}$] is convective heat transfer coefficient for surface i and A_i [$\text{m}^2 \text{m}^{-2}$] is area of the surface i per building foot print area. Surface i can correspond to indoor elements such as ceiling, walls, floor, building mass, and windows. T_{si} [K] is the temperature of the inner layer of elements, T_{in} [K] is indoor temperature, T_{out} [K] is the outdoor temperature averaged over building height, T_{supp} [K] is supply temperature, \dot{m}_{inf} [$\text{kg s}^{-1} \text{m}^{-2}$] is mass flow rate of infiltration (exfiltration) per building footprint area, \dot{m}_{vent} [$\text{kg s}^{-1} \text{m}^{-2}$] is mass flow rate of ventilated air in the HVAC system per building footprint area, $Q_{\text{int,sens}}$ is total internal heat gains, f_{rd} is radiant fraction of sensible internal heat gain, and f_{lat} is the latent fraction of the internal heat gains.

A similar balance equation can be derived for latent heat to determine the time evolution of the indoor air specific humidity as well as the dehumidification load Q_{dehum} [W m^{-2}] [28]

$$\forall \rho L \frac{dQ_{\text{in}}}{dt} = \pm Q_{\text{ven,lat}} \pm Q_{\text{inf,lat}} \pm Q_{\text{int}} f_{\text{lat}}, \quad (2.116)$$

where the latent heat fluxes can be parameterized as

$$Q_{\text{inf,sens}} = \pm \dot{m}_{\text{inf}} L (|Q_{\text{out}} - Q_{\text{in}}|) \quad (2.117)$$

$$Q_{\text{ven,lat}} = \pm \dot{m}_{\text{ven}} L (|Q_{\text{supp}} - Q_{\text{in}}|), \quad (2.118)$$

where L [J kg^{-1}] is latent heat of vaporization, Q_{out} is outdoor specific humidity [kg kg^{-1}], Q_{in} is indoor specific humidity [kg kg^{-1}], and Q_{supp} is supply specific humidity [kg kg^{-1}].

Note that energy consumption by gas combustion (e.g. cooking) Q_{gas} and water heating

Q_{water} [both in W m^{-2}] do not influence indoor air temperature or specific humidity, but such energy consumption sources appear in the waste heat Equations 2.107 and 2.108. These terms are determined from schedules [28].

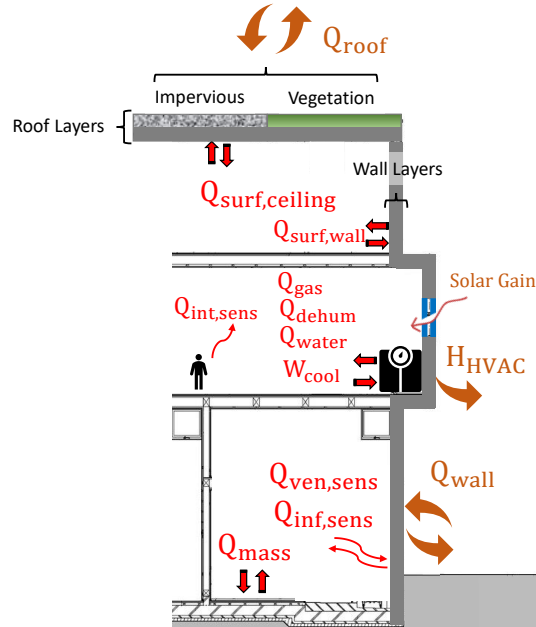


Figure 2.7: Building Energy Model (BEM).

2.2.5 Hydrology Model

Modeling of ecohydrological processes in natural areas has been undertaken for decades [20, 57, 105, 169]. Attention to this aspect in the urban areas has recently become popular to support sustainable urban water management and improved understanding of urban ecology.

In this work, urban hydrological exchanges in the presence of precipitation and ecophysiological behavior of urban trees, road vegetation, and roof vegetation are modeled. The hydrology model solves the surface water balance equations for impervious surfaces, soil surfaces, and interception on urban vegetation, and it calculates transpiration as a function of soil moisture, photosynthetic activity, and vapor pressure deficit. The VCWG adopts the urban hydrology model developed by Meili et al. (2020) [129] with technical modifications that improve prediction of urban climate variables.

2.2.5.1 Water Interception

The transient equation for interception of water by urban vegetation (trees, roof and road vegetation) and horizontal surfaces (impervious, bare soil, and soil underneath low vegetation) can be obtained as [129]

$$\frac{dInt}{dt} = P_{\text{precip}} + P_{\text{runon}} - D - E_{\text{int}}, \quad (2.119)$$

where Int [mm] is the intercepted water, P_{precip} [mm s^{-1}] is the fraction of total precipitation that reaches the surface, P_{runon} [mm s^{-1}] is runoff, D [mm s^{-1}] is the water system outflow in forms of infiltration, deep leakage, and runoff, and E_{int} [mm s^{-1}] is the evaporation from intercepted water. It is assumed that the surface runoff and soil water leakage at the roof level travel directly to the sewer system and do not affect the water balance in the urban canyon.

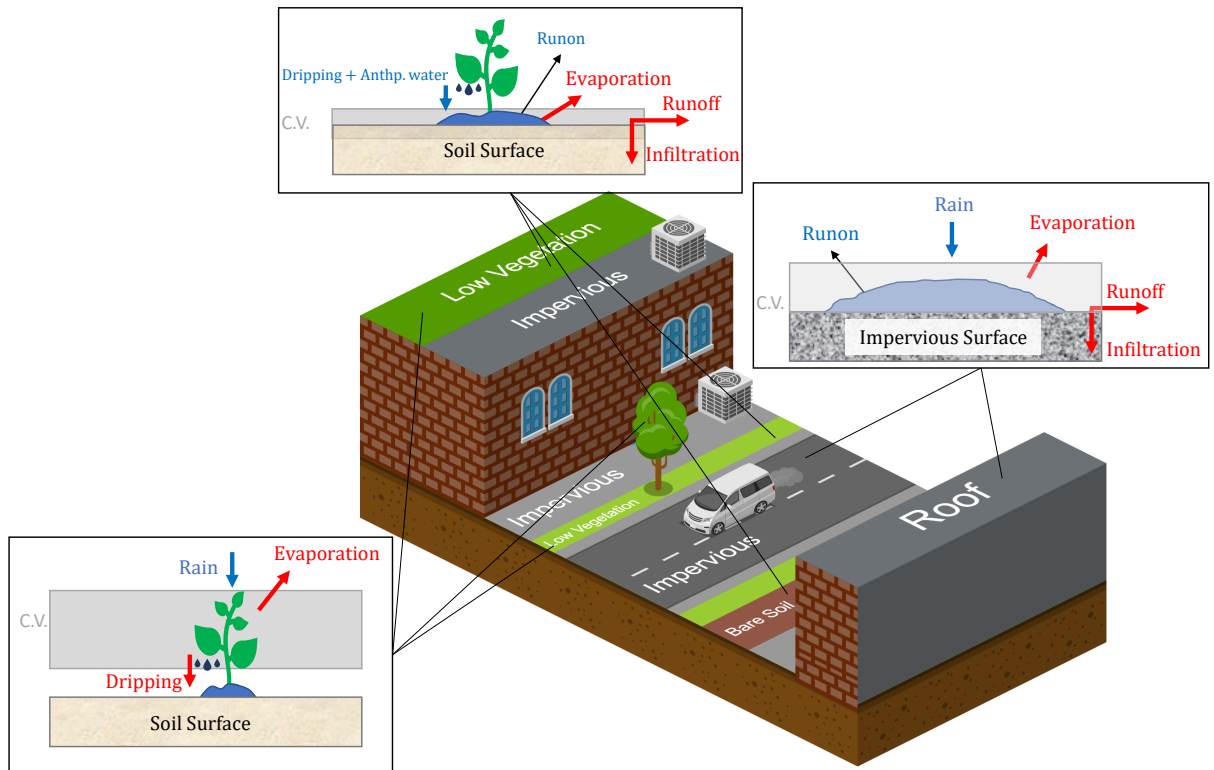


Figure 2.8: Water balance in the urban area; blue arrows are the source terms, red arrows are the sink terms, and black arrow is indicator.

Plant Canopy Interception

The dynamics of interception of water by vegetation can be written as [83, 129]

$$\frac{dInt_i}{dt} = P_{\text{precip}} - D_{\text{sat}} - D_{\text{drip}} - E_{\text{int}}, \quad (2.120)$$

where Int_i [mm] is the interception of water by low vegetation (Int_{veg}) or high vegetation (Int_{tree}), P_{precip} [mm s^{-1}] is the fraction of total incoming precipitation P [mm s^{-1}] onto the plant leaves and can be determined as a function of LAI and SAI as follows [117]

$$P_{\text{precip}} = C_{\text{fol}}P, \quad (2.121)$$

where $C_{\text{fol}} = (1 - e^{-k(LAI+SAI)})$ [m^2 vegetated area m^{-2} PFT area] is fractional vegetation cover and can vary between 0 and 1 depending on the plant type, $k = 0.75$ is model constant, and PFT area is plant functional type area which depends on plant type. The outflow from the interception of water on the urban plant is partitioned into the saturation excess from the interception storage of foliage D_{sat} [mm s^{-1}] and the dripping water D_{drip} [mm s^{-1}] [56]

$$D_{\text{sat}} = \begin{cases} \frac{Int - Int_{\text{max}}}{dt} & Int > Int_{\text{max}} \\ 0 & Int < Int_{\text{max}} \end{cases} \quad (2.122)$$

$$D_{\text{drip}} = K_c e^{g_c(Int - Int_{\text{max}})}, \quad (2.123)$$

where Int [mm] is the intercepted water at the current simulation time, Int_{max} [mm] is the maximum interception capacity of the plant, $K_c = 0.06/3600$ [mm s^{-1}] is the drainage rate coefficient, and $g_c = 3.7$ [mm^{-1}] is the exponential decay parameter. The maximum interception capacity can vary from a vegetation type to another as a function of LAI, SAI, and vegetation type parameter, $S_{\text{p,Int}}$ [mm] [129]

$$Int_{\text{max}} = S_{\text{p,Int}}(LAI + SAI). \quad (2.124)$$

Impervious Surface

The transient water balance at the impervious surface can be written as [129]

$$\frac{dInt_{\text{imp}}}{dt} = P_{\text{precip}} + P_{\text{runon}} - D_{\text{lk}} - D_{\text{runoff}} - E_{\text{int}}, \quad (2.125)$$

where P_{precip} [mm s^{-1}] is the fraction of total incoming precipitation that reaches the imper-

vious surface. P_{precip} at the roof level is equal to the total incoming precipitation, while at the ground level an additional term is considered due to the dripping from trees. Depending on the properties of impervious surface including roughness and micro-depressions, the available water at the surface can exceed that of maximum interception capacity. Based on Horton overland flow, excess water can leave the system as the surface runoff D_{runoff} [mm s^{-1}], and a fraction can stay in the system as the surface runoff P_{runon} [mm s^{-1}]. The leakage D_{lk} [mm s^{-1}] from an impervious surface is a function of hydraulic conductivity, which is small for asphalt and paved surfaces. Impervious roofs are assumed to be impermeable.

Soil Surface

The transient water budget at the bare soil surface can be derived as [129]

$$\frac{dInt_{\text{soil}}}{dt} = P_{\text{precip}} + P_{\text{runon}} - Inf - D_{\text{runoff}} - E_{\text{int}}, \quad (2.126)$$

where P_{precip} [mm s^{-1}] is the precipitation that reaches the surface underneath the vegetation (see Equation 2.121) and P_{runon} [mm s^{-1}] is runoff that did not leave the system in the previous time step. The infiltration rate Inf [mm s^{-1}] into the soil columns of bare and vegetated ground is limited by the infiltration capacity of the soil. The infiltration capacity is calculated by assuming a Dirichlet boundary condition at the surface with soil water potential of zero. Then, comparing the available water at the surface and infiltration capacity, the water flux enters the soil column and provides the Neumann boundary condition. The surface runoff D_{runoff} [mm s^{-1}] is calculated by comparing the amount of water left in the system after infiltration into the soil column with the maximum interception capacity. This equation is used for bare soil and soil underneath the low vegetation at the ground and roof levels.

Surface Runoff and Runon

As discussed in the previous sections, the surface runoff can be generated when the water into the soil exceeds the infiltration capacity, the available water at the surface exceeds the interception capacity, and the soil columns become saturated. Once the water balance equation for each type of surfaces is solved, we can calculate the total surface runoff as [56, 57]

$$D_{\text{runoff}}^{\text{total}} = f_v D_{v,\text{runoff}} + f_b D_{b,\text{runoff}} + f_i D_{i,\text{runoff}}, \quad (2.127)$$

where f_v , f_b , and f_i are the fractions of the ground or roof covered by vegetation, bare soil, and impervious surface, respectively. A fraction of total runoff can stay in the system in the

form of runoff

$$P_{\text{runon}}^{\text{total}} = f_{\text{runon}} D_{\text{runoff}}^{\text{total}}, \quad (2.128)$$

where f_{runon} is between 0 and 1. A homogeneous distribution of runoff is assumed either at the roof or ground level.

2.2.5.2 Subsoil water interaction

Vertical and horizontal distribution of soil moisture in an urban area is one of the important preconditions for urban climate models. Soil moisture influences water and energy exchanges in the atmosphere and vadose (unsaturated) zone, which is defined as the part of earth spanning from land surface to the position at which the ground water is at atmospheric pressure. The vadose zone interacts with the active rooting zone and provides water needed for growth of vegetation, affects water balance at the surface by absorbing surface water and energy exchanges via changing latent heat flux, and controls the transmission of water from land surface to groundwater [82, 150, 190]. As shown in Figure 2.9, the vadose zone in an urban area is divided into the three soil columns underneath the vegetated, bare, and impervious surfaces. There is only one soil column at the roof level for green roofs. The first few layers of the soil column underneath the impervious surface do not contribute to water balances.

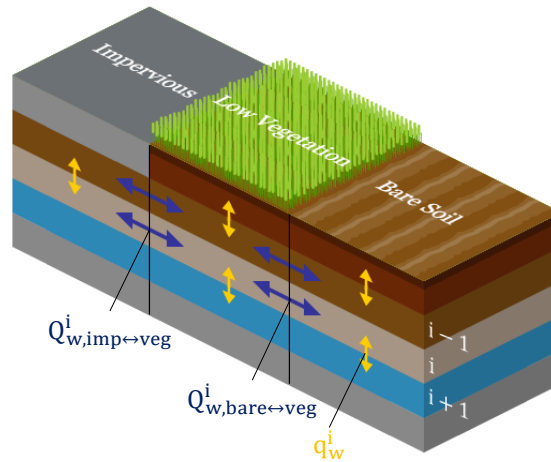


Figure 2.9: Partitioning of Soil Column.

The vertical water movement in the soil columns is modeled using the one-dimensional

Richards equation, which is based on the ordinary laws of hydrodynamics and the driving forces are gravity and the pressure gradient forces [129]

$$\frac{\partial \theta}{\partial t} = \frac{\partial}{\partial z_{\text{soil}}} \left[K_v(\theta) \frac{\partial \Psi_s(\theta)}{\partial z_{\text{soil}}} + K_v(\theta) \right] - \hat{Q}_w - e_{\text{soil}} - t_{\text{veg}} - t_{\text{tree}}, \quad (2.129)$$

where z_{soil} [mm] is soil layer depth, θ is the soil moisture content [$\text{m}^3 \text{m}^{-3}$], K_v [mm s^{-1}] is the vertical hydraulic conductivity, Ψ_s [mm] is the capillary potential due to the pressure gradient, \hat{Q}_w [s^{-1}] is sink term due to latent fluxes, e_{soil} [s^{-1}] is sink term due to soil evaporation, t_{veg} [s^{-1}] is sink term due to water uptake for transpiration of low vegetation, t_{tree} [s^{-1}] is sink term due to water uptake for transpiration of trees. This nonlinear partial differential equation is first solved vertically for each soil column using the method of lines, which is adopted for unsaturated flow problems in soil physics [107]. This method reduces the transient partial differential equation to a system of ordinary differential equations, which makes it more efficient in terms of computational time. A non-uniform grid with a higher resolution near the surface is generated for each soil column. Then, the vertical Richards equation is coupled to the simplified horizontal equation, where the latter describes the dynamics of horizontal water flux for each layer

$$d_{z,i} \frac{d\theta_i}{dt} = (Q_{\text{ver},i-1} - Q_{\text{ver},i}) + (Q_{\text{lat},i}^{\text{in}} - Q_{\text{lat},i}^{\text{out}}) - \sum_{j=1}^{n_g} E_{\text{soil},j} - \sum_{j=1}^{n_g} T_{\text{tree},j} \cdot r_{\text{tree},i,j} - \sum_{j=1}^{n_g} T_{\text{veg},j} \cdot r_{\text{veg},i,j}, \quad (2.130)$$

where $d_{z,i}$ [mm] is layer depth, $Q_{\text{ver},i-1}$ and $Q_{\text{ver},i}$ [mm s^{-1}] are the vertical water fluxes in and out of layer i , $Q_{\text{lat},i}^{\text{in}}$ and $Q_{\text{lat},i}^{\text{out}}$ [mm s^{-1}] are the lateral water fluxes in and out of the layer, and $E_{\text{soil},j}$ [mm s^{-1}] is soil evaporation of surface j , which exists only in the first layer. In the presence of low vegetation and trees, the sink term due to the transpiration of low vegetation $T_{\text{veg},j}$ [mm s^{-1}] and trees $T_{\text{tree},j}$ [mm s^{-1}] from surface j should be taken into account. T_{veg} and T_{tree} are weighted based on their fraction of root biomass in the layer $r_{\text{veg},i,j}$ [-] and $r_{\text{tree},i,j}$ [-] of surface j . The low vegetation at the roof and ground levels can only access water stored in the soil column underneath the vegetated fraction of the surface. The horizontal distribution of tree root can be set to either have access to all three soil columns, or depending on the size of the tree, it can have access to a fraction of them [129]. Four possible vertical root biomass profiles are implemented in VCWG, including exponential root profile [83], linear-dose response root profile [41], linear-dose response profile with tap roots [57], and a constant profile. These profiles can be specified based on the rooting depth that contains 50% (Z_{R50}

[mm]) and 95% (Z_{R95} [mm]) of the root, and the maximum rooting depth $Z_{R,max}$ [mm]. The latter should always be less than the total soil depth. The total water that the root of a plant type has access to can be determined as $\theta_R = \sum_{i=1}^n r_i \theta_i$, where r_i and θ_i are the fraction of biomass and soil moisture content at the layer i , respectively.

In Equation 2.130, the vertical water fluxes can be calculated as

$$Q_{ver,i} = \bar{K}_{v,i} \left(1 + \frac{\Psi_{S,i} - \Psi_{S,i+1}}{d_{z,i+1}^c} \right), \quad (2.131)$$

where $\bar{K}_{v,i}$ [mm s^{-1}] is averaged vertical unsaturated hydraulic conductivity between two neighbor layers and $d_{z,i+1}^c$ [mm] is the central distance between two neighboring layers. The vertical water flux at the first and last layers enter the soil column at the surface in forms of infiltration and the water leaves the system as deep leakage, respectively. During extreme events, when precipitation is high or snow melts, the vertical water at the last layer may exceed the maximum capacity of the water table depth. In this case, the excess water is transported to the layers above and ultimately contributes to the saturation of soil layers and the surface runoff/runon.

The lateral water flux from soil column k to the soil column j at layer i can be calculated as

$$Q_{lat,i,k \rightarrow j}^{in} = a_r \left[\bar{K}_{v,i,k \rightarrow j} \frac{\Psi_{S,i,k} - \Psi_{S,i,j}}{d_y} \right] \left(\frac{d_{z,i}}{f_j w_{can}} \right), \quad (2.132)$$

where a_r [-] represents the anisotropy of hydraulic conductivity by dividing the horizontal to vertical hydraulic conductivity, $\bar{K}_{v,i,k \rightarrow j}$ [mm s^{-1}] is the average of vertical hydraulic conductivity of soil layer i in soil column k and j , d_y [mm] is a model constant that represents the length scale on which the difference between soil water content contributes to the lateral water flux, which is normalized by the width of soil column $f_j w_{can}$ [mm].

Chapter 3

Results and Discussion: VCWG v1.3.2

3.1 Model Configuration

VCWG v1.3.2 intends to integrate various submodels introduced in the previous chapter to create an integrated simulation platform capable of predicting urban climate and building energy performance variables. This version does not include the hydrologic model, cannot be forced from the top of the urban domain using mesoscale data products, and does not offer the opportunity to investigate simulation output variables on a spatial grid of the urban environment (see Figure 3.1). These additions will be discussed in the following chapter. The model can predict climate variables within a neighborhood scale at a maximum time step of 5 minutes. VCWG v1.3.2 consists of five integrated submodels

1. A rural model forces meteorological boundary conditions on VCWG v1.3.2 based on a surface energy balance model (Equation 2.1), used to calculate the surface heat fluxes and the soil temperature profile in the rural site, and the Monin-Obukhov similarity theory, used to compute friction velocity and vertical profiles of temperature and specific humidity in the atmospheric surface layer (Equations 2.15,2.12,2.17). The Bowen ratio is used to solve the surface energy balance model in rural areas. So, the sensible heat flux (Equation 2.4) is calculated using the formulation of Louis and latent heat flux is determined from the Bowen ratio in the rural area;
2. An urban one-dimensional vertical diffusion model is used to calculate the vertical profiles of cross- and along- canyon wind speed (Equations 2.91 and 2.92), potential temperature (Equation 2.103), specific humidity (Equation 2.109), and turbulence kinetic energy (Equation 2.100) in the urban area considering the effects of trees, buildings,

and building energy systems. The model is forced at the top of the domain by the rural model and at the levels within the canopy by surface energy balance;

3. A building energy model is used to calculate the building energy fluxes (Equation 2.111) and waste heat (Equation 2.107 and 2.108) released to the urban environment;
4. A radiation model with trees is used to compute the longwave (Equation 2.40) and shortwave (Equation 2.34) radiation fluxes between the urban canyon, trees, and the sky; and
5. An urban surface energy balance model is used to calculate surface heat fluxes, including sensible (Equation 2.43), latent (Equation 2.77), and conductive heat fluxes (Equations 2.78 and 2.79) for roofs, walls and streets. The only moisture source is tree foliage.

In this chapter, first, the VCWG v1.3.2 model results are evaluated against micro-climate field measurements. Next, the model performance is explored with various parametric simulations. A uniform Cartesian grid with 2 m vertical resolution is used. The boundary condition for potential temperature and specific humidity equations (Equations 2.103 and 2.109) are determined from the rural model. The flow is assumed to be pressure-driven with the pressure gradient of $\rho u_*^2 / H_{\text{top}}$ [$\text{kg m}^{-2} \text{s}^{-2}$], which is decomposed into the x and y directions based on the wind angle and canyon orientation. This pressure gradient is forced as source terms on the momentum Equations 2.91 and 2.92. Thus, the aim of VCWG v1.3.2 is to calculate momentum, temperature, specific humidity, and turbulence kinetic energy exchanges for the centre of each cell in the vertical direction based on the boundary conditions and source/sink terms obtained from the rural model, the building energy model, and the surface energy balance model applied to all urban surfaces (i.e., as fixed values, fluxes, or source/sink terms).

3.2 Evaluation

3.2.1 Observation and Forcing Datasets

To evaluate the model, VCWG's predictions are compared to observations from the Basel UrBan Boundary Layer Experiment (BUBBLE) [37, 170], which was conducted for eight months from December 2001 to July 2002. The urban micro-climate field measurements were

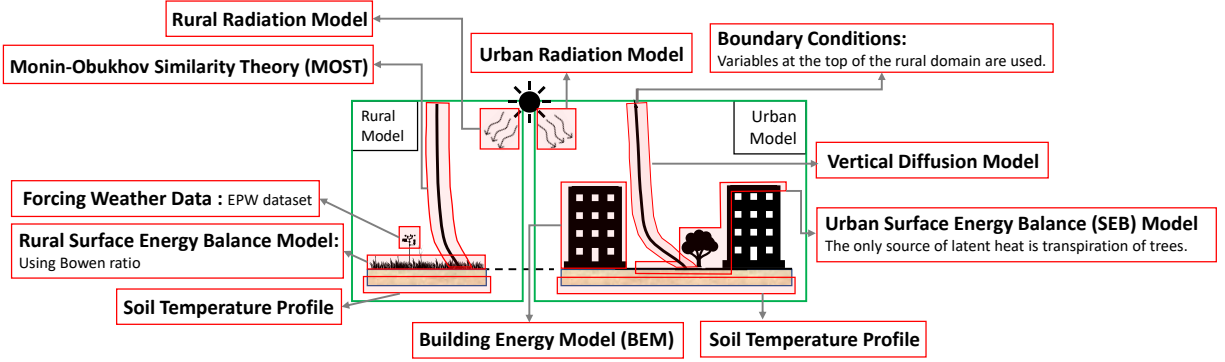


Figure 3.1: Overview of the Vertical City Weather Generator (VCWG) v1.3.2.

conducted in Basel, Switzerland, in a typical quasi two-dimensional urban canyon (47.55°N and 7.58°E). An EPW file is used to force the VCWG simulations with rural measurements. The rural measurements correspond to a site 7 km south-east of the city (47.53°N and 7.67°E). The average building height for the urban area is $H_{\text{avg}} = 14.6$ [m], and the plan area density is $\lambda_p = 0.54$ [-]. The urban canyon axis is oriented in the northeast-southwest direction with a canyon axis angle of $\theta_{\text{can}} = 65^\circ$. The x and y directions are set to be cross- and the along-canyon, respectively. The frontal area density is $\lambda_f = 0.37$ [-]. In BUBBLE, wind speed was measured at $z = 2.5, 13.9, 17.5, 21.5, 25.5,$ and 31.25 [m] a.g.l.; potential temperature was measured at $z = 3.6, 11.3, 14.7, 17.9, 22.4,$ and 31.7 [m] a.g.l.; and relative humidity was measured at $z = 2.5$ and 25.5 [m] a.g.l. The dataset provides the measurements averaged every 10 min. The model predictions of air temperature, wind speed, and specific humidity are compared to the observations on an hourly basis.

The input parameters representing the urban area are listed in Table 3.1. The input parameters are inferred from variables, datasets, and simulation codes in the literature that pertains to the BUBBLE campaign and associated models, as well as general assumptions found in the literature [26, 37, 55, 63, 75, 84, 129, 145, 165, 174, 210]. In this table, note that the choices of average building height $H_{\text{avg}} = 14.6$ [m], street width $w = 18.2$ [m], and building width to street width ratio $b/w = 1.1$ [-] provide $\lambda_p = b/(w + b) = 0.52$ [-] and $\lambda_f = H_{\text{avg}}/(w + b) = 0.38$ [-], which are remarkably close to morphometric variables reported by Christen and Vogt (2004) [37]. The simulations are conducted for eight months from December 2001 to July 2002. Usually, the first 24 hours of each month are treated as the model spin-up period. For analysis of each month, the simulation time is approximately 1

min, however, it can vary slightly depending on the grid spacing and time step.

3.2.2 Potential Temperature

To compare VCWG results with measured meteorological variables from the BUBBLE campaign, the BIAS, Root Mean Square Error (RMSE), and coefficient of determination R^2 are computed for pairs of model versus observed values every hour for available altitudes and months. This analysis is performed for wind speed, potential temperature, and specific humidity. Figure 3.2 and Table 3.2 show the scatter plots of the observed versus simulated values of potential temperature as well as the statistical metrics used for the comparison. Over all altitudes and months, on average, the BIAS, RMSE, and R^2 for potential temperature are 0.25 [K], 1.41 [K], and 0.82, respectively. These statistics are comparable to what has been reported in the literature for similar models that were compared against observations. For instance, Lauwaet et al. (2016) [106] reported BIAS, RMSE, and R^2 of 0.76 [K], 1.32 [K], and 0.88, respectively, near ground by comparing model and observation values in a summer. Meili et al. (2020) [129] reported BIAS, RMSE, and R^2 of -0.1 [K], 2.2 [K], and 0.98, respectively, near ground by comparing model and observation values in a full year. Mussetti et al. (2020) [145] reported BIAS, RMSE, and R^2 of 0.40 [K], 1.53 [K], and 0.95, respectively, near ground by comparing model and observation values in a summer. Ryu et al. (2016) [174] reported BIAS and RMSE of 0.67 [K] and 0.99 [K], respectively, near ground by comparing model and observation values in a summer. Bueno et al. (2012a) [26] reported average BIAS and RMSE of 0.6 [K] and 0.9 [K] near the ground for June 2002. For the same month, VCWG predicts the BIAS, RMSE, and R^2 of -0.1 [K], 0.72 [K], and 0.95, respectively, near the ground. This comparison reveals that the BIAS and RMSE are improved (reduced) compared to the predecessor UWG model.

Figure 3.3 shows the diurnal variation of the observed versus simulated values of potential temperature averaged for every hour of the day for the available months. The diurnal patterns in temperature reveal that the model has a similar skill in predicting the potential temperature at all hours in lower elevations ($z = 3.6$ to 14.7 [m]). This performance is comparable to other models that show a well-captured diurnal variation of potential temperature at low altitudes [26, 100, 129, 145]. However, the diurnal pattern in temperature can deviate between the model and observations at higher elevations ($z = 17.9$ to 31.7 [m]), especially during midday hours. This can be attributed to more complex flow patterns in the above-roof-level space due to heat advection, horizontal heterogeneity of the urban site,

Table 3.1: List of input parameters used in VCWG for model evaluation; input variables are extracted from assumptions, datasets, and simulation codes available in the literature [26, 37, 55, 63, 75, 84, 129, 145, 165, 174, 210].

Parameter	Source	Symbol	Value
Latitude [°N]	[37]	lat	47.55
Longitude [°E]	[37]	lon	7.58
Average buildings height [m]	[37]	H_{avg}	14.6
Width of canyon [m]	[37]	$w_x=w_y=w$	18.2
Building width to canyon width ratio [-]	[37]	$b_x/w_x=b_y/w_y=b/w$	1.1
Leaf Area Index [$\text{m}^2 \text{m}^{-2}$]	[55],[210],[145]	LAI	0-1
Tree height [m]	[174]	h_t	8
Tree crown radius [m]	[174]	r_t	2.5
Tree distance from wall [m]	[174]	d_t	3
Ground fractions of vegetation and impervious surface [-]	[174]	$f_{\text{veg}}, f_{\text{imp}}$	0,1
Roof fractions of vegetation and impervious surface [-]	[174]	$f_{\text{veg}}, f_{\text{imp}}$	0,1
Building type	[37], [26]	-	Mid rise apartment
Urban albedos (roof, ground, wall, vegetation) [-]	[26],[174]	$\alpha_R, \alpha_G, \alpha_W, \alpha_V$	0.15, 0.15, 0.15, 0.2
Urban emissivities (roof, ground, wall, vegetation) [-]	[26],[174]	$\varepsilon_R, \varepsilon_G, \varepsilon_W, \varepsilon_V$	0.95, 0.95, 0.95, 0.95
Rural overall albedo [-]	[26]	α_{rur}	0.2
Rural overall emissivity [-]	[26]	ε_{rur}	0.95
Rural aerodynamic roughness length [m]	[165],[26]	$z_{0,\text{rur}} = 0.1h_{\text{rur}}$	0.2
Rural roughness length for temperature [m]	[63],[129]	$z_{\Theta,\text{rur}} = 0.1z_{0,\text{rur}}$	0.02
Rural roughness length for specific humidity [m]	[84],[129]	$z_{Q,\text{rur}} = 0.1z_{0,\text{rur}}$	0.02
Rural zero displacement height [m]	[75]	$d_{\text{rur}} = 0.5h_{\text{rur}}$	1
Rural Bown ratio [-]	[37]	β_{rur}	0.9
Ground aerodynamic roughness length [m]	[26]	z_{0G}	0.02
Roof aerodynamic roughness length [m]	[26]	z_{0R}	0.02
Vertical resolution [m]	-	Δz	2
Time step [s]	-	Δt	60
Canyon axis orientation [°N]	[37]	θ_{can}	65
Urban boundary condition	-	-	Rural model
Urban surface energy balance model	-	-	EB

Table 3.2: BIAS [K], RMSE [K], and R^2 [-] for VCWG predictions of potential temperature against the BUBBLE observations for different altitudes and months.

Altitude z [m]	Statistic	Dec.	Jan.	Feb.	Mar.	Apr.	May	Jun.	Jul.	Average
3.6	BIAS [K]	0.35	0.16	0.58	0.25	0.78	0.81	-0.1	-0.25	0.32
	RMSE [K]	1.10	1.02	1.78	1.90	1.72	1.59	0.72	0.90	1.34
	R^2	0.97	0.70	0.80	0.72	0.62	0.89	0.95	0.88	0.82
11.3	BIAS [K]	0.11	-0.19	0.60	0.23	0.50	0.87	-0.22	-0.23	0.21
	RMSE [K]	1.07	1.17	1.7	1.84	1.59	1.34	0.79	0.96	1.31
	R^2	0.97	0.68	0.81	0.69	0.68	0.90	0.93	0.86	0.81
14.7	BIAS [K]	0.20	-0.22	0.70	0.34	0.57	1.03	-0.12	-0.16	0.29
	RMSE [K]	1.16	1.25	1.78	1.84	1.57	1.33	0.97	1.11	1.38
	R^2	0.96	0.66	0.81	0.70	0.71	0.89	0.92	0.87	0.82
17.9	BIAS [K]	0.26	-0.21	0.75	0.36	0.55	0.99	-0.35	-0.35	0.25
	RMSE [K]	1.19	1.27	1.82	1.85	1.54	1.30	1.14	1.31	1.43
	R^2	0.96	0.68	0.81	0.69	0.73	0.90	0.93	0.86	0.82
22.4	BIAS [K]	0.29	-0.22	0.77	0.38	0.56	0.99	-0.45	-0.42	0.24
	RMSE [K]	1.20	1.30	1.85	1.88	1.50	1.30	1.29	1.49	1.48
	R^2	0.96	0.68	0.81	0.68	0.74	0.90	0.93	0.86	0.82
31.7	BIAS [K]	0.28	-0.28	0.78	0.37	0.58	0.95	-0.64	-0.57	0.18
	RMSE [K]	1.17	1.35	1.87	1.90	1.52	1.31	1.43	1.69	1.53
	R^2	0.96	0.67	0.81	0.65	0.68	0.89	0.93	0.84	0.81
Average	BIAS [K]	0.25	-0.16	0.70	0.32	0.59	0.94	-0.31	-0.33	0.25
	RMSE [K]	1.15	1.23	1.8	1.87	1.57	1.36	1.06	1.24	1.41
	R^2	0.96	0.68	0.81	0.69	0.69	0.90	0.93	0.86	0.82

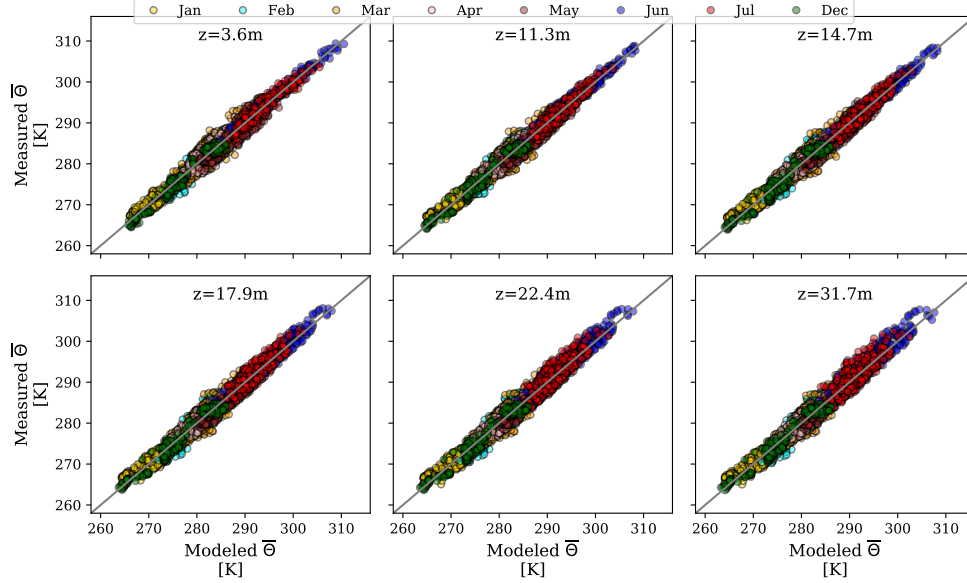


Figure 3.2: Scatter plots of observed (BUBBLE) versus simulated (VCWG) values of potential temperature for different altitudes and months; each data point corresponds to a 1-hour comparison between the model and observation.

and the above-roof-level shear layer.

3.2.3 Wind Speed

Figure 3.4 and Table 3.3 show the scatter plots of the observed versus simulated values of wind speed as well as the statistical metrics used for the comparison. Considering all altitudes and months, the average BIAS, RMSE, and R^2 are $0.67 \text{ [m s}^{-1}\text{]}$, $1.06 \text{ [m s}^{-1}\text{]}$, and 0.41 , respectively. Although the comparison reveals a reasonable BIAS and RMSE, the R^2 is lower than the values reported for comparisons of potential temperature and specific humidity. This can be explained by the fact that the urban morphology is highly heterogeneous, the measurement of wind is location specific, and that the wind speed and direction can change considerably within each hour. Heterogeneous urban morphology results in the great spatial variability of the components of wind velocity vector as a function of wind direction and wind speed [2, 92, 93]. On the other hand, forced by hourly rural measurements, VCWG assumes a regular urban morphology and predicts the volume-averaged horizontal wind velocity components. So it is expected to obtain lower R^2 values. Other models also often report lower R^2 values for wind speed compared to potential temperature and spe-

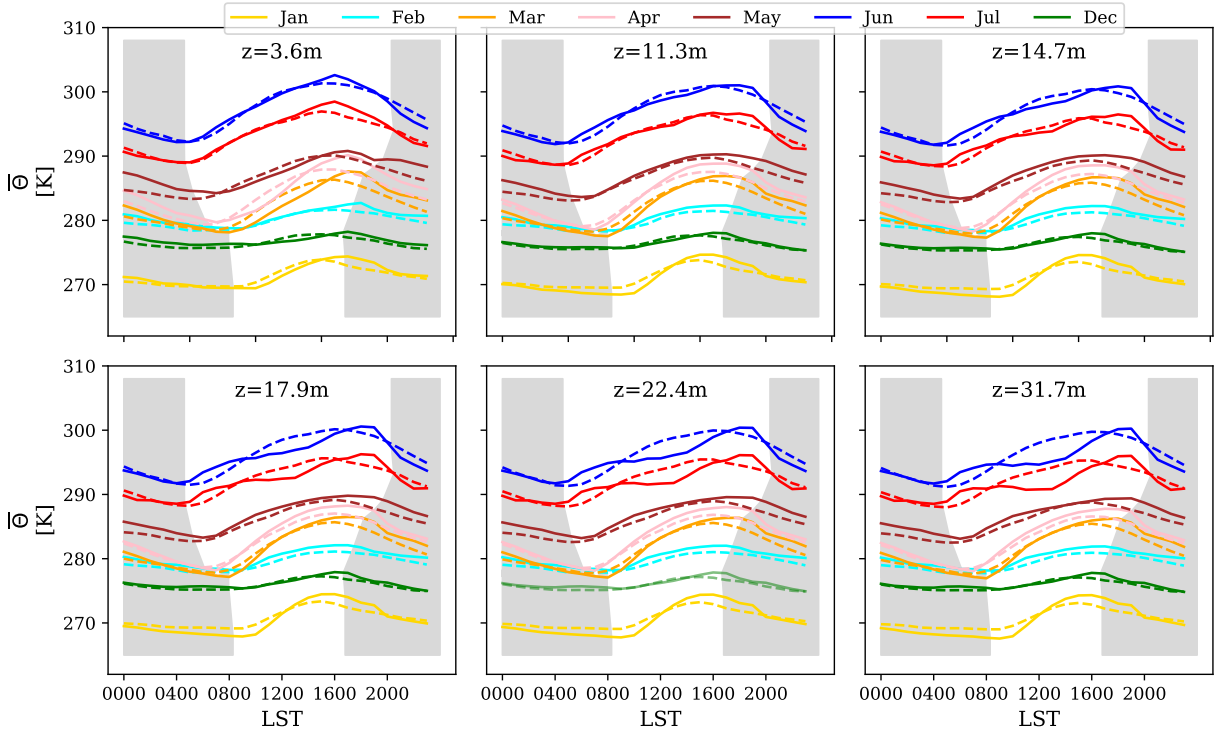


Figure 3.3: Comparison between the observed (BUBBLE) versus simulated (VCWG) values of potential temperature; the hourly means are shown; nighttime indicated with shaded regions; solid line: model and dashed line: observation; times in Local Standard Time (LST).

cific humidity [145]. Overall our BIAS, RMSE, and R^2 values are in agreement with values reported in the literature. For instance, Lemonsu et al. (2012) [109] reported a range in BIAS of -0.16 to 0.56 [m s^{-1}]. They also reported a range in RMSE of 0.40 to 0.69 [m s^{-1}]. Mussetti et al. (2020) [145] reported the BIAS, RMSE, and R^2 of 0.61 [m s^{-1}], 1.31 [m s^{-1}], and 0.70 , respectively.

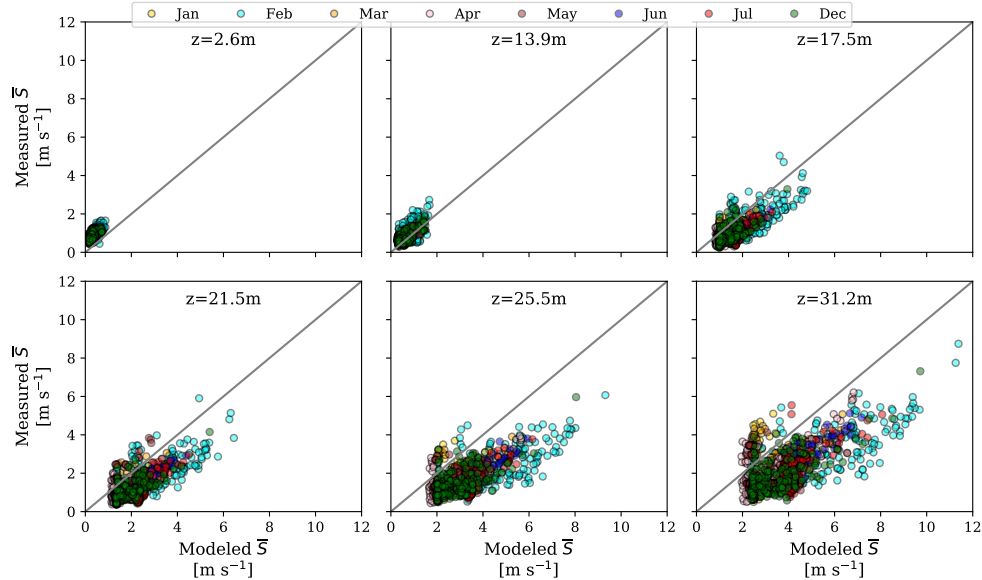


Figure 3.4: Scatter plots of observed (BUBBLE) versus simulated (VCWG) values of wind speed for different altitudes and months; each data point corresponds to a 1-hour comparison between the model and observation.

3.2.4 Specific Humidity

Figure 3.5 and Table 3.4 show the scatter plots of the observed versus simulated values of specific humidity as well as the statistical metrics used for the comparison, respectively. Note that specific humidity data were only available in June-July 2002. Over all altitudes and the available months, on average, the BIAS, RMSE, and R^2 for specific humidity are 0.00057 [kg kg^{-1}], 0.0010 [kg kg^{-1}], and 0.85 , respectively. These statistics are comparable to what has been reported in the literature for similar models that were compared against observations. For instance, Mussetti et al. (2020) [145] reported BIAS, RMSE, and R^2 of -0.00109 [kg kg^{-1}], 0.00152 [kg kg^{-1}], and 0.74 , respectively, above the urban canopy for comparisons of model and observations in summer. Lemonsu et al. (2012) [109] reported a range in BIAS of

Table 3.3: BIAS [m s^{-1}], RMSE [m s^{-1}], and R^2 [-] for VCWG predictions of wind speed against the BUBBLE observations for different altitudes and months.

Altitude z [m]	Statistic	Dec.	Jan.	Feb.	Mar.	Apr.	May	Jun.	Jul.	Average
2.6	BIAS [m s^{-1}]	-0.5	-0.6	-0.59	-0.49	-0.59	-0.40	-0.51	-0.49	-0.52
	RMSE [m s^{-1}]	0.41	0.49	0.46	0.41	0.47	0.33	0.40	0.40	0.42
	R^2	0.55	0.19	0.59	0.47	0.32	0.07	0.43	0.34	0.37
13.9	BIAS [m s^{-1}]	-0.24	-0.35	-0.43	-0.24	-0.28	-0.38	-0.17	-0.18	-0.28
	RMSE [m s^{-1}]	0.22	0.27	0.38	0.21	0.23	0.35	0.18	0.18	0.25
	R^2	0.55	0.26	0.44	0.5	0.43	0.39	0.29	0.35	0.4
17.5	BIAS [m s^{-1}]	0.69	0.43	0.83	0.55	0.54	0.48	0.88	0.87	0.66
	RMSE [m s^{-1}]	0.53	0.36	0.74	0.46	0.47	0.37	0.74	0.79	0.56
	R^2	0.5	0.29	0.56	0.56	0.47	0.08	0.43	0.48	0.42
21.5	BIAS [m s^{-1}]	0.99	0.65	1.27	0.73	0.72	0.73	1.13	1.15	0.92
	RMSE [m s^{-1}]	0.73	0.56	1.00	0.64	0.63	0.67	0.97	1.08	0.79
	R^2	0.56	0.30	0.52	0.58	0.4	0.21	0.43	0.51	0.44
25.5	BIAS [m s^{-1}]	1.7	0.94	2.3	1.2	1.25	1.23	1.96	1.93	1.56
	RMSE [m s^{-1}]	1.27	0.82	1.83	0.97	0.99	1.03	1.67	1.69	1.29
	R^2	0.51	0.38	0.54	0.52	0.50	0.28	0.4	0.46	0.45
31.2	BIAS [m s^{-1}]	1.96	0.98	2.63	1.24	1.24	1.39	2.10	2.08	1.70
	RMSE [m s^{-1}]	1.50	0.95	2.11	1.18	1.09	1.30	1.78	1.85	1.47
	R^2	0.47	0.14	0.58	0.49	0.41	0.17	0.51	0.47	0.41
Average	BIAS [m s^{-1}]	0.77	0.34	1.00	0.50	0.48	0.51	0.90	0.89	0.67
	RMSE [m s^{-1}]	0.78	0.58	1.09	0.64	0.65	0.68	0.96	1.00	1.06
	R^2	0.52	0.26	0.54	0.52	0.42	0.20	0.42	0.43	0.41

Table 3.4: BIAS [kg kg^{-1}], RMSE [kg kg^{-1}], and R^2 [-] for VCWG predictions of specific humidity against the BUBBLE observations for different altitudes and months.

Altitude z [m]	Statistic	Jun.	Jul.	Average
2.5	BIAS [kg kg^{-1}]	0.00081	0.00056	0.00069
	RMSE [kg kg^{-1}]	0.0012	0.00086	0.0010
	R^2	0.86	0.84	0.85
25.5	BIAS [kg kg^{-1}]	0.00049	0.00042	0.00045
	RMSE [kg kg^{-1}]	0.0014	0.00074	0.0010
	R^2	0.84	0.86	0.85
Average	BIAS [kg kg^{-1}]	0.00065	0.00049	0.00057
	RMSE [kg kg^{-1}]	0.0013	0.0008	0.0010
	R^2	0.85	0.85	0.85

-0.00116 to -0.0005 [kg kg^{-1}]. They also reported a range in RMSE of 0.00081 to 0.00172 [kg kg^{-1}].

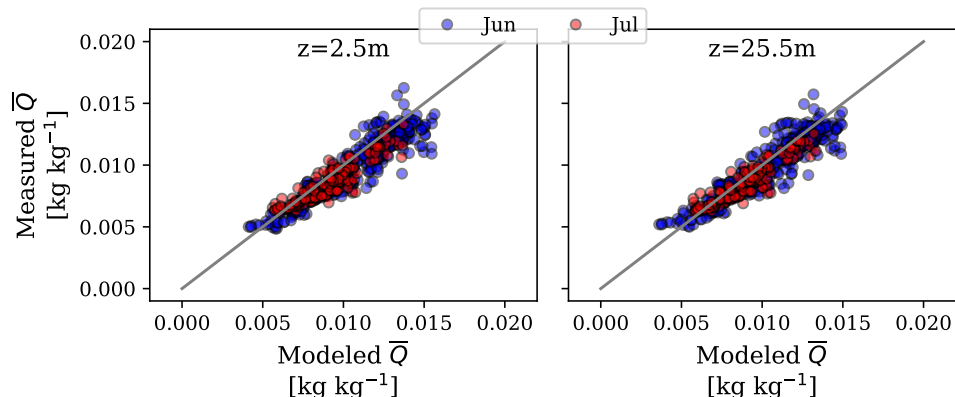


Figure 3.5: Scatter plots of observed (BUBBLE) versus simulated (VCWG) values of specific humidity for different altitudes and months; each data point corresponds to a 1-hour comparison between the model and observation.

Figure 3.6 shows the diurnal variation of the observed versus simulated values of specific humidity averaged for every hour of the day for June-July 2002. While the diurnal variation is predicted by the model, some deviations are noted between the model and the observation. The model overpredicts the values at night, while it underpredicts the values during mid day, especially at $z = 25.5$ [m]. This could be due to the assumptions of the rural model to generate the vertical profile of specific humidity. In this model, the latent heat flux in the rural area is parameterized as a function of the sensible heat flux and a fixed Bowen ratio.

However, the Bowen ratio can vary diurnally [86]. This can result in a slight miscalculation of the latent heat flux and a forcing boundary condition for specific humidity on top of the modeling domain.

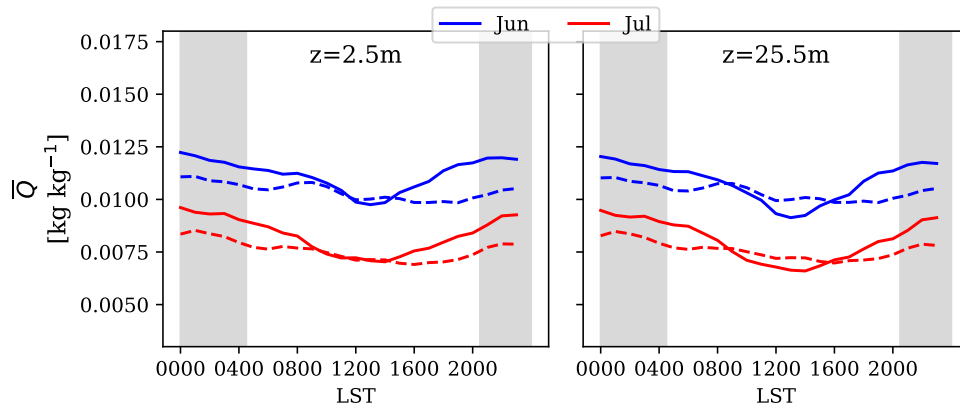


Figure 3.6: Comparison between the observed (BUBBLE) versus simulated (VCWG) values of specific humidity; the hourly means are shown; nighttime indicated with shaded regions; solid line: model and dashed line: observation; times in Local Standard Time (LST).

3.2.5 Urban Heat Island (UHI)

To compare VCWG results with measured UHI [K] from the BUBBLE campaign, the BIAS, RMSE, and R^2 are computed for pairs of hourly models versus observed values for the available months. UHI [K] for the observation is computed by considering the difference between the temperature measurements inside the canyon at $z = 3.6$ [m] and those temperatures provided by the EPW dataset. For VCWG, UHI [K] is calculated by considering the difference between the temperature prediction inside the canyon at $z = 3$ [m] and those temperatures provided by the EPW dataset. Figure 3.7 and Table 3.5 show the diurnal variation of UHI (for both observations and simulations) as well as the statistical metrics used for the comparison. On average, the BIAS, RMSE, and R^2 for UHI [K] are 0.36 [K], 1.2 [K], and 0.35, respectively. VCWG predictions of UHI [K] are more successful for the months of December, January, April, May, June, and July ($R^2 > 0.3$) than for months of February and March ($R^2 < 0.2$). The deviations in predicting UHI [K] may be attributed to several factors. The heterogeneity of the urban environment and placement of urban sensors may result in sensing slightly warmer or colder temperatures than the spatial average due to the spatial

Table 3.5: BIAS [K], RMSE [K], and R^2 [-] for VCWG predictions of UHI [K] against the BUBBLE observations for different months.

Statistic	Dec.	Jan.	Feb.	Mar.	Apr.	May	Jun.	Jul.	Average
BIAS [K]	0.35	0.16	0.58	0.25	0.78	0.81	-0.1	0.06	0.36
RMSE [K]	1.04	0.92	1.63	1.72	1.48	1.42	0.66	0.57	1.2
R^2	0.32	0.37	0.16	0.12	0.50	0.51	0.37	0.47	0.35

variability of temperature [145]. Also, the relative position of the rural site with respect to the urban site, variation of dominant wind directions over different seasons, and horizontal advective transport of heat from the rural area may confound the prediction of UHI. Given that VCWG does not consider all such variations due to simplifying assumptions, it is expected to predict different values of UHI [K] over different seasons in comparison to the observations. Nevertheless, overall, the statistics of the UHI [K] comparison are in reasonable agreement with those reported by other models. For example, Mussetti et al. (2020) [145] reported BIAS, RMSE, and R^2 values of -1.88 [K], 1.66 [K], and 0.55 , respectively, for near-ground predictions of UHI [K] in the summer.

3.3 Exploration

3.3.1 Forcing Datasets

The VCWG performance is assessed by evaluating the model performance as a function of the urban configurations (λ_p [-], λ_f [-], LAD [$\text{m}^2 \text{m}^{-3}$]), building energy configuration (building type, thermal efficiency, coefficient of performance, location of building waste heat release), radiation configuration (canyon aspect ratio and axis angle), different seasons, and different climate zones. Except for the analysis of different seasons and climate zones, all explorations are performed by VCWG simulations of the urban micro-climate in Basel, Switzerland, for two weeks starting 15 June 2002, concurrent with the BUBBLE campaign. For analysis of different seasons, simulation results of VCWG are provided for Vancouver for an entire year in a period in the early 2000s. For different climate zones, VCWG simulations are conducted for other cities for a two-week period during the summer season. More details on the explorations are provided in the subsequent sections. Such analyses will provide more information on spatio-temporal variation of the atmospheric meteorological variables and reveal the complexity of urban micro-climate modeling. Additionally, the potential and limitations of VCWG will be discussed.

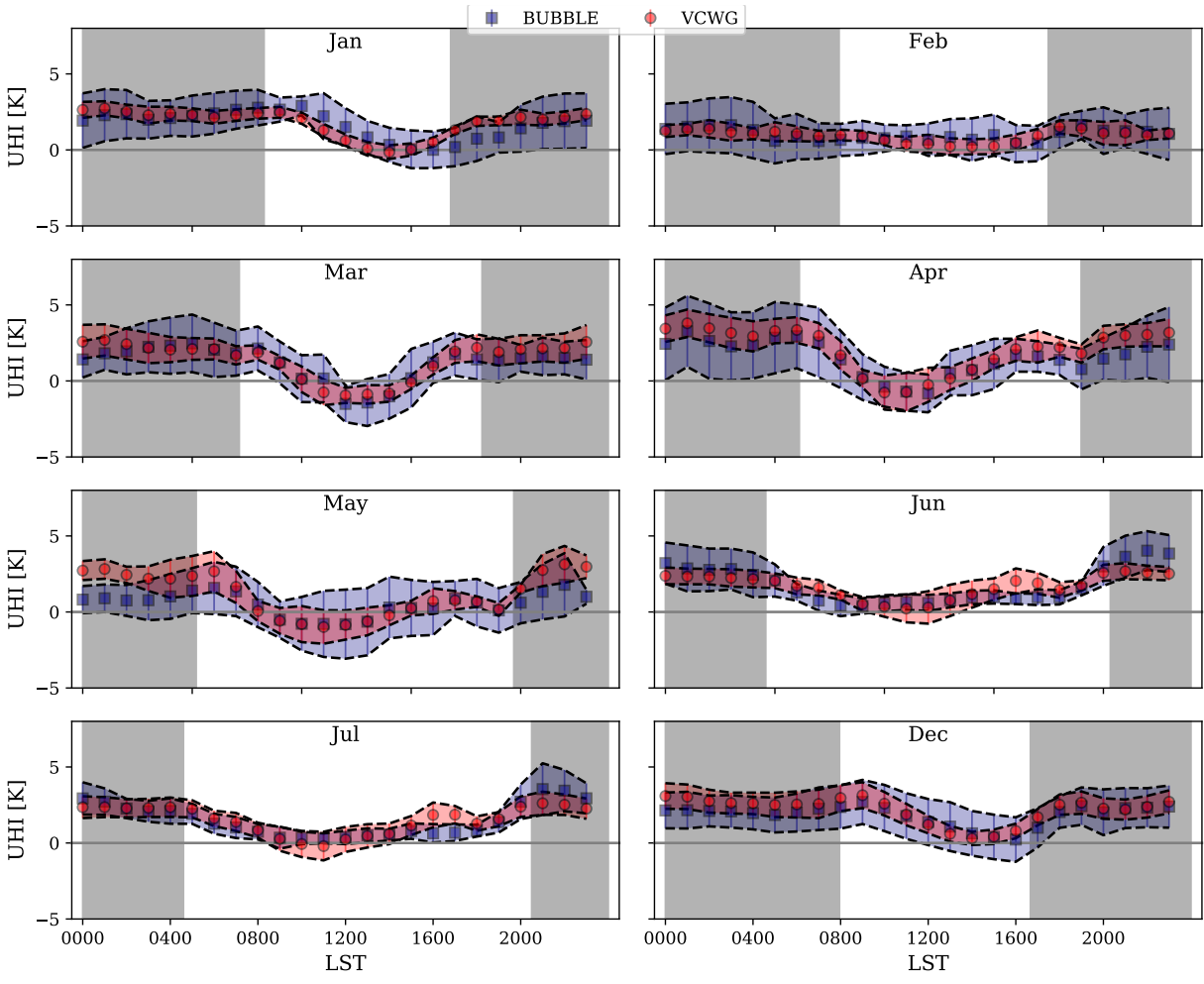


Figure 3.7: Hourly mean and standard deviation (band) of UHI [K] in each month for the observed (BUBBLE) and predicted (VCWG) values; nighttime indicated with shaded regions; times in Local Standard Time (LST).

3.3.2 Urban Plan and Frontal Area Densities

In urban canopy modeling, two parameters often used to describe building and canyon geometries are plan area density λ_p [-], which is the ratio of the total plan area of the buildings to the total urban flat-earth surface area, and the frontal area density λ_f [-], which is the ratio of the total frontal area (facing wind) to the total urban flat-earth surface area. An urban area can be characterized by different types of land use, where each type may have a different plan and frontal area densities varying from high values in industrial and commercial districts to low values associated with the land used for public transportation [205]. Most development in an urban area could be associated with changing λ_p [-] and λ_f [-], which can alter the local climate in different ways, such as air and surface temperatures, building energy consumption, and thermal and wind comfort levels [44, 50].

Two case studies $\lambda_p = 0.46$ and 0.54 [-] (associated with canyon widths of 25 and 18.2 m) are explored to assess the model and see how the urban micro-climate changes when the plan area density decreases. Here, except for canyon width, all other model input parameters are kept the same as the evaluation simulations. Figure 3.8 shows typical nighttime and daytime profiles of potential temperature, horizontal wind speed, specific humidity, and turbulence kinetic energy in the urban area associated with model simulations for two weeks corresponding to the BUBBLE field campaign. In this case, higher λ_p [-] is associated with more shading and, therefore, lower potential temperatures during the day. During the nighttime, the temperature difference between the cases is not as much as in the daytime. However, still slightly higher temperatures can be obtained when plan area density is higher. Additionally, more urban surfaces by higher λ_p [-] impose more drag and consequently reduce wind speed and turbulence kinetic energy during both daytime and nighttime, which can also be depicted in Fig. 3.8. No change in specific humidity is noted in this exploration.

Further investigations are performed for different frontal area densities $\lambda_f = 0.37$ and 0.51 [-] (associated with building heights 14.6 and 20 m) by model simulations for two weeks associated with the BUBBLE field campaign. Here, except for building height, all other model input parameters are kept the same as the evaluation simulations. At first glance, the cities with high-rise buildings are supposed to release more heat into the outdoor environment due to greater urban surfaces, but tall buildings can provide solar shading during the daytime and decrease the temperature of the surfaces. As shown in Fig. 3.9, an increase in λ_f [-] reduces the potential temperature in the urban area during the day. However, due to the lack of shortwave radiation during nighttime and the fact that urban surfaces are the main source of heat that can be released into the atmosphere, higher λ_f [-] results in higher potential

temperatures at nighttime because of longwave radiation trapping. Moreover, increasing frontal area density tends to increase surface roughness and consequently slow down wind speed and reduce the turbulence kinetic energy within the canyon during both daytime and nighttime, which can also be depicted in Fig. 3.9. No change in specific humidity is noted in this exploration. Note that skin drag is mostly related to roof level drag, which is less in magnitude compared to form drag caused by the building walls. This hypothesis can be confirmed using this exploration study. When λ_p is changed, it is noticed that wind speed profiles respond to a lesser extent compared to when λ_f is changed. The VCWG results are also consistent with previous studies in the literature [44, 181, 212]. The findings reported here highlight the careful considerations that need to be accounted for by city planners.

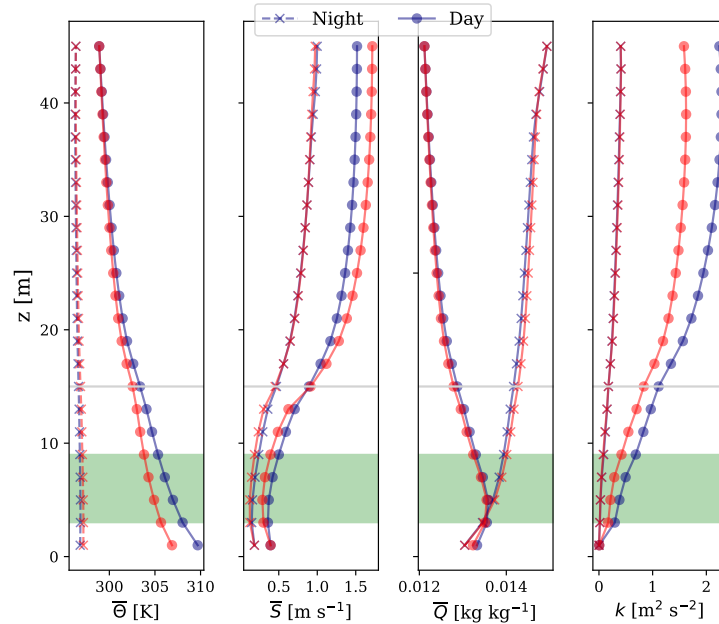


Figure 3.8: Effect of plan area density λ_p [-] on the profiles of potential temperature, horizontal wind speed, specific humidity, and turbulence kinetic energy during nighttime (averaged from 0000 to 0400 LST) and daytime (averaged from 1200 to 1600 LST); red: $\lambda_p = 0.54$ [-], blue: $\lambda_p = 0.46$ [-]; tree crown with non-zero LAD [$\text{m}^2 \text{m}^{-3}$] shown in shaded green; building height shown with grey line; times in Local Standard Time (LST).

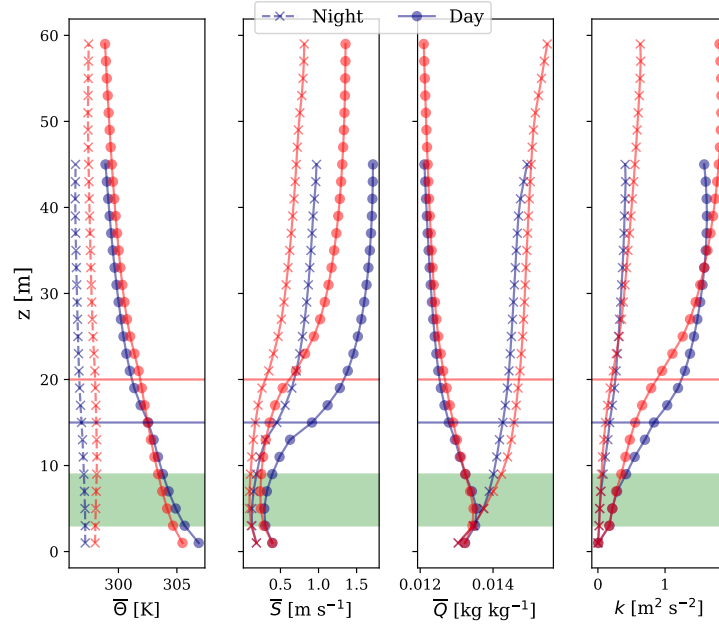


Figure 3.9: Effect of frontal area density $\lambda_f[-]$ on the profiles of potential temperature, horizontal wind speed, specific humidity, and turbulence kinetic energy during nighttime (averaged from 0000 to 0400 LST) and daytime (averaged from 1200 to 1600 LST); red: $\lambda_f = 0.51$ [-], blue: $\lambda_f = 0.37$ [-]; tree crown with non-zero LAD [$\text{m}^2 \text{m}^{-3}$] shown in shaded green; building heights shown with red and blue lines; times in Local Standard Time (LST).

3.3.3 Leaf Area Density

Urban trees interact with the other urban elements by providing shade to reduce the temperature of surfaces, removing the stored heat in the canyon substantially, and induce drag to reduce wind speed [101, 112, 167]. The capability of VCWG to take into account these effects is assessed by investigating two case studies with LAD [$\text{m}^2 \text{m}^{-3}$] representing trees with canyon-average foliage densities of 0.1 and 0.2 [$\text{m}^2 \text{m}^{-3}$], respectively, by model simulations for two weeks associated with the BUBBLE field campaign. Here, except for LAD [$\text{m}^2 \text{m}^{-3}$], all other model input parameters are kept the same as the evaluation simulations. The result is shown in Fig. 3.10. The cooling effect of the trees is evident when the average LAD [$\text{m}^2 \text{m}^{-3}$] of tree foliage increases, resulting in a decrease of potential temperature within the canyon, particularly during the day when the shading effect of trees lowers the surface temperatures and the evapotranspiration of trees lowers the air temperature. Such effects not only can improve thermal comfort at the pedestrian level, but also can reduce the building energy consumption in the summertime [5, 186]. On the other hand, the urban trees are thought to be a sink of momentum and turbulence kinetic energy by exerting drag and damping the flow fluctuations [65, 211]. This effect can also be modeled by VCWG, which predicts slightly lower level of wind speed within the canyon with increasing LAD [$\text{m}^2 \text{m}^{-3}$]. Increasing LAD [$\text{m}^2 \text{m}^{-3}$] reduces the turbulence kinetic energy, possibly due to the combined effects of reducing wind speed, LAD [$\text{m}^2 \text{m}^{-3}$], and the drag coefficient for tree foliage C_{DV} [-], influencing the wake production term S_{wake} [$\text{m}^2 \text{s}^{-3}$] [98]. Increasing LAD [$\text{m}^2 \text{m}^{-3}$], however, results in higher levels of specific humidity due to higher evapotranspiration of trees during the daytime. The analysis obtained from this exploration is in reasonable agreement with previous works [65, 112, 186, 211]. Trees are recognized to be essential urban elements to moderate extreme wind speeds and heat waves, particularly during the warm season.

3.3.4 Building Energy Configuration

The building energy model within VCWG is explored by VCWG simulations under different building types, cooling system Coefficient Of Performance (COP) [-], heating system thermal efficiency η_{heat} [-], and location of the release of building waste heat F_{st} [-]. Two building types are considered, the mid-rise apartment and a hospital, with specifications provided in Table 3.6. It can be noted that the infiltration rate, ventilation rate, volumetric flow for water heating, and waste heat fluxes associated with gas combustion, electricity consumption, and

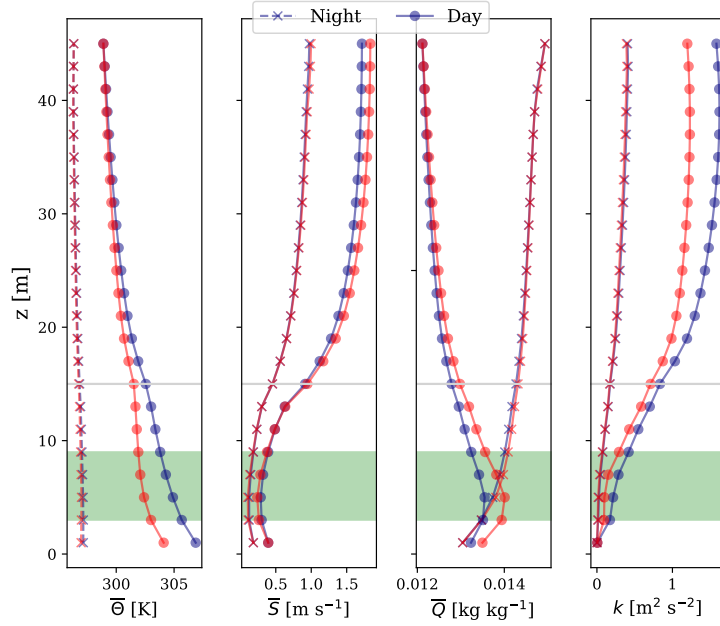


Figure 3.10: Effect of leaf area density profiles LAD [$\text{m}^2 \text{ m}^{-3}$] on the profiles of potential temperature, horizontal wind speed, specific humidity, and turbulence kinetic energy during nighttime (averaged from 0000 to 0400 LST) and daytime (averaged from 1200 to 1600 LST); red: $LAD = 0.2$ [$\text{m}^2 \text{ m}^{-3}$], blue: $LAD = 0.1$ [$\text{m}^2 \text{ m}^{-3}$]; tree crown with non-zero LAD [$\text{m}^2 \text{ m}^{-3}$] shown in shaded green; building height shown with a grey line; times in Local Standard Time (LST).

Table 3.6: Specifications of the building energy configuration for two building types; values extracted from the Urban Weather Generator (UWG) model [26]; the infiltration is expressed as Air Changes per Hour (ACH [-]).

Building type → Building specification ↓	Mid-rise apartment	Hospital
COP [-]	3.13	5.2
η_{heat} [-]	0.8	0.8
Infiltration (ACH [-])	0.64	0.22
Ventilation [$L s^{-1} m^{-2}$]	0.45	1.8
Average waste heat flux from gas combustion [$W m^{-2}$]	0	13
Average waste heat flux from electricity consumption [$W m^{-2}$]	5	17
Average waste heat flux from lighting [$W m^{-2}$]	5	22

lighting for a hospital are substantially greater than those for a mid-rise apartment. Note that construction material properties are also different among different building types, which are specified in VCWG schedules. Two sets of COP [-] and η_{heat} [-] are considered for a mid-rise apartment. For an energy-efficient building default values $COP = 3.13$ [-] and $\eta_{\text{heat}} = 0.8$ [-] are used, while for a low-energy-efficient building values $COP = 1$ [-] and $\eta_{\text{heat}} = 0.4$ [-] are used. Note that these values for a low-energy efficient building are below permitted building code values in the U.S., but these values are chosen to amplify the effects on urban climate variables predicted by VCWG for clarity. For the location of the release of building waste heat, three conditions are assumed: all waste heat is released at street level ($F_{\text{st}} = 1$); half of the waste heat is released at street level ($F_{\text{st}} = 0.5$); and all waste heat is released at roof level ($F_{\text{st}} = 0$). In these simulations, except for building type, COP [-], η_{heat} [-], and F_{st} [-], all other model input parameters are kept the same as the evaluation simulations.

Figure 3.11 shows the effect of building type on hourly mean and standard deviation of cooling/heating waste heat, dehumidification waste heat, gas combustion waste heat, water heating waste heat, and UHI [K] calculated for model simulations for two weeks. The waste heat fluxes are reported per unit building footprint area. It can be noted that the building energy system operates under heating mode for a few hours before sunrise, while it runs under cooling mode for the majority of the daytime period. It can be noted that a hospital results in higher values of waste heat and UHI [K], so the potential impact of an energy-intensive hospital on the urban climate may be higher than a mid-rise apartment.

Figure 3.12 shows the effect of COP [-] and η_{heat} [-] on hourly mean and standard deviation of waste heats and UHI [K] calculated for model simulations for two weeks. It can be noted that lower COP [-] and η_{heat} [-] result in higher values of waste heats and slightly

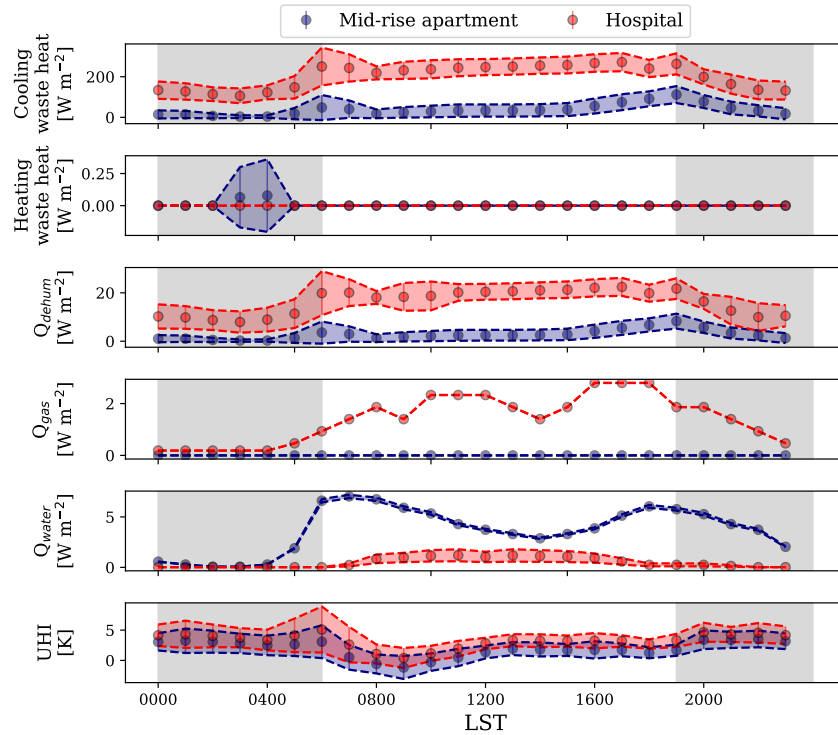


Figure 3.11: Effect of building type on cooling/heating waste heat, dehumidification waste heat, gas combustion waste heat, water heating waste heat, and UHI [K]; diurnal variation of mean and standard variation (band) are shown using data obtained over a two-week period; nighttime is shown with shaded regions; times in Local Standard Time (LST).

higher UHI [K], so the potential impact of an energy-intensive building on the urban climate may be higher than an energy-efficient building. Most particularly, it can be noted that lower heating system thermal efficiency results in greater waste heat flux for water heating.

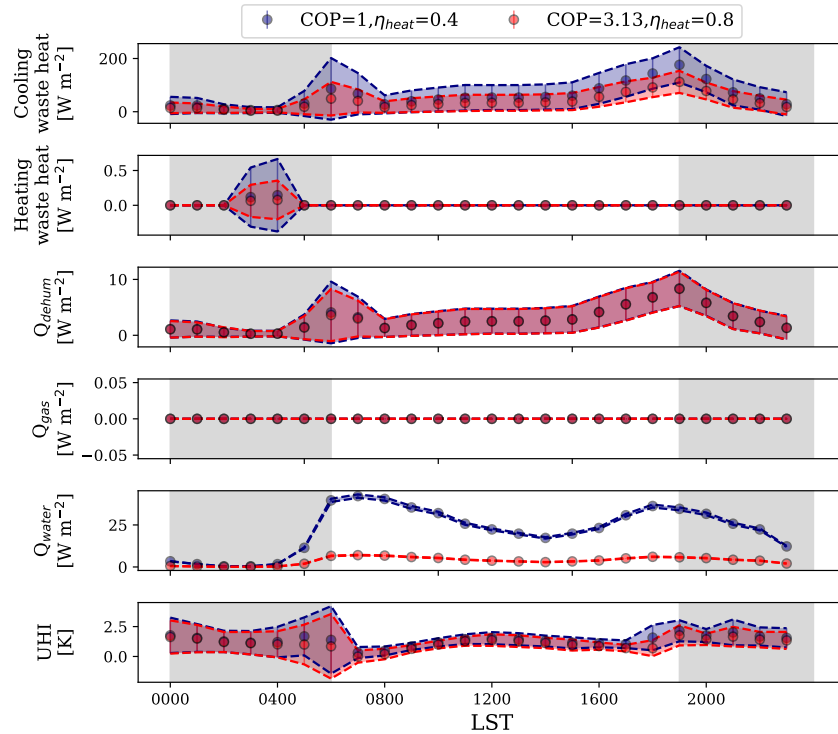


Figure 3.12: Effect of building cooling system Coefficient Of Performance (COP [-]) and heating system thermal efficiency (η_{heat} [-]) on cooling/heating waste heat, dehumidification waste heat, gas combustion waste heat, water heating waste heat, and UHI [K]; diurnal variation of mean and standard variation (band) are shown using data obtained over a two-week period; nighttime is shown with shaded regions; times in Local Standard Time (LST).

Figure 3.13 shows the effect of F_{st} [-] on hourly mean and standard deviation of UHI [K] calculated for model simulations for two weeks. The figure considers cases where all waste heat is released at the street level ($F_{st} = 1$), half of the waste heat is released at street level, and the other half of waste heat is released at roof level ($F_{st} = 0.5$), and all waste heat is released at roof level ($F_{st} = 0$). According to this analysis, on average, the UHI [K] value for the case with $F_{st} = 1$, is higher by 1 [K] than the case with $F_{st} = 0$. This can be attributed to a more effective mechanism to diffuse the waste heat upward due to higher wind speed and turbulence kinetic energy when this heat is released above roof level compared to when

it is released near street level. Depending on the urban configuration and amount of urban vegetation, the location of waste heat release could affect UHI by even higher magnitudes.

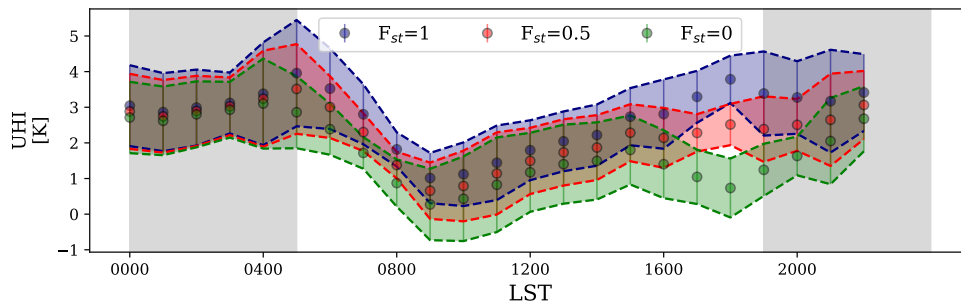


Figure 3.13: Effect of the location of waste heat release on UHI [K]; diurnal variation of mean and standard deviation (band) are shown using data obtained over a two-week period; nighttime is shown with shaded regions; times in Local Standard Time (LST); blue: all waste heat released at street level ($F_{st} = 1$); red: half of the waste heat released at street level ($F_{st} = 0.5$); green: all waste heat released at roof level ($F_{st} = 0$).

3.3.5 Radiation Configuration

The radiation model within VCWG is explored by VCWG simulations under different canyon aspect ratios H_{avg}/w [-] and different street canyon axis angles θ_{can} [$^{\circ}$] with respect to the north axis to investigate the effects on shortwave and longwave fluxes. For exploring the effect of canyon aspect ratio on these fluxes, values of $H_{avg}/w = 0.8$ and 1.6 [-] are used while keeping $\theta_{can} = 0^{\circ}$, while for exploring the effect of street canyon axis angle on these fluxes, values of $\theta_{can} = 0$ and 90° with respect to the north axis are used with keeping $H_{avg}/w = 0.8$ [-]. For these explorations, VCWG simulations are conducted for two weeks, and hourly mean values for radiative fluxes are reported. Here, except for H_{avg}/w [-] and θ_{can} [$^{\circ}$], all other model input parameters are kept the same as the evaluation simulations.

Figure 3.14 shows the shortwave S [$W\ m^{-2}$] and longwave L [$W\ m^{-2}$] radiative fluxes for different canyon aspect ratios. It can be seen that the net shortwave radiation flux, i.e. incoming S^{\downarrow} [$W\ m^{-2}$] minus outgoing S^{\uparrow} [$W\ m^{-2}$] fluxes, by the roof is not affected by the canyon aspect ratio, while the interior surfaces of the urban canyon absorb lower amounts of shortwave radiation fluxes for the higher canyon aspect ratio. This is expected since a higher canyon aspect ratio creates more shading effects on interior canyon surfaces compared to a lower canyon aspect ratio. Focusing on the net shortwave radiation fluxes on the road and

tree, it is noted that for the higher aspect ratio canyon, the fluxes are more pronounced near noon Local Standard Time (LST), while for the lower aspect ratio canyon, the fluxes are pronounced in more hours before and after noon LST. This is expected since a higher aspect ratio canyon creates more shading effects on times before and after noon LST compared to a lower aspect ratio canyon. Focusing on the net longwave radiation fluxes, i.e., incoming L^\downarrow [W m^{-2}] minus outgoing L^\uparrow [W m^{-2}] fluxes, it is noted that the roof is not affected by the canyon aspect ratio, while the road and wall surfaces of the urban canyon lose lesser amounts of longwave radiation for the higher canyon aspect ratio, both during nighttime and daytime. This can be understood as higher longwave radiation trapping by the higher canyon aspect ratio. For trees, it can be seen that during daytime, there can be a net longwave radiation gain (as opposed to loss) due to lower vegetation temperatures compared to the surrounding surfaces.

Figure 3.15 shows the radiative fluxes for different street canyon axis angles. It can be seen that the shortwave radiation flux absorbed by the roof is not affected by the street canyon axis angle, while the interior surfaces of the urban canyon show different responses to absorbing the shortwave radiation flux given the street canyon axis angle. With $\theta_{\text{can}} = 90^\circ$ the road surface absorbs the shortwave radiation flux over more hours during the day, given that the combined direct and diffuse shortwave fluxes reach the road surface at both low and high solar zenith and azimuth angles from the east and west directions. On the other hand, with $\theta_{\text{can}} = 0^\circ$ the road surface absorbs the shortwave radiation flux in hours around noon LST, given that this flux reaches the road surface effectively only at low solar zenith and azimuth angles from the north direction. With $\theta_{\text{can}} = 90^\circ$ the wall surface absorbs the shortwave radiation flux in most hours during midday, given that this flux reaches the wall surface with multiple combinations of solar zenith and azimuth angles. On the other hand, with $\theta_{\text{can}} = 0^\circ$ the wall surface absorbs little shortwave radiation flux in hours around noon LST, given that this flux does not reach the wall surface when the solar azimuth angle is from the north direction. Focusing on the net longwave radiation flux components, the road exhibits a net longwave radiation loss over more prolonged hours of daytime when $\theta_{\text{can}} = 90^\circ$. The walls exhibit a higher net longwave radiation loss during daytime when $\theta_{\text{can}} = 0^\circ$. For trees, again, it can be seen that during the daytime, there can be a net longwave radiation gain (as opposed to loss) due to lower vegetation temperatures compared to the surrounding surfaces.

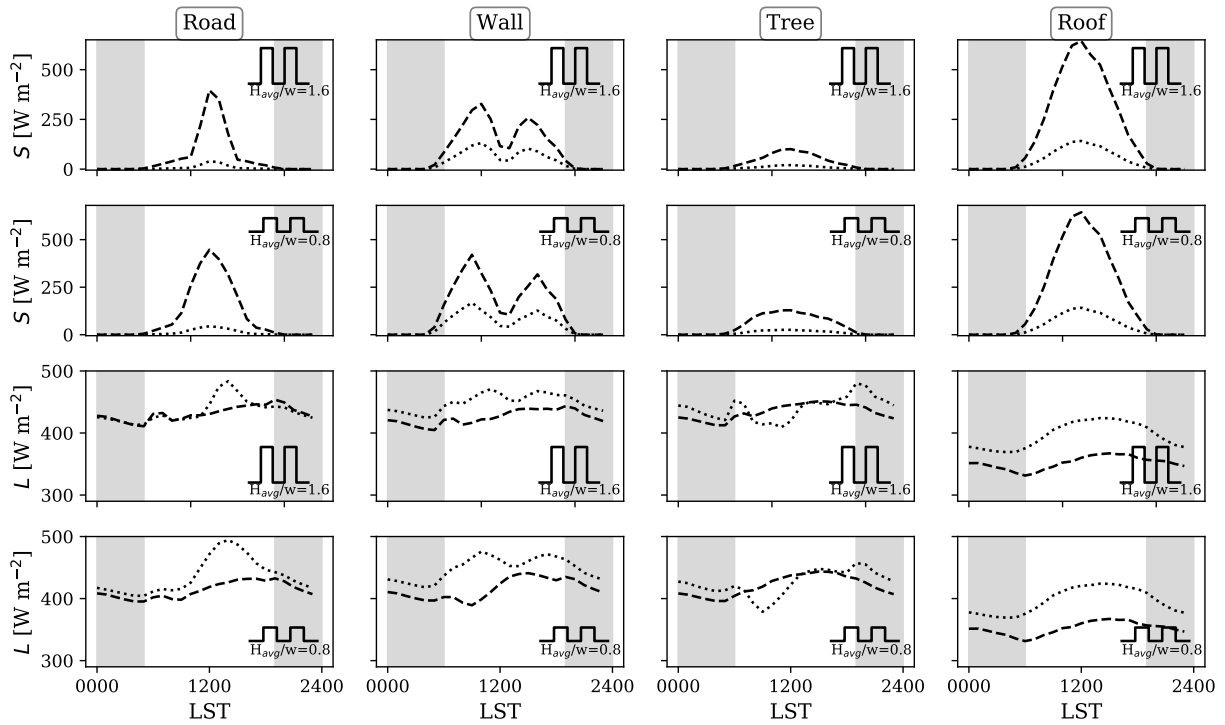


Figure 3.14: Effect of canyon aspect ratio H_{avg}/w [-] on hourly mean absolute values of shortwave S [W m^{-2}] and longwave L [W m^{-2}] radiation fluxes after reflections; incoming fluxes (S^\downarrow and L^\downarrow [W m^{-2}]) shown using dashed lines; outgoing fluxes (S^\uparrow and L^\uparrow [W m^{-2}]) shown using dotted lines; diurnal variation of mean is shown using data obtained over a two-week period; nighttime is shown with shaded regions; times in Local Standard Time (LST).

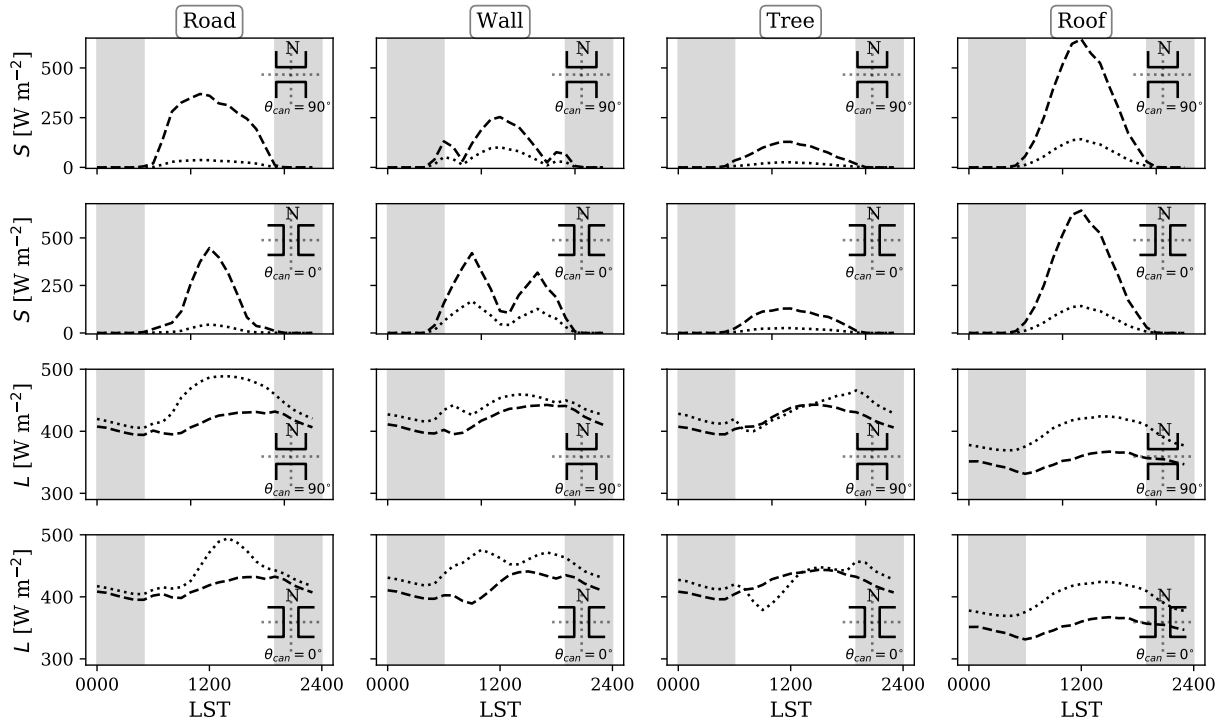


Figure 3.15: Effect of street canyon axis angle θ_{can} [$^{\circ}$] on hourly mean absolute values of shortwave S [W m^{-2}] and longwave L [W m^{-2}] radiation fluxes; incoming fluxes (S^{\downarrow} and L^{\downarrow} [W m^{-2}]) shown using dashed lines; outgoing fluxes (S^{\uparrow} and L^{\uparrow} [W m^{-2}]) shown using dotted lines; diurnal variation of mean is shown using data obtained over a two-week period; nighttime is shown with shaded regions; times in Local Standard Time (LST).

3.3.6 Seasonal Variations

Performance of VCWG is assessed over different seasons with simulations for Vancouver for an entire year in a period in the early 2000s. The model input parameters are chosen to correspond to a plan area density of $\lambda_p = 0.39$ [-], a ratio of total surface to lot area of about 2.2 [-], and a canyon angle of $\theta_{\text{can}} = -45^\circ$ [172].

Figure 3.16 shows the VCWG results for the hourly mean values of UHI [K] in each month of the year in Vancouver, Canada. It can be noted that in general early daytime UHI [K] values are lower than nighttime values, as expected. Also, the greatest UHI [K] values are noted to occur in August and September. The seasonal variation of UHI [K] as predicted by VCWG is in agreement with a similar map reported by Oke et al. (2017) [156].

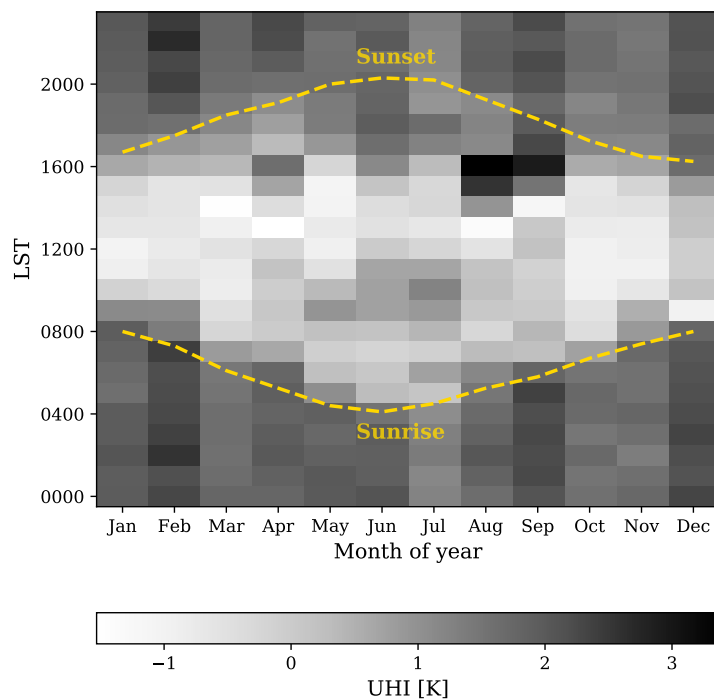


Figure 3.16: Hourly mean values of UHI [K] in each month in Vancouver, Canada, as predicted by VCWG; sunrise and sunset times are denoted by dashed lines; times in Local Standard Time (LST).

Figure 3.17 shows the profiles of potential temperature, horizontal wind speed, specific humidity, and turbulence kinetic energy during nighttime (averaged at 0200 LST) and daytime (averaged at 1400 LST) in different seasons for the Vancouver simulation. It is notable

that the potential temperature and specific humidity profiles reflect the seasonal patterns (low values in the winter and high values in the summer). Wind speed and turbulence kinetic energy profiles do not reveal notable seasonal variations.

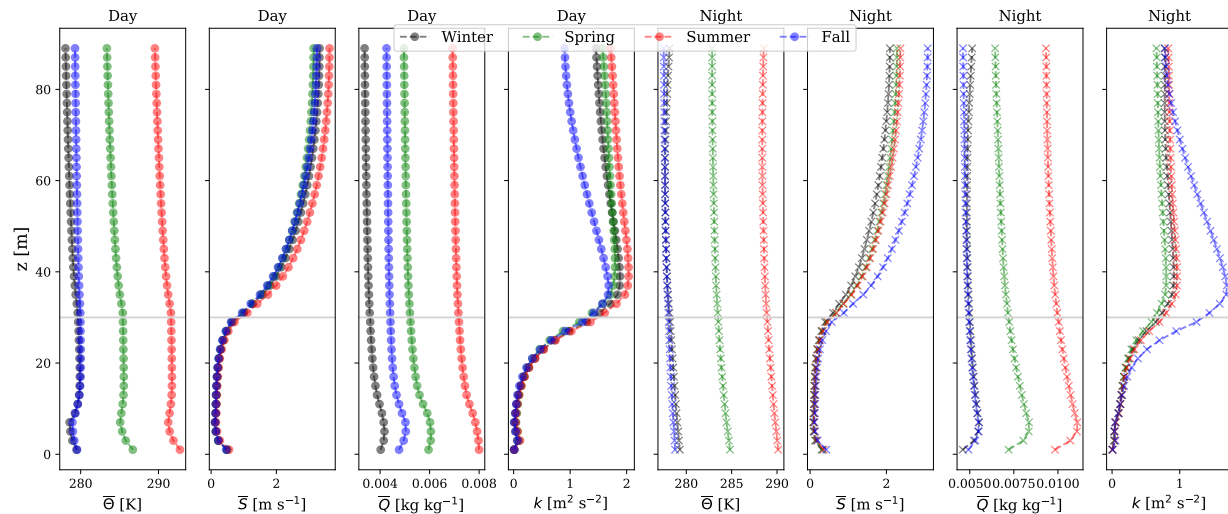


Figure 3.17: Profiles of potential temperature, horizontal wind speed, specific humidity, and turbulence kinetic energy during nighttime (averaged at 0200 LST) and daytime (averaged at 1400 LST) in different seasons; black: winter, green: spring, red: summer, and blue: fall; building height shown with grey line; times in Local Standard Time (LST).

3.3.7 Other Climates

The VCWG is further explored by predicting UHI [K] in different cities with different climate zones, including Buenos Aires in February 1996, a city in the southern hemisphere with a hot and humid climate, Vancouver in September 2011, representing a moderate oceanic climate, Osaka in August 1989, with a subtropical climate, and Copenhagen in June 1999, representing a cold and temperate climate. All simulations are conducted for two weeks and then the hourly mean and standard deviations of UHI are calculated (see Fig. 3.18). In all simulations it is assumed that all of the building waste heat is released at roof level, i.e. $F_{st} = 0$.

For Buenos Aires, VCWG predicts UHI values of +2.5, +0.1, -0.5, and +2.4 [K] at 0300, 0900, 1500, and 2100 LST, respectively. The observed values for the same hours were +2.1, +1, +0.1, and +1.5, respectively. On average, the VCWG predictions of UHI

(+1.1 [K]) are in good agreement with those of the observation (+1.2 [K]) [31]. In case of Vancouver, VCWG predicts maximum and minimum values of UHI equal to +2.7 and +0.1 [K], respectively. The observed values for the maximum and minimum UHI were +3.8 and -1 [K], respectively [172], in reasonable agreement with the predictions. Case studies in Japan have reportedly obtained urban warming in large and developed cities such as Osaka, which is the interest in this study. This effect is also predicted by VCWG that shows a monthly-averaged UHI of +1.78 [K], which is consistent with a monthly-average of +2.2 [K] simulated using meso-scale modelling [103]. UHI [K] in Copenhagen is reported to change between +0.25 and +1.5 [K] depending on the wind speed [118], which agrees reasonably well with the VCWG predictions of UHI [K] varying from a -0.4 [K] to +1.9 [K].

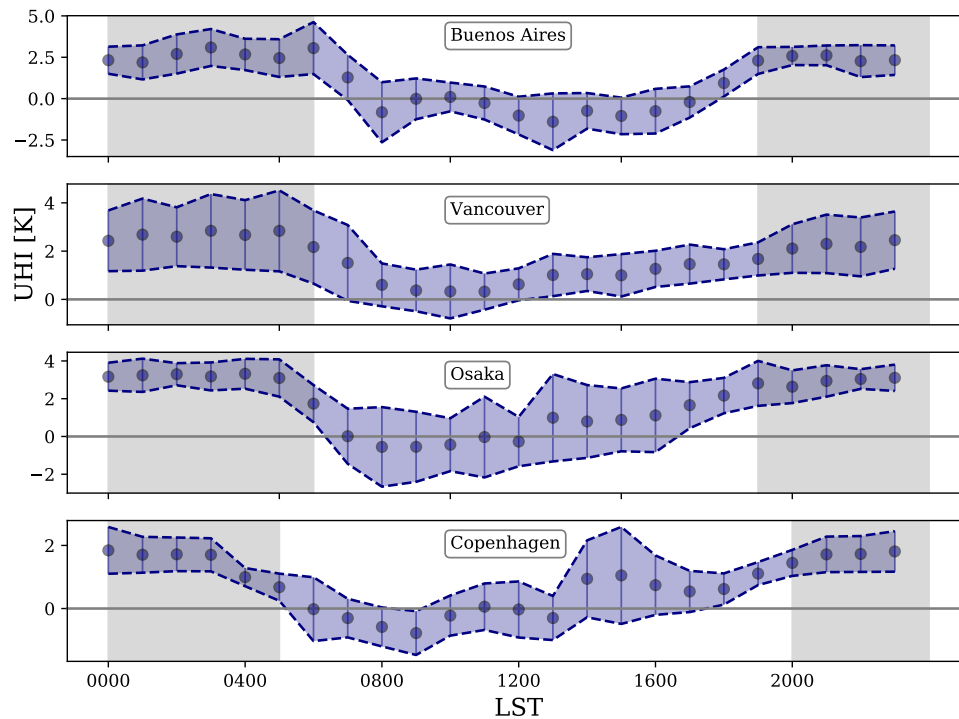


Figure 3.18: Diurnal variation of the UHI [K], as predicted by VCWG, in Buenos Aires, Vancouver, Osaka, and Copenhagen; diurnal variation of mean and standard deviation (band) are shown using data obtained over a two-week period; nighttime is shown with shaded regions; times in Local Standard Time (LST).

Chapter 4

Results and Discussion: VCWG v2.0.0

4.1 Model Configuration

VCWG v2.0.0 preserves most features of VCWG v1.3.2, but it adds extra physical models and functionalities to predict urban climate and building energy performance variables. This version includes a hydrologic model, can be forced from the top of the urban domain using mesoscale data products, and offers the opportunity to investigate simulation output variables on a spatial grid of the urban environment (see Figure 4.1). VCWG v2.0.0 consists of six integrated submodels

1. A rural model forces meteorological boundary conditions on VCWG v1.3.2 based on a surface energy balance model (Equations 2.1), used to calculate the surface heat fluxes and the soil temperature profile in the rural site, and the Monin-Obukhov similarity theory, used to compute friction velocity and vertical profiles of temperature and specific humidity in the atmospheric surface layer (Equations 2.15, 2.12, and 2.17). The Penman-Monteith (PM) method is used to solve the surface energy balance model in the rural area. So, the latent heat flux is calculated using Equation 2.6;
2. An urban one-dimensional vertical diffusion model is used to calculate the vertical profiles of cross- and along- canyon wind speed (Equations 2.91 and 2.92), potential temperature (Equation 2.103), specific humidity (Equation 2.109), and turbulence kinetic energy (Equation 2.100) in the urban area considering the effects of trees, buildings, and building energy systems. The model can be forced at the top of the domain either by the rural model or a top forcing dataset (which is provided by the user) and at the bottom by surface energy and water balances;

3. A building energy model is used to calculate the building energy fluxes (Equation 2.111) and waste heat (Equations 2.107 and 2.108) of building imposed on the urban environment;
4. A radiation model with trees is used to compute the longwave (Equation 2.40) and shortwave (Equation 2.34) radiation fluxes between the urban canyon, trees, and the sky;
5. An urban surface energy balance model is used to calculate surface heat fluxes, including sensible (Equation 2.43), latent (Equation 2.52), and conductive heat fluxes (Equations 2.78 and 2.79). The moisture sources include not only evaporation from tree foliage but also the wet surfaces and soil columns, which contribute to the urban energy balance; and
6. An urban hydrology model is used to obtain ecophysiological behavior of urban trees and low vegetation at the ground and roof levels and calculate urban hydrological exchanges (Equation 2.119) and soil water content profile (Equation 2.129) in the presence of precipitation.

In this chapter, first, the VCWG v2.0.0 model results are evaluated against the microclimate field measurements, including the BUBBLE dataset in Basel [170] and the Vancouver Sunset dataset [47]. The simulation results are also compared with the predecessor version and other studies. Next, the model performance is explored by various parametric simulations.

To evaluate the model against the BUBBLE dataset, the boundary conditions for potential temperature and specific humidity equations (Equations 2.103 and 2.109) are determined from the rural model. The flow is assumed to be pressure-driven with the pressure gradient of $\rho u_*^2/H_{\text{top}}$ [$\text{kg m}^{-2} \text{s}^{-2}$], which is decomposed into the x and y directions based on the wind angle and canyon orientation. This pressure gradient is forced as source terms on the momentum Equations 2.91 and 2.92. Evaluation of VCWG v2.0.0 against Vancouver Sunset dataset is conducted by forcing the model using the top forcing approach (see Figure 2.1). Thus, the potential temperature, specific humidity, and x and y momentum equations (Equations 2.103, 2.109, 2.91, and 2.92) are solved using the Dirichlet boundary condition at the top and Neumann boundary condition at the bottom. In this case the source term in the momentum equations are forced to zero, i.e. $\rho u_*^2/H_{\text{top}} = 0$ [kg m^{-2}]. The same approach is used for model exploration in Vancouver.

A uniform Cartesian grid with 1 m vertical resolution is used for all evaluation and exploration analyses that are conducted in this chapter. VCWG v2.0.0 is also equipped with a function that can automate the GIS processes to simulate urban climate within a spatial raster dataset.

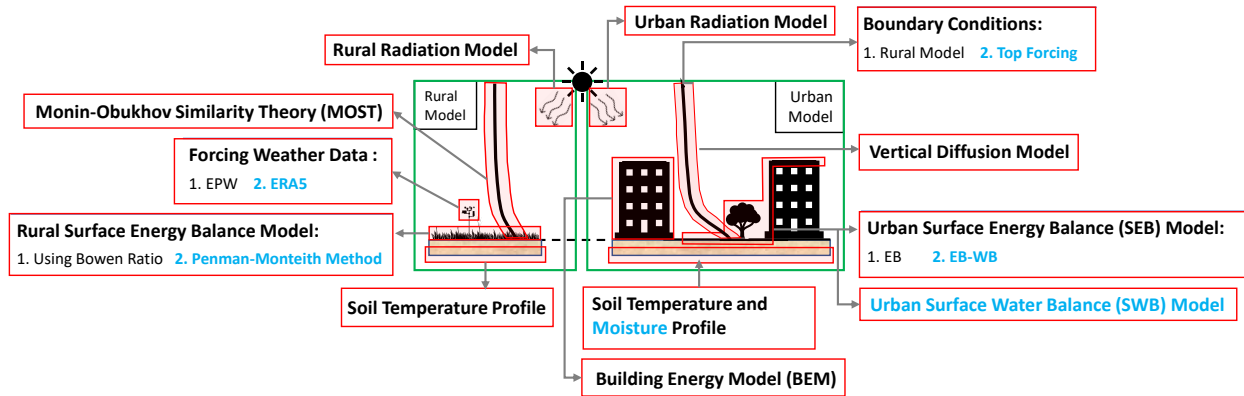


Figure 4.1: Overview of the Vertical City Weather Generator (VCWG) v2.0.0. The new additions in VCWG v2.0.0 are highlighted in blue.

4.2 Evaluation

4.2.1 Observation and Forcing Datasets

The results of the VCWG v2.0.0 are compared to the measured data from the BUBBLE campaign and Vancouver Sunset datasets. A brief description of the BUBBLE field campaign is provided in Section 3.2.1. The model predictions of air temperature, wind speed, specific humidity, sensible and latent heat fluxes are compared to the BUBBLE observations on an hourly basis. The measurement in the nearby rural area is used to force the model. Measurement in the Sunset neighborhood of Vancouver (49.226°N and 123.078°W) consists of air temperature and relative humidity at 26 [m] a.g.l, incoming shortwave, and longwave radiation fluxes at 26.2 [m] a.g.l, barometric pressure, latent, and sensible heat fluxes at 28.8 [m] a.g.l. The dataset provides the measurements averaged every 5 [min]. The urban canyon axis is oriented in the north direction with a canyon axis angle of $\theta_{\text{can}} = 0^{\circ}$. The measured downwelling shortwave and longwave radiation fluxes, air temperature, humidity, and pres-

Table 4.1: List of input parameters used in VCWG v2.0.0 for model evaluation in Vancouver; input variables are extracted from assumptions, datasets, and simulation codes available in the literature [47, 100].

Parameter	Symbol	Value
Latitude [$^{\circ}$ N]	lat	49.226
Longitude [$^{\circ}$ W]	lon	123.078
Average buildings height [m]	H_{avg}	5
Width of canyon [m]	$w_x=w_y=w$	23
Building width to canyon width ratio [-]	$b_x/w_x=b_y/w_y=b/w$	0.4
Leaf Area Index [$\text{m}^2 \text{m}^{-2}$]	LAI	0.39
Tree height [m]	h_t	5
Tree crown radius [m]	r_t	2
Tree distance from wall [m]	d_t	2.5
Ground fractions of vegetation, impervious, and soil surface [-]	$f_{\text{veg}}, f_{\text{imp}}, f_{\text{bare}}$	0.5,0.5,0
Roof fractions of vegetation and impervious [-]	$f_{\text{veg}}, f_{\text{imp}}$	0,1
Building type	-	Mid-rise apartment
Urban albedos (roof, ground, wall, vegetation) [-]	$\alpha_R, \alpha_G, \alpha_W, \alpha_V$	0.13, 0.14, 0.2, 0.27
Urban emissivities (roof, ground, wall, vegetation) [-]	$\varepsilon_R, \varepsilon_G, \varepsilon_W, \varepsilon_V$	0.95,0.95,0.95,0.95
Ground aerodynamic roughness length [m]	z_{0G}	0.02
Roof aerodynamic roughness length [m]	z_{0R}	0.02
Vertical resolution [m]	Δz	1
Time step [s]	Δt	60
Canyon axis orientation [$^{\circ}$ N]	θ_{can}	0.0
Urban boundary condition	-	Top Forcing
Urban surface energy balance model	-	EB-WB

sure are used to force the model at the top of the simulation domain. The model predictions of sensible and latent heat fluxes are compared to the Vancouver Sunset observations on an hourly basis.

The input parameters representing the urban area in Basel and Vancouver are listed in Tables 3.1 and 4.1, respectively. The input parameters for Vancouver are inferred from variables, datasets, and simulation codes in the literature that pertains to the Vancouver Sunset campaign and associated models, as well as general assumptions found in the literature [47, 100]. In Table 4.1, note that the choices of average building height $H_{\text{avg}} = 5.0$ [m], street width $w = 23.0$ [m], and building width to street width ratio $b/w = 0.4$ [-] provide $\lambda_p = b/(w + b) = 0.29$ [-] and $\lambda_f = H_{\text{avg}}/(w + b) = 0.16$ [-]. For the Basel case, the simulations are conducted for 15 days with one day of spin-up period starting from June 15, 2002. For the Vancouver case, the simulations are conducted for five months from May 2008 to September 2008 with one day of spin-up period. The simulation time step for both analyses is 1 [min].

4.2.2 Potential Temperature, Wind Speed, and Specific Humidity

To compare VCWG v2.0.0 results with measured meteorological variables from the BUBBLE campaign, the BIAS, Root Mean Square Error (RMSE), and coefficient of determination R^2 are computed for pairs of model versus observed values every hour for available altitudes. This analysis is performed for wind speed, potential temperature, and specific humidity. The results from VCWG v1.3.2 and VCWG v2.0.0 are provided in Table 4.2 for better cross-comparison. VCWG v2.0.0 simulation results show improvement in RMSE and R^2 for potential temperature, as the RMSE is decreased by 0.5 [K] and R^2 is increased by 0.05 [-]. In contrast to the predecessor version, the VCWG v2.0.0 overestimates the air temperature near the ground ($z = 3.6$ [m]) with approximately the same magnitude. However, the RMSE and R^2 are improved at this altitude, which can be attributed to the better representation of sensible and latent heat fluxes. At higher altitudes, the improved rural and urban surface energy balance models result in lower RMSE and higher R^2 . Over all altitudes, on average, the BIAS, RMSE and R^2 for potential temperature using VCWG v2.0.0 are -0.53 [K], 0.56 [K], and 0.98 [-], respectively.

Considering all altitudes, the average BIAS, RMSE, and R^2 for wind speed are -0.46 [m s^{-1}], 0.44 [m s^{-1}], and 0.46 [-], which are improved in comparison to the predecessor version of the model. VCWG v2.0.0 also shows better performance in estimating the specific humidity within and above the canyon. The average BIAS, RMSE, and R^2 for specific humidity are 0.0000 [kg kg^{-1}], 0.0003 [kg kg^{-1}], and 0.98 [-], respectively. Such improvement is mainly attributed to the incorporation of the hydrology model and more accurate representation of latent heat flux sources in the column model.

4.2.3 Sensible and Latent Heat Fluxes

The VCWG v2.0.0 is further assessed based on the comparison between the measured and simulated urban sensible heat flux H_{urban} [W m^{-2}] and urban latent heat flux LE_{urban} [W m^{-2}] above the canyon. H_{urban} and LE_{urban} are calculated as a function of temperature and specific humidity gradients, respectively, obtained from the column model and turbulent

Table 4.2: BIAS, RMSE, and R^2 for VCWG v1.3.2 and v2.0.0 predictions of potential temperature $\bar{\Theta}$ [K], wind speed \bar{S} [m s^{-1}], and specific humidity \bar{Q} [kg kg^{-1}] against the BUBBLE observations for different altitudes and months (green shaded cells show improvement and red shaded cells show deterioration in the predictions).

Altitude z [m]	Statistic	VCWG v1.3.2			VCWG v2.0.0			Difference		
		$\bar{\Theta}$	\bar{S}	\bar{Q}	$\bar{\Theta}$	\bar{S}	\bar{Q}	$\bar{\Theta}$	\bar{S}	\bar{Q}
2.5	BIAS	-	-0.51	0.00081	-	-0.68	0.0001	-	-	-
	RMSE	-	0.4	0.0012	-	0.67	0.0004	-	0.27	0.0008
	R^2	-	0.43	0.86	-	0.25	0.97	-	0.18	0.07
3.6	BIAS	-0.1	-	-	0.12	-	-	-	-	-
	RMSE	0.72	-	-	0.61	-	-	0.11	-	-
	R^2	0.95	-	-	0.98	-	-	0.03	-	-
11.3	BIAS	-0.22	-	-	-0.50	-	-	-	-	-
	RMSE	0.79	-	-	0.55	-	-	0.24	-	-
	R^2	0.86	-	-	0.97	-	-	0.11	-	-
13.9	BIAS	-	-0.17	-	-	-0.58	-	-	-	-
	RMSE	-	0.18	-	-	0.58	-	-	0.4	-
	R^2	-	0.84	-	-	0.25	-	-	0.59	-
14.7	BIAS	-0.12	-	-	-0.60	-	-	-	-	-
	RMSE	0.97	-	-	0.56	-	-	0.31	-	-
	R^2	0.92	-	-	0.98	-	-	0.06	-	-
17.5	BIAS	-	0.88	-	-	-0.46	-	-	-	-
	RMSE	-	0.74	-	-	0.50	-	-	0.24	-
	R^2	-	0.84	-	-	0.45	-	-	0.29	-
17.9	BIAS	-0.35	-	-	-0.68	-	-	-	-	-
	RMSE	1.14	-	-	0.58	-	-	0.56	-	-
	R^2	0.86	-	-	0.99	-	-	0.13	-	-
21.5	BIAS	-	1.13	-	-	-0.33	-	-	-	-
	RMSE	-	0.97	-	-	0.43	-	-	0.54	-
	R^2	-	0.43	-	-	0.45	-	-	0.02	-
22.4	BIAS	-0.45	-	-	-0.75	-	-	-	-	-
	RMSE	1.29	-	-	0.57	-	-	0.72	-	-
	R^2	0.86	-	-	0.98	-	-	0.12	-	-
25.5	BIAS	-	1.96	0.00049	-	-0.3	-0.0001	-	-	-
	RMSE	-	1.67	0.0014	-	0.44	0.0003	-	1.23	0.0011
	R^2	-	0.4	0.84	-	0.60	0.98	-	0.2	0.14
31.2	BIAS	-	2.1	-	-	-0.42	-	-	-	-
	RMSE	-	1.78	-	-	0.40	-	-	1.38	-
	R^2	-	0.51	-	-	0.74	-	-	0.23	-
31.7	BIAS	-0.64	-	-	-0.78	-	-	-	-	-
	RMSE	1.43	-	-	0.50	-	-	0.97	-	-
	R^2	0.93	-	-	0.99	-	-	0.06	-	-
Average	BIAS	-0.31	0.9	0.00065	-0.53	-0.46	0.0000	-	-	-
	RMSE	1.06	0.96	0.0013	0.56	0.44	0.0003	0.5	0.52	0.001
	R^2	0.93	0.42	0.42	0.98	0.46	0.98	0.05	0.04	0.56

diffusion coefficient (K_m [$\text{m}^2 \text{s}^{-1}$]) as follows

$$H_{\text{urban}} = - \left(\rho C_p \frac{K_m}{Pr_t} \frac{\partial \bar{\Theta}}{\partial z} \right)_{z=z_{\text{obs}}} \quad (4.1)$$

$$LE_{\text{urban}} = - \left(\rho L \frac{K_m}{Sc_t} \frac{\partial \bar{Q}}{\partial z} \right)_{z=z_{\text{obs}}}, \quad (4.2)$$

where z_{obs} is the height at which sensible/latent heat fluxes are measured, and Pr_t and Sc_t are turbulent Prandtl and Schmidt numbers, respectively. For the Basel case, the heat fluxes are measured at an altitude of 31.7 [m]. Figure 4.2 shows the time series comparison between the results from both versions of the model and the BUBBLE dataset. VCWG v1.3.2 and v2.0.0 can follow the same diurnal pattern as the observation. While VCWG v2.0.0 overestimates the midday sensible heat flux, it performs better than the predecessor version, which underestimates sensible heat flux over the period of simulation, which can be attributed to the better performance of the surface energy balance model in the new version. An appropriate representation of latent heat source/sink terms in the urban area leads to better estimation of the latent heat flux, as VCWG v2.0.0 can capture the LE_{urban} peaks that occur shortly after rainfall events. The statistical analysis provided in Table 4.3 shows that VCWG v2.0.0 results in lower RMSE and higher R^2 relative to the results from VCWG v1.3.2. VCWG v2.0.0 results in BIAS, RMSE, and R^2 of 22 [W m^{-2}], 34.3 [W m^{-2}], and 0.88 [-], respectively, for sensible heat flux and -17.3 [W m^{-2}], 23.1 [W m^{-2}], and 0.35 [-], respectively, for latent heat flux. Considering the short evaluation period using VCWG v2.0.0, the model shows reasonable performance in comparison to the previous studies that reported BIAS of -4.15 [W m^{-2}] [174] and -71.8 [W m^{-2}] [89] and RMSE of 38.9 [W m^{-2}] [174] and 100.2 [W m^{-2}] [89] for sensible heat flux and BIAS of -20.6 [W m^{-2}] [174] and RMSE of 33.8 [W m^{-2}] [174] and 36.0 [W m^{-2}] [89] for latent heat flux.

The capability of VCWG v2.0.0 to predict latent and sensible heat fluxes over longer periods of time is evaluated against the Vancouver Sunset dataset. For this analysis, the model is forced at the top of the urban domain using the observed dataset over five months. Figure 4.3 illustrates the cross-comparison between VCWG v2.0.0 simulation results and the field measurements. The simulated and observed urban sensible heat flux show reasonable agreement with a BIAS, RMSE, and R^2 of 0.65 [W m^{-2}], 18.1 [W m^{-2}], and 0.94 [-], respectively (see Table 4.3). Compared to the previous studies, Oleson et al. (2007) [158] obtained BIAS of 62 [W m^{-2}], RMSE of 81 [W m^{-2}], and R^2 of 0.87 [-] using an urban parameterization for a global climate model. The results from the Surface Urban Energy

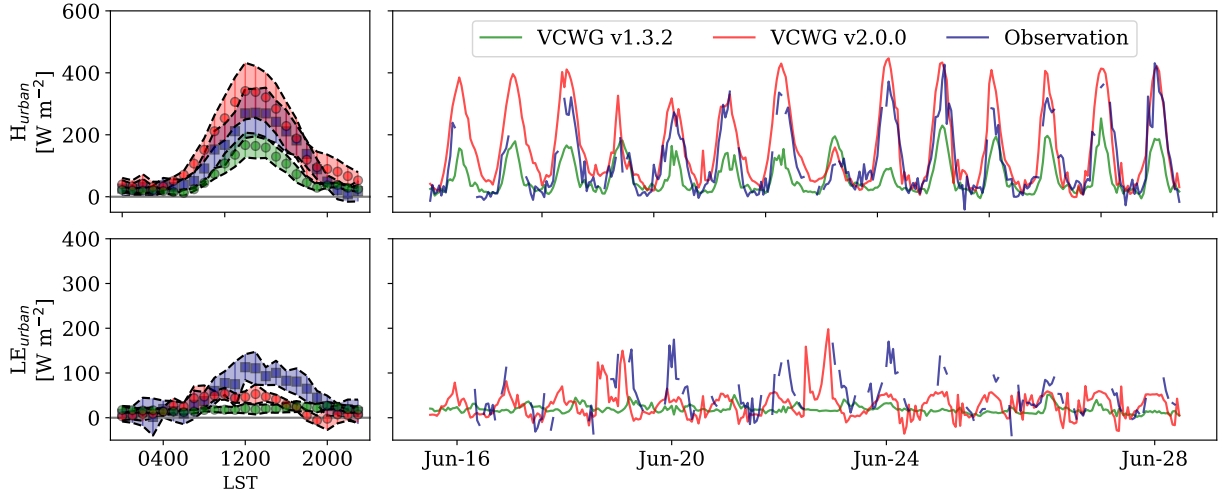


Figure 4.2: Comparison between the BUBBLE dataset (blue) versus simulated values of sensible and latent heat fluxes above the urban area using VCWG v1.3.2 (green) and VCWG v2.0.0 (red); the hourly means are shown; times in Local Standard Time (LST); simulation for a two-week period in June 2002.

and Water balance Scheme (SUEWS) model showed RMSE of $39.1 \text{ [W m}^{-2}\text{]}$ and R^2 of 0.77 [-] [84]. This comparison signifies the adequate performance of VCWG v2.0.0. Urban latent heat flux is also well-captured with the model. The statistics show that VCWG v2.0.0 simulated LE_{urban} with a BIAS, RMSE, and R^2 of $1.35 \text{ [W m}^{-2}\text{]}$, $27.7 \text{ [W m}^{-2}\text{]}$, and 0.55 [-], respectively, compared to the other studies that reported BIAS of $-4 \text{ [W m}^{-2}\text{]}$ [158], $1.9 \text{ [W m}^{-2}\text{]}$ [129], RMSE of $16 \text{ [W m}^{-2}\text{]}$ [158], $32.5 \text{ [W m}^{-2}\text{]}$ [84], $26.8 \text{ [W m}^{-2}\text{]}$ [129], and R^2 of 0.35 [-] [158], 0.74 [-] [84], 0.62 [-] [129]. This demonstrates the reasonable performance of VCWG v2.0.0 relative to observations and previous studies.

4.3 Exploration

4.3.1 Forcing Datasets

The performance of VCWG is assessed by evaluating the model for different seasons, coverages of urban trees and ground vegetation, roof types (green/cool roof), and Local Climate Zones (LCZs). All explorations are performed by VCWG v2.0.0 simulations of the urban micro-climate variables in Vancouver, Canada. For the season and roof type analyses, the model is automated to run for a whole year in 2007. The other analyses are conducted in

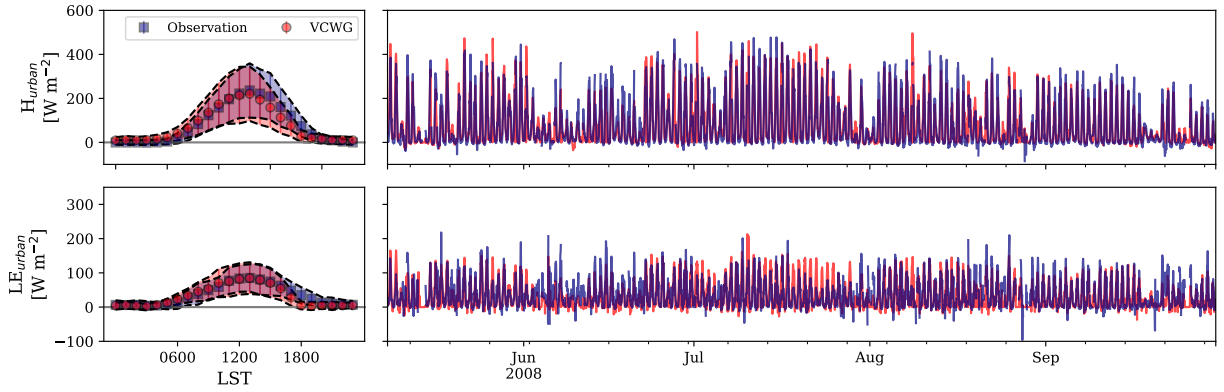


Figure 4.3: Comparison between the Vancouver Sunset dataset versus simulated values of sensible and latent heat fluxes above the urban area using VCWG v2.0.0; the hourly means are shown; times in Local Standard Time (LST); simulation for a 5-month period in 2008.

Table 4.3: BIAS, RMSE, and R^2 for VCWG predictions of sensible and latent heat fluxes [W m^{-2}] against the observations and previous studies.

Urban Fluxes	VCWG v1.3.2			VCWG v2.0.0			Literature		
	BIAS	RMSE	R^2	BIAS	RMSE	R^2	BIAS	RMSE	R^2
H_{urban} (Vancouver)	-	-	-	0.65	18.1	0.94	62 ¹	81 ¹ ,39.1 ³	0.87 ¹ ,0.77 ³
H_{urban} (Basel)	-45.2	63.5	0.58	22.0	34.3	0.88	-4.15 ² , -71.8 ⁴	38.9 ² , 100.2 ⁴	-
LE_{urban} (Vancouver)	-	-	-	1.35	27.7	0.55	-4 ¹	16 ¹ , 32.5 ³	0.35 ¹ , 0.74 ³
LE_{urban} (Basel)	-28.7	37.1	0.28	-17.3	23.1	0.35	-20.6 ²	33.8 ² , 36.0 ⁴	-

¹Oleson et al. (2007) [158] evaluation period is 15 days. ²Ryu et al. (2016) [174] evaluation period is 30 days. ³Järvi et al. (2011) [84] evaluation period is 147 days. ⁴Kawai et al. (2009) [89] evaluation period is 39 days

Table 4.4: List of input parameters used in VCWG v2.0.0 for seasonal exploration in Vancouver.

Parameter	Symbol	Value
Latitude [$^{\circ}$ N]	lat	49.226
Longitude [$^{\circ}$ W]	lon	123.078
Average buildings height [m]	H_{avg}	10.0
Width of canyon [m]	$w_x=w_y=w$	23.0
Building width to canyon width ratio [-]	$b_x/w_x=b_y/w_y=b/w$	0.4
Tree height [m]	h_t	8.0
Tree crown radius [m]	r_t	1.5
Tree distance from wall [m]	d_t	2.2
Ground fractions of vegetation, impervious, and soil surface [-]	$f_{\text{veg}}, f_{\text{imp}}, f_{\text{bare}}$	0.5,0.5,0
Roof fractions of vegetation and impervious [-]	$f_{\text{veg}}, f_{\text{imp}}$	0,1
Leaf area index [$\text{m}^2 \text{m}^{-2}$]	LAI	Variable
Building type	-	Mid-rise apartment
Urban albedos (roof, ground, wall, vegetation) [-]	$\alpha_R, \alpha_G, \alpha_W, \alpha_V$	0.13, 0.14, 0.2, 0.27
Urban emissivities (roof, ground, wall, vegetation) [-]	$\varepsilon_R, \varepsilon_G, \varepsilon_W, \varepsilon_V$	0.95, 0.95, 0.95, 0.95
Vertical resolution [m]	Δz	1
Time step [s]	Δt	300
Canyon axis orientation [$^{\circ}$ N]	θ_{can}	0.0
Urban boundary condition	-	Top Forcing
Urban surface energy balance model	-	EB-WB

a warm month. Spatial distribution of climate variables is simulated by coupling the automated GIS processes function with VCWG v2.0.0. For these analyses, the ERA5 dataset is used to force the model at the top of the urban domain at an elevation of 90 [m]. The input parameters representing the urban area and the model options used for these explorations are listed in Table 4.4. Depending on the type of analysis, the input parameters vary within a reasonable range that is discussed in the subsequent sections.

4.3.2 Seasonal Variations

Compared to the regions close to the equator, the areas at higher latitudes experience stronger seasonal variability in the cycle of surface energy and water fluxes [15]. The amount of solar radiation flux reaching the Earth’s surface and the solar zenith angle both vary significantly over the course of a year, leading to different meteorological conditions, shading effects, foliage amounts, soil moisture content, patterns of anthropogenic fluxes, and building energy performance.

Performance of VCWG v2.0.0 is assessed over different seasons with simulations for Vancouver for an entire year in 2007. The seasonal LAI cycle describes the vegetation condition

and controls photosynthesis activities, water, and CO₂ conductance and flux.

4.3.2.1 Sensible and Latent Heat Fluxes

As shown in Figure 4.4, the urban area is characterized by higher latent and sensible heat fluxes in the warm season (Apr-Sep). While the sensible and latent heat fluxes follow approximately the same trend and magnitude during the cold season (Jan-Mar and Oct-Dec), sensible heat flux is substantially higher during the summer months. Although the sensible heat flux in cold months is considerably lower, it still transfers energy from surfaces to the urban boundary layer with a daytime mean value of 60 [W m⁻²]. This suggests that the building waste heat and other anthropogenic activities in the urban areas are dominant during cold months (see Figure 4.6). The larger values of heat fluxes in the summer months is mainly attributed to the larger magnitude of solar radiation fluxes interacting with the surface and growth of active vegetation. The latent heat flux is mainly characterized by moisture availability in the urban area. Due to the high impervious surface coverage in the urban area, the latent heat flux exhibits less seasonal variation. However, more active vegetation in the warm months contributes significantly to the total latent heat flux and increases daytime mean value of latent heat flux from 50 [W m⁻²] in the winter to 90 [W m⁻²] in the summer. In other words, higher net radiation in the warm months leads to a higher vapor pressure deficit. However, this analysis is a strong function of the climate zone. For instance, tropical regions (e.g., Singapore) experience less variability in latent heat flux with fluctuations around 80 [W m⁻²] [129]. On the other hand, regions at higher altitudes show more variability, which is consistent with the findings in this thesis (e.g., Melbourne: latent heat flux from 40 [W m⁻²] in the winter to 140 [W m⁻²] in the summer [15, 129]; London: latent heat flux from 20 [W m⁻²] in the winter to 80 [W m⁻²] in the summer [97]). Precipitation and anthropogenic water (e.g., irrigation) are the main contributors to the latent heat flux in urban areas. Prescribed time series of anthropogenic water for vegetated and bare surfaces can be considered in the simulation. Days with more precipitation, particularly in the warm months, are more likely to have increased latent heat flux and decreased sensible heat flux (e.g., late August and early September in Figure 4.4). The results obtained from this exploration are in reasonable agreement with other studies [15, 97, 129].

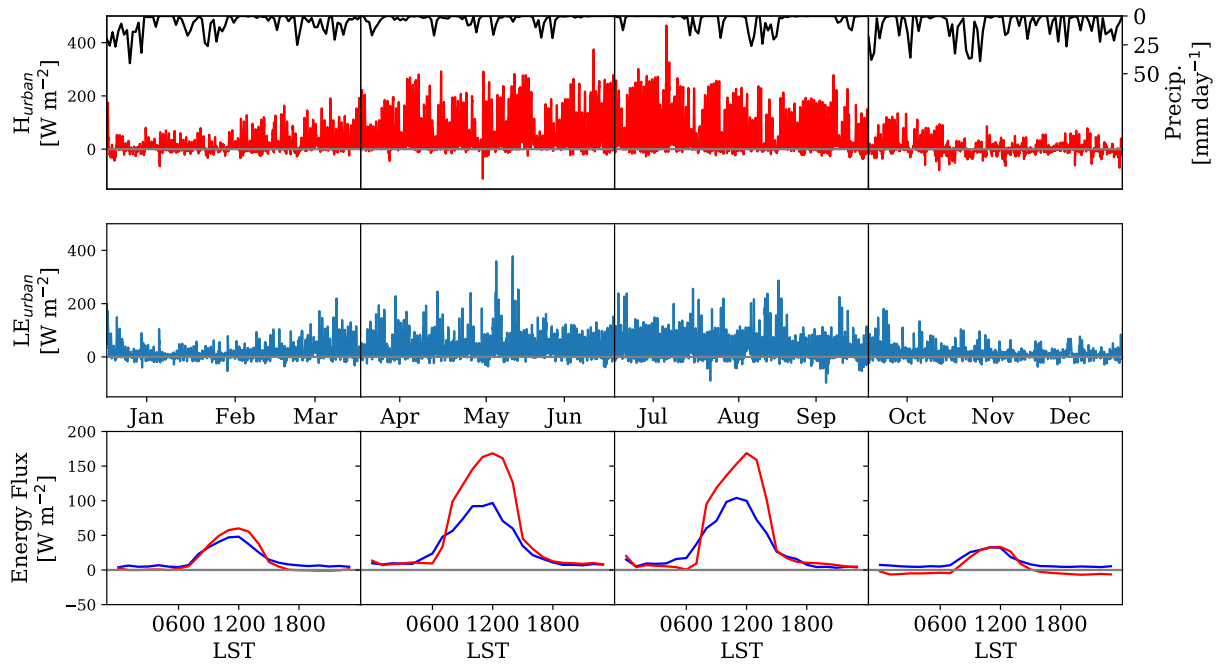


Figure 4.4: Hourly sensible and latent heat fluxes [W m^{-2}] in Vancouver: (top) sensible heat flux above the canyon over the course of a year; (middle) latent heat flux above the canyon over the course of a year; (bottom) mean diurnal variation of latent (blue) and sensible (red) heat fluxes for Jan-Mar, Apr-Jun, Jul-Sep, and Oct-Dec. The black line shows daily precipitation [mm day^{-1}].

4.3.2.2 Surface Temperatures

Due to the high variability of radiative, thermal, and moisture properties of the urban surfaces, they more likely experience different temperatures through a diurnal cycle. The surface temperature controls the magnitude and direction of heat fluxes at the surface. Figure 4.5 shows the daytime and nighttime percentiles of urban surface temperatures in January, May, August, and November, which are indicative of each season. Diurnal variation of the roof temperature is considerably higher than the other surfaces, as roofs are directly exposed to solar radiation fluxes and are less influenced by the in-canyon surfaces. In the warm months (May and August), all surfaces experience higher temperatures than the canyon air temperature except ground vegetation that remains close to the air temperature. During the nighttime, there is a substantial decrease in roof temperature, while building walls have the highest temperatures, and the temperature of vegetation remains close to the air temperature. The same pattern was observed by Christen et al. (2012) [36] and Aliabadi et al. (2019) [8], where roof and lawn temperatures fell below the canyon air temperature during nighttime. In general, surfaces with higher temperature fluctuations (roof) exhibit considerably higher daytime temperatures than the canyon air temperature, which is consistent with the findings in the literature [36, 139]. This analysis signifies the effect of replacing natural areas by impervious surfaces.

4.3.2.3 Building Energy Performance

Building waste heat released into the atmosphere is considered as the main source of anthropogenic heat in the urban areas and is controlled by heating and cooling demand [176]. In cold months, when the building energy system is on heating mode, the building heat emission dominates the urban sensible heat flux and can alter the urban air temperatures [18]. Figure 4.6 shows the daily mean and maximum of building energy fluxes over an entire year in Vancouver. The heating and cooling demands are at their maximum in cold months (January, February, and December) and warm months (July and August), respectively. Shoulder seasons are the transition period from cooling (heating) mode to heating (cooling) mode, for fall (spring). A small amount of energy is required for dehumidification in the warm months. It is common to experience few periods with low outdoor air temperature in the warm seasons, and the building energy system is required to convert to heating mode, which is well-captured by VCWG.

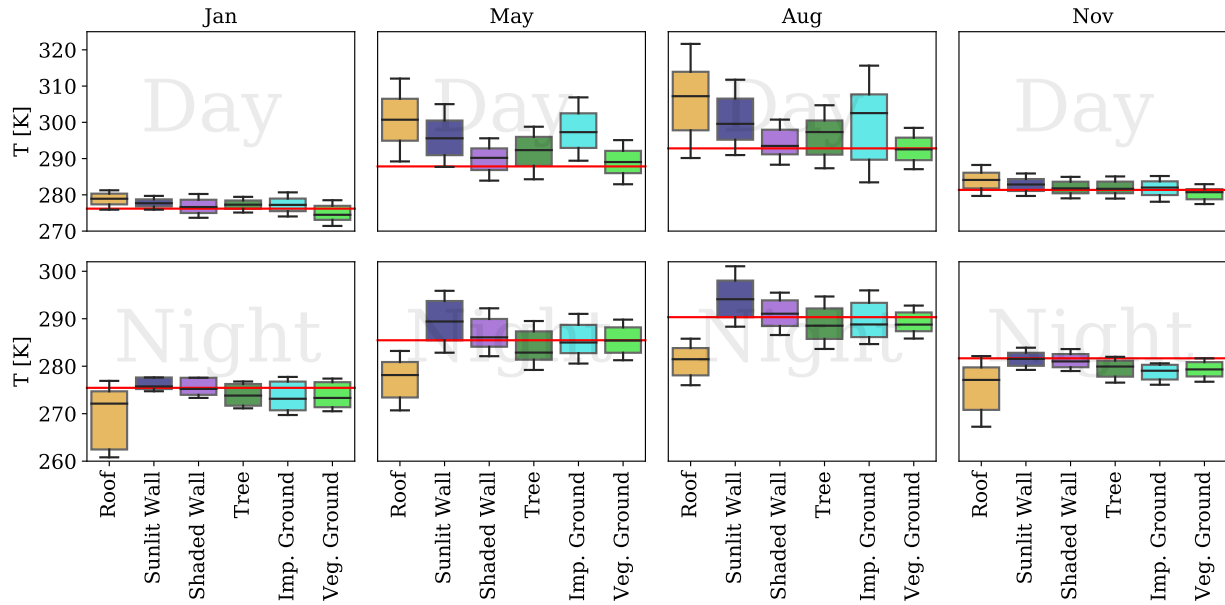


Figure 4.5: Variability of urban surface temperatures in January, May, August, and November in Vancouver; roof is impervious and ground is partially covered by vegetation; the box plot represents 5th, 25th, 50th, 75th, and 95th percentiles for temperature; red line is canyon air temperature; top row is daytime and bottom row is nighttime; daytime temperatures are sampled from 1000 to 1400 LST and nighttime temperatures are sampled from 2200 to 0200 LST.

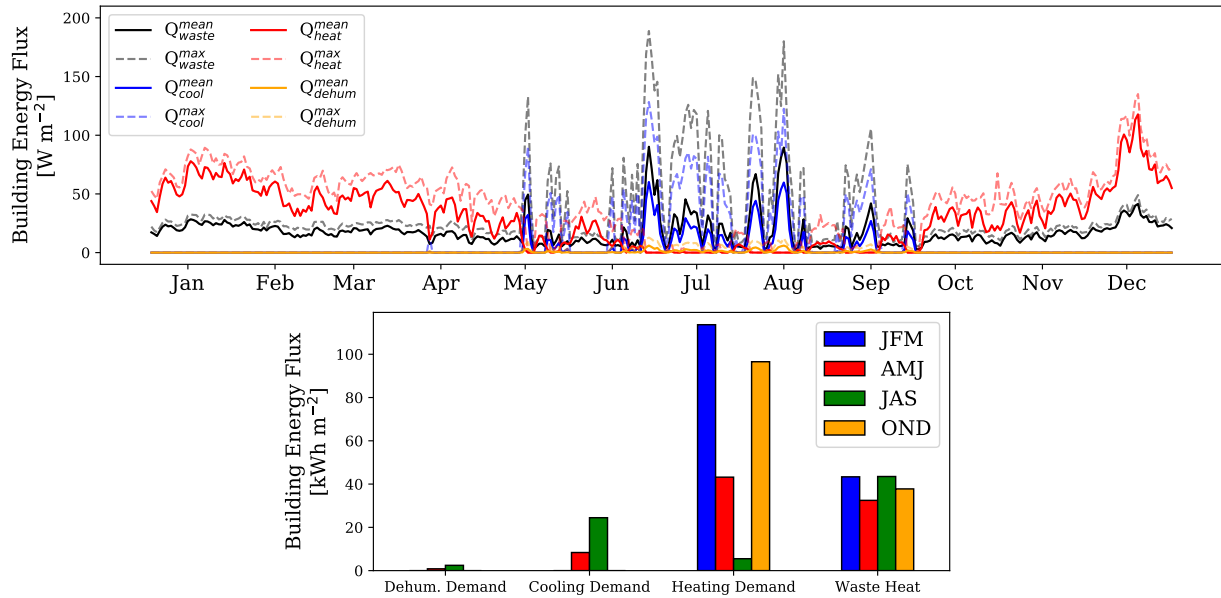


Figure 4.6: Seasonal variation of hourly mean and maximum building energy fluxes including cooling demand (Q_{cool}), dehumidification demand (Q_{dehum}), heating demand (Q_{heat}), and building waste heat (Q_{waste}); the solid line is daily mean and dashed line is daily maximum of the variable. The bar plot is the integrated energy flux within JFM (January, February, and March), AMJ (April, May, and June), JAS (July, August, and September), and OND (October, November, and December) months. The simulation is conducted for Vancouver.

4.3.2.4 Water Budget Analysis

Water budget analysis in urban areas is mostly carried out on a seasonal or annual basis, which provides insight into the urban water management to cope with extreme weather conditions [121]. In an urban unit, the precipitation and anthropogenic water (e.g., garden irrigation) are the main water inputs to the urban hydrologic cycle that are partitioned into surface runoff, evaporation, leakage at the bottom of the soil column, and depression storage [121, 134]. Performance of VCWG to take into account the seasonal variation of water budget terms is assessed. Figure 4.7 depicts the monthly variation of water balance terms for an entire year in Vancouver. In warm months, a large fraction of input water (precipitation plus anthropogenic water) is returned to the atmosphere via evaporation in forms of evapotranspiration, soil evaporation, and intercepted water evaporation. Due to the replacement of natural areas by impervious surfaces in the urban area, a considerable fraction of precipitations moves over land. This surface runoff is higher during cold seasons, when cold weather restricts water evaporation. Urban runoff usually hits a peak during and immediately after rainfall events. In general, the ratio of surface runoff to precipitation varies from 0.3 in the winter to 0.1 in the summer. The same pattern has been observed in the Oakridge, Vancouver, suburban area in 1982, where maximum evaporation and surface runoff were reported in June and January, respectively [68]. During warm months, particularly in July, rainfall is reduced significantly and urban vegetation and soil are the main sources for water evaporation. As shown in Figure 4.8, this period of the year experiences extensive soil moisture depletion; water storage in the urban unit is approximately zero; and leakage is at its minimum. Extreme precipitation events, which usually occur in the cold months, replenish the soil column, increase soil moisture content, and may surpass the maximum capacity of the soil. Figure 4.8 shows the soil moisture content of the impervious and vegetated ground columns at different depths. The first two layers underneath the impervious surface are impermeable. The soil water content in these layers is less variable as it exhibits reduced interaction with the atmosphere and vegetation roots. However, the upper layers of the vegetated ground soil column exhibit more variations and are significantly influenced by the amount of precipitation. Deeper layers of soil are less influenced by the weather conditions and show variation at the larger time scales. The pattern of annual variation of soil moisture is in reasonable agreement with the study by Meili et al. (2020) [129].

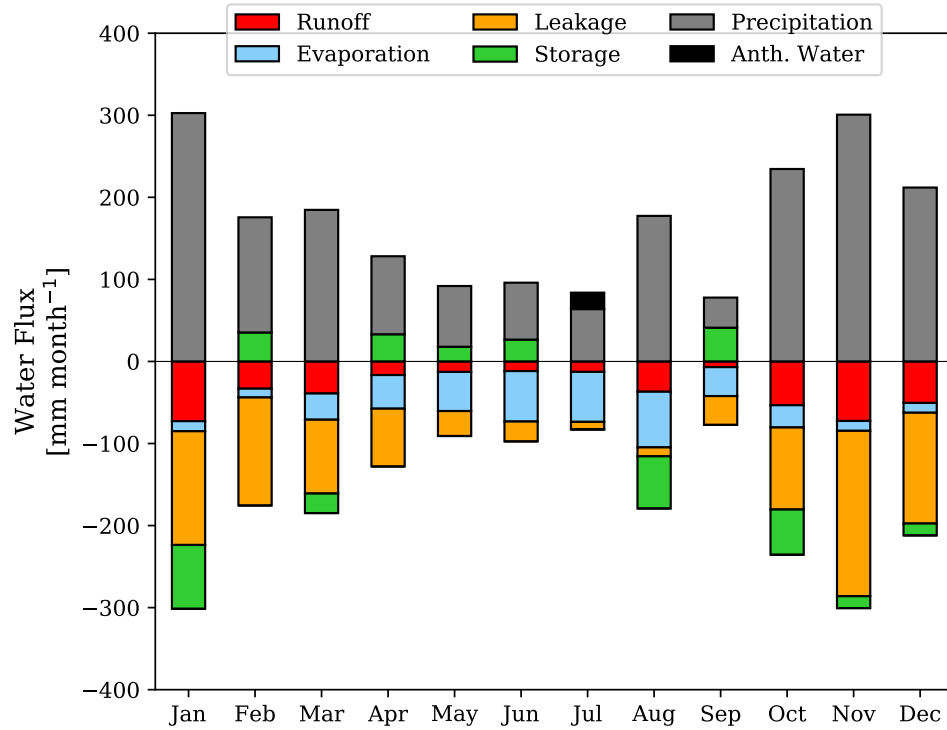


Figure 4.7: Monthly variation of water balance components for Vancouver in 2007; hourly terms in the water balance equation are integrated over time to calculate the monthly magnitude for all sink and source terms.

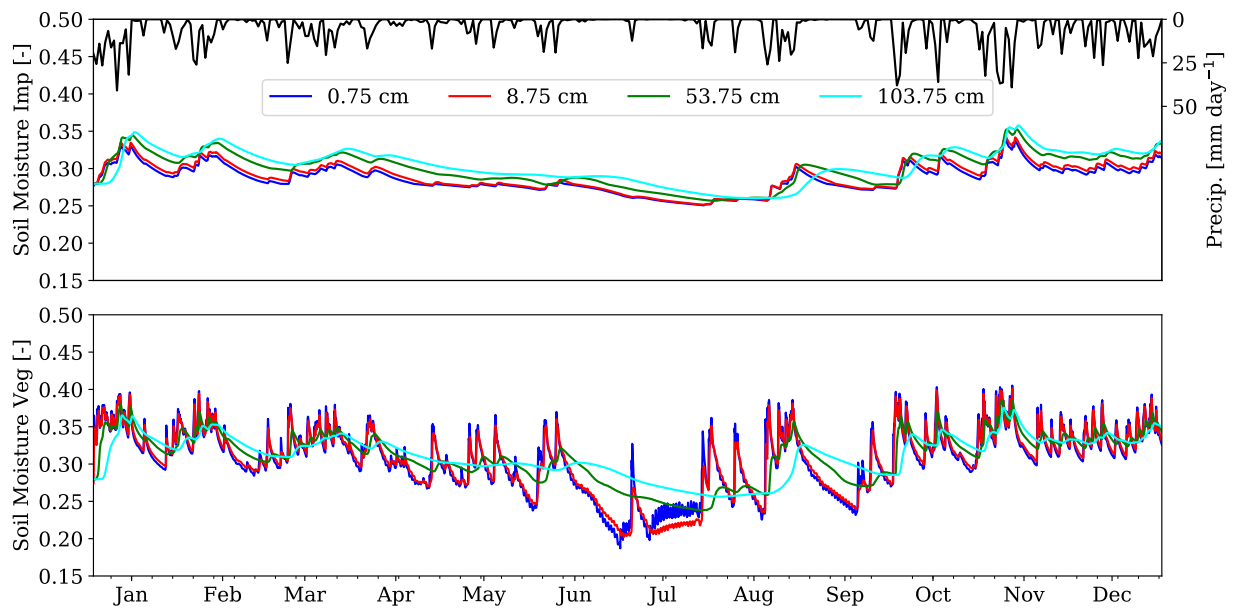


Figure 4.8: Soil moisture content in soil columns of impervious ground (top) and vegetated ground (bottom) at 0.75, 8.75, 53.75, and 103.75 [cm] depth measured from the surface, positive, downward into the soil over the course of a year in Vancouver; the black line is daily precipitation [mm day⁻¹].

4.3.3 Effect of Urban Trees on Model Output Variables

The building cooling energy demand and outdoor thermal comfort are major concerns during the warm seasons in different climate zones. As discussed in Section 3.3.3, the countermeasure of urban trees can mitigate the negative impacts of urban overheating and cool down the outdoor air temperature. Based on outdoor environmental conditions, the amount of energy received, emitted, and stored in the building envelop can directly affect the building energy performance and reciprocally the building waste heat released into the urban atmosphere. Urban trees provide shade and decrease wall temperatures, which reduce the amount of solar radiation fluxes at the warm walls and transmission of heat through the building envelop by conduction. The mitigation of the outdoor air temperature due to the presence of trees can also reduce the sensible heat flux between the building surfaces and the atmosphere [79, 188, 195, 198]. Thus, it is expected that trees may regulate the building energy performance.

The capability of VCWG v2.0.0 to take into account these effects is assessed by investigating three cases with LAI [$\text{m}^2 \text{m}^{-2}$] representing trees leaf area indices of 1, 2, and 3 [$\text{m}^2 \text{m}^{-2}$], by model simulations for Vancouver in July. The model is forced by ERA5 dataset at the top of the domain. The other model input variables are listed in Table 4.4. More vegetation acts to increase latent heat flux and specific humidity but to reduce air temperature and sensible heat flux during daytime, which is evident in Figure 4.9. Such effects not only can improve thermal comfort at the pedestrian level, but also can reduce the building energy consumption in the summertime, as shown in Figure 4.10. The average of daily maximum building energy fluxes, including dehumidification demand, cooling demand, and building waste heat, are calculated for July. The addition of more vegetation by increasing LAI from 1 to 3 [$\text{m}^2 \text{m}^{-2}$] can reduce the cooling energy demand and building waste heat by 25% and 15%, respectively. This energy saving is mainly attributed to the effect of tree-shading and consequent reduction of available solar radiation flux at the walls, as well as evapotranspiration to reduce sensible heat flux. The analysis obtained from this exploration is in reasonable agreement with previous work [4, 184, 198]. The simulation results of ENVI-met model in Thessaloniki, Greece, resulted in saving of cooling energy demand by 13% to 15%, depending on the planting scenario [198]. Other studies have reported that shade by trees can reduce the cooling energy demand by 25% for a residential building in Los Angeles [4] and by 10% to 50% for residential buildings in different climate zones in California [184].

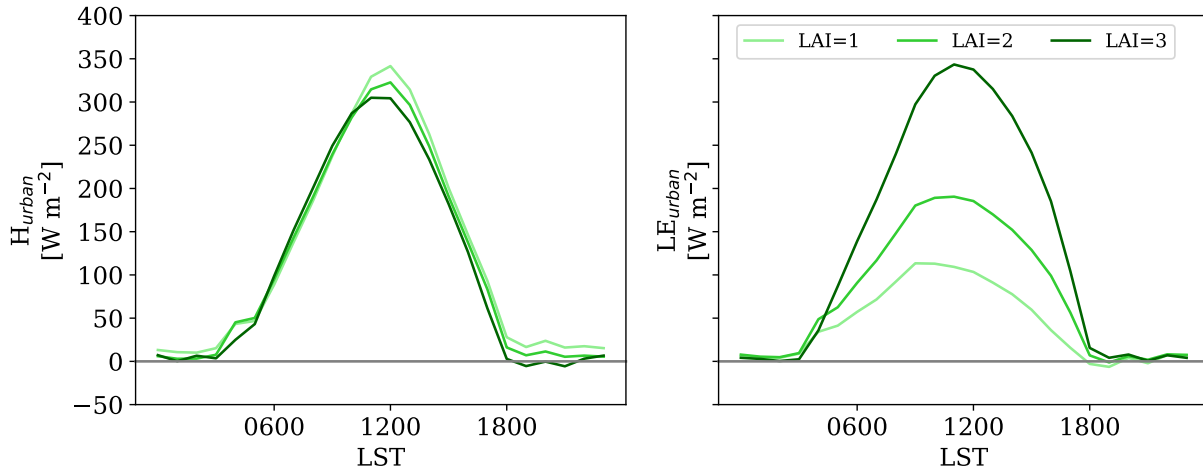


Figure 4.9: Effect of urban trees on the sensible and latent heat fluxes above the canyon in July. The heat fluxes are diurnally averaged at the height of 30 [m] from ground in July 2007 in Vancouver.

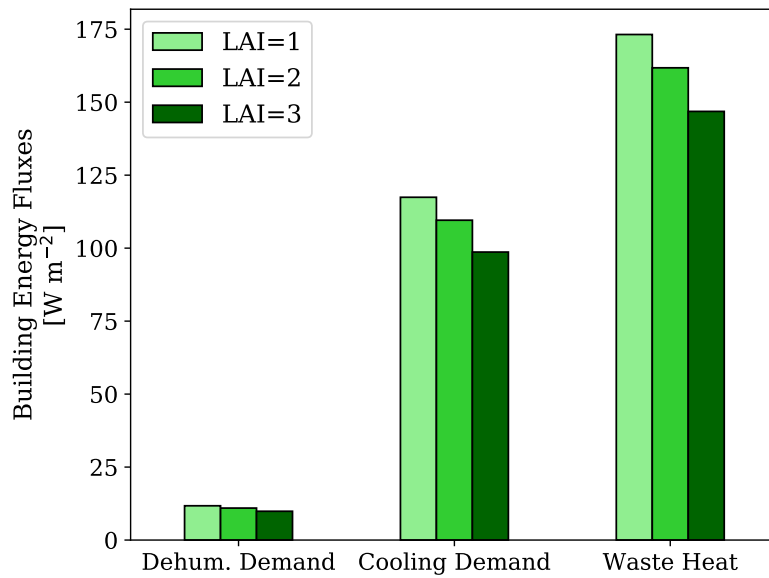


Figure 4.10: Effect of urban trees on the dehumidification demand, cooling energy demand, and waste heat of building. The building energy fluxes are mean of daily maximum in July 2007 in Vancouver.

4.3.4 Effect of Low Vegetation on Model Output Variables

Vegetation can alter the energy and water balance in the urban area and ultimately mitigate the negative impacts of UHI and urban flooding during extreme climate events. The effect of low vegetation on urban heat fluxes and water budget terms are assessed for Vancouver in the summer. The other model input variables are listed in Table 4.4. Increasing fraction of ground covered by low vegetation (f_{veg}) from 0.2 to 0.8 can reduce Bowen ratio (ratio of sensible heat flux to latent heat flux) of the urban area from 2 to 1 (see Figure 4.11). This suggests that not only trees can regulate the urban climate variables, but also low vegetation can reduce the amount of urban warming. Urban vegetation also has the desired effect of reducing flood hazards in the urban area. As shown in Figure 4.12, increasing f_{veg} from 0 to 1 can substantially decrease the surface runoff from 1.7 [mm day⁻¹] to almost zero, while evaporation flux and deep leakage increase. The results from this exploration are consistent with the simulation results from the UT&C model, where increasing f_{veg} from 0 to 1 for a case study in Singapore resulted in the reduction of surface runoff of 4.5 [mm day⁻¹] to zero with mean daily rainfall of 5 [mm day⁻¹] [129].

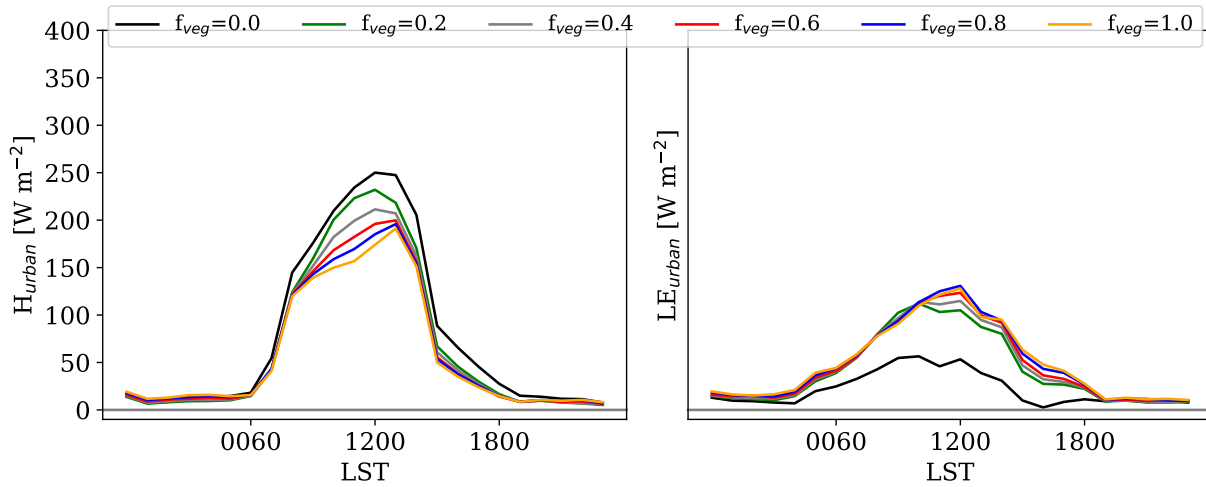


Figure 4.11: Effect of low vegetation coverage (f_{veg}) on urban sensible and latent heat fluxes [$W m^{-2}$] above the canyon for Vancouver in July 2007; f_{veg} varies from 0 (road is all impervious surface) to 1 (road is all vegetation).

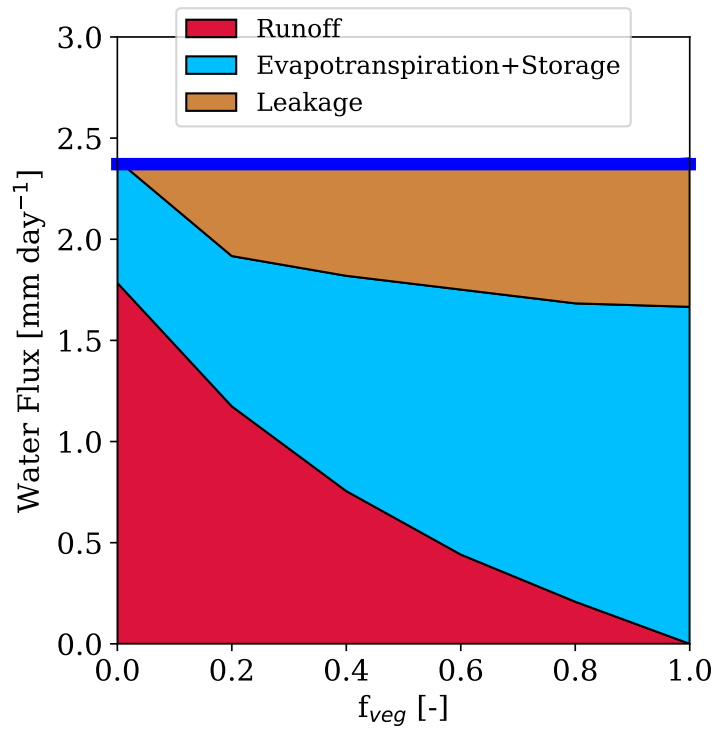


Figure 4.12: Effect of low vegetation coverage (f_{veg}) on mean daily water budget terms [mm day⁻¹] for Vancouver in July 2007; storage term is not significant, so it is added to the evaporation term; f_{veg} varies from 0 (road is all covered by impervious surface) to 1 (road is all covered by vegetation); blue line is mean daily rainfall [mm day⁻¹].

4.3.5 Effects of Green and Cool Roofs on Model Output Variables

Given the growing demand for energy in urban areas, numerous energy saving technologies have been employed to mitigate the environmental effects of buildings and improve building energy performance. Green and cool roofs are common technologies for reducing heat in urban areas, building energy demand, and moderating roof and canyon surface temperatures. Roof vegetation provides a natural cooling system, insulates the building envelop from direct exposure to solar radiation, regulates the temperature and humidity of urban environment, and reduces adverse effects of extreme rainfall events due to high water storage capacity (see Figure 4.13). He et al. (2020) [77] simulated the performance of a building with green roof in Shanghai and showed that this technology can save the cooling energy demand by 6.2%. Cool roofs with radiative properties of high solar albedo and high thermal emissivity, reduce urban heat, surface temperature, and improve building energy performance. Such urban environment regulation is accomplished by reflecting more solar radiation fluxes and absorbing less heat, compared to the standard roofs [45, 62]. Simulation results obtained from integrating BEP-BEM into WRF in a semi-arid urban environment (Phoenix and Tucson) showed that cool roofs can reduce the cooling energy demand by 14% [177].

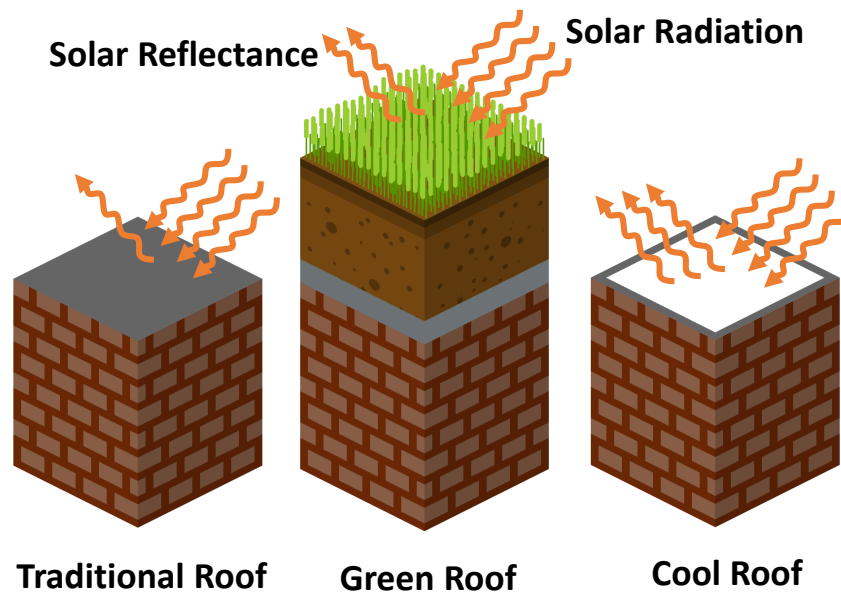


Figure 4.13: Comparison between the response of traditional, green, and cool roofs to solar radiation fluxes.

The effects of green and cool roofs on urban heat mitigation, roof surface temperature, and building energy performance are studied by simulating VCWG for an entire year in Vancouver. For the base case simulation, the roof surface is all covered by impervious surface and the radiative properties are as listed in Table 4.4. For the green roof scenario, half of the roof surface is covered by low vegetation with leaf area index (LAI) of 2.5 [$\text{m}^2 \text{m}^{-2}$] and soil layer thickness of 100 [mm]. To investigate the environmental effect of a cool roof, the surface albedo is increased to 0.7 [-], which is common for roofs coating with high reflective material [77].

Figure 4.14 compares the mean diurnal variation of urban sensible heat flux of the base, green roof, and cool roof cases in different seasons. Green and cool roofs can reduce daytime urban sensible heat flux by 40% and 18% during warm months, respectively. Due to shorter daytime length in the cold months, the cooling effects of green and cool roofs are less significant. Cool roofs can decrease daytime roof surface temperatures by 10 [K] in the summer with no change in nighttime surface temperatures, as expected (see Figure 4.15). While green roofs reduce surface temperatures to a lesser extent than cool roofs, they can decrease temperature fluctuations more effectively, particularly in warm months. Plant type, the fraction of roof vegetation coverage, and soil properties control the green roof performance. In terms of annual building energy performance, buildings with cool roofs save 16.1% cooling energy demand and 16.0% dehumidification demand. However, buildings with green roofs are less efficient and only save 5.2% cooling energy demand and 5.0% dehumidification energy demand. Figure 4.16 illustrates the maximum building energy loads and sensible waste heat from buildings to the atmosphere for different seasons. It is worth noting that these technologies work more effectively in the warm months as they can increase heating demand during the cold months due to their cooling effects, which can be observed from this analysis. Additionally, green and cool roofs reduce annual building waste heat by 4% and 1%, respectively, and they are more useful during the warm months.

4.3.6 Variation of Local Climate Zone and Model Output Variables

The local urban climate is primarily influenced by urban morphometric variables such as building plan area density, frontal area density, anthropogenic activities, and urban vegetation. There could be some pre-defined diurnal/seasonal schedule for human activities. However, some other factors, such as urban morphometric variables, could vary over a longer

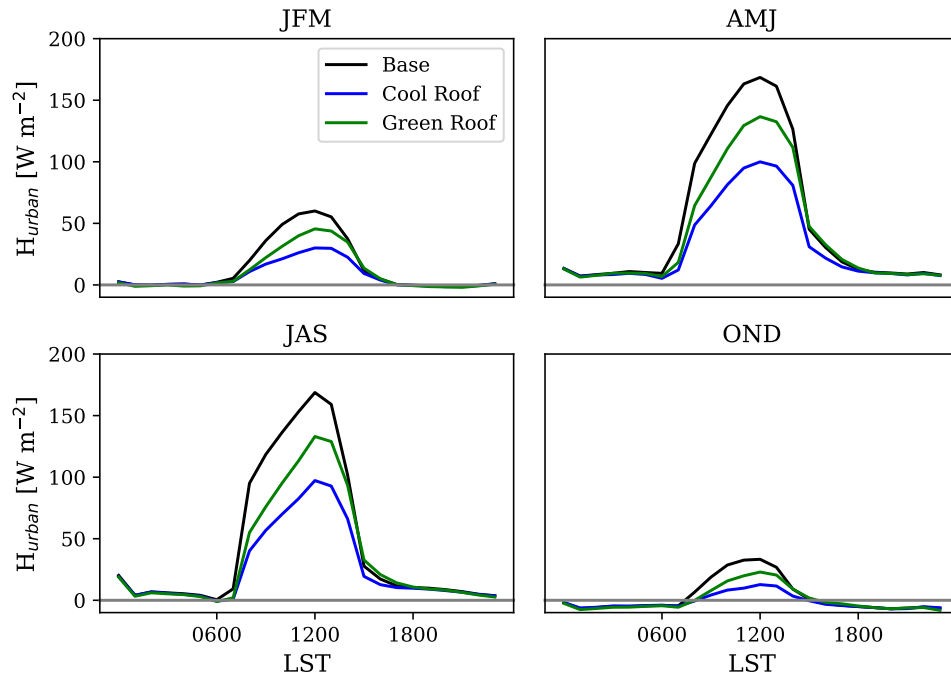


Figure 4.14: Effects of green and cool roofs on urban sensible heat flux [$W m^{-2}$] in different seasons; the sensible heat fluxes are diurnally-averaged over January-February-March (JFM), April-May-June (AMJ), July-August-September (JAS), and October-November-December (OND) for Vancouver in 2007.

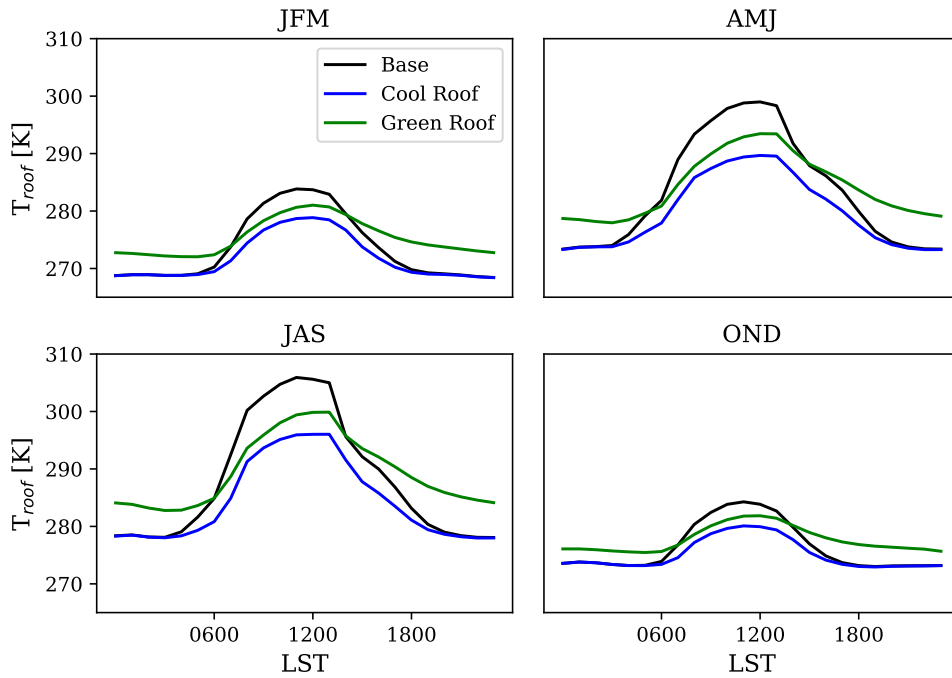


Figure 4.15: Effects of green and cool roofs on roof surface temperature [K] in different seasons; the surface temperatures are diurnally-averaged over January-February-March (JFM), April-May-June (AMJ), July-August-September (JAS), and October-November-December (OND) in Vancouver 2007.

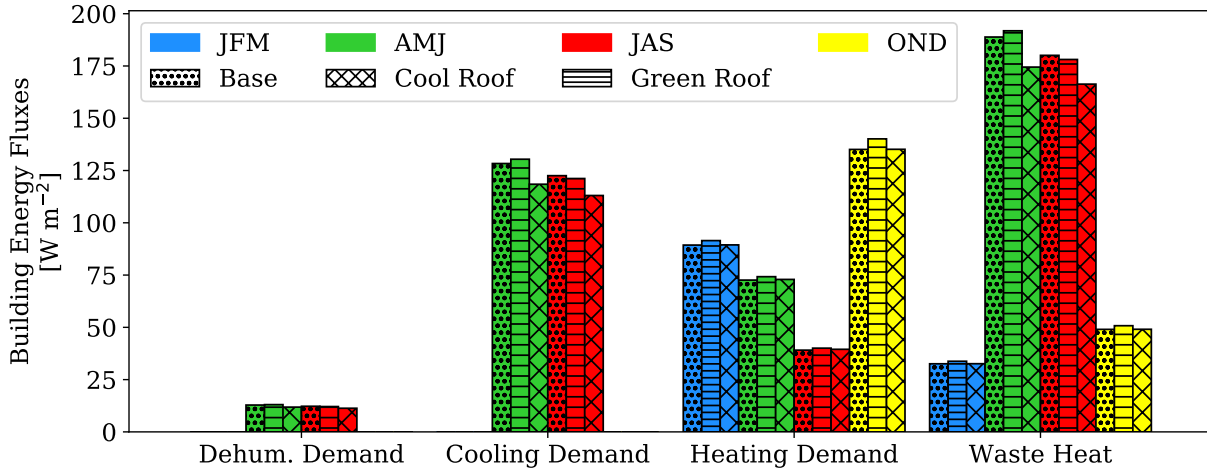


Figure 4.16: Effects of green and cool roofs on building energy performance in different seasons; the building energy fluxes are mean of daily maximum over January-February-March (JFM), April-May-June (AMJ), July-August-September (JAS), and October-November-December (OND) in Vancouver 2007.

time scale. One may experience different climate conditions within a city, which could be more sensible by traveling from the high-density built-up regions to the areas with more open space and ultimately rural areas. Stewart and Oke (2012) [192] developed the Local Climate Zone (LCZ) classification that identifies a region based on its ability to modify local surface climates. The surface thermal properties, land cover and land structure define LCZ 1 as compact highrise to LCZ 9 as sparsely built areas. In this classification LCZ 10 is considered as an area with heavy industrial activities and LCZs A to G represent natural areas, which are out of scope of this thesis (For further details, readers are referred to Stewart and Oke (2012) [192]).

In this section, the capability of VCWG to simulate climate variables within the urban roughness sublayer for a typical city is investigated. It is assumed that the urban area is extended from LCZ 1 at the center to LCZ 9 far from the center. Figure 4.17 shows the spatial variation of plan area density (λ_p [-]), leaf area index of urban trees (LAI_{tree} [$m^2 m^{-2}$]), canyon aspect ratio (H/W [-]), and the fraction of ground covered by vegetation (f_{veg} [-]). The building area density and canyon aspect ratio vary from 0.6 to 0.2 [-] and 3.0 to 0.2 [-], respectively. Such a setup alongside with the urban trees is accompanied with ground-sky view factor variations from 0.15 [-] in the compact highrise region to 0.9 [-] in the sparsely built region. The range of variation of these parameters is consistent with the

typical properties that are considered for LCZ 1 to LCZ9 [192]. More high and low vegetation covers are considered as moving away from high-density built-up areas by changing f_{veg} for ground and LAI_{tree} from 0.1 to 0.85 and 1 to 4 [$\text{m}^2 \text{m}^{-2}$], respectively.

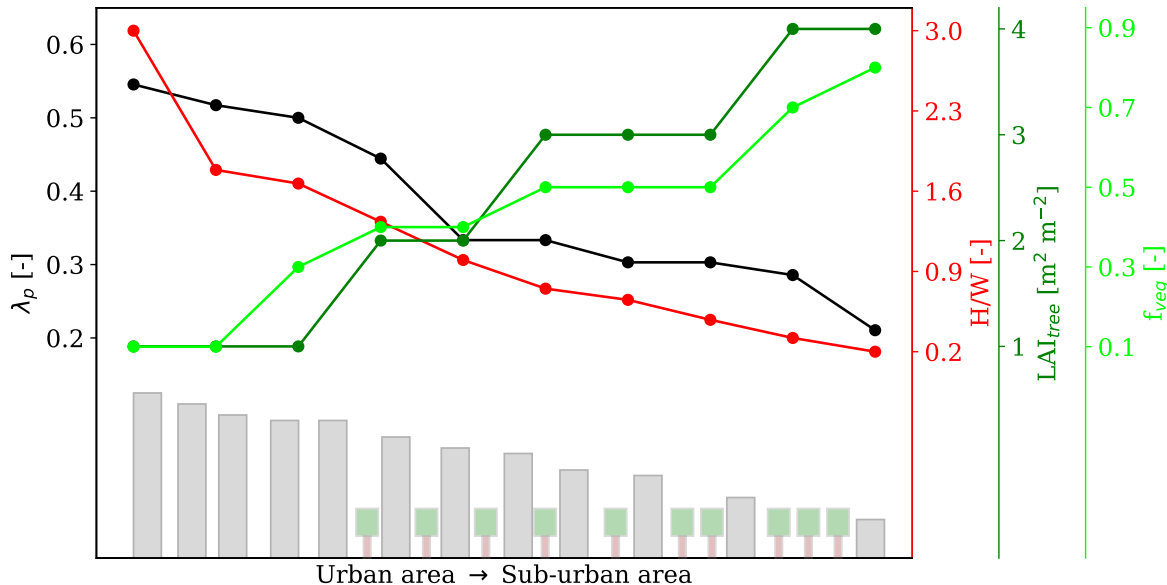


Figure 4.17: Spatial variation of urban morphometric parameters including plan area density (λ_p [-]), leaf area index of urban trees (LAI_{tree} [$\text{m}^2 \text{m}^{-2}$]), canyon aspect ratio (H/W [-]), and fraction of ground covered by vegetation (f_{veg} [-]) for a typical city.

It has been observed that nocturnal UHI increases as urban heat flux increases and wind speed decreases [151, 156]. As shown in Figure 4.19, built-up areas slow down wind speed within the canyon and consequently reduce turbulent mixing. Lower magnitude of forcing wind speed during nighttime facilitates trapping of heat within the canyon and increasing air temperatures. Figures 4.18 and 4.20 show larger magnitudes of air potential temperatures and sensible heat fluxes in the compact highrise region, respectively. Thus, higher temperature in high-density built-up areas than the surrounding sub-urban and rural areas can lead to nocturnal UHI. For the daytime, areas with higher canyon aspect ratio (H/W [-]) trap building released waste heat, which can lead to higher surface and air potential temperatures and urban sensible heat fluxes (see Figures 4.18 and 4.20). As discussed earlier, urban vegetation can significantly cool down urban environments. Increasing urban vegetation as moving away from the urban center can increase latent heat fluxes by 100 [W m^{-2}], particularly during daytime (see Figure 4.20). This process comes with lowering sensible heat

fluxes by $150 \text{ [W m}^{-2}\text{]}$ and canyon air temperatures by 3 [K] , as shown in Figures 4.18 and 4.20, respectively.

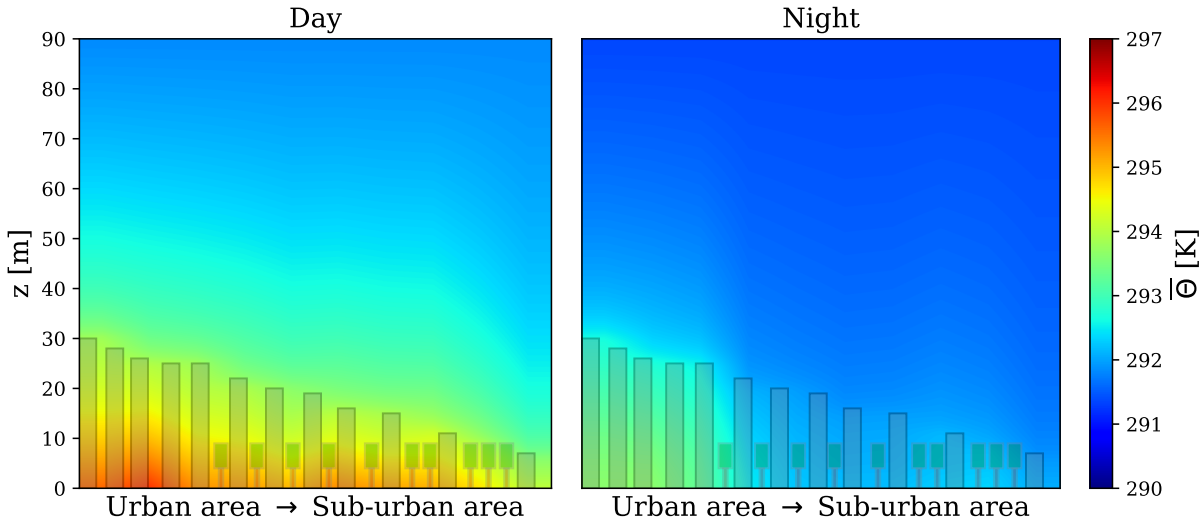


Figure 4.18: Color plots of air potential temperature distribution from Local Climate Zone (LCZ) 1 to LCZ 9 at 1300 LST (left) and 2100 LST (right) in the summer; simulations are for Vancouver in 2007 for July.

4.3.7 Spatial Distribution of Model Output Variables for a Neighborhood

As discussed earlier, urban areas are characterized by high spatial variability of surface properties, land coverage, and population density. Hence, scientists, engineers, and urban planners require accurate estimation of urban climate and weather variables with reasonable spatial resolution.

VCWG is equipped with a pre-processor function to automate the Geographic Information System (GIS) processes. At the first step, if a rural dataset is required to force the model, the pre-processor finds the nearest rural area in the upwind of the urban site. If the model is set to run using the top forcing approach, the appropriate ERA5 dataset above the urban area can be retrieved. Urban morphology can be obtained from the geographic file provided by the user or other source of land cover dataset including OpenStreetMap [160], OSMnx [17], and World Urban Database and Access Portal Tools (WUDAPT) [24]. OSMnx

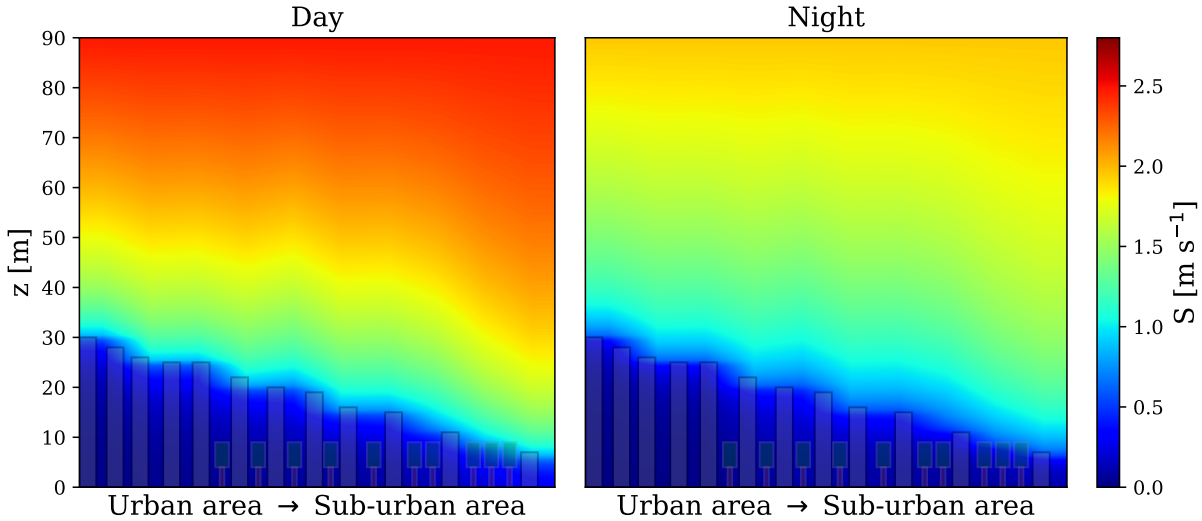


Figure 4.19: Color plots of wind speed distribution from Local Climate Zone (LCZ) 1 to LCZ 9 at 1300 LST (left) and 2100 LST (right) in the summer; simulations are for Vancouver in 2007 for July.

is a tool that can analyze street network, retrieve building footprints, elevation, and download data from OpenStreetMap data. WUDAPT characterizes the built-up areas using the LCZ classification approach. In the current analysis, the Vancouver geometric parameters are obtained from the City of Vancouver open data portal [38], and OSMnx and WUDAPT are used in a consistent way to modify the dataset. Every grid cell of this raster file contains building geometries, fraction of ground covered by vegetation, bare soil, impervious surface, land cover, and view factors. The view factors are calculated as a function of urban morphometric parameters using the ray tracing method. Then VCWG simulations are conducted for each latitude and longitude of the raster file and calculate model output variables for each grid cell independently. Figure 4.21 shows the urban area in Vancouver considered for this simulation. VCWG is simulated for 7 days in 2007 starting from July first with a time step of 5 [min] and vertical resolution of 1 [m]. The horizontal spatial resolution of the domain is 100 [m] (see Figure 4.22), which is consistent with the WUDAPT dataset.

Figures 4.23 to 4.25 depict the mean spatial distribution of canyon potential temperature, sensible heat flux, and latent heat flux during daytime (1100 to 1300 LST) and nighttime (2200 to 0000 LST). It is evident that the residential neighborhood close to Shaughnessy Park (latitude = 49.256° , longitude = -123.135°), where it is highly covered by low and high

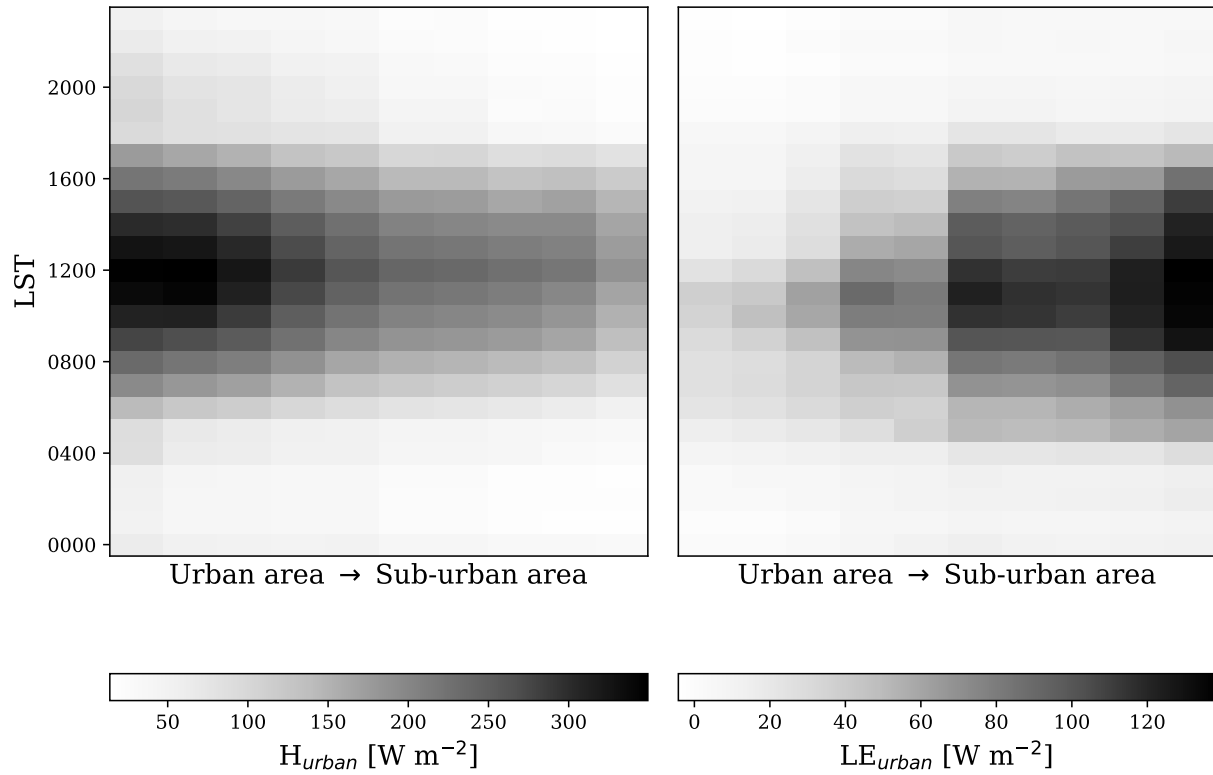


Figure 4.20: Diurnal variation of sensible heat flux (left) and latent heat flux (right) of urban and sub-urban areas for LCZ 1 to LCZ 9.

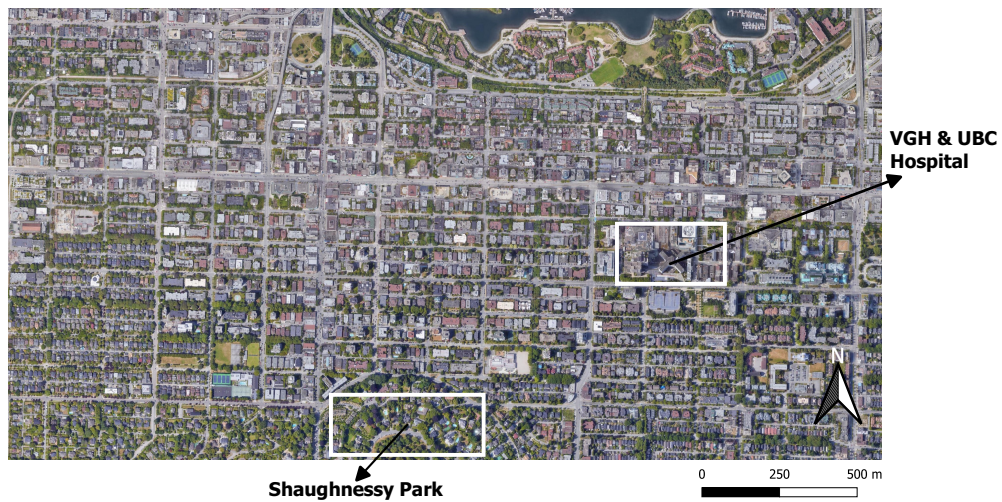


Figure 4.21: The VCWG domain for spatial analysis in Vancouver.

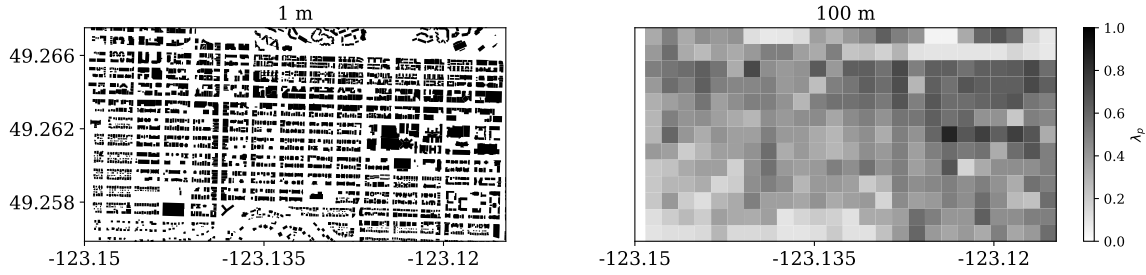


Figure 4.22: Plan area density (λ_p [-]) calculated at 1 [m] resolution (left) and 100 [m] resolution (right) in Vancouver.

vegetation, has the low magnitude of sensible heat flux and high magnitude of latent heat flux. Such a cooling effect provides lower temperatures in this neighborhood. The eastern part of the simulation domain (latitude = 49.265° to 49.270°, longitude = -123.128° to -123.120°) is mainly occupied with high-rise buildings (such as Vancouver General Hospital (VGH) & UBC Hospital Foundation and BC Cancer Research Center) and less amount of vegetation, which leads to higher cooling demand and building waste heat (see Figure 4.26). So, the nighttime canyon air potential temperature is expected to be higher within this region, as well-captured by VCWG (see Figure 4.23).

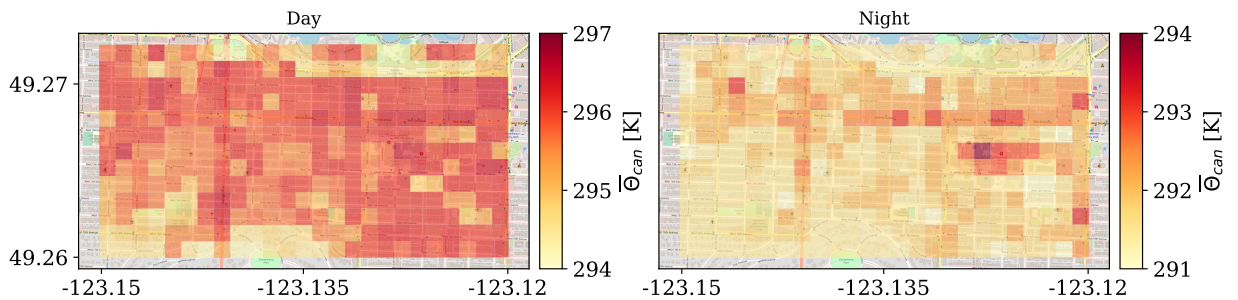


Figure 4.23: Spatial distribution of mean daytime (left) and nighttime (right) canyon air potential temperature Θ_{can} [K] from July 1 to July 7 in Vancouver in 2007; a neighborhood is chosen in the Lower Main Land.

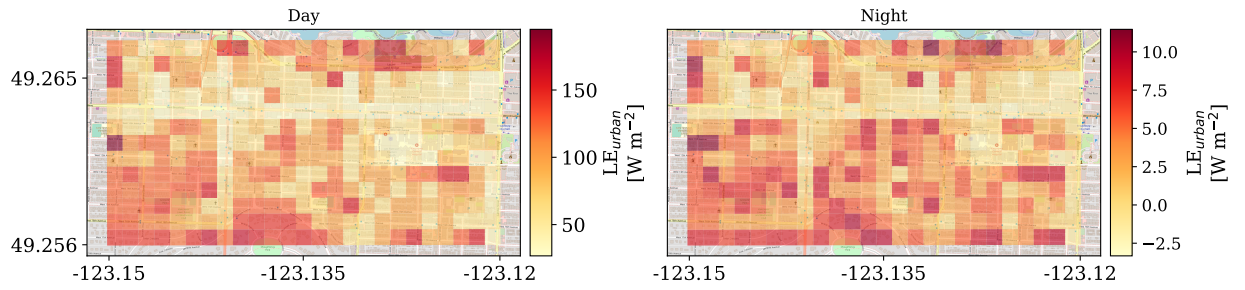


Figure 4.24: Spatial distribution of mean daytime (left) and nighttime (right) latent heat flux LE_{urban} [$W m^{-2}$] from July 1 to July 7 in Vancouver in 2007; a neighborhood is chosen in the Lower Main Land.

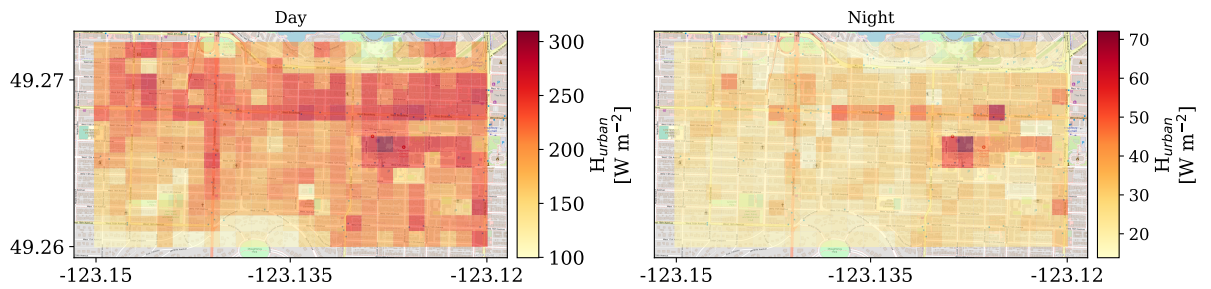


Figure 4.25: Spatial distribution of mean daytime (left) and nighttime (right) sensible heat flux H_{urban} [$W m^{-2}$] from July 1 to July 7 in Vancouver in 2007; a neighborhood is chosen in the Lower Main Land.

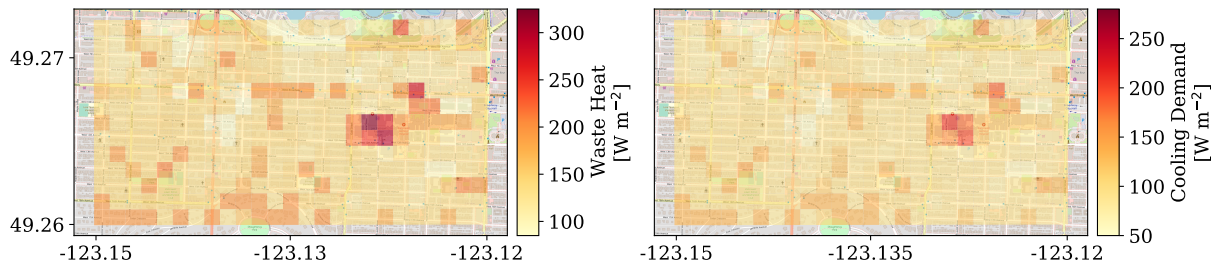


Figure 4.26: Spatial distribution of daily maximum building waste heat (left) and cooling demand (right) [$W m^{-2}$] from July 1 to July 7 in Vancouver in 2007; a neighborhood is chosen in the Lower Main Land.

Chapter 5

Summary and Conclusions

This thesis has been motivated by the lack of a computationally-efficient and operationally-simple urban microclimate model, which considers the effects of urban vegetation, urban hydrology, building energy, and the connection to the surrounding rural area. The major developments in this thesis include coupling the surface energy and water balance models with a vertical diffusion model, which provides a dynamic interaction with the building energy fluxes, and provide a climate-prediction tool that can perform spatial urban climate variable analysis from the neighborhood scale to the city scale. The developed model is called the Vertical City Weather Generator (VCWG) and has been integrated and refined at two stages.

The first version, VCWG v1.3.2 integrates a rural model, an urban vertical diffusion model, a radiation model with trees, and a building energy model. Forced with weather data from a nearby rural site, the rural model is used to solve for the vertical profiles of potential temperature, specific humidity, and friction velocity at 10 m a.g.l. The rural model also calculates a horizontal pressure gradient. The rural model outputs are applied to a vertical diffusion urban microclimate model that solves vertical transport equations for potential temperature, momentum, specific humidity, and turbulence kinetic energy. The urban vertical diffusion model is also coupled to the radiation and building energy models using two-way interaction. The aerodynamic and thermal effects of urban elements, surface vegetation, and trees are considered. This version of VCWG does not include an urban hydrologic model to account for moisture exchange processes at surfaces and subsurfaces.

In the next version, VCWG v2.0.0 accounts for the surface and sub-surface water balance that lead to the adequate representation of moisture sources/sinks in the vertical diffusion model. This version of VCWG also provides the capability to be forced from the top of

the urban domain using measurements or meso-scale model variables, eliminating the need for a rural model using mesoscale data products if desired. This version of VCWG is also equipped with utility codes to be able to be simulated on a spatial grid at neighborhood or city scales automatically.

The models are evaluated against field measurements that are conducted in Basel, Switzerland (BUBBLE dataset) and the Sunset neighborhood in Vancouver, Canada. The capability of the models is assessed by conducting various explorations with respect to building energy performance, urban hydrology, climate zones, urban morphometric parameters, and seasonal variations. These analyses demonstrate that VCWG is well-designed for many practical applications in urban planning, architecture, and engineering consulting.

5.1 Vertical City Weather Generator (VCWG) v1.3.2

The Vertical City Weather Generator (VCWG) v1.3.2 is developed to calculate vertical profiles of meteorological variables including, potential temperature, wind speed, specific humidity, and turbulence kinetic energy in an urban area. The VCWG v1.3.2 is composed of four sub-models for ingestion of urban parameters and meteorological variables in a rural area (as input and boundary conditions) and prediction of the meteorological variables in a nearby urban area, the building energy performance variables, and the short and longwave radiation transfer processes. VCWG v1.3.2 combines elements of several previous models developed by Santiago and Martilli (2010) [182], Bueno et al. (2014) [29], Krayenhoff (2014)[98], Krayenhoff et al. (2015) [101], and Meili et al. (2020)[129] to generate a model with the ability to predict vertical profiles of urban meteorological variables, forced by rural measurements, and with two-way coupling with both building energy and radiation models.

To evaluate VCWG v1.3.2, its predictions of potential temperature, wind speed, specific humidity, sensible heat flux, and latent heat flux (on top of the urban domain) are compared to observations of the Basel UrBan Boundary Layer Experiment (BUBBLE) micro-climate field campaign for eight months from December 2001 to July 2002 [37, 170]. The model evaluation indicates that the VCWG v1.3.2 predicts vertical profiles of meteorological variables in reasonable agreement with field measurements. The average BIAS, RMSE, and R^2 for potential temperature are 0.25 [K], 1.41 [K], and 0.82, respectively. The average BIAS, RMSE, and R^2 for wind speed are 0.67 [m s^{-1}], 1.06 [m s^{-1}], and 0.41, respectively. The average BIAS, RMSE, and R^2 for specific humidity are 0.00057 [kg kg^{-1}], 0.0010 [kg kg^{-1}], and 0.85, respectively. In addition, the average BIAS, RMSE, and R^2 for Urban Heat Island

(UHI) are 0.36 [K], 1.2 [K], and 0.35, respectively. Based on the evaluations, the model performance is comparable to the performance of similar models.

The performance of the model is further explored to investigate the effects of urban configurations such as plan and frontal area densities, varying levels of vegetation, building energy configuration, radiation configuration, seasonal variations, and different climate zones on the model predictions. Sensitivity experiments are conducted by changing the building plane area density λ_p [-], frontal area density λ_f [-], and leaf area density profile, and the results show that VCWG v1.3.2 can reasonably capture the change in urban climate variables. The performance of the building energy model is assessed by investigation of the effect of building type, coefficient of performance of the air conditioning system, thermal efficiency of the heating system, and location of building waste heat release on building energy fluxes and the consequent effects on the outdoor environment. The radiation model responses to different canyon aspect ratios and street canyon axes are assessed. In a separate exploration, VCWG v1.3.2 adequately captures the seasonal variation of vertical profiles of potential temperature, wind speed, specific humidity, and turbulence kinetic energy. The VCWG model is further explored by predicting UHI [K] in different cities with different climate zones, including Buenos Aires, Vancouver, Osaka, and Copenhagen, and the results are in great agreement with the previous studies. The exploration results also show results that agree with known urban physical processes and observations.

The results obtained from this model development show that the urban microclimate model VCWG v1.3.2 can successfully extend the spatial dimension of preexisting bulk flow (single-layer) urban microclimate models in the vertical direction, while it also considers the relationship of the urban microclimate model to the rural meteorological measurements and the building energy conditions. The effects of the key urban elements such as building configuration, building energy systems (e.g. location of condensers and exhaust stacks), surface vegetation, and trees are considered.

5.2 Vertical City Weather Generator (VCWG) v2.0.0

While the performance of VCWG v1.3.2 is consistent with expectations and comparable to the other urban climate models, simple parameterization of moisture sources/sinks and lack of forcing datasets near surface levels at rural sites restrict its application to non-rainy days and locations with available rural measurements. The development of VCWG v2.0.0 was motivated by these limitations.

VCWG v2.0.0 is composed of not only the predecessor version’s sub-models (rural model, urban vertical diffusion model, building energy model, radiation model, and urban surface energy balance model) but also an urban hydrology model, and alternative options for the forcing variables in the rural site and boundary condition at the top of the urban domain using mesoscale data products. The urban hydrology model, adopted from Meili et al. (2020) [129], is dynamically linked to the surface energy balance model and predicts surface and subsurface water balances and ecophysiological behavior of urban trees and low vegetation at the ground and roof levels. The surface energy balance in rural areas can be determined using the Penman-Monteith method [11] or Bowen ratio approach. To overcome the limitation of availability of rural forcing variables, VCWG v2.0.0 can retrieve data from the ERA5 reanalysis dataset. Alternative to the rural model, VCWG v2.0.0 can force the urban model based on the forcing variables at the top of the domain, which is provided by the user. This option is particularly useful when the user wants to couple the model with a mesoscale model. VCWG v2.0.0 is also equipped with a function that can automate the Geographic Information System (GIS) processes to simulate urban climate within a spatial raster dataset.

To evaluate VCWG v2.0.0, its predictions of potential temperature, wind speed, and specific humidity are compared to the BUBBLE dataset and the results from VCWG v1.3.2. The model evaluation indicates that the VCWG v2.0.0 improves the prediction of vertical profiles of meteorological variables. The average BIAS, RMSE, and R^2 for potential temperature are -0.53 [K], 0.56 [K], and 0.98 , respectively. The average BIAS, RMSE, and R^2 for wind speed are -0.46 [m s^{-1}], 0.44 [m s^{-1}], and 0.46 , respectively. The average BIAS, RMSE, and R^2 for specific humidity are 0.0000 [kg kg^{-1}], 0.0003 [kg kg^{-1}], and 0.98 , respectively. The capability of VCWG v2.0.0 to simulate urban sensible and latent heat fluxes is also evaluated against BUBBLE and Vancouver Sunset datasets. The results show that VCWG v2.0.0 can predict the heat fluxes in reasonable agreement with the observed datasets. For the BUBBLE case, the inclusion of urban hydrology reduces BIAS and RMSE of sensible heat flux by 23.2 [W m^{-2}] and 29.2 [W m^{-2}], respectively, and increases the R^2 by 0.3 [-]. The statistics for latent heat flux also exhibit an improvement, as BIAS and RMSE are decreased by 11.4 [W m^{-2}] and 14 [W m^{-2}] and R^2 is increased by 0.07 [-]. These statistics provide evidence that VCWG v2.0.0 represents an improvement relative to VCWG v1.3.2 because it provides more accurate predictions of urban climate variables.

Various explorations including seasonal variations, effects of trees on urban energy fluxes and building energy performance, effects of ground vegetation on urban water balance, performance of model in different Local Climate Zones (LCZ), effects of green and cool roofs

on model output variables, and spatial analysis of simulation results, are conducted to assess the performance of VCWG v2.0.0. For the seasonal analysis, model input parameters are prepared for an entire year in Vancouver, seasonal variation of sensible and latent heat fluxes, urban facade temperatures, building energy fluxes, and water budget terms are captured well. The model responses to precipitation are evident in the time series, where during or shortly after rain-fall events latent heat flux increases, sensible heat flux decreases, and surface runoff increases. Furthermore, depletion of soil moisture in warm months, when precipitation is less frequent and shorter, is well simulated by VCWG v2.0.0. Investigation of cooling effects of urban trees on building energy performance show that trees with LAI of 3 [$\text{m}^2 \text{m}^{-2}$] can reduce cooling energy demand by 25% compared to trees with LAI of 1 [$\text{m}^2 \text{m}^{-2}$]. The exploration on the effect of ground vegetation on water balance demonstrates that increasing low vegetation can reduce surface runoff to a great extent. In another exploration, green and cool roofs are shown to reduce the building cooling demand by 5.2% and 16.1%, respectively, in July in Vancouver, respectively. The capability of VCWG v2.0.0 to simulate climate variables within the urban roughness sublayer for Local Climate Zone (LCZ) 1 to LCZ 9 is investigated. The model is shown to adequately capture the trapping of heat in compact highrise zones. Finally, VCWG v2.0.0 is equipped with a pre-processor function to automate the (GIS) processes. This tool is able to simulate the model within a raster file, which describe the spatial distribution of urban morphometric parameters. This analysis is successfully accomplished with 100 [m] spatial resolution and 5 [min] temporal resolution for 7 days in July in Vancouver.

The results obtained from these evaluations and explorations show that VCWG v2.0.0 can successfully overcome the limitations of VCWG v1.3.2 and combine most of the necessary sub-models that are required for accurate prediction of urban climate variables.

5.3 Limitations and Future Work

While this thesis contributes to the development of a new urban climate model that overcomes several limitations of the previous studies, limitations remain. This section discusses the limitations of VCWG and provides suggestions for further model development and future work.

The model geometry is simplified as an urban canyon with symmetric and regular dimensions, which can be more realistically represented if more considerations are to be taken into account about nonuniform distribution of building dimensions. Also the building energy

model in VCWG is a single-zone model, assuming a uniform temperature with height in both indoor and outdoor environments. This limitation can be overcome by improving the radiation model, urban vertical diffusion model, and the building energy model so that wall and indoor temperatures can vary with height, allowing the development of a multi-zone building energy model. In addition, the horizontal advection from the rural area can be considered and parameterized in future work. This necessitates addition of urban boundary-layer models. Future studies can also focus on improvement of flow-field parameterization or include additional source/sink terms in the transport equations to model horizontal motions, eddies, and flow fluctuations in the urban area, which is realistically very three-dimensional and heterogeneous. VCWG can also be used as a diagnostic tool to investigate the simulation results obtained from complex models. Other sub-models (e.g. air pollution model) can be integrated into VCWG. The building energy model of VCWG can be adjusted to consider renewable energy technologies (e.g. solar collectors and wind turbines), which could result in more realistic estimation of building energy performance while using these technologies. In fact a version of VCWG v1.4.4 has been developed by Aliabadi et al. (2021) with such capability [9]. VCWG can be improved to include snow processes. Also, VCWG can be investigated and improved in terms of its prediction of urban climate variables during extreme meteorological events (e.g. storms and flooding). At present, the VCWG model can account for the spatial variation of urban micro-climate in a computationally-efficient manner independent of an auxiliary meso-scale model. However, there is still a lack of representation of meteorological processes that can only be captured by mesoscale models.

Bibliography

- [1] ADNOT, J., RIVIERE, P., MARCHIO, D., BECIRSPAHIC, S., LOPES, C., BLANCO, I., PEREZ-LOMBARD, L., ORTIZ, J., PAPA-KONSTANTNOU, N., DOUKAS, P., ET AL. Energy efficiency and certification of central air conditioners (EECCAC). *Study for the DG Transportation-Energy (DGTREN) of the Commission of the EU, Paris* (2003).
- [2] AFSHARI, A., AND RAMIREZ, N. Improving the accuracy of simplified urban canopy models for arid regions using site-specific prior information. *Urban Climate* 35 (2021), 100722.
- [3] AHMADI-BALOUTAKI, M., AND ALIABADI, A. A. A very large-eddy simulation model using a reductionist inlet turbulence generator and wall modeling for stable atmospheric boundary layers. *Fluid Dynamics* 56, 3 (2021), 413–432.
- [4] AKBARI, H. Shade trees reduce building energy use and CO₂ emissions from power plants. *Environmental Pollution* 116 (2002), S119–S126.
- [5] AKBARI, H., POMERANTZ, M., AND TAHA, H. Cool surfaces and shade trees to reduce energy use and improve air quality in urban areas. *Solar Energy* 70, 3 (2001), 295–310.
- [6] ALIABADI, A. A., KRAYENHOFF, E. S., NAZARIAN, N., CHEW, L. W., ARMSTRONG, P. R., AFSHARI, A., AND NORFORD, L. K. Effects of roof-edge roughness on air temperature and pollutant concentration in urban canyons. *Boundary-Layer Meteorology* 164, 2 (2017), 249–279.
- [7] ALIABADI, A. A., MORADI, M., AND BYERLAY, R. A. E. The budgets of turbulence kinetic energy and heat in the urban roughness sublayer. *Environmental Fluid Mechanics* (2021).
- [8] ALIABADI, A. A., MORADI, M., CLEMENT, D., LUBITZ, W. D., AND GHARABAGHI, B. Flow and temperature dynamics in an urban canyon under a comprehensive set of wind directions, wind speeds, and thermal stability conditions. *Environmental Fluid Mechanics* 19, 1 (2019), 81–109.

- [9] ALIABADI, A. A., MORADI, M., MCLEOD, R. M., CALDER, D., AND DERNOVSEK, R. How Much Building Renewable Energy Is Enough? The Vertical City Weather Generator (VCWG v1.4.4). *Atmosphere* 12, 7 (2021), 882.
- [10] ALIABADI, A. A., VERIOTES, N., AND PEDRO, G. A very large-eddy simulation (VLES) model for the investigation of the neutral atmospheric boundary layer. *Journal of Wind Engineering and Industrial Aerodynamic* 183 (2018), 152–171.
- [11] ALLEN, R. G., SMITH, M., PEREIRA, L. S., AND PERRIER, A. An update for the calculation of reference evapotranspiration. *ICID Bull.* 43, 2 (1994), 35–92.
- [12] ARMSON, D., STRINGER, P., AND ENNOS, A. R. The effect of tree shade and grass on surface and globe temperatures in an urban area. *Urban Forestry and Urban Greening* 11, 3 (2012), 245–255.
- [13] BARLOW, J. F. Progress in observing and modelling the urban boundary layer. *Urban Climate* 10 (2014), 216–240.
- [14] BASU, S., AND LACSER, A. A cautionary note on the use of Monin-Obukhov similarity theory in very high-resolution large-eddy simulations. *Boundary-Layer Meteorology* 163 (2017), 351–355.
- [15] BEST, M., AND GRIMMOND, C. S. B. Analysis of the seasonal cycle within the first international urban land-surface model comparison. *Boundary-Layer Meteorology* 146, 3 (2013), 421–446.
- [16] BLOCKEN, B. Computational fluid dynamics for urban physics: Importance, scales, possibilities, limitations and ten tips and tricks towards accurate and reliable simulations. *Building and Environment* 91 (2015), 219–245.
- [17] BOEING, G. OSMnx: New methods for acquiring, constructing, analyzing, and visualizing complex street networks. *Computers, Environment and Urban Systems* 65 (2017), 126–139.
- [18] BOHNENSTENGEL, S. I., HAMILTON, I., DAVIES, M., AND BELCHER, S. E. Impact of anthropogenic heat emissions on London’s temperatures. *Quarterly Journal of the Royal Meteorological Society* 140, 679 (2014), 687–698.
- [19] BORNSTEIN, R. D. The two-dimensional URBMET urban boundary layer model. *Journal of Applied Meteorology* 14, 8 (1975), 1459–1477.
- [20] BOTTER, G., PORPORATO, A., RODRIGUEZ-ITURBE, I., AND RINALDO, A. Basin-scale soil moisture dynamics and the probabilistic characterization of carrier hydrologic flows: Slow, leaching-prone components of the hydrologic response. *Water Resources Research* 43, 2 (2007), W02417.

- [21] BOURBIA, F., AND BOUCHERIBA, F. Impact of street design on urban microclimate for semi arid climate (Constantine). *Renewable Energy* 35, 2 (2010), 343–347.
- [22] BRITTER, R. E., AND HANNA, S. R. Flow and dispersion in urban areas. *Annu. Rev. Fluid Mech* 35, 1 (2003), 469–496.
- [23] BROADBENT, A. M., COUTTS, A. M., NICE, K. A., DEMUZERE, M., KRAYENHOFF, E. S., TAPPER, N. J., AND WOUTERS, H. The air-temperature response to green/blue-infrastructure evaluation tool (TARGET v1. 0): an efficient and user-friendly model of city cooling. *Geoscientific Model Development* 12, 2 (2019), 785–803.
- [24] BROUSSE, O., MARTILLI, A., FOLEY, M., MILLS, G., AND BECHTEL, B. WUDAPT, an efficient land use producing data tool for mesoscale models? integration of urban LCZ in WRF over Madrid. *Urban Climate* 17 (2016), 116–134.
- [25] BRUTSAERT, W. *Evaporation into the atmosphere*. Springer, Dordrecht, 1982.
- [26] BUENO, B., NORFORD, L. K., HIDALGO, J., AND PIGEON, G. The urban weather generator. *Journal of Building Performance Simulation* 6, 4 (2012), 269–281.
- [27] BUENO, B., NORFORD, L. K., PIGEON, G., AND BRITTER, R. Combining a detailed building energy model with a physically-based urban canopy model. *Boundary-Layer Meteorology* 140, 3 (2011), 471–489.
- [28] BUENO, B., PIGEON, G., NORFORD, L. K., ZIBOUCHE, K., AND MARCHADIER, C. Development and evaluation of a building energy model integrated in the TEB scheme. *Geoscientific Model Development* 5, 3 (2012), 433–448.
- [29] BUENO, B., ROTH, M., NORFORD, L. K., AND LI, R. Computationally efficient prediction of canopy level urban air temperature at the neighbourhood scale. *Urban Climate* 9 (2014), 35–53.
- [30] BUSINGER, J. A., WYNGAARD, J. C., IZUMI, Y., AND BRADLEY, E. F. Flux-profile relationships in the atmospheric surface layer. *Journal of the Atmospheric Sciences* 28, 2 (1971), 181–189.
- [31] CAMILLONI, I., AND BARRUCAND, M. Temporal variability of the Buenos Aires, Argentina, urban heat island. *Theoretical and Applied Climatology* 107, 1-2 (2012), 47–58.
- [32] CAMPBELL, G. S., AND NORMAN, J. *An introduction to environmental biophysics*. Springer Science & Business Media, 2012.
- [33] CHEN, F., KUSAKA, H., BORNSTEIN, R., CHING, J., GRIMMOND, C. S. B., GROSSMAN-CLARKE, S., LORIDAN, T., MANNING, K. W., MARTILLI, A., MIAO,

- S., SAILOR, D., SALAMANCA, F. P., TAHA, H., TEWARI, M., WANG, X., WYSZOGRODZKI, A. A., AND ZHANG, C. The integrated WRF/urban modelling system: development, evaluation, and applications to urban environmental problems. *Int. J. Climatol.* 31, 2 (2011), 273–288.
- [34] CHIN, H.-N. S., LEACH, M. J., SUGIYAMA, G. A., LEONE JR, J. M., WALKER, H., NASSTROM, J. S., AND BROWN, M. J. Evaluation of an urban canopy parameterization in a mesoscale model using VTMX and URBAN 2000 data. *Monthly Weather Review* 133, 7 (2005), 2043–2068.
- [35] CHOE, J. S., BANG, K. W., AND LEE, J. H. Characterization of surface runoff in urban areas. *Water Science and Technology* 45, 9 (2002), 249–254.
- [36] CHRISTEN, A., MEIER, F., AND SCHERER, D. High-frequency fluctuations of surface temperatures in an urban environment. *Theoretical and Applied Climatology* 108, 1 (2012), 301–324.
- [37] CHRISTEN, A., AND VOGT, R. Energy and radiation balance of a central European city. *International Journal of Climatology* 24, 11 (2004), 1395–1421.
- [38] CITY OF VANCOUVER. Building footprints retrieved from <https://opendata.vancouver.ca/pages/home/>, 2009. Accessed: 1 January 2021.
- [39] COCEAL, O., AND BELCHER, S. E. A canopy model of mean winds through urban areas. *Quarterly Journal of the Royal Meteorological Society* 130, 599 (2004), 1349–1372.
- [40] COLLIER, C. G. The impact of urban areas on weather. *Quarterly Journal of the Royal Meteorological Society* 132, 614 (2006), 1–25.
- [41] COLLINS, D. B. G., AND BRAS, R. L. Plant rooting strategies in water-limited ecosystems. *Water Resources Research* 43, W06407 (2007).
- [42] CONRY, P., FERNANDO, H., LEO, L., SHARMA, A., POTOSNAK, M., AND HELLMANN, J. Multi-scale simulations of climate-change influence on Chicago heat island. In *ASME 2014 4th Joint US-European Fluids Engineering Division Summer Meeting collocated with the ASME 2014 12th International Conference on Nanochannels, Microchannels, and Minichannels* (Chicago, Illinois, USA, August 3-7, 2014), American Society of Mechanical Engineers.
- [43] COSGROVE, A., AND BERKELHAMMER, M. Downwind footprint of an urban heat island on air and lake temperatures. *npj Climate and Atmospheric Science* 1, 1 (2018), 46.

- [44] COUTTS, A. M., BERINGER, J., AND TAPPER, N. J. Impact of increasing urban density on local climate: spatial and temporal variations in the surface energy balance in Melbourne, Australia. *Journal of Applied Meteorology and Climatology* 46, 4 (2007), 477–493.
- [45] COUTTS, A. M., DALY, E., BERINGER, J., AND TAPPER, N. J. Assessing practical measures to reduce urban heat: Green and cool roofs. *Building and Environment* 70 (2013), 266–276.
- [46] CRANK, P. J., SAILOR, D. J., BAN-WEISS, G., AND TALEGHANI, M. Evaluating the ENVI-met microscale model for suitability in analysis of targeted urban heat mitigation strategies. *Urban Climate* 26 (2018), 188–197.
- [47] CRAWFORD, B., AND CHRISTEN, A. Spatial source attribution of measured urban eddy covariance CO₂ fluxes. *Theoretical and Applied Climatology* 119, 3 (2015), 733–755.
- [48] DUPONT, S., OTTE, T. L., AND CHING, J. K. S. Simulation of meteorological fields within and above urban and rural canopies with a mesoscale model. *Boundary-Layer Meteorology* 113, 1 (2004), 111–158.
- [49] DYER, A. J. A review of flux-profile relationships. *Boundary-Layer Meteorology* 7, 3 (1974), 363–372.
- [50] EMMANUEL, R., AND STEEMERS, K. Connecting the realms of urban form, density and microclimate. *Build. Res. Inf.* 46, 8 (2018), 804–808.
- [51] ERELL, E., AND WILLIAMSON, T. Simulating air temperature in an urban street canyon in all weather conditions using measured data at a reference meteorological station. *International Journal of Climatology* 26, 12 (2006), 1671–1694.
- [52] FAN, Y., LI, Y., BEJAN, A., WANG, Y., AND YANG, X. Horizontal extent of the urban heat dome flow. *Scientific Reports* 7, 1 (2017), 11681.
- [53] FAN, Y., LI, Y., AND YIN, S. Interaction of multiple urban heat island circulations under idealised settings. *Building and Environment* 134 (2018), 10–20.
- [54] FAN, Y., LI, Y., AND YIN, S. Non-uniform ground-level wind patterns in a heat dome over a uniformly heated non-circular city. *International Journal of Heat and Mass Transfer* 124 (2018), 233–246.
- [55] FAROUX, S., KAPTUÉ TCHUENTÉ, A. T., ROUJEAN, J.-L., MASSON, V., MARTIN, E., AND LE MOIGNE, P. ECOCLIMAP-II/Europe: a twofold database of ecosystems and surface parameters at 1 km resolution based on satellite information for use in land surface, meteorological and climate models. *Geoscientific Model Development* 6, 2 (2013), 563–582.

- [56] FATICHI, S. *The modeling of hydrological cycle and its interaction with vegetation in the framework of climate change*. PhD thesis, Technische Universität Braunschweig, Braunschweig, 2010.
- [57] FATICHI, S., IVANOV, V. Y., AND CAPORALI, E. A mechanistic ecohydrological model to investigate complex interactions in cold and warm water-controlled environments: 1. theoretical framework and plot-scale analysis. *Journal of Advances in Modeling Earth Systems* 4, 2 (2012), M05002.
- [58] FERNANDO, H. Fluid dynamics of urban atmospheres in complex terrain. *Annual Review of Fluid Mechanics* 42 (2010), 365–389.
- [59] FOUNDA, D., AND SANTAMOURIS, M. Synergies between urban heat island and heat waves in Athens (Greece), during an extremely hot summer (2012). *Scientific Reports* 7, 1 (2017), 10973.
- [60] FRANK, A., HEIDEMANN, W., AND SPINDLER, K. Modeling of the surface-to-surface radiation exchange using a Monte Carlo method. *Journal of Physics: Conference Series* 745, 3 (2016), 032143.
- [61] FUTCHER, J. A. 658-ICE TEA CITY. In *25th Conference on Passive and Low Energy Architecture* (Dublin, October 22-24, 2008).
- [62] GANGULY, A., CHOWDHURY, D., AND NEOGI, S. Performance of building roofs on energy efficiency—a review. *Energy Procedia* 90 (2016), 200–208.
- [63] GARRATT, J. *The Atmospheric Boundary Layer*. Cambridge University Press, London, 1994.
- [64] GARUMA, G. F. Review of urban surface parameterizations for numerical climate models. *Urban Climate* 24 (2018), 830–851.
- [65] GIOMETTO, M. G., CHRISTEN, A., EGLI, P. E., SCHMID, M. F., TOOKE, R. T., COOPS, N. C., AND PARLANGE, M. B. Effects of trees on mean wind, turbulence and momentum exchange within and above a real urban environment. *Advances in Water Resources* 106 (2017), 154–168.
- [66] GOWARDHAN, A. A., PARDYJAK, E. R., SENOCAK, I., AND BROWN, M. J. A CFD-based wind solver for an urban fast response transport and dispersion model. *Environmental Fluid Mechanics* 11, 5 (2011), 439–464.
- [67] GRIMMOND, C. S. B., BEST, M., BARLOW, J., ARNFIELD, A. J., BAIK, J.-J., BAKLANOV, A., BELCHER, S., BRUSE, M., CALMET, I., CHEN, F., CLARK, P., DANDOU, A., ERELL, E., FORTUNIAK, K., HAMDI, R., KANDA, M., KAWAI, T., KONDO, H., KRAYENHOFF, S., LEE, S. H., LIMOR, S.-B., MARTILLI, A., MASSON, V., MIAO, S., MILLS, G., MORIWAKI, R., OLESON, K., PORSON, A.,

- SIEVERS, U., TOMBROU, M., VOOGT, J., AND WILLIAMSON, T. Urban surface energy balance models: model characteristics and methodology for a comparison study. In *Meteorological and Air Quality Models for Urban Areas*, A. Baklanov, C. S. B. Grimmond, A. Mahura, and M. Athanassiadou, Eds. Springer, Berlin, 2009, pp. 97–123.
- [68] GRIMMOND, C. S. B., AND OKE, T. R. Urban water balance: 2. results from a suburb of Vancouver, British Columbia. *Water Resources Research* 22, 10 (1986), 1404–1412.
- [69] GRIMMOND, C. S. B., AND OKE, T. R. Aerodynamic properties of urban areas derived from analysis of surface form. *J. Appl. Meteorol.* 38, 9 (1999), 1262–1292.
- [70] GRIMMOND, C. S. B., SOUCH, C., AND HUBBLE, M. D. Influence of tree cover on summertime surface energy balance fluxes, San Gabriel Valley, Los Angeles. *Clim. Res.* 6, 1 (1996), 45–57.
- [71] GROS, A., BOZONNET, E., AND INARD, C. Cool materials impact at district scale: Coupling building energy and microclimate models. *Sustainable Cities and Society* 13 (2014), 254–266.
- [72] HAGHIGHI, E., SHAHRAEENI, E., LEHMANN, P., AND OR, D. Evaporation rates across a convective air boundary layer are dominated by diffusion. *Water Resources Research* 49, 3 (2013), 1602–1610.
- [73] HAMDI, R., AND MASSON, V. Inclusion of a drag approach in the Town Energy Balance (TEB) scheme: Offline 1D evaluation in a street canyon. *Journal of Applied Meteorology and Climatology* 47 (2008), 2627–2644.
- [74] HAN, J.-Y., BAIK, J.-J., AND LEE, H. Urban impacts on precipitation. *Asia-Pacific Journal of Atmospheric Sciences* 50, 1 (2014), 17–30.
- [75] HANNA, S. R., AND BRITTER, R. E. *Wind flow and vapor cloud dispersion at industrial and urban sites*. American Institute of Chemical Engineers, New York, 2002.
- [76] HARMAN, I. N., BEST, M. J., AND BELCHER, S. E. Radiative exchange in an urban street canyon. *Boundary-Layer Meteorology* 110, 2 (2004), 301–316.
- [77] HE, Y., YU, H., OZAKI, A., AND DONG, N. Thermal and energy performance of green roof and cool roof: A comparison study in Shanghai area. *Journal of Cleaner Production* 267 (2020), 122205.
- [78] HIDALGO, J., MASSON, V., AND GIMENO, L. Scaling the daytime urban heat island and urban-breeze circulation. *Journal of Applied Meteorology and Climatology* 49, 5 (2010), 889–901.

- [79] HSIEH, C.-M., LI, J.-J., ZHANG, L., AND SCHWEGLER, B. Effects of tree shading and transpiration on building cooling energy use. *Energy and Buildings* 159 (2018), 382–397.
- [80] HU, X.-M., XUE, M., KLEIN, P. M., ILLSTON, B. G., AND CHEN, S. Analysis of urban effects in Oklahoma City using a dense surface observing network. *Journal of Applied Meteorology and Climatology* 55, 3 (2016), 723–741.
- [81] HUSAIN, S. Z., ALAVI, N., BÉLAIR, S., CARRERA, M., ZHANG, S., FORTIN, V., ABRAHAMOWICZ, M., AND GAUTHIER, N. The multibudget Soil, Vegetation, and Snow (SVS) scheme for land surface parameterization: Offline warm season evaluation. *Journal of Hydrometeorology* 17, 8 (2016), 2293–2313.
- [82] HUSAIN, S. Z., BÉLAIR, S., AND LEROYER, S. Influence of soil moisture on urban microclimate and surface-layer meteorology in Oklahoma City. *Journal of Applied Meteorology and Climatology* 53, 1 (2014), 83–98.
- [83] IVANOV, V. Y., BRAS, R. L., AND VIVONI, E. R. Vegetation-hydrology dynamics in complex terrain of semiarid areas: 1. a mechanistic approach to modeling dynamic feedbacks. *Water Resources Research* 44, 3 (2008), W03429.
- [84] JÄRVI, L., GRIMMOND, C. S. B., AND CHRISTEN, A. The Surface Urban Energy and Water balance Scheme (SUEWS): Evaluation in Los Angeles and Vancouver. *Journal of Hydrology* 411, 3-4 (2011), 219–237.
- [85] JOFFRE, S. M., KANGAS, M., HEIKINHEIMO, M., AND KITAIGORODSKII, S. A. Variability of the stable and unstable atmospheric boundary-layer height and its scales over a Boreal forest. *Boundary-Layer Meteorology* 99, 3 (2001), 429–450.
- [86] KALANDA, B. D., OKE, T. R., AND SPITTLEHOUSE, D. L. Suburban Energy Balance Estimates for Vancouver, B.C., Using the Bowen Ratio-Energy Balance Approach. *Journal of Applied Meteorology* 19, 7 (1980), 791–802.
- [87] KAR, S. K., LIOU, Y.-A., AND HA, K.-J. Aerosol effects on the enhancement of cloud-to-ground lightning over major urban areas of South Korea. *Atmospheric Research* 92, 1 (2009), 80–87.
- [88] KASTNER-KLEIN, P., BERKOWICZ, R., AND BRITTER, R. The influence of street architecture on flow and dispersion in street canyons. *Meteorology and Atmospheric Physics* 87, 1-3 (2004), 121–131.
- [89] KAWAI, T., RIDWAN, M. K., AND KANDA, M. Evaluation of the simple urban energy balance model using selected data from 1-yr flux observations at two cities. *Journal of Applied Meteorology and Climatology* 48, 4 (2009), 693–715.

- [90] KIKEGAWA, Y., GENCHI, Y., YOSHIKADO, H., AND KONDO, H. Development of a numerical simulation system toward comprehensive assessments of urban warming countermeasures including their impacts upon the urban buildings' energy-demands. *Applied Energy* 76, 4 (2003), 449–466.
- [91] KLEEREKOPER, L., VAN ESCH, M., AND SALCEDO, T. B. How to make a city climate-proof, addressing the urban heat island effect. *Resources, Conservation and Recycling* 64 (2012), 30–38.
- [92] KLEIN, P., AND CLARK, J. V. Flow variability in a North American downtown street canyon. *Journal of Applied Meteorology and Climatology* 46, 6 (2007), 851–877.
- [93] KLEIN, P. M., AND GALVEZ, J. M. Flow and turbulence characteristics in a suburban street canyon. *Environmental Fluid Mechanics* 15, 2 (2015), 419–438.
- [94] KOCHANSKI, A. K., PARDYJAK, E. R., STOLL, R., GOWARDHAN, A., BROWN, M. J., AND STEENBURGH, W. J. One-way coupling of the WRF-QUIC urban dispersion modeling system. *Journal of Applied Meteorology and Climatology* 54, 10 (2015), 2119–2139.
- [95] KONDO, H., GENCHI, Y., KIKEGAWA, Y., OHASHI, Y., YOSHIKADO, H., AND KOMIYAMA, H. Development of a multi-layer urban canopy model for the analysis of energy consumption in a big city: structure of the urban canopy model and its basic performance. *Boundary-Layer Meteorology* 116, 3 (2005), 395–421.
- [96] KONO, T., ASHIE, Y., AND TAMURA, T. Mathematical derivation of spatially-averaged momentum equations for an urban canopy model using underlying concepts of the immersed boundary method. *Boundary-Layer Meteorology* 135, 2 (2010), 185–207.
- [97] KOTTHAUS, S., AND GRIMMOND, C. S. B. Energy exchange in a dense urban environment-part I: Temporal variability of long-term observations in central London. *Urban Climate* 10 (2014), 261–280.
- [98] KRAYENHOFF, E. S. *A multi-layer urban canopy model for neighbourhoods with trees*. PhD thesis, University of British Columbia, Vancouver, 2014.
- [99] KRAYENHOFF, E. S., CHRISTEN, A., MARTILLI, A., AND OKE, T. R. A multi-layer radiation model for urban neighbourhoods with trees. *Boundary-Layer Meteorology* 151, 1 (2014), 139–178.
- [100] KRAYENHOFF, E. S., JIANG, T., CHRISTEN, A., MARTILLI, A., OKE, T. R., BAILEY, B. N., NAZARIAN, N., VOOGT, J. A., GIOMETTO, M. G., STASTNY, A., ET AL. A multi-layer urban canopy meteorological model with trees (BEP-Tree): Street tree impacts on pedestrian-level climate. *Urban Climate* 32 (2020), 100590.

- [101] KRAYENHOFF, E. S., SANTIAGO, J.-L., MARTILLI, A., CHRISTEN, A., AND OKE, T. R. Parametrization of drag and turbulence for urban neighbourhoods with trees. *Boundary-Layer Meteorology* 156, 2 (2015), 157–189.
- [102] KRAYENHOFF, E. S., AND VOOGT, J. A. A microscale three-dimensional urban energy balance model for studying surface temperatures. *Boundary-Layer Meteorology* 123, 3 (2007), 433–461.
- [103] KUSAKA, H., HARA, M., AND TAKANE, Y. Urban climate projection by the WRF model at 3-km horizontal grid increment: dynamical downscaling and predicting heat stress in the 2070’s August for Tokyo, Osaka, and Nagoya metropolises. *Journal of the Meteorological Society of Japan* 90B (2012), 47–63.
- [104] KUSAKA, H., KONDO, H., KIKEGAWA, Y., AND KIMURA, F. A simple single-layer urban canopy model for atmospheric models: comparison with multi-layer and slab models. *Boundary-Layer Meteorology* 101, 3 (2001), 329–358.
- [105] LAIO, F., PORPORATO, A., RIDOLFI, L., AND RODRIGUEZ-ITURBE, I. Plants in water-controlled ecosystems: active role in hydrologic processes and response to water stress: II. probabilistic soil moisture dynamics. *Advances in Water Resources* 24, 7 (2001), 707–723.
- [106] LAUWAET, D., DE RIDDER, K., SAEED, S., BRISSON, E., CHATTERJEE, F., VAN LIPZIG, N. P. M., MAIHEU, B., AND HOOYBERGHS, H. Assessing the current and future urban heat island of Brussels. *Urban Climate* 15 (2016), 1 – 15.
- [107] LEE, H., MATTHEWS, C. J., BRADDOCK, R. D., SANDER, G. C., AND GANDOLA, F. A MATLAB method of lines template for transport equations. *Environmental Modelling & Software* 19, 6 (2004), 603–614.
- [108] LEE, S.-H., AND PARK, S.-U. A vegetated urban canopy model for meteorological and environmental modelling. *Boundary-Layer Meteorology* 126, 1 (2008), 73–102.
- [109] LEMONSU, A., MASSON, V., SHASHUA-BAR, L., ERELL, E., AND PEARLMUTTER, D. Inclusion of vegetation in the Town Energy Balance model for modelling urban green areas. *Geoscientific Model Development* 5, 6 (2012), 1377–1393.
- [110] LI, D., AND BOU-ZEID, E. Synergistic interaction between urban heat islands and heat waves: The impact in cities is larger than the sum of its parts. *Journal of Applied Meteorology and Climatology* 52, 9 (2013), 2051–2064.
- [111] LIU, J., AND NIYOGI, D. Meta-analysis of urbanization impact on rainfall modification. *Scientific Reports* 9, 1 (2019), 7301.

- [112] LOUGHNER, C. P., ALLEN, D. J., ZHANG, D.-L., PICKERING, K. E., DICKERSON, R. R., AND LANDRY, L. Roles of urban tree canopy and buildings in urban heat island effects: parameterization and preliminary results. *Journal of Applied Meteorology and Climatology* 51, 10 (2012), 1775–1793.
- [113] LOUIS, J.-F. A parametric model of vertical eddy fluxes in the atmosphere. *Boundary-Layer Meteorology* 17, 2 (1979), 187–202.
- [114] LUKETICH, A. M., PAPUGA, S. A., AND CRIMMINS, M. A. Ecohydrology of urban trees under passive and active irrigation in a semiarid city. *PloS one* 14, 11 (2019), e0224804.
- [115] LUNDQUIST, K. A., CHOW, F. K., AND LUNDQUIST, J. K. An immersed boundary method for the Weather Research and Forecasting model. *Monthly Weather Review* 138, 3 (2010), 796–817.
- [116] MAHAT, V., TARBOTON, D. G., AND MOLOTCH, N. P. Testing above-and below-canopy representations of turbulent fluxes in an energy balance snowmelt model. *Water Resources Research* 49, 2 (2013), 1107–1122.
- [117] MAHFOUF, J.-F., AND JACQUEMIN, B. A study of rainfall interception using a land surface parameterization for mesoscale meteorological models. *Journal of Applied Meteorology and Climatology* 28, 12 (1989), 1282–1302.
- [118] MAHURA, A., BAKLANOV, A., PETERSEN, C., NIELSEN, N. W., AND AMSTRUP, B. Verification and case studies for urban effects in HIRLAM numerical weather forecasting. In *Meteorological and Air Quality Models for Urban Areas*, A. Baklanov, C. S. B. Grimmond, A. Mahura, and M. Athanassiadou, Eds. Springer, Berlin, 2009, pp. 143–150.
- [119] MANSELL, M. G. *Rural and urban hydrology*. Thomas Telford, London, 2003.
- [120] MARONGA, B., GRYSCHKA, M., HEINZE, R., HOFFMANN, F., KANANI-SÜHRING, F., KECK, M., KETELSEN, K., LETZEL, M. O., SÜHRING, M., AND RAASCH, S. The Parallelized Large-Eddy Simulation Model (PALM) version 4.0 for atmospheric and oceanic flows: model formulation, recent developments, and future perspectives. *Geoscientific Model Development* 8, 8 (2015), 2515–2551.
- [121] MARSALEK, J., CISNEROS, B. J., KARAMOUZ, M., MALMQUIST, P.-A., GOLDENFUM, J. A., AND CHOCAT, B. *Urban water cycle processes and interactions: Urban Water Series-UNESCO-IHP*, vol. 2. CRC Press, Paris, 2008.
- [122] MARTILLI, A., CLAPPIER, A., AND ROTACH, M. W. An urban surface exchange parameterisation for mesoscale models. *Boundary-Layer Meteorology* 104, 2 (2002), 261–304.

- [123] MARTILLI, A., AND SANTIAGO, J. L. CFD simulation of airflow over a regular array of cubes. part II: analysis of spatial average properties. *Boundary-Layer Meteorology* 122, 3 (2007), 635–654.
- [124] MASSON, V. A physically-based scheme for the urban energy budget in atmospheric models. *Boundary-Layer Meteorology* 94, 3 (2000), 357–397.
- [125] MASSON, V., GOMES, L., PIGEON, G., LIOUSSE, C., PONT, V., LAGOUARDE, J. P., VOOGT, J., SALMOND, J., OKE, T. R., HIDALGO, J., LEGAIN, D., GARROUSTE, O., LAC, C., CONNAN, O., BRIOTTET, X., LACHÉRADE, S., AND TULET, P. The Canopy and Aerosol Particles Interactions in TOulouse Urban Layer (CAPITOUL) experiment. *Meteorology and Atmospheric Physics* 102 (2008), 135–157.
- [126] MASSON, V., GRIMMOND, C. S. B., AND OKE, T. R. Evaluation of the Town Energy Balance (TEB) scheme with direct measurements from dry districts in two cities. *Journal of Applied Meteorology and Climatology* 41, 10 (2002), 1011–1026.
- [127] MAUREE, D., BLOND, N., AND CLAPPIER, A. Multi-scale modeling of the urban meteorology: Integration of a new canopy model in the WRF model. *Urban Climate* 26 (2018), 60–75.
- [128] MCGRANE, S. J. Impacts of urbanisation on hydrological and water quality dynamics, and urban water management: a review. *Hydrological Sciences Journal* 61, 13 (2016), 2295–2311.
- [129] MEILI, N., MANOLI, G., BURLANDO, P., BOU-ZEID, E., CHOW, W. T. L., COUTTS, A. M., DALY, E., NICE, K. A., ROTH, M., TAPPER, N. J., VELASCO, E., VIVONI, E. R., AND FATICHI, S. An urban ecohydrological model to quantify the effect of vegetation on urban climate and hydrology (UT&C v1.0). *Geoscientific Model Development* 13, 1 (2020), 335–362.
- [130] MEMON, R. A., LEUNG, D. Y. C., AND LIU, C.-H. A review on the generation, determination and mitigation of urban heat island. *Journal of Environmental Sciences* 20, 1 (2008), 120–128.
- [131] MIAO, C., SUN, Q., BORTHWICK, A. G., AND DUAN, Q. Linkage between hourly precipitation events and atmospheric temperature changes over China during the warm season. *Scientific Reports* 6 (2016), 22543.
- [132] MIAO, S., AND CHEN, F. Formation of horizontal convective rolls in urban areas. *Atmospheric Research* 89, 3 (2008), 298–304.
- [133] MILLS, G. An urban canopy-layer climate model. *Theoretical and Applied Climatology* 57, 3-4 (1997), 229–244.

- [134] MITCHELL, V. G., MCMAHON, T. A., AND MEIN, R. G. Components of the total water balance of an urban catchment. *Environmental Management* 32, 6 (2003), 735–476.
- [135] MOENG, C.-H., DUDHIA, J., KLEMP, J., AND SULLIVAN, P. Examining two-way grid nesting for large eddy simulation of the PBL using the WRF model. *Monthly Weather Review* 135, 6 (2007), 2295–2311.
- [136] MONIN, A. S., AND OBUKHOV, A. M. Basic regularity in turbulent mixing in the surface layer of the atmosphere. *Tr. Akad. Nauk SSSR Geophys. Inst.*, 24 (1957), 163–187.
- [137] MORADI, M., DYER, B., NAZEM, A., NAMBIAR, M. K., NAHIAN, M. R., BUENO, B., MACKEY, C., VASANTHAKUMAR, S., NAZARIAN, N., KRAYENHOFF, E. S., NORFORD, L. K., AND ALIABADI, A. A. The Vertical City Weather Generator (VCWG v1.3.2). *Geosci. Model Dev.* 14, 2 (2021), 961–984.
- [138] MORIWAKI, R., KANDA, M., SENOO, H., HAGISHIMA, A., AND KINOUCHI, T. Anthropogenic water vapor emissions in Tokyo. *Water Resources Research* 44, W11424 (2008).
- [139] MORRISON, W., KOTTHAUS, S., GRIMMOND, C. S. B., INAGAKI, A., YIN, T., GASTELLU-ETCHEGORRY, J.-P., KANDA, M., AND MERCHANT, C. J. A novel method to obtain three-dimensional urban surface temperature from ground-based thermography. *Remote Sensing of Environment* 215 (2018), 268–283.
- [140] MORTEZAZADEH, M., JANDAGHIAN, Z., AND WANG, L. L. Integrating CityFFD and WRF for modeling urban microclimate under heatwaves. *Sustainable Cities and Society* 66 (2021), 102670.
- [141] MORTEZAZADEH, M., AND WANG, L. An adaptive time-stepping semi-Lagrangian method for incompressible flows. *Numerical Heat Transfer, Part B: Fundamentals* 75, 1 (2019), 1–18.
- [142] MORTEZAZADEH, M., AND WANG, L. L. A high-order backward forward sweep interpolating algorithm for semi-Lagrangian method. *International Journal for Numerical Methods in Fluids* 84, 10 (2017), 584–597.
- [143] MORTEZAZADEH, M., AND WANG, L. L. SLAC—a semi-Lagrangian artificial compressibility solver for steady-state incompressible flows. *International Journal of Numerical Methods for Heat & Fluid Flow* 29, 6 (2019), 1965–1983.
- [144] MORTEZAZADEH, M., AND WANG, L. L. Solving city and building microclimates by fast fluid dynamics with large timesteps and coarse meshes. *Building and Environment* 179 (2020), 106955.

- [145] MUSSETTI, G., BRUNNER, D., HENNE, S., ALLEGRI, J., KRAYENHOFF, E. S., SCHUBERT, S., FEIGENWINTER, C., VOGT, R., WICKI, A., AND CARMELIET, J. COSMO-BEP-Tree v1.0: a coupled urban climate model with explicit representation of street trees. *Geoscientific Model Development* 13, 3 (2020), 1685–1710.
- [146] NAZARIAN, N., AND KLEISSL, J. Realistic solar heating in urban areas: air exchange and street-canyon ventilation. *Building and Environment* 95 (2016), 75–93.
- [147] NAZARIAN, N., KRAYENHOFF, E. S., AND MARTILLI, A. A one-dimensional model of turbulent flow through “urban” canopies (MLUCM v2.0): updates based on large-eddy simulation. *Geoscientific Model Development* 13, 3 (2020), 937953.
- [148] NAZARIAN, N., MARTILLI, A., AND KLEISSL, J. Impacts of realistic urban heating, Part I: spatial variability of mean flow, turbulent exchange and pollutant dispersion. *Boundary-Layer Meteorology* 166, 3 (2018), 367–393.
- [149] NICE, K. A., COUTTS, A. M., AND TAPPER, N. J. Development of the VTUF-3D v1.0 urban micro-climate model to support assessment of urban vegetation influences on human thermal comfort. *Urban Climate* 24 (2018), 1052–1076.
- [150] NIMMO, J. R. Unsaturated zone flow processes. *Encyclopedia of hydrological sciences* (2006).
- [151] OKE, T. R. City size and the urban heat island. *Atmospheric Environment (1967)* 7, 8 (1973), 769–779.
- [152] OKE, T. R. The distinction between canopy and boundary-layer urban heat islands. *Atmosphere* 14, 4 (1976), 268–277.
- [153] OKE, T. R. The energetic basis of the urban heat island. *Quarterly Journal of Royal Meteorological Society* 108, 455 (1982), 1–24.
- [154] OKE, T. R. Street design and urban canopy layer climate. *Energy and Buildings* 11, 1-3 (1988), 103 – 113.
- [155] OKE, T. R., JOHNSON, G. T., STEYN, D. G., AND WATSON, I. D. Simulation of surface urban heat islands under ‘ideal’ conditions at night part 2: Diagnosis of causation. *Boundary-Layer Meteorology* 56, 4 (1991), 339–358.
- [156] OKE, T. R., MILLS, G., CHRISTEN, A., AND VOOGT, J. A. *Urban Climates*. Cambridge University Press, London, 2017.
- [157] OKE, T. R., SPRONKEN-SMITH, R. A., JÁUREGUI, E., AND GRIMMOND, C. S. B. The energy balance of central Mexico City during the dry season. *Atmospheric environment* 33, 24-25 (1999), 3919–3930.

- [158] OLESON, K. W., BONAN, G. B., FEDDEMA, J., VERTENSTEIN, M., AND GRIMMOND, C. S. B. An urban parameterization for a global climate model. part I: Formulation and evaluation for two cities. *Journal of Applied Meteorology and Climatology* 47, 4 (2008), 1038–1060.
- [159] OLESON, K. W., DAI, Y., BONAN, G., BOSILOVICH, M., DICKINSON, R., DIRMEYER, P., HOFFMAN, F., HOUSER, P., LEVIS, S., NIU, G.-Y., ET AL. Technical description of the Community Land Model (CLM). *Tech. Note NCAR/TN-461+STR* (2004). Boulder.
- [160] OPENSTREETMAP CONTRIBUTORS. Planet dump retrieved from <https://planet.osm.org>, 2017. Accessed 1 January 2021.
- [161] PAULSON, C. A. The mathematical representation of wind speed and temperature profiles in the unstable atmospheric surface layer. *J. Appl. Meteorol.* 9, 6 (1970), 857–861.
- [162] PENMAN, H. L. Natural evaporation from open water, bare soil and grass. *Proceedings of the Royal Society of London. Series A. Mathematical and Physical Sciences* 193, 1032 (1948), 120–145.
- [163] POPE, S. B. *Turbulent flows*. Cambridge University Press, Cambridge, 2000.
- [164] RAMAMURTHY, P., AND BOU-ZEID, E. Contribution of impervious surfaces to urban evaporation. *Water Resources Research* 50, 4 (2014), 2889–2902.
- [165] RAUPACH, M. R., ANTONIA, R. A., AND RAJAGOPALAN, S. Rough-wall turbulent boundary layers. *Applied Mechanics Review* 44, 1 (1991), 1–25.
- [166] RAUPACH, M. R., THOM, A. S., AND EDWARDS, I. A wind-tunnel study of turbulent flow close to regularly arrayed rough surfaces. *Bound.-Lay. Meteorol.* 18, 4 (1980), 373–397.
- [167] REDON, E. C., LEMONSU, A., MASSON, V., MORILLE, B., AND MUSY, M. Implementation of street trees within the solar radiative exchange parameterization of TEB in SURFEX v8.0. *Geoscientific Model Development* 10, 1 (2017), 385–411.
- [168] RESLER, J., KRČ, P., BELDA, M., JURUŠ, P., BENEŠOVÁ, N., LOPATA, J., VLČEK, O., DAMAŠKOVÁ, D., EBEN, K., DERBEK, P., MARONGA, B., AND KANANI-SÜHRING, F. PALM-USM v1. 0: A new urban surface model integrated into the PALM large-eddy simulation model. *Geoscientific Model Development* 10, 10 (2017), 3635–3659.
- [169] RODRIGUEZ-ITURBE, I., PORPORATO, A., RIDOLFI, L., ISHAM, V., AND COXI, D. Probabilistic modelling of water balance at a point: the role of climate, soil and vegetation. *Proceedings of the Royal Society of London. Series A: Mathematical, Physical and Engineering Sciences* 455, 1990 (1999), 3789–3805.

- [170] ROTACH, M. W., VOGT, R., BERNHOFER, C., BATCHVAROVA, E., CHRISTEN, A., CLAPPIER, A., FEDDERSEN, B., GRYNING, S. E., MARTUCCI, G., MAYER, H., MITEV, V., OKE, T. R., PARLOW, E., RICHNER, H., ROTH, M., ROULET, Y. A., RUFFIEUX, D., SALMOND, J. A., SCHATZMANN, M., AND VOOGT, J. A. BUBBLE—an urban boundary layer meteorology project. *Theoretical and Applied Climatology* 81, 3 (2005), 231–261.
- [171] ROTH, M. Review of atmospheric turbulence over cities. *Quarterly Journal of the Royal Meteorological Society* 126, 564 (2000), 941–990.
- [172] RUNNALLS, K. E., AND OKE, T. R. Dynamics and controls of the near-surface heat island of Vancouver, British Columbia. *Physical Geography* 21, 4 (2000), 283–304.
- [173] RYU, Y.-H., BAIK, J.-J., AND LEE, S.-H. A new single-layer urban canopy model for use in mesoscale atmospheric models. *Journal of Applied Meteorology and Climatology* 50, 9 (2011), 1773–1794.
- [174] RYU, Y.-H., BOU-ZEID, E., WANG, Z.-H., AND SMITH, J. A. Realistic representation of trees in an urban canopy model. *Boundary-Layer Meteorology* 159 (2016), 193–220.
- [175] SABATER, M. ERA5-land hourly data from 1981 to present. *Copernicus Climate Change Service (C3S) Climate Data Store (CDS)* (2019).
- [176] SAILOR, D. J. A review of methods for estimating anthropogenic heat and moisture emissions in the urban environment. *International Journal of Climatology* 31, 2 (2011), 189–199.
- [177] SALAMANCA, F., GEORGESCU, M., MAHALOV, A., MOUSTAOU, M., AND MARTILLI, A. Citywide impacts of cool roof and rooftop solar photovoltaic deployment on near-surface air temperature and cooling energy demand. *Boundary-Layer Meteorology* 161, 1 (2016), 203–221.
- [178] SALAMANCA, F., GEORGESCU, M., MAHALOV, A., MOUSTAOU, M., AND WANG, M. Anthropogenic heating of the urban environment due to air conditioning. *Journal of Geophysical Research: Atmospheres* 119, 10 (2014), 5949–5965.
- [179] SALAMANCA, F., KRPO, A., MARTILLI, A., AND CLAPPIER, A. A new building energy model coupled with an urban canopy parameterization for urban climate simulations—part I. formulation, verification, and sensitivity analysis of the model. *Theoretical and Applied Climatology* 99, 3-4 (2010), 331–344.
- [180] SANEINEJAD, S., MOONEN, P., DEFRAEYE, T., DEROME, D., AND CARMELIET, J. Coupled CFD, radiation and porous media transport model for evaluating evaporative cooling in an urban environment. *Journal of Wind Engineering and Industrial Aerodynamics* 104-106 (2012), 455–463.

- [181] SANTIAGO, J. L., KRAYENHOFF, E. S., AND MARTILLI, A. Flow simulations for simplified urban configurations with microscale distributions of surface thermal forcing. *Urban Climate* 9 (2014), 115–133.
- [182] SANTIAGO, J. L., AND MARTILLI, A. A dynamic urban canopy parameterization for mesoscale models based on computational fluid dynamics Reynolds-Averaged Navier-Stokes microscale simulations. *Bound.-Lay. Meteorol.* 137, 3 (2010), 417–439.
- [183] SIMÓN-MORAL, A., SANTIAGO, J. L., AND MARTILLI, A. Effects of unstable thermal stratification on vertical fluxes of heat and momentum in urban areas. *Boundary-Layer Meteorology* 163, 1 (2017), 103–121.
- [184] SIMPSON, J. R., AND MCPHERSON, E. G. Potential of tree shade for reducing residential energy use in California. *Journal of Arboriculture* 22, 1 (1996), 10–18.
- [185] SIU, L. W., AND HART, M. A. Quantifying urban heat island intensity in Hong Kong SAR, China. *Environmental Monitoring and Assessment* 185, 5 (2013), 4383–4398.
- [186] SOUCH, C. A., AND SOUCH, C. The effect of trees on summertime below canopy urban climates: a case study Bloomington, Indiana. *Journal of Arboriculture* 19, 5 (1993), 303–312.
- [187] SOULHAC, L., SALIZZONI, P., CIERCO, F.-X., AND PERKINS, R. The model SIR-ANE for atmospheric urban pollutant dispersion; part I, presentation of the model. *Atmospheric Environment* 45, 39 (2011), 7379–7395.
- [188] SRIVANIT, M., AND HOKAO, K. Evaluating the cooling effects of greening for improving the outdoor thermal environment at an institutional campus in the summer. *Building and Environment* 66 (2013), 158–172.
- [189] STAVROPULOS-LAFFAILLE, X., CHANCIBAULT, K., BRUN, J.-M., LEMONSU, A., MASSON, V., BOONE, A., AND ANDRIEU, H. Improvements to the hydrological processes of the town energy balance model (TEB-veg, SURFEX v7.3) for urban modelling and impact assessment. *Geoscientific Model Development* 11, 10 (2018), 4175–4194.
- [190] STEPHENS, D. B. *Vadose zone hydrology*. CRC press, Boca Raton, 1995.
- [191] STEWART, I. D. Why should urban heat island researchers study history? *Urban Climate* 30 (2019), 100484.
- [192] STEWART, I. D., AND OKE, T. R. Local climate zones for urban temperature studies. *Bulletin of the American Meteorological Society* 93, 12 (2012), 1879–1900.
- [193] STULL, R. B. *An introduction to boundary layer meteorology*. Kluwer Academic Publishers, Dordrecht, The Netherlands, 1988.

- [194] TALBOT, C., BOU-ZEID, E., AND SMITH, J. Nested mesoscale large-eddy simulations with WRF: performance in real test cases. *J. Hydrometeorol.* 13, 5 (2012), 1421–1441.
- [195] TAN, Z., LAU, K. K.-L., AND NG, E. Planning strategies for roadside tree planting and outdoor comfort enhancement in subtropical high-density urban areas. *Building and Environment* 120 (2017), 93–109.
- [196] THEEUWES, N. E., BARLOW, J. F., TEULING, A. J., GRIMMOND, C. S. B., AND KOTTHAUS, S. Persistent cloud cover over mega-cities linked to surface heat release. *npj Climate and Atmospheric Science* 2, 1 (2019), 15.
- [197] TSENG, Y.-H., MENEVEAU, C., AND PARLANGE, M. B. Modeling flow around bluff bodies and predicting urban dispersion using large eddy simulation. *Environmental Science and Technology* 40, 8 (2006), 2653–2662.
- [198] TSOKA, S., LEDUC, T., AND RODLER, A. Assessing the effects of urban street trees on building cooling energy needs: The role of foliage density and planting pattern. *Sustainable Cities and Society* 65 (2021), 102633.
- [199] WALESH, S. G. *Urban surface water management*. John Wiley & Sons, New York, 1991.
- [200] WANG, C., WANG, Z.-H., AND YANG, J. Cooling effect of urban trees on the built environment of contiguous United States. *Earth’s Future* 6, 8 (2018), 1066–1081.
- [201] WANG, H., SKAMAROCK, W. C., AND FEINGOLD, G. Evaluation of scalar advection schemes in the advanced research WRF model using large-eddy simulations of aerosol-cloud interactions. *Monthly Weather Review* 137, 8 (2009), 2547–2558.
- [202] WANG, Z.-H. Geometric effect of radiative heat exchange in concave structure with application to heating of steel I-sections in fire. *International Journal of Heat and Mass Transfer* 53, 5-6 (2010), 997–1003.
- [203] WANG, Z.-H. Monte Carlo simulations of radiative heat exchange in a street canyon with trees. *Solar Energy* 110 (2014), 704 – 713.
- [204] WANG, Z.-H., BOU-ZEID, E., AND SMITH, J. A. A coupled energy transport and hydrological model for urban canopies evaluated using a wireless sensor network. *Quarterly Journal of the Meteorological Society* 139, 675 (2013), 1643–1657.
- [205] WONG, M. S., NICHOL, J. E., TO, P. H., AND WANG, J. A simple method for designation of urban ventilation corridors and its application to urban heat island analysis. *Building and Environment* 45, 8 (2010), 1880–1889.
- [206] YAGHOUBIAN, N., AND KLEISSL, J. Effect of reflective pavements on building energy use. *Urban Climate* 2 (2012), 25–42.

- [207] YANG, J., WANG, Z.-H., CHEN, F., MIAO, S., TEWARI, M., VOOGT, J. A., AND MYINT, S. Enhancing hydrologic modelling in the coupled Weather Research and Forecasting-urban modelling system. *Boundary-Layer Meteorology* 155, 1 (2015), 87–109.
- [208] YANG, J., WANG, Z.-H., GEORGESCU, M., CHEN, F., AND TEWARI, M. Assessing the impact of enhanced hydrological processes on urban hydrometeorology with application to two cities in contrasting climates. *Journal of Hydrometeorol.* 17, 4 (2016), 1031–1047.
- [209] YANG, X., AND LI, Y. The impact of building density and building height heterogeneity on average urban albedo and street surface temperature. *Building and Environment* 90 (2015), 146–156.
- [210] YANG, X., LI, Y., LUO, Z., AND CHAN, P. W. The urban cool island phenomenon in a high-rise high-density city and its mechanisms. *Int. J. Climatol.* 37, 2 (2017), 890–904.
- [211] YUAN, C., NORFORD, L. K., AND NG, E. A semi-empirical model for the effect of trees on the urban wind environment. *Landscape and Urban Planning* 168 (2017), 84–93.
- [212] ZAJIC, D., FERNANDO, H. J. S., CALHOUN, R., PRINCEVAC, M., BROWN, M. J., AND PARDYJAK, E. R. Flow and turbulence in an urban canyon. *Journal of Applied Meteorology and Climatology* 50, 1 (2011), 203–223.
- [213] ZENG, X., AND DICKINSON, R. E. Effect of surface sublayer on surface skin temperature and fluxes. *Journal of Climate* 11, 4 (1998), 537–550.
- [214] ZHANG, X., FRIEDL, M. A., SCHAAF, C. B., STRAHLER, A. H., AND SCHNEIDER, A. The footprint of urban climates on vegetation phenology. *Geophysical Research Letters* 31, L12209 (2004).
- [215] ZHOU, B., RYBSKI, D., AND KROPP, J. P. The role of city size and urban form in the surface urban heat island. *Scientific Reports* 7, 1 (2017), 4791.
- [216] ZHOU, D., ZHAO, S., ZHANG, L., SUN, G., AND LIU, Y. The footprint of urban heat island effect in China. *Scientific Reports* 5 (2015), 11160.

Appendix A

Published Work

A.1 Peer-Reviewed Journal Papers

1. Moradi, M., Dyer, B., Nazem, A., Nambiar, M. K., Nahian, M. R., Bueno, B., Mackey, C., Vasanthakumar, S., Nazarian, N., Krayenhoff, E. S., Norford, L. K., Aliabadi, A. A. (2021), ‘The Vertical City Weather Generator (VCWG v1.3.2)’, **Geoscientific Model Development**, 14(2) 961-984. [Chapters 1, 2, 3 and 5]
2. Moradi, M., Krayenhoff, E. S., Norford, L. K., Aliabadi, A. A. (2021), ‘A comprehensive indoor-outdoor urban climate model with hydrology: The Vertical City Weather Generator (VCWG v2.0.0)’, **Building and Environment**, under review [Chapters 1,2,4 and 5]
3. Aliabadi, A. A., Moradi, M., McLeod, R. M., Calder, D., Dernovsek, R. (2021), ‘How much Building Renewable Energy is Enough? the Vertical City Weather Generator (VCWG v1.4.4)’, **Atmosphere**, 12(7), 882.
4. Aliabadi, A. A., Moradi, M., Byerlay, R. A. E. (2021), ‘The Budgets of Turbulence Kinetic Energy and Heat in the Urban Roughness Sublayer’, **Environmental Fluid Mechanics**.
5. Nambiar, M. K., Bayerly, R. A., Nazem, A., Nahian, M. R., Moradi, M., Aliabadi, A. A., (2020), ‘A Tethered Air Blimp (TAB) for Observing the Microclimate over a Complex Terrain’, **Geoscientific Instrumentation, Methods, and Data Systems**, 9(1), 193-211.

6. Aliabadi, A. A., Moradi, M., Clement, D., Lubitz, W. D., Gharabaghi, B., (2019), ‘Flow and Temperature Dynamics in an Urban Canyon Under a Comprehensive Set of Wind Directions, Wind Speeds, and Thermal Stability Conditions’, **Environmental Fluid Mechanics**, 19(1), 81-109.

A.2 Refereed Conferences

1. Aliabadi, A. A., Moradi, M., (January 12-16, 2020), ‘The Budget of Turbulence Kinetic Energy and Heat in the Urban Roughness Sublayer’, **100th American Meteorological Society Annual Meeting**, Boston, USA.
2. Moradi, M., Dyer, B., Nambiar, M. K., Nazem, A., Nahian, M. R., Lubitz, W. D., Krayenhoff, E. S. & Aliabadi, A. A. (June 2-5, 2019), ‘A Vertical Diffusion Model to Predict Profiles of Temperature within the Lower Atmospheric Surface Layer: Simple or Complicated?’, **Canadian Society for Mechanical Engineering (CSME) International Congress**, London, Canada.
3. Aliabadi, A. A., Moradi, M., Clement, D., Lubitz, W. D., Gharabaghi, B., (August 6-10, 2018), ‘Complete Characterization of Turbulence in an Urban Canyon Under All Wind Directions, Wind Speeds, and Thermal Stability Conditions’, **14th Symposium on the Urban Environment**, New York, USA.
4. Moradi, M., Lubitz, W. D., Krayenhoff, E. S., Aliabadi, A. A., (May 27-30, 2018), ‘Scaling and Machine Learning Analysis of Turbulent Fluxes of Momentum and Heat in the Microclimate of an Urban Canyon’, **Canadian Society for Mechanical Engineering International Congress**, Toronto, Canada.

Appendix B

Code Availability

The source code is available under the GPL 3.0 license at <https://opensource.org/licenses/GPL-3.0> and can be downloaded by contacting the author or from <https://github.com/MMoradi-Eng>.